1st MYGEC

1st Mediterranean Young Geotechnical Engineers Conference

Double Events - MYGEC & EYGEC

23-24th September, 2019

Kefaluka Resort Hotel Bodrum, Muğla-Turkey

PROCEEDINGS

www.mygec2019.org

1st MYGEC
1st Mediterranean Young Geotechnical Engineers Conference
Double Events - MYGEC & EYGEC
23-24th September, 2019
Kefaluka Resort Hotel Bodrum, Muğla-Turkey

Turkish Society for ISSMGE (ZMGM)

Muğla Sıtkı Koçman University (MSKU)

International Society for Soil Mechanics and Geotechnical Engineering (ISSMGE)

Proceedings of the

1st Mediterranean Young Geotechnical Engineers Conference

23-24 Eylül 2019, Bodrum, Turkey

EDITORS

Deniz ÜLGEN

Altuğ SAYGILI

Mehmet Rifat KAHYAOĞLU

Selda DURMAZ

Onur TOYGAR

Aysu GÖÇÜGENCİ

COMMITTEES

Organizing Committee

Deniz ÜLGEN (Muğla Sıtkı Koçman University)

Altuğ SAYGILI (Muğla Sıtkı Koçman University)

M. Rifat KAHYAOĞLU (Muğla Sıtkı Koçman University)

Onur TOYGAR (Muğla Sıtkı Koçman University)

Selda DURMAZ (Muğla Sıtkı Koçman University)

Aysu GÖÇÜGENCİ (Muğla Sıtkı Koçman University)

MUYAP-Construction Society (Muğla Sıtkı Koçman University)

Advisory Committee

Prof.Dr. Charles W.W. Ng (President of ISSMGE)

Prof.Dr. Mario MANASSERO (Vice-President of the ISSMGE for Europe (2017-2021))

Prof.Dr. Roger FRANK (President of the ISSMGE (2013-2017))

Prof.Dr. Neil TAYLOR (ISSMGE Secretary General)

Prof.Dr. Fatma BALIGH (Immediate Past ISSMGE Vice President for Africa)

Prof.Dr. George GAZETAS (Hellenic Society of SMGE - President)

Prof.Dr. Cavit ATALAR (Near East University)

Prof.Dr. Safiye Feyza ÇİNİCİOĞLU (ZMGM-Turkish Society for ISSMGE-President)

MSc. Müge İNANIR (ZMGM-Turkish Society for ISSMGE-Board Member)

Prof.Dr. Recep İYİSAN (ZMGM-Turkish Society for ISSMGE-Board Member)

Prof.Dr. Kutay ÖZAYDIN (ZMGM-Turkish Society for ISSMGE-Board Member)

Prof.Dr. Hilmi Turan DURGUNOĞLU (ZMGM-Turkish Society for ISSMGE-Board Member)

Prof.Dr. Fazlı Erol GÜLER (ZMGM-Turkish Society for ISSMGE-Board Member)

Prof.Dr. Kemal Önder ÇETİN (ZMGM-Turkish Society for ISSMGE-Board Member)

Prof.Dr. Mehmet Muhit BERİLGEN (ZMGM-Turkish Society for ISSMGE-Board Member)

Prof.Dr. İlknur BOZBEY (ZMGM-Turkish Society for ISSMGE-Board Member)

Scientific Committee

Prof. Dr. Castorina Silva VIEIRA (University of Porto)

Prof. Dr. Fabrice EMERIAULT (Grenoble Institute of Technology)

Prof. Dr. Khalid Mohamed ELZAHABY (Housing and Building National Research Centre)

Prof. Dr. Luljeta BOZO (Polis University (Professor Emeritus))
Prof. Dr. Nicola MORACI (Mediterranean University of Reggio Calabria)
Prof. Dr. Sabid ZEKAN (University of Tuzla)
Prof. Dr. Smail HADDADI (University of Science and Technology Houari Boumediene)
Prof. Dr. Talal AWWAD (Eurasian National University • Faculty of Architecture and Construction)
Assoc.Prof.Dr. Bojan ŽLENDER (Transportation Engineering and Architecture in Maribor, Slovenia)
Assoc.Prof. Dr. Sami MONTASSAR (University of Tunis El Manar)
Assist. Prof. Dr. Aneta HERBUT (Wroclaw University of Science and Technology)
Assist.Prof. Dr. Erion BUKACI (Universiteti Politeknik i Tiranës)
Assist.Prof. Dr. Jovan PAPIC (Ss. Cyril and Methodius University)
Dr. Fernando PARDO DE SANTAYANA (Laboratorio de Geotecnia)
Dr. Grigorios TSINIDIS (VCE - Vienna Consulting Engineers ZT GmbH)
Dr. Houssine EJJAAOUANI (Laboratoire Public d'Essais et d'Etudes)
Assoc.Prof. Dr. Cihan Taylan AKDAĞ (Türk-Alman University)
Assoc.Prof. Dr. Nazile URAL (Bilecik Şeyh Edebali University)
Assoc.Prof. Dr. Sedat SERT (Sakarya University)
Assist.Prof. Dr. Berrak TEYMÜR (İstanbul Technical University)
Assist.Prof. Dr. Ebru AKIŞ (Atılım University)
Assist.Prof. Dr. Evren SEYREK (Dumlupınar University)
Assist.Prof. Dr. Hakkı Oral ÖZHAN (Altınbaş University)
Assist.Prof. Dr. Mehmet Can BALCI (Batman University)
Assist.Prof. Dr. Mehmet Cemal ACAR (Erciyes University)
Assist.Prof. Dr. Murat HAMDERİ (Türk-Alman University)
Assist.Prof. Dr. Müge AKIN (Abdullah Gül University)
Assist.Prof. Dr. Nejan HUVAJ (Middle East Technical University)
Assist.Prof. Dr. Rahim Kağan AKBULUT (Atatürk University)
Assist.Prof. Dr. Selçuk BİLDİK (Nişantaşı University)
Assist.Prof. Dr. Şevki ÖZTÜRK (Erzurum Technical University)
Assist.Prof. Dr. Tanay KARADEMİR (İstanbul Bilgi University)
Assist.Prof. Dr. Uğur DAĞDEVİREN (Dumlupınar University)
Assist.Prof. Dr. Volkan KALPAKCI (Hasan Kalyoncu University)
Assist.Prof. Dr. Yeşim Sema ÜNSEVER (Uludağ University)
Assist.Prof. Dr. Zeynep Neşe KURT ALBAYRAK (Atatürk University)
Dr. Murat Ergenekon SELÇUK (Yıldız Teknik University)

Dr. Tolga Y. ÖZÜDOĞRU (İstanbul Technical University)

Dr. A. Anıl YUNATÇI (GEODESTEK ZEMAR LTD.)

Dr. Aslı ÖZÖKESKİN ÇEVİK (ART GEODESIGN MÜŞAVIRLIK MÜHENDISLIK TIC. A.Ş.)

Dr. Elif YILMAZ (GEOSTAR PROJE DANIŞMANLIK MÜH.SAN.TIC.LTD.ŞTI.)

Dr. Hüsnü Korhan ÖZALP (ENAR MÜH. MİM. DANIŞMANLIK LTD. ŞTİ.)

M.Sc. Alp GÖKALP (KASKTAŞ A.Ş)

M.Sc. Ece KURT BAL (SENTEZ İNŞAAT SAN VE TİC LTD.ŞTİ.)

M.Sc. Emel HACIALİOĞLU (ZEMİN ETÜD VE TASARIM A.Ş.)

M.Sc. Mustafa KOÇ (DESTECH)

M.Sc. Orhan Esat İNANIR (GEOGRUP İNŞAAAT)

M.Sc. Ozan DADAŞBİLGE (GEOCON)

M.Sc. Önder AKÇAKAL (ZETAŞ ZEMİN TEKNOLOJİSİ A.Ş.)

M.Sc. Serkan AKSU (TREVI AŞ)

M.Sc. Sevinç Şehnaz AKTAŞ (EMAY)

SPONSORS

Workshop Sponsor

FUGRO

Gold Sponsor

ZEMİN ETÜD ve TASARIM A.Ş.

Silver Sponsor

TREVI

Bronze Sponsors

BODTO
T.C. BODRUM TİCARET ODASI
BODRUM CHAMBER OF COMMERCE

SCIENTIFIC PROGRAMME

Monday, 23th September, 2019

09.00 – 10:00	Registration
10.00 – 10:30	Welcome Ceremony
	Chairperson: Prof. S. Feyza Çinicioğlu
10:30 – 11:15	**Keynote Speaker: Prof. Lyesse Laloui** **Topic: Tailor-made soil properties with novel bio-geo-chemical means**
11:15 – 11:30	Coffee Break
	Chairperson: Prof. Kemal Önder Çetin
11:30 – 12:15	**Keynote Speaker: Prof. George Gazetas** **Topic: Learning from observations of geotechnical performance in earthquakes**
12:15 – 13:30	Lunch Break
13:30 – 14:45	Session I **Chairperson: Prof. Lyesse Laloui**
	Thermal conductivity behavior of tincal added sand-bentonite mixtures Yeliz Yükselen Aksoy, Mesut Şahin Irgat
	Membrane behavior of clay soils permeated with multi-electrolyte aqueous solutions Nicolò Guarena, Andrea Dominijanni, Mario Manassero
	Evaluation of compaction and consolidation behavior of sand-bentonite mixtures with pumice additive Esra Güneri, Yeliz Yükselen Aksoy
	Categorizing the sedimentation characteristics of bentonites based on physico-chemical properties El Hassen ABD Moulana, Esra Dikişci, Ali Hakan Ören
	The effect of ulexite additive on the engineering properties of sand-bentonite mixtures for liners S. Gizem Alpaydın, Yeliz Yükselen Aksoy
14:45 – 15:00	Coffee Break
15:00 – 16:00	Session II **Chairperson: Assoc. Prof. Ali Hakan Ören**
	Numerical evaluation of the soil behavior during impact driving of pipe-piles Reza Daryaei, Montaser Bakroon, Daniel Aubram, Frank Rackwitz

	Influence of base grouting on load distribution in a bored pile Adam Krasiński, Mateusz Wiszniewski
	Finite element-based geotechnical risk analysis for anchor-supported deep excavations Sinem Bozkurt, Sami Oğuzhan Akbaş
	Socket roughness effect on side shear resistance prediction of rock-socketed piles José Gregorio Gutiérrez-Ch, Svetlana Melentijevic, Salvador Senent, Rafael Jimenez
16:00 – 16:15	Coffee Break
16:15 – 17:15	Session III **Chairperson: Assoc. Prof. Okan Önal**
	Seismic hazard analyses in micro scale for Manisa city center Esra Güneri, Ender Başarı
	Seismic coefficient assessment of concrete faced rock fill dams Selda Durmaz, Deniz Ülgen
	Numerical evaluation of the pipe-pile buckling during vibratory driving in sand Montaser Bakroon, Reza Daryaei, Daniel Aubram, Frank Rackwitz
	Numerical study on reducing the ground borne vibration using open trench and rubber-chips filled trench wave barriers Mohammad Mouaz Hassoun, Deniz Ülgen, Onur Toygar, Selda Durmaz

Tuesday, 24th September, 2019

	Chairperson: Prof. George Gazetas
08:30 – 09:15	**Keynote Speaker: Assoc. Prof. Wissem Frikha** **Topic: The use of stone columns for liquefaction mitigation**
09:15 – 09:30	Coffee Break
	Chairperson: Dr. M. Rifat Kahyaoğlu
09:30 – 10:15	**Keynote Speaker: Prof. Yeliz Yükselen Aksoy** **Topic: Specific surface area and pore size distribution: How these parameters affect engineering behavior of fine grained soils**
10:15 – 10:30	Coffee Break
	Chairperson: Assoc. Prof. Wissem Frikha
10:30 – 11:15	**Keynote Speaker: Dr. Sebahat Gök Kalmaz** **Topic: Recent challenges in geotechnical features in Dubai, UAE**

11:15– 11:30	Coffee Break
11:30 – 12:30	Session IV **Chairperson: Prof. Fatma Baligh**
	The importance of the horizontal soil stresses on the bearing capacity of a foundation pile Shilton Rica, Stefan Van Baars, Borana Kullolli
	Main causes of injection bore anchors failures within CIS Countries Vladimir Matsiy
	Rigid inclusions as a foundation support system in soft clay Bahattin Berk Ayraçma, Berrak Teymür, Ozan Alver
	A rheological model to describe the mechanical response of earth embankments on piled foundation Viviana Mangraviti, Luca Flessati, Claudio di Prisco
12:30 – 13:30	Lunch Break
13:30 -14:30	Session V **Chairperson: Prof. Yeliz Yükselen Aksoy**
	Behavior of strip footing near slope under eccentric loading Messaoud Baazouzi, Badis Mazouz, Khalifa Abech, Boudiaf Khaoula
	An improved design for soil-nailed walls using limit equilibrium analysis Jean De Sauvage
	Critical slip surface determination in slope stability analysis using optimization algorithms Panagiotis Aivaliotis Apostolopoulos, Dimitrios Loukidis
	Development of direct shear and triaxial test procedures on microbially treated sand samples Mert Tunalı, Emre Duman, Yılmaz Emre Sarıçiçek, Onur Pekcan, Rafig Gurbanov, Ayşe Gül Gözen
14:30 – 14:45	Coffee Break
14:45 – 15:30	Session VI **Chairperson: Dr. Altuğ Saygılı**
	An elasto-plastic model for clays subjected to changes in pore fluid chemical composition Giulia Scelsi, Gabriele Della Vecchia, Guido Musso
	Effect of silica fume and fiber reinforcement on strength in lime stabilized kaolinite clay Meral Dayan, Altuğ Saygılı
	Behavior of rocks under thermal effect - A review Mohamed Ahmed Mohamed Sobhey Mohamed Labeeb, Mostafa El Sawwaf, Marawan Shahien, Ahmed Farouk

15:30 – 15:45	Coffee Break
15:45 – 16:45	Session VII **Chairperson: Prof. İlknur Bozbey**
	Hydrological and geotechnical monitoring network installed in slope movements at Flores Island Letícia Moniz, Paulo Amaral, Filipe Marques, Ana Maria Malheiro
	A method to derive the soil-nail interface stiffness from pull-out tests Jean De Sauvage, Frederico Lara Diniz Oliveira
	A sophisticated quality control method in infrastructure projects: "Continuous compaction control" Rukiye Korkmaz
	Treatment of structural damages of an individual house by humidifying its clayey foundation soil – The MACH Project Lamine Ighil Ameur, Lucile Saussaye, David Mathon
16:45 – 17:00	Coffee Break
17:00 – 17:30	Closing Ceremony

TABLE OF CONTENTS

EFFECT OF SILICA FUME AND FIBER REINFORCEMENT ON STRENGTH IN LIME STABILIZED KAOLINITE CLAY

Meral Dayan, *Muğla Sıtkı Koçman University, Dept. of Civil Eng., meral_045@hotmail.com*

Altuğ Saygılı*, *Muğla Sıtkı Koçman University, Dept. of Civil Eng., saygili@mu.edu.tr*

ABSTRACT

This research was conducted to study the effect of polypropylene fiber-silica fume mixture addition on the geotechnical properties of lime rich kaolinite. Control and modified samples were compacted at optimum moisture content and cured for 28 days and tested for compression. For SEM imaging, specimens were cured for 1 year. Polypropylene fiber, silica fume and fiber-silica fume mixture increased the unconfined compressive strength values and changed the ductility behavior of the lime rich kaolinite specimens. Silica fume particles reacted with lime rich kaolinite as an extra silica source needed for hydration reactions. CSH gel products were formed, which surrounded the kaolinite particles. Fibers improved the friction resistance, interlock effect was created by cementation reactions between lime stabilized soil, fibers and silica fume. Silica fume and fiber modified lime rich clay reached the maximum strength at 0.25% fiber and 10% silica fume added specimens, strength values started to decrease with increasing fiber ratios. Silica fume, synthetic fiber and fiber-silica fume modified samples had an increase in compressive strength values and the ductility behavior of specimens have changed. The results indicated that fiber-silica fume modified kaolinite clay can be an environmentally friendly alternative in soil stabilization projects by utilizing an industrial waste.

Keywords: Soil Stabilization, Clays, Industrial Wastes, Silica Fume, Fibers.

1. INTRODUCTION

Constructing structures on weak soils creates problems during and after the construction phase in the form of slope instability, excessive settlement and bearing failure. Improvement of engineering properties such as compressibility and shear strength characteristics of soft soils can be undertaken by several ground improvement techniques [1-3]. Ground improvement methods include use of admixtures, soil replacement, compaction, preloading, and thermal methods [4-7].

Utilizing existing clayey soil in subgrade or backfill applications after stabilization has become popular due to environmental and economic reasons [8, 9]. An increasing number of studies in recent years show that strength of clayey soils has been improved by mixing soils with fly ash and cement to improve the compressive strength [10-15].

Many researchers studied natural, manufactured, and by-product materials for stabilizing the fine grained soils. Investigations conducted by researchers showed that silica fume improved geotechnical properties of the fine-grained soils such as hydraulic conductivity, unconfined compressive strength, and swelling behaviors [16-18].

Cai et al. investigated polypropylene fiber (0.05%, 0.15% and 0.25% by weight) and lime (2%, 5% and 8% by weight) modification on clayey soils [19]. Results showed that lime, fiber

content and curing period increased compressive strength values. The optimum strength gain was achieved with 5% lime in this study. Fratalocchi et al. conducted laboratory and test pad experiments on lime stabilization [20]. Low compressibility and high shear strength was observed on laboratory work and tests pads. Mukhtar et al. worked with lime stabilization on highly expansive clays [21]. Results indicated that 5% lime is the optimum amount for reactions in soil stabilization with lime on expansive soils.

Soil is capable of withstanding compressive and shear forces however it demonstrates low performance with tensile forces. Soils modified with randomly distributed fiber created attention in geotechnical engineering and many studies have been conducted with natural and synthetic fibers in soil reinforcement [2, 16, 22]. Results obtained from current studies indicated that the strength increase occurs because of fiber strength, fiber content and friction between soil and fiber interface. Incorporation of fibers in geotechnical projects is a trending topic for researchers because natural and synthetic fibers are economic options to alternative construction materials [23, 24]. Additionally, synthetic fibers can also be produced from recycled materials which reduces environmental impacts.

The main objective of this study is to examine the silica fume and synthetic fibers' interworking performance as a stabilizing agent in the lime stabilized kaolinite samples. To achieve this objective, natural and stabilized kaolinite samples have been tested in the laboratory. In addition, microstructure analysis has been conducted through scanning electron microscopy.

2. MATERIALS AND METHODS

2.1. Materials

Kaolinite was supplied from Canakkale region in Northwest Turkey. According to the United Soil Classification System, the soil is a low plasticity inorganic clay (CL). The silica fume used in this research was obtained from Eti Electrometallurgy Inc. located in Antalya, Southwest Turkey. Slaked lime was supplied from Mugla, Turkey. Considering the UCS performances together with cost–benefit advantages, the effective dosage rates of stabilizers were separately found as 5% for lime [2, 19, 21].

Silica fume is a valuable by-product pozzolanic material mostly effective in high performance concrete production having average grain diameter about 0.1 μm and unit weight 200-250 kg/cm3.

Synthetic polypropylene fibers were supplied from Polypropylene Fiber Inc. located in Istanbul, Turkey. The polypropylene fibers were 12 mm. in length and 30 μm to 40 μm in diameter, having specific gravity 0.91 g/cm3, with tensile strength of 600 MPa, elastic modulus of 3 GPa and linear strain at failure of 25 percent.

2.2. Sample Preparation

The required amounts of kaolinite, lime, silica fume and fibers for each sample were mixed in dry state. The kaolinite specimens were enriched with 5 percent by weight lime to provide extra calcium for the cementation reactions [19,21]. The specimens were mixed with silica fume content changing from 0 to 10 percent and fiber content varying from 0 to 1 percent by weight. The standard proctor compaction test was conducted through ASTM D698-12e2 to determine maximum dry unit weight and optimum moisture content.

Samples were compacted at maximum dry density and optimum moisture content using Harvard mini compactor for unconfined compression testing in which the specimen size was 34 mm. in diameter by 72 mm. in height. After compaction, samples were wrapped with cling

film and afterwards with aluminum foil to preserve the moisture, then stored in a humidity and temperature controlled curing room. In total, 96 samples were prepared, in the testing setup three duplicate samples for each sample type was tested. The unconfined compressive strength values of modified clay samples were determined in accordance with the ASTM D2166M-16.

To investigate interaction and cementitious bonds between lime rich clay, silica fume particles and synthetic fibers, modified samples were analyzed with scanning electron microscope (SEM). The test results were interpreted with JEOL JSM-7600F scanning electron microscope at Muğla Sıtkı Koçman University Central Research Laboratory.

3. RESULTS AND DISCUSSION

Figure 1 illustrates the stress-strain curves of the modified lime rich clay with fibers at various silica fume content. As shown in Figure 1, samples with 0% silica fume content showed ductile behavior while the other samples reached maximum strength values at lower strain, ranging from 1 to 2%, with the rise in silica fume content. Cementation reactions probably were the main factors on the change in the ductility of the modified lime rich clay as silica fume content increased [25].

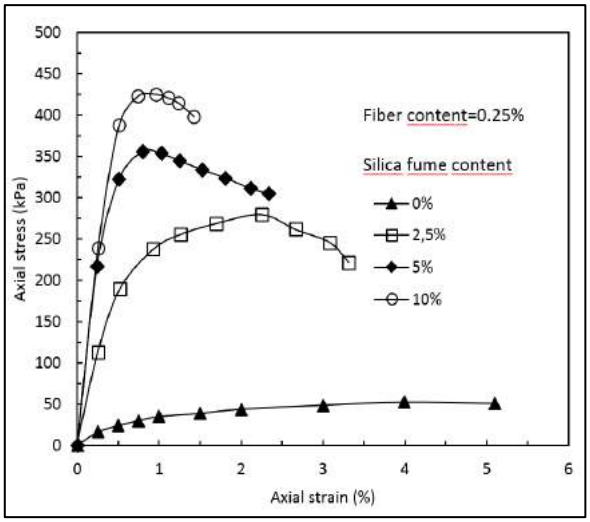

***Figure 1**. Stress-strain graph of samples modified with varying silica fume content*

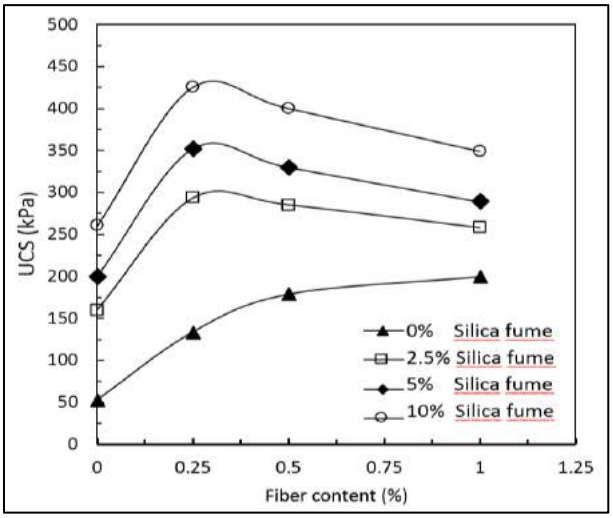

***Figure 2**. Effect of polypropylene fiber on the unconfined compressive strength with varying silica fume contents*

The effect of the silica fume, synthetic fiber and silica fume-fiber mixtures on the unconfined compressive strength values are displayed in Figure 2. Compared to control samples (CF0S0), the strength values of the stabilized samples containing 0.25% fiber and 10% silica fume (CF0.25S10) increased 8 times (Figure 2). Performance gain in the stabilized samples is attributed to the internal friction of silica fume grains and cementation reactions within clay, lime and silica fume [26].

Figure 3 and 4 show the scanning electron microscope images of the modified kaolinite clay samples after 1 year curing. CSH gel and lime rich kaolinite remaining on the sheared sample's synthetic polypropylene fiber strip are visible in the image. The plant root effect distributed stresses in a wider area and fiber strip pulled off cemented soil material while shearing, however the fiber itself was not ruptured [27].

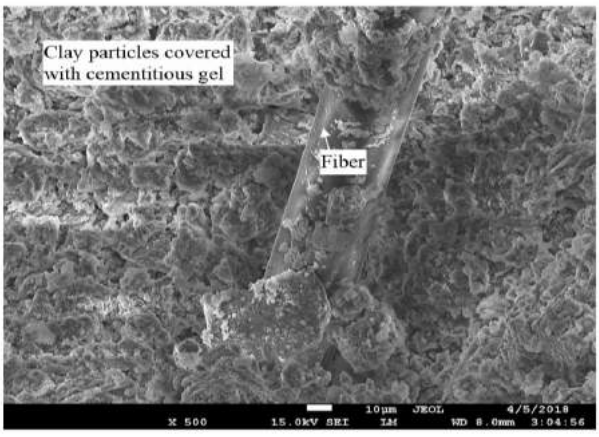

***Figure 3**. Image of fiber and silica fume modified clay with 0.25% fiber and 10% silica fume after 1 year curing (CF0.25S10-magnification 500x)*

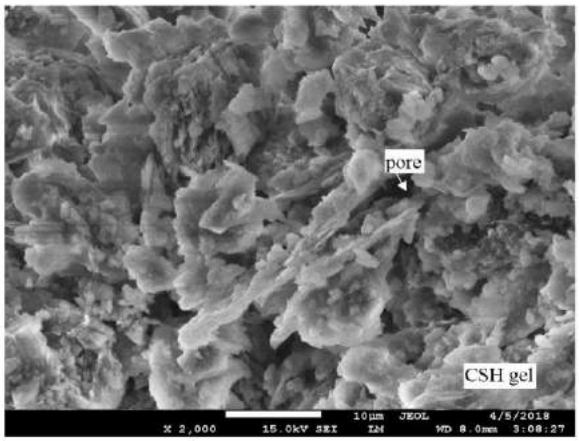

***Figure 4**. Silica fume and lime modified kaolinite covered with cementitious products after 1 years of curing (CF0.25S10-magnification 2000x)*

Silica fume particles reacted with lime rich kaolinite and with hydration reactions CSH gel products were formed, which surrounded the kaolinite particles as seen in Figure 4. CSH gel filled the voids of the modified samples [28].

The soil matrix had a stronger structure after the curing period and caused a significant increase in strength and ductility behavior as seen in the experimental results.

4. CONCLUSION

The following outcomes are obtained from this study:

•Silica fume, synthetic fiber and fiber-silica fume mixture addition increased the UCS and changed the ductility behavior of lime rich kaolinite specimens.

•From the SEM micrographs it is seen that silica fume addition with lime helped to create CSH gel. Pores are filled with hydration products and the modified structure of the soil matrix affected the strength properties.

•To conclude, fiber-silica fume mixture can be utilized in kaolinite clay stabilization. This method decreases the stabilization costs by utilizing a by-product material (silica fume) in an advantageous manner in geotechnical applications.

ACKNOWLEDGEMENT

The research work described herein was supported by Mugla Sitki Kocman University Scientific Research Project Office (BAP 16-057). The financial support is gratefully acknowledged.

REFERENCES

[1] Yetimoglu, T., Inanir, M. and Inanir, O.E., 2005. *"A study on bearing capacity of randomly distributed fiber-reinforced sand fills overlying soft clay",* Geotextiles and Geomembranes, 23(2): 174–183.

[2] Tang, C.S., Shi, B., Gao, W., Chen, F. and Cai, Y., 2007. *"Strength and mechanical behavior of short polypropylene fiber reinforced and cement stabilized clayey soil"*, Geotextiles and Geomembranes, 25(3): 194–202.

[3] Saygili, A., 2015. *"Use of waste marble dust for stabilization of clayey soil",* Materials Science Medziagotyra, 21(4): 601–606.

[4] Nelson, J.D. and Miller, D.J., 1992. "*Expansive Soils: Problems and Practice in Foundation and Pavement Engineering"*, John Wiley and Sons. Inc., New York.

[5] Anggraini, V., Asadi, A., Syamsir, A. and Huat, B.B.K., 2017. *"Three point bending flexural strength of cement treated tropical marine soil reinforced by lime treated natural fiber"*, Measurement, 111: 158-166.

[6] Mohanty, S.K., Pradhan, P.K. and Mohanty, C.R., 2017. *"Stabilization of expansive soil using industrial wastes"*, Geomechanics and Engineering, An Int'l Journal, 12(1): 111-125.

[7] Kim, Y., Dang, M.Q., Do, T.M. and Lee, J.K., 2018. *"Soil stabilization by ground bottom ash and red mud"*, Geomechanics and Engineering, An Int'l Journal, 16(1): 105-112.

[8] Consoli, N.C., Bassani, M.A.A. and Festugato, L., 2010. *"Effect of fiber-reinforcement on the strength of cemented soils"*, Geotextiles and Geomembranes, 28 (4): 344-351.

[9] Nagrale, P.P. and Patil, A.P., 2017. *"Improvement in engineering properties of subgrade soil due to stabilization and its effect on pavement response"*, Geomechanics and Engineering, An Int'l Journal, 12(2): 257-267.

[10] Kaniraj, S.R. and Havanagi, V.G., 1999. *"Compressive strength of cement stabilized fly ash soil mixtures",* Cement and Concrete Research, 29(5): 673-677

[11] Baykal, G., Edincliler, A. and Saygılı, A., 2004. *"Highway embankment construction using fly ash in cold regions"*, Resources, Conservation and Recycling, 42(3): 209-222.

[12] Baykal, G. and Saygılı, A., 2012. *"A new technique to improve freeze–thaw durability of fly ash"*, Fuel, 102: 221-226.

[13] Kolias, S., Kasselouri-Rigopoulou, V. and Karahalios, A., 2005. *"Stabilization of clayey soils with high calcium fly ash and cement"*, Cement Concrete Composites, 27(2): 301-313.

[14] Horpibulsuk, S., Rachan, R., Suddeepong, A. and Chinkulkijniwat, A., 2011. *"Strength development in cement admixed Bangkok clay: laboratory and field investigations"*, Soils and Foundation, 51 (2): 239-251.

[15] Horpibulsuk, S., Suddeepong, A., Chinkulkijniwat, A. and Liu, M.D. (2012), *"Strength and compressibility of lightweight cemented clays",* Applied Clay Science, 69: 11-21.

[16] Prabakar, J. and Sridhar, R.S., 2002. *"Effect of random inclusion of sisal fibre on strength behavior of soil"*, Construction and Building Materials, 16(2): 123–131.

[17] Kalkan, E., 2011. *"Impact of wetting–drying cycles on swelling behavior of clayey soils modified by silica fume",* Applied Clay Science, 52(4): 345–352.

[18] Alrubaye, A.J., Hasan, M. and Fattah, M.Y., 2018. *"Effects of using silica fume and lime in the treatment of kaolin soft clay"*, Geomechanics and Engineering, An Int'l Journal, 14(3): 247-255.

[19] Cai, Y., Shi, B., Ng, C.W.W. and Tang, C., 2006. *"Effect of polypropylene fibre and lime admixture on engineering properties of clayey soil"*, Engineering Geology 87: 230-240.

[20] Fratalocchi, E., Bellezza, I., Di Sante, M. and Pasqualini, E., 2009. *"Mix-design, construction and controls of lime stabilized embankments"*, Proceedings of the 17th International Conference on Soil Mechanics and Geotechnical Engineering, 3: 2248-2251.

[21] Mukhtar, M., Lasledj, A. and Alcover, J.F., 2010. *"Behavior and mineralogy changes in lime treated expansive soil at 20 °C"*, Applied Clay Science, 50(2): 191-198.

[22] Edincliler, A., Baykal, G. and Saygili, A., 2010. *"Influence of different processing techniques on the mechanical properties of used tires in embankment construction",* Waste Management, 30(6):1073–1080.

[23] Puppala, A.J. and Musenda, C., 1998. *"Investigation of geofiber reinforcement method on strength, swell, and shrinkage characteristic of soils"*, Proceedings of Fifth International Conference on Composites Engineering, Las Vegas.

[24] Güllü, H. and Fedakar, H.I., 2017. *"Unconfined compressive strength and freeze-thaw resistance of sand modified with sludge ash and polypropylene fiber*", Geomechanics and Engineering, An Int'l Journal, 13(1): 25-41.

[25] Chen, M., Shen, S., Arulrajah, A., Wu, H. and Hou, D., 2015. *"Laboratory evaluation on the effectiveness of polypropylene fibers on the strength of fiber-reinforced and cement-stabilized Shanghai soft clay"*, Geotextiles and Geomembranes, 43(6): 515-523.

[26] Harianto, T., Hayashi, S., Du, Y. and Suetsugu, D., 2009. *"Experimental Investigation on Strength and Mechanical Behavior of Compacted Soil-fiber Mixtures",* In: Li G, Chen Y, Tang X (eds) Geosynthetics in Civil and Environmental Engineering, pp. 392-397, Springer, Berlin, Heidelberg.

[27] Anggraini, V., Asadi, A., Huat, B.B.K. and Nahazanan, H., 2015. *"Effects of coir fibers on tensile and compressive strength of lime treated soft soil"*, Measurement, 59: 372-381.

[28] Goodarzi, A.R., Akbari, H.R. and Salimi, M., 2016. *"Enhanced stabilization of highly expansive clays by mixing cement and silica fume"*, Applied Clay Science, 132: 675-684.

RIGID INCLUSIONS IN FOUNDATION SUPPORT SYSTEMS

Bahattin Berk Ayraçma, *Istanbul Technical University, ayracma@itu.edu.tr*

Berrak Teymür, *Istanbul Technical University, teymurb@itu.edu.tr*

Ozan Alver, *Istanbul Technical University, alver16@itu.edu.tr*

ABSTRACT

In the context of this study, usage of rigid inclusions in foundation systems is investigated. The method consists of pile-like inclusions placed under the foundation, which are disconnected from the foundation slab, while a cushion layer acts as a load transfer platform between the structure and soil-rigid inclusion medium. Thus, load distribution and load transfer mechanisms that govern the stability of structures that favor such design show major differences compared to the traditional deep foundation systems such as piled raft foundations. Examination of the mentioned characteristics of the usage of rigid inclusions in soil opens a new study area in geotechnical engineering. In this paper, possible advantages and disadvantages on the topic are studied. The static behavior of rigid inclusions are investigated on a caisson bridge foundation model using axisymmetric and plane strain model conditions. The site consists of a soft clay layer and vertical inclusions behave as floating (friction) piles. Finite element numerical models that include rigid inclusions are analyzed in terms of structural and geotechnical aspects. Responses of the connected and disconnected foundation systems are compared in terms of axial load, settlement, shaft resistance and efficiency. Analysis results indicate that it is possible to reduce the axial load carried by the piles depending on the thickness of the cushion layer and pile spacing. Benefits of rigid inclusions and their utilization in foundation engineering are discussed.

Keywords: Rigid Inclusions, Disconnected Piles, Piled Raft Foundation, Load Transfer Platform, Load Transfer Mechanism.

1. INTRODUCTION

Depending on the soil conditions and structural properties, a shallow foundation type might be insufficient against the geotechnical problem on hand in terms of bearing capacity and/or excessive settlements. Under the circumstances, the engineering solution may involve the improvement of the soil properties or the design of a deep foundation system that meets the project requirements. Soil improvement can be simply explained as the use of different techniques depending on geological conditions to improve the engineering properties of soil such as its stiffness and hydraulic conductivity so that it can safely withstand the loads from a structure. Adopting piles in the design of a deep foundation system is a common practice. Loads from the structure in this case are transferred into deeper soil layers that can resist them. Both methods have their advantages and disadvantages to them. It requires sufficient investigation and planning to choose the particular solution that is best fitted to the present problem. Traditional pile supported foundation systems are connected to a pile cap or raft. Structural load is either assumed to be carried solely by the piles or partially by soil. Pile – foundation connection is a critical point for the system as the maximum axial load is expected to occur

here. Critical bending moment from the lateral loads or eccentric loading also develops at this point. Importance of the pile – raft/cap connection is crucial for the system.

To reduce the internal forces acting on the pile head and lower the expenses of the deep foundation system, a relatively recent method is to disconnect the piles from the foundation slab and leave a gap in the system. In some cases, the difficulty of establishing a structural connection between foundation base and piles as in deep offshore structures makes it a necessity to disconnect the vertical elements from the foundation. The Rion-Antirion bridge in Greece [1] and İzmit Bay Bridge in Turkey [2] are both instances of the system, often described as innovative solutions in the literature. Beneath the foundation, a cushion layer consists of compact material like gravel or a thin concrete bed is placed above the pile group. This layer acts as a load transfer medium that preferably uniformly distributes the structural load to the piles and foundation soil. Mechanism of the load distribution through this layer is a complex progress. Static and dynamic response of the disconnected system is a developing topic yet to be investigated by researchers.

Some of the main variables that affect the disconnected pile systems can be defined as; thickness of the cushion layer, pile spacing, strength parameters of the cushion layer and magnitude of the load. In this study, effects on the thickness of the cushion layer and pile spacing is chosen as the subject. Both pile spacing and cushion thickness are primary parameters that govern the load transfer mechanism of the system.

2. LOAD TRANSFER MECHANISM

In the absence of a physical pile to foundation connection, the structural load is transferred through a gravel or usually an unreinforced concrete mattress. Purpose of this layer, other than obviously filling the gap between pile heads and raft, is to uniformly distribute the load to the piles. A significant amount of load is also carried by the soil underneath, leading to a decrease in the axial load along the piles. Since there is no structural connection at pile heads, bending moment is expected to be zero at this point. Location of the maximum axial load should shift towards the middle of the pile, which depends on the magnitude of the load, skin friction along the shaft and soil settlement around the pile. Aside from the soil properties, friction/adhesion force that is developed around a pile depends on the relative axial displacement of the pile. When all load is supported by the piles, piles would show larger displacement than the surrounding soil at the respective depth. However, in case of disconnected piles, some of the load will be carried by the soil. Within the soil body that is closer to the pile head, because of the high stiffness of the vertical support elements in comparison to soil, rigid inclusions are to experience less settlement than the soil at the same depth. This results to a negative skin friction on the shaft, until to the point where both settlements get equal to each other. The depth where the relative displacement of the pile becomes zero is often named as neutral axis. The neutral axis coincides with the location of the maximum axial load of a pile.

One of the main aspects that define the load transfer mechanism of the disconnected pile elements is the ratio of the load that is carried by the vertical inclusions to the total vertical load. The term often expressed as efficiency, E is difficult to fully discern because of the complexity of the mechanism through the load transfer platform. In the literature it is investigated using empirical formulas, analytical expressions with assumed failure surfaces, numerical solutions and experimental methods such as scaled models and centrifuge tests [3]. Main dependencies of the mechanism can be summed up by load magnitude, pile spacing and diameter, thickness of the load transfer platform and soil properties. Usage of geosynthetic materials to distribute the load more evenly can be considered another factor to the load transfer mechanism. Blanc et

al. also studied the effects of a geosynthetic layer placed under the load transfer platform in terms of the systems efficiency and differential settlement [4].

Chevalier et al. investigated the load transfer mechanism through the load transfer platform based on Carlsson's assumption [5]. The kinematics behind the redirection of the load from the cushion layer to the piles is in a form of an inverse pyramid with an angle close to the peak friction angle of the granular material that forms the load transfer platform [6]. Using an inverse pyramid assumption as the load distribution mechanism leads to a pile to carry more load as the cushion thickness increases, thus also increasing the efficiency of the system.

3. NEUTRAL PLANE

To investigate the negative friction phenomenon and its depth along a vertical inclusion element, a single friction pile in soft clay (c_u = 40 kPa) with a diameter of 1 m is analyzed under uniform static structural load. The load transfer platform consist of a dense granular bed (ϕ' = 40°, c' = 1.0 kPa). The thickness of the cushion layer varies in range of 0.5 – 3.0 m. Vertical inclusion is modelled as a volume with linear elastic properties.

Figure 1 illustrates the vertical displacement of soil and rigid inclusion. The point where the relative displacement between the two material becomes zero shows the location of the neutral plane. To get more precise values for the depth of the neutral plane, cross section along the interface of pile – soil is investigated. Shear stress developed on the section (σ_{xy}) is plotted.

As the thickness of the load transfer platform increases, depth of the negative skin friction and hence depth of the neutral plane increases. In Table 1, depth of the zero skin friction from the soil surface is shown for 95 kPa and 240 kPa loads. Effect of the load on the depth of the neutral plane decreases as the thickness of the granular mattress increases.

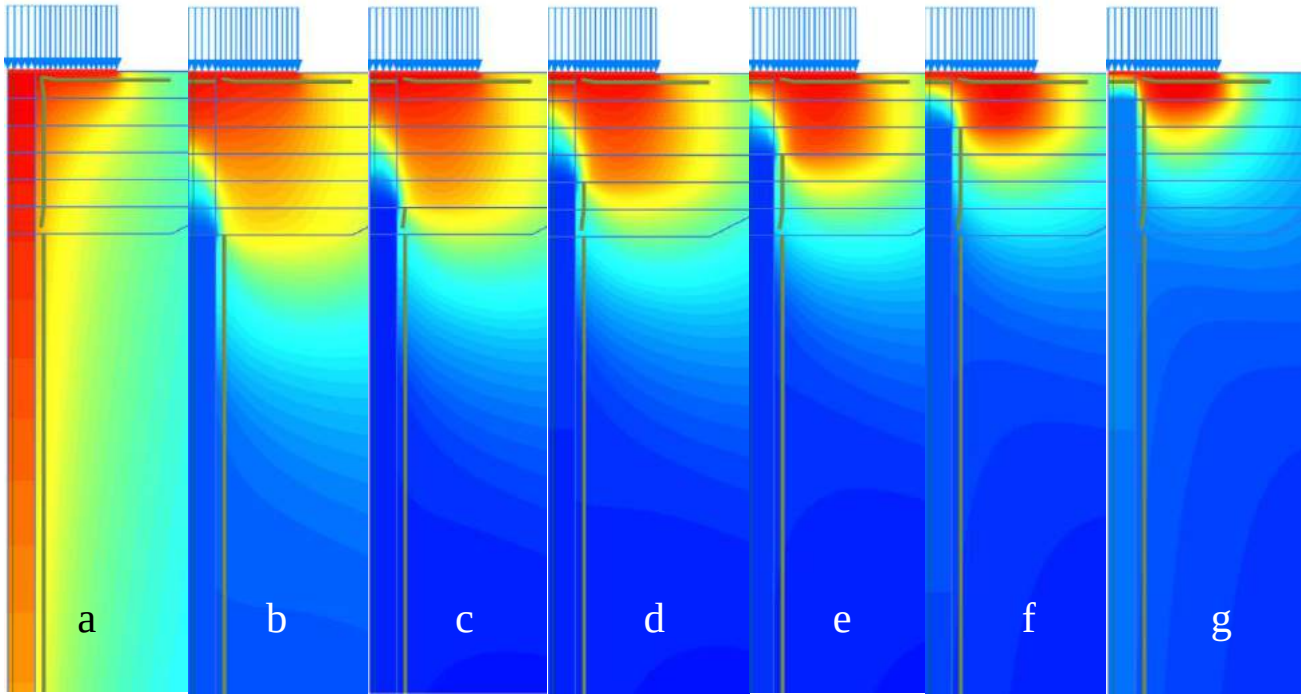

Figure 1. *Relative displacement of pile – soil for varying cushion thicknesses: a) No cushion, b) 3m, c) 2.5m, d) 2m, e) 1.5m, f) 1m, g) 0.5m.*

Table 1. *Location of neutral plane in axisymmetric model.*

		Neutral Plane Location, m	
	Load, kPa	**95**	**240**
	Connected Pile	0	0
	Raft	-	-
Load Trasfer Platform	0.5 m	4.2	3.4
	1.0 m	6.3	5.3
	1.5 m	7.6	6.5
	2.0 m	8.3	7.6
	2.5 m	8.7	8.5
	3.0 m	8.9	9.3

During the load transfer through the cushion layer, soil nodes above the pile head show less vertical displacement compared to the surrounding layer. This leads to the formation of an arching effect within the load transfer platform. To observe this effect in the numerical analysis, a model with multiple piles is needed. As such, a model containing three piles is created with the same soil conditions.

In terms of the location of the neutral plane, thus negative friction developed along the pile shafts, the behavior of the model is similar to the axisymmetric model. Depth of the neutral plane decreasing as the thickness of the load transfer platform decreases. Magnitude of the load does not affect the location of the neutral plane in a significant manner. Table 2 shows the depth of the neutral plane for 95 and 160 kPa loads with varying cushion thickness values.

Table 2. *Location of neutral plane in plane strain model.*

		Neutral Plane Location, m					
	Load, kPa →	**95**	**160**	**95**	**160**	**95**	**160**
	Pile Location →	**Center Pile**		**Outer Pile**			
				Center Side		**Outer Side**	
	Connected Pile	0	0	0	0	0	0
	Raft	-	-	-	-	-	-
Load Trasfer Platform	0.5 m	4.6	4.6	19.5	19.1	3.2	2.8
	1.0 m	5.7	5.7	20.0	19.8	4.5	4.2
	1.5 m	6.3	6.1	20.1	20.1	5.4	5.1
	2.0 m	6.8	6.5	20.1	20.1	6.0	5.7
	2.5 m	7.3	6.7	20.2	20.3	6.4	6.2
	3.0 m	7.7	6.7	20.3	20.5	6.6	6.5

Figure 2 illustrates the vertical displacement of the connected system and system with 3.0 m load transfer platform. When the vertical pile element is not at the center, for corner piles, depth of the neutral plane has different values for left (facing center) and right (facing outwards) side of the pile.

Numerical analysis results indicate that the thickness of the load transfer platform has a relatively greater effect on the depth of the neutral plane than the magnitude of the load. Physical centrifuge tests performed on the subject reveal the depth as a linear function of the surrounding soil's settlement [7].

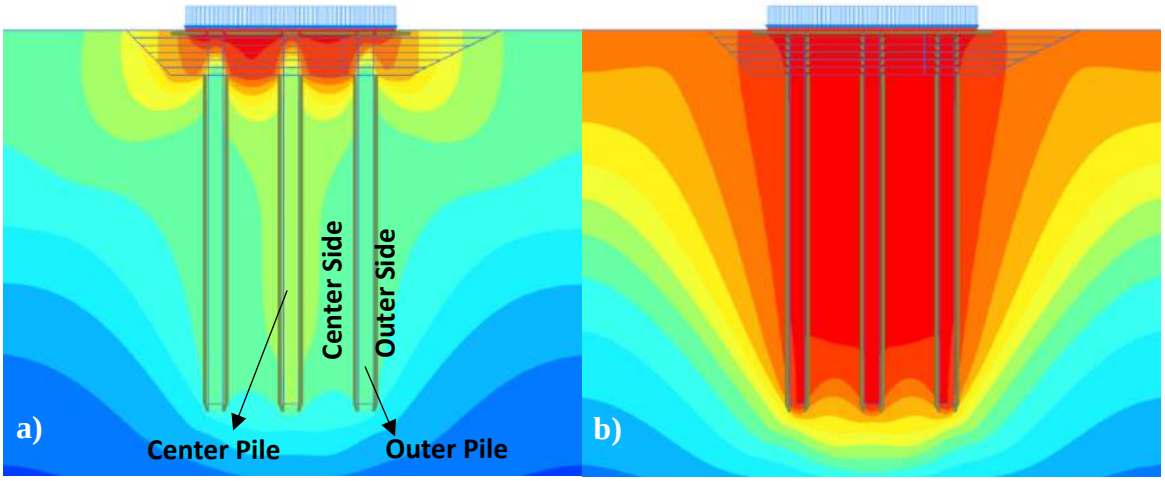

Figure 2. *Vertical displacement of a) Connected pile system b) System having 3.0 m load transfer platform*

4. SETTLEMENTS

Settlement of the foundation system depends on the load transfer platform's thickness and magnitude of the load. Settlement values for particular loads of 95 kPa and 240 kPa are given in Table 3.

Table 3. *Settlements at the center of the raft.*

		Settlement, mm	
	Load, kPa	**95**	**240**
	Connected Pile	2.4	6.3
	Raft	86.8	244.3
Load Trasfer Platform	0.5 m	11.3	21.9
	1.0 m	13.2	35.0
	1.5 m	14.0	39.6
	2.0 m	13.2	41.2
	2.5 m	12.4	40.0
	3.0 m	11.7	39.6

Although there is not a drastic difference between different conditions, the results indicate no simple linear relation exists between settlement and cushion thickness. As the thickness increases, settlement also increases until a certain cushion height has been reached, then starts to decrease with an increase in height. In terms of settlement, connected single pile gives the lowest value, wherein raft only foundation system is unable to carry the load and show excessive settlements. However, the overall behavior of the system becomes more brittle as well.

In another model, piles are modelled as embedded beam row elements to consider the out of plane direction to some degree. Section of the model can be seen in Figure 3. To see the effects of the pile spacing, varying center to center distance of the pile elements are investigated. Table 4 shows the settlement of the foundation for different model types respect to pile spacing under 95 kPa uniform loading.

Table 4. *Settlement values for varying cushion thicknesses and pile spacing.*

Model Type	Cushion Thickness (m)	Settlement (cm) Center to Center Spacing (m) 3.5	5	7	10
Raft	-	21.4	21.4	21.4	21.4
Connected Pile	-	4.5	5.8	7.8	12
Rigid Inclusions	1	6.6	8.9	10.9	12.5
	2	6.2	8.2	9.9	11.5
	3	5.9	7.7	9.3	10.8

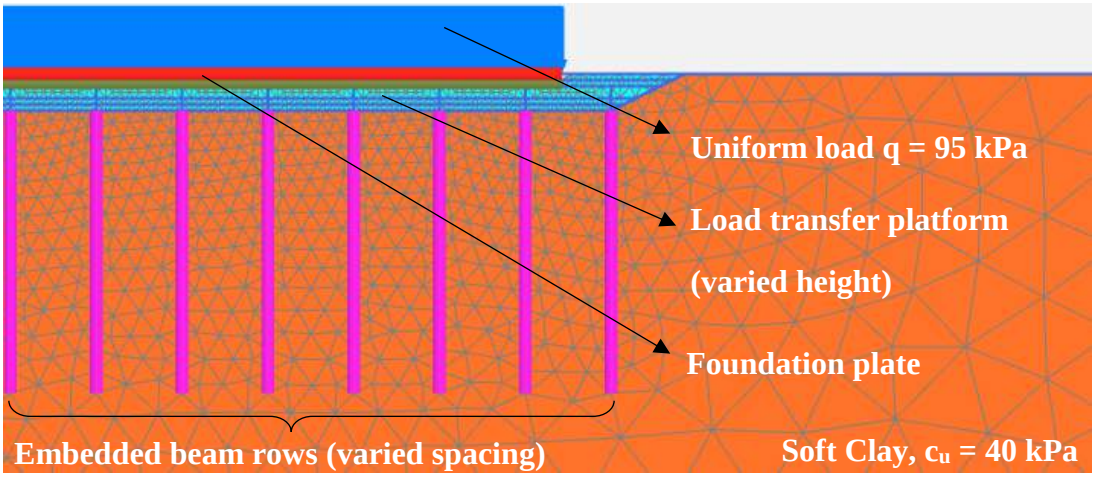

Figure 3. *Section of the model produced by utilizing embedded beam elements.*

Similar to the other models, for cushion thicknesses of 1.0, 2.0 and 3.0 m total vertical settlement of the foundation decreases with the height of the load transfer platform. Lowering the pile spacing also decreases the settlement values as expected. However, group effect is another parameter to be considered in this case.

5. AXIAL LOADS

Internal forces developed along the embedded beam row elements are investigated for the understanding of static behavior of the connected and disconnected pile elements in the model. Center to center pile spacing varies between 3.5 – 10 m. Axial load transferred from the foundation and load transfer platform to the pile heads are shown in Table 5. Efficiency defined as the ratio of the total load carried by pile elements to the total vertical load is also given in the table.

For the same spacing intervals, as the load transfer platform thickness increases, load carried by the piles, thus efficiency increases. However, in all cases, the efficiency is relatively smaller than the case where the piles are structurally connected to the pile cap. In the presence of a load transfer platform, a significant percentage of the total load is carried by the foundation soil. By utilizing the bearing capacity of the soil underneath the cushion layer, it helps to reduce the internal forces developed on the piles. For varying pile spacing, the analysis results indicate that an increase in the distance between piles lower the efficiency of the system by inducing more pressure to the soil under the load transfer platform. Findings related to pile spacing and load transfer platform thickness coincide with the experimental studies in the literature.

Table 5. *Variation of total pile load and efficiency for different cushion thicknesses and pile spacing.*

Model Type	Cushion Thickness (m)	Spacing (m)	Total Pile Load (kN)	Total Load (kN)	Efficiency (%)
Connected Piles	-	3.5	31962.35	32585	**98.1**
	-	5	45197.5	47500	**95.2**
	-	7	57470	65170	**88.2**
	-	10	65223	95000	**68.7**
Rigid Inclusions	1	3.5	13557.46	29925	**45.3**
	1	5	15242	42750	**35.7**
	1	7	16368.24	59850	**27.3**
	1	10	18596	85500	**21.7**
	2	3.5	14560.56	29925	**48.7**
	2	5	16395.8	42750	**38.4**
	2	7	18412.8	59850	**30.8**
	2	10	18711.2	85500	**21.9**
	2.5	3.5	14787.15	29925	**49.4**
	2.5	5	16792.7	42750	**39.3**
	2.5	7	18796.26	59850	**31.4**
	2.5	10	19346.4	85500	**22.6**
	3	3.5	16376.15	29925	**54.7**
	3	5	18928.3	42750	**44.3**
	3	7	20938.82	59850	**35.0**
	3	10	21391	85500	**25.0**

Centrifuge modelling tests performed by Okyay et al. point out the importance of the pile cap ratio and platform thickness in the load transfer mechanism. A sufficient load platform height is needed for the arching effect to develop within the load transfer cushion and to evenly redistribute the structural load onto the pile elements [8]. Figure 4 illustrates the load carrying mechanism of the piles for the cases of connected and disconnected elements. Maximum displacement, axial and unit shaft friction forces are shown for the connected system and system having 3.0 m load transfer platform thickness. Pile spacing is 7.0 m in both cases. For the disconnected pile, axial load increases until the depth of neutral axis, wherein for structurally connected pile maximum axial load develops at the pile head and decrease from that value with depth.

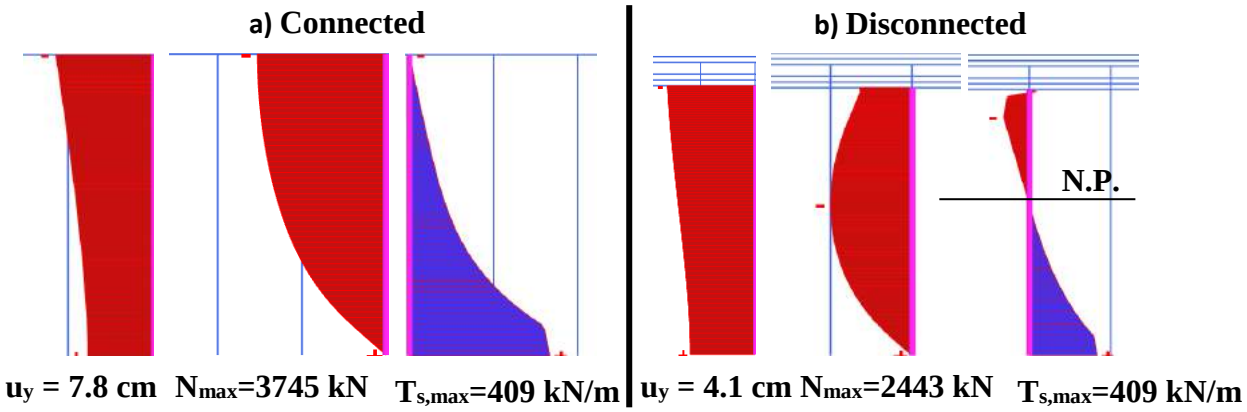

Figure 4. *Axial load and skin resistance developed on a) Connected pile, b) Disconnected pile*

6. CONCLUSION

Utilizing a structurally disconnected pile – foundation system with a cushion layer in-between as a load transfer medium could show benefits. A load transfer platform positioned between pile elements and foundation slab distributes the total load to the piles and soil underneath the platform. Unlike traditional piled foundation systems, a significant amount of the load can be carried by the soil. This helps to reduce the axial load along the piles. Eliminating the structural connection between pile head and pile cap can reduce the costs and improve the construction process, especially in places where it is difficult to establish such connection such as offshore structures and piers.

Although the analysis indicate connected pile systems show minimum settlements, systems that utilizes disconnected piles with a load transfer platform still demonstrates relatively small settlements in comparison to a shallow foundation.

The load transfer mechanism of disconnected pile systems leads to the development of a negative skin friction in the upper portion of the piles. Neutral plane, the depth where the shaft resistance becomes zero, depends on the magnitude of the load and height of the load transfer platform. As the thickness of the load transfer platform increases, depth of the neutral plane increases linearly.

In terms of 1.0, 2.0 and 3.0 load transfer platform thicknesses, settlement decreases with the height of the cushion layer.

The ratio between the axial load carried by piles and total load, efficiency, increases with the thickness of the load transfer platform, and decrease with the pile-to-pile spacing.

Maximum axial force developed along the pile decreases with the utilization of a load transfer platform between the piles and pile cap. Location of the maximum axial load coincides with the location of the neutral plane instead of occurring at the pile head.

REFERENCES

[1] Pecker, A., 2004. *"Design and Construction of the Rion Antirion Bridge"*, GeoTrans 2004, California, Los Angeles, USA : July 27-31.

[2] Steenfelt, J. S., Foged, B. & Augustesen, A. H., 2015. *"Izmit Bay Bridge Geotechnical Challenges and Innovative Solutions",* International Journal of Bridge Engineering, 3 (3), 53-68.

[3] Tradigo, F., Pisano, F., Prisco, C. & Mussi, A., 2014. *"Non-linear Soil-structure Interaction in Disconnected Piled Raft Foundations"*, Computer and Geotechnics, 63, 121-134.

[4] Blanc, M., Rault, G., Thorel, L., Almeida, M. S. S. & Almedia, M. C. F., 2012. *"Centrifuge Investigation of the Load Transfer Mechanism Above Rigid Inclusion"*, Proceedings of Eurofuge 2012, Delft.

[5] Carlsson, B., 1987. *"Armerad jord beräkningsprinciper för vertikala väggar, branta slänter, bankar på lös undergrund, bankra på pålar",* Terrateam AB, Linköping, Sweden.

[6] Chevalier, B., Villard, P. & Combe, G., 2011. *"Investigation of Load-Transfer Mechanisms in Geotechnical Earth Structures with Thin Fill Platforms Reinforced by Rigid Inclusions",* International Journal of Geomechanics, 11 (3), 239-250.

[7] Fioravante, V., 2011. *"Load Transfer From a Raft to a Pile With an Interposed Layer"*, Geotechnique, 2, 121-132.

[8] Okyay, U. S., Dias, D., Thorel, L. & Rault, G., 2013. *"Centrifuge Modeling of a Pile-Supported Granular Earth-Platform"*, J. Geotech. Geoenviron. Eng., 2014, 140(2), 04013015-1-12.

CATEGORIZING THE SEDIMENTATION CHARACTERISTICS OF BENTONITES BASED ON PHYSICO-CHEMICAL PROPERTIES

El Hassen Abd Moulana *, *Dokuz Eylül University, Department of Civil Engineering, elhassen.abdmoulana@ogr.deu.edu.tr*
Esra Dikişci, *Dokuz Eylül University, Department of Civil Engineering, esradikisci@hotmail.com*
A. Hakan Ören, *Dokuz Eylül University, Department of Civil Engineering,* ali.oren*@deu.edu.tr*

ABSTRACT

Sedimentation is the process of allowing particles in suspension to settle down under the effect of gravity. Settling behavior is one of the most important characteristics occurs when clay particles settle in the sea or when clay particles transported with a river flow. Therefore, many researchers have suggested some tests to gain insight into the sedimentation mechanism and sedimentation formation characteristics. This study aimed to categorize the physico-chemical properties of bentonites with the sedimentation characteristics in different pore fluids the sedimentation tendencies of bentonites were correlated with the physico-chemical properties of bentonites such as consistency limits, clay contents, cation exchange capacity, specific surface area and smectite content. The results showed that physico-chemical properties of bentonite have fair relationships with the sedimentation characteristics.

Keywords: Sedimentation, Bentonites, Geosynthetic Clay Liners (Gcls), Correlations

1. INTRODUCTION

Bentonite is composed of montmorillonite mineral which is widely used in various industrial products. Due to its low hydraulic conductivity ($\leq 2.0\times10^{-11}$ m/s), it is also the main constituent of geosynthetic clay liners (GCLs) and sand-bentonite mixtures (SBMs).

Determining the hydraulic conductivity of bentonites is a time consuming process. The test that is to be conducted on bentonite is complex and the equipment used during testing is expensive (especially when flexible wall permeameter is used). Although hydraulic conductivity test must be performed in every case, some other tests are also carried out to support the results or to estimate the hydraulic conductivity of bentonite in a simple and quick way. One of the most significant test that has been considered so far is swell index test. In that test, the swelling ability of bentonite can be determined by freely pouring the bentonite using different liquids and the swell volume is recorded after one day of hydration. Then, the tendency of swelling in these liquids can be compared with the hydraulic conductivity of the bentonite. However, swell index test has some disadvantages such as: (i) formation of flocs on the liquid surface and rapid settling, (ii) existence of entrapped air within flocs, and (iii) irregular surface of settled bentonite that make it hard to record the correct value of swell index. Therefore, alternative test method may be suggested such as sedimentation test which has less handicaps with respect to swell index test.

Sedimentation is the process of settling down of suspended particles in water by gravity. Imai (1980a) has been categorized sedimentation characteristics as: (i) Dispersed free settling, (ii) flocculated free settling, (iii) zone settling (consist of flocculation, settling and consolidation

stages), and (iv) consolidation settling. Based on Imai's (1980) study, Sridharan and Prakash (2001) simplified the sedimentation behavior and classified as dispersed free settling and flocculated free settling. After a while, Kaya et al. (2006a) proposed another type of settling named as "mixed settling" in which the heavier particles settle immediately, and the remaining particles form flocs (or aggregates) to serve flocculation settling.

Sedimentation characteristics of any type of soil basically depend on two major factors such as solid to liquid ratio and pore medium chemistry. Imai (1980b) showed how sedimentation characteristics change with the solid to liquid ratio and pore fluid chemistry of the medium. Increase in the concentration of the pore medium or solid to liquid ratio led to facilitate the flocculation type of settling. In addition to this, some factors like particles size, clay contents, and smectite content have an influence on the sedimentation characteristics as well. Sridharan and Prakash (1999) have suggested that the sedimentation under different environments is strongly influenced by the clay mineralogy of soils. Kaya et al. investigated (2006b) the settling characteristics of kaolin clay under different concentration levels and pH conditions and reported that there is fair relationship within these factors.

Although several studies with sedimentation tests have been conducted so far, most of these studies were applied using natural soils or clays. In this study, however, the sedimentation behavior of 2 g of bentonite was evaluated. Swell index test is conducted with 2 g of bentonite and immediately after recording the swell volume, sedimentation test can be carried out by vigorously shaking the graduated cylinder. Then, the settling regimes of the particle can be observed. After recording the swell index value the sedimentation test can be performed on the same samples no need to prepare any new sample and since the same sample is used, the correlation efficiency of swell index and sedimentation behavior (or volume) to different properties of bentonite can be compared within each other more realistically. In this study, only sedimentation behavior of bentonites and its correlations with some basic index properties of bentonite have been reported.

2. MATERIALS AND METHODS

2.1. Materials

Total of 8 bentonites were used in this study which had been obtained from different places. Three of them were taken from GCLs manufactured by the local producer and remaining has been collected from the available companies in the local market. Some of the bentonites used in this study were rich of sodium and polymer-treated; some were in their natural form. All bentonites were oven dried at 105°C before starting the tests. After drying, they were grinded in a mortar and passed through No 200 sieve (< 0.075 mm). Then, all samples were kept in plastic bags until testing. Then, sedimentation tests were conducted in 100 mL graduated cylinders using deionized water (DIW).

2.2. Methods

For the sedimentation test, the graduated cylinder was initially filled with water until 90 mL level, then, 2 g of bentonite were poured in the cylinder to determine the swell index as described in ASTM:D5890-11 (2011). When all bentonites were poured in water, the level of water in the cylinder was raised to 100 mL. After 24 hours of hydration the swell index was recorded and the graduated cylinder was vigorously shaking until all bentonite particles were mixed into the water. Then, the graduated cylinder was stand over a desk and time was initiated. Suspension started to settle down and the sedimentation behavior was examined throughout the

test duration. Sedimentation volumes were also recorded at the end of 1, 2, 5, 10, 15, 30, 60, 120, 240, 480 and 1440 minutes (sometimes with extended reading times).

The well-known consistency limits tests were conducted as specified in ASTM:D4318-05 (2005). The clay contents of the bentonites were determined from sieve and hydrometer analyses (ASTM:D422-63 2007). The cation exchange capacities (CEC) were measured by washing bentonites in the sequence of 1M ammonium acetate, isopropanol and 1M potassium chloride. Finally, the filtrates were transferred to spectrophotometer and the nitrogen concentrations were measured (ASTM:D7503-10 2010). The specific surface areas (SSA) of bentonites were measured using methylene blue and filter paper. The details of about this test can be found in (Ören et al. 2018; Yukselen-Aksoy and Kaya 2010). The physicochemical properties of bentonites are presented in Table 1.

Table 1. *The Physico-Chemical Properties of Bentonites*

Bentonite	**Liquid Limit (%)**	**Plastic Limit (%)**	**Clay Content (%)**	**Cation Exchange Capacity (cmol/kg)**	**Specific Surface Area (m^2/g)**
B-1	283	48	67	85	832
B-2	529	38	73	73	637
B-3	552	41	78	105	607
B-4	149	42	31	78	475
B-5	397	34	78	61	587
B-6	417	44	78	69	612
B-7	385	58	76	81	n.d.
B-8	240	53	54	73	n.d.

n.d.: not determined

3. RESULTS AND DISCUSSIONS

Similar to Kaya et al (2006b), the sedimentation characteristics of bentonite were separated into three herein. The first one was characterized as the fast settling of particles through the bottom of the graduated cylinder. This fast settling formed an accumulated layer at the bottom which was followed by diffused particle layer over it. In this case, the sedimentation volume increased with time, because accumulation was in upward direction. This type of settling is called as accumulated sedimentation (AS) and the settling curve of this behavior is given in Figure 1a. The second type of settling was in the flocculated form (Figure 1b). In this type of settling, the particles immediately formed aggregates and settle down together. Since sedimentation was in downward direction, the sediment volume decreased with time and a clear water was formed over the flocs. This type of settling is named as flocculated sedimentation (FS). In between of AS and FS, Figure 1c shows the third type of settling called as mixed sedimentation (MS) in which the settling begun as accumulation and then turned to flocculation with time.

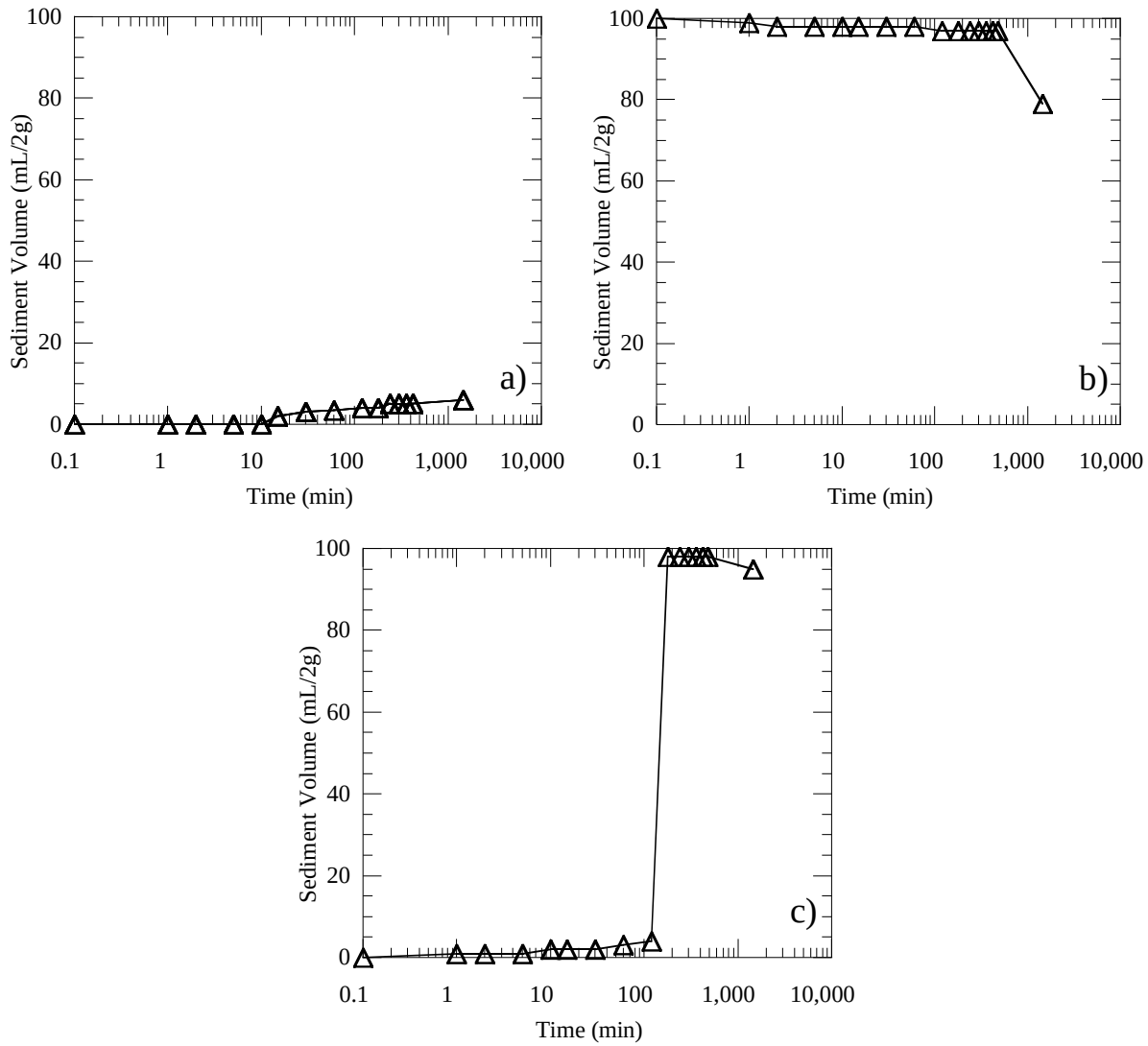

Figure 1. *Sedimentation behaviors of bentonites as a function of time: a) Accumulation sedimentation (AS), b) mixed sedimentation (MS), and c) flocculated sedimentation (FS).*

The sedimentation type and final sediment volumes of bentonites are summarized in Table 2. The sedimentation type of B-1, B-3, B-4, B-7 and B-8 was AS, whereas that of B-2 and B-5 was MS. Only B-6 showed FS type of settling behavior (Table 2). On the other hand, the greatest final sediment volume was obtained for bentonite which had FS type of sedimentation behavior (B-6 and 73 mL/2g). Final sediment volumes were significantly lower for MS than for FS and AS.

Table 2. *The Sedimentation Characteristics and Final Sediment Volumes of Bentonites*

Bentonite	**B-1**	**B-2**	**B-3**	**B-4**	**B-5**	**B-6**	**B-7**	**B-8**
Sedimentation Type	AS	MS	AS	AS	MS	FS	AS	AS
Final Sediment Volume (mL/2g)	8	2	4	6	1	73	7	4

The consistency limits are considered as an index property of the soil that has wide applicability in geotechnical engineering. Therefore, sedimentation characteristics were initially categorized based on index properties (i.e. liquid and plastic limits) of bentonites. For example, the sedimentation behavior was only AS type when the liquid limit was less than 300% (Figure 2a) or the plastic limit was more than 45% (Figure 2b). In contrast, AS, MS or FS type of settling was observed when the liquid limit was more than 300% (Figure 2a) or plastic limit was less than 45% (Figure 2b).

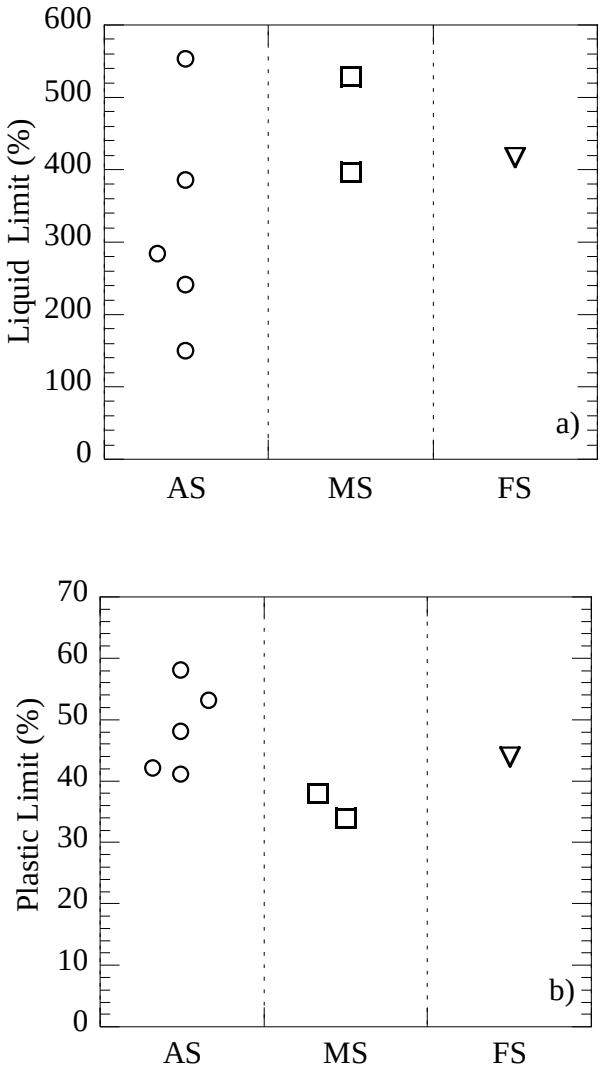

Figure 2. *Categorizing the Sedimentation Behavior Based on Consistency Limits of Bentonites*

The relationship between final sediment volume and index property of bentonite cannot be established. Because, only the sediment volumes obtained with AS had the tendency to increase with the increasing of liquid limit. Thus, only the final sediment volumes obtained with AS were correlated with the liquid limit of bentonites. Figure 3 shows that increase in the liquid limit led to decrease the final sediment volume.

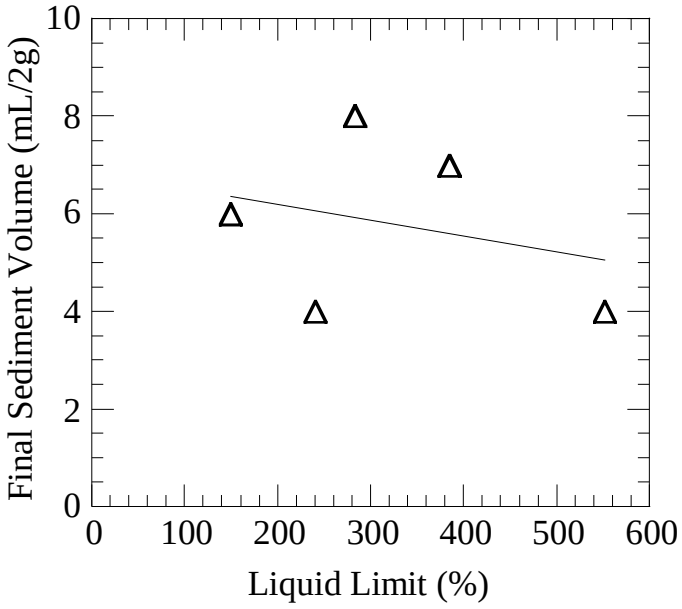

Figure 3. *Relationship between Liquid Limits and Final Sediment Volumes of Bentonites*

The sedimentation characteristics of bentonite can also be evaluated in terms of clay content as shown in Figure 4. Unlike MS and FS, AS type of settling can be observed within wide range of clay contents (Figure 4).

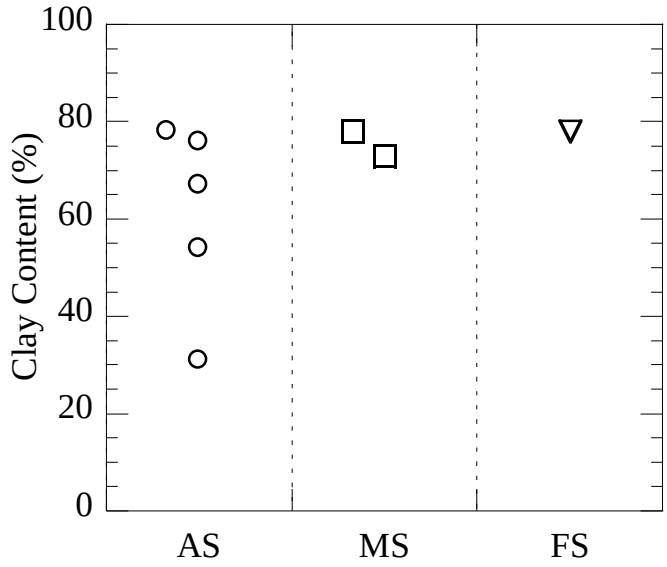

Figure 4. *Categorizing the Sedimentation Behavior Based on Clay Contents of Bentonites*

The categorization of sedimentation behavior is finally made by considering the specific surface area (SSA) and cation exchange capacity (CEC) of bentonites. Figure 5a-b show the variations of these parameters with the sedimentation behavior. The range of AS was 475-830 m^2/g and 73-81 cmol/kg, when SSA and CEC are taken into consideration, respectively. However, the ranges are limited when the sedimentation behavior was MS or FS. Note that, the bentonites

used in this study served AS type of settling and the data set should be increased by adding different types of bentonites to draw a solid conclusion.

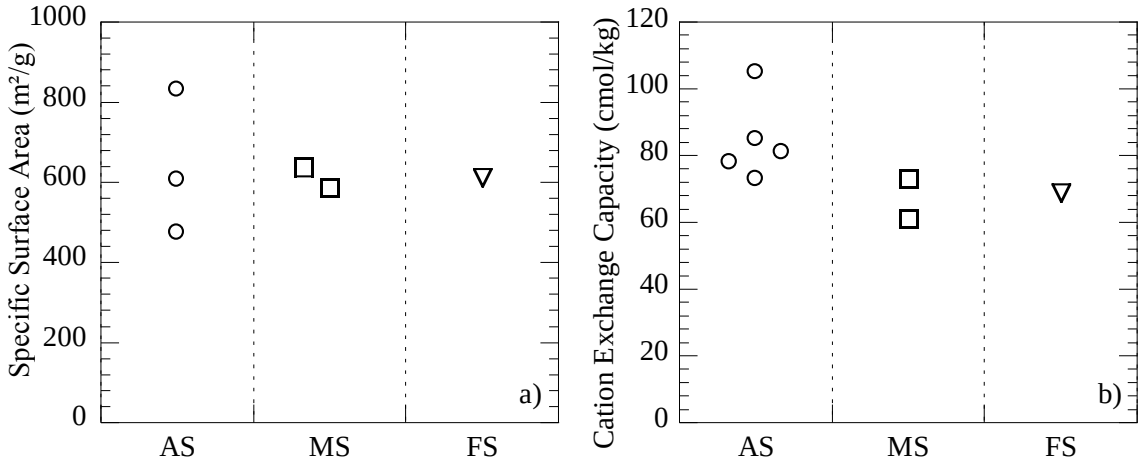

Figure 5*. Categorizing the Sedimentation Behavior Based on Physicochemical Parameters of Bentonites*: a) SSA and b) CEC.

4. CONCLUSION

The present paper discusses the sedimentation characteristic of bentonites which were conducted after swell index tests and with 2g. Then, the sedimentation characteristics were evaluated based on physico-chemical properties of bentonites. In this study, 8 bentonites were tested for this purpose. Five of these bentonites served AS type of settling, whereas the rest of them served MS (two) and FS (one).

Interesting results were obtained from this study. For example, if the bentonite has lower liquid limit, higher plastic limit and lower clay content, then, this bentonite will possibly settle in AS form. However, if bentonite should have higher liquid limit, lower plastic limit, higher clay content, then AS, MS or FS type of settling can be observed. In contrast, it is hard to say such kind of conclusion when SSA and CEC are taken into consideration.

REFERENCES

[1] Imai, G., 1980. "*Settling behavior of clay suspension*". Soils and Foundations, 20(2):61-77.

[2] Sridharan, A., Prakash, K. 2001. "*Settling behaviour and clay mineralogy*". Soils and Foundations, 41(2):105-109.

[3] Kaya, A., Ören, A. H., Yükselen, Y., 2006. "*Settling of kaolinite in different aqueous environment*". Marine Georesources and Geotechnology, 24(3):203-218.

[4] Sridharan, A., Prakash, K., 1999. "*Influence of clay mineralogy and pore-medium chemistry on clay sediment formation*", Canadian Geotechnical Journal, 36(5):961-966.

[5] ASTM D5890-11, 2011. "*Standard test method for swell index of clay mineral component of geosynthetic clay liners",* ASTM International, USA.

[6] Aksoy, Y.Y., Kaya, A., 2010. "*Method dependency of relationships between specific surface area and soil physicochemical properties*", Applied Clay Science, 50(2):182-190.

EVALUATION OF COMPACTION AND CONSOLIDATION BEHAVIOR OF SAND-BENTONITE MIXTURES WITH PUMICE ADDITIVE

Esra Güneri*, *Dokuz Eylul University, The Graduate School of Natural and Applied Sciences, esra_cetinorgu@hotmail.com*

Yeliz Yükselen Aksoy, *Dokuz Eylul University, Department of Civil Engineering, yeliz.yukselen@deu.edu.tr*

ABSTRACT

The number of studies on the thermal behavior of soils have increased because of increase in number and type of energy structures in last decades. The soils around energy structures must retain without any changes at their engineering properties against temperature changes or thermal cycles. Pumice is used for increasing thermal resistivity of materials in industry. It is expected that when the pumice is added to the soil, it increases the thermal resistance of the sand-bentonite mixtures. For that reason, 10% and 20% pumice were added to sand-bentonite mixtures and compaction, consolidation behaviors at room temperature were investigated. According to the results of the compaction tests, the maximum dry unit weight decreased in the presence of 10% and 20% pumice when compared with 10% bentonite-90% sand (10B-90S) and 20% bentonite-80% sand (20B-80S) mixtures. The results of consolidation tests showed that as pumice content increases in the mixture the total vertical strain increased.

Keywords: Pumice, Compaction, Consolidation, Bentonite, Sand.

1. INTRODUCTION

The studies on the interaction of soils with heat in energy piles, nuclear waste insulation, waste handling facilities, gas pipelines, electricity transmission lines have been increased considerably in last decades. The engineering behavior of soils change depending on thermal conditions. As a result of exposure of clay to heat, existing clay components expand and causes increase in distances between clay layers [1; 2; 3] and also pore volume and pore size increased with temperature [4].

Pumice is a volcanic rock with trapped gas bubbles formed during volcanic eruptions [5] it is made up of Si, Al, K, Na, and Fe oxides, with a small percentage of Ca, Mg, Mn, and Ti oxides [6]. Pumice is a raw material which is formed as a result of volcanic activities and is used in many applications. The pumice is used in construction, textile, agriculture, chemistry, industry, filtration and brick-ceramic production. Pumice is a highly porous material and usually there is no connection between these pores. Therefore, it is a low permeability material. The specific density of pumice is 2.5 g/cm^3, the porosity is between 45% and 70% and the hardness is between 5-6. The pH of the pumice value is around 7.0. The average melting temperature of the pumice is 1343 °C [7]. There is no change in the volume of the pumice under the 760 °C. The studies have shown that the heat resistance of pumice is high. Pumice is available in two forms in nature, as acidic and basic. Acidic pumice has white and dirty white color and basic pumice has brown or black color. The density of acidic pumice is lower than the basic pumice.

In the landfill and nuclear waste isolation as impermeable liners sand-bentonite mixtures are used. Because bentonite is a material with low permeability and high water retention capacity. Bentonite is a highly swelling clay and shrinks when becomes dry. Therefore, it is used by mixing with sand in landfills. In order to increase the heat resistance of sand-bentonite mixtures pumice which is a highly temperature resistive material can be used. For that reason, the aim of this study is to investigate compaction and consolidation behavior of sand-bentonite mixtures in the presence of 10% and 20% pumice. The results of this study is a part of ongoing project. For that reason, the test results which were performed on sand-bentonite mixtures under room temperature are given in this manuscript. In the frame of ongoing project the same tests will be performed under high temperature (80 °C).

2. MATERIAL CHARACTERIZATION AND METHODS

2.1. Material Characterization

In this study, the tests were performed on the sand-bentonite mixtures. The bentonite sample was taken from Eczacıbaşı Esan Mining Company and it is Na-bentonite. Pumice was supplied from Pomza Export Mining Company. According to the results of sieve analysis 20.7% of the sand is fine material and it was used as sieved through No. 6 sieve. The bentonite and pumice was sieved through No. 40 sieve. The sand and bentonite samples were dried for 24 hours in the oven at 105 ^{o}C. The 10% bentonite-sand and 20% bentonite-sand mixtures were used in the tests and these mixtures will be called as 10B-90S and 20B-80S, respectively. The pumice was added to the sand-bentonite mixtures without drying. However, the initial water content of pumice was determined at the beginning of the each test and initial water content was considered in the water content calculations. It was changed between 3-5%. The dry unit weight of the pumice is 12.98 kN/m^3 and specific gravity is 2.50. The physico-chemical properties of the bentonite and sand were given in Table 1.

Table 1. *The physico-chemical properties of the materials*

Property	**Sample**	
	Bentonite	**Sand**
Specific gravity	2.70	2.63
Liquid limit (%)	476.0	-
Plastic limit (%)	70.10	-

2.2. Methods

The 10% or 20% pumice were added to the 10% and 20% sand-bentonite mixtures by dry weight. In these mixtures the 10% or 20% of the total mixture amount was adjusted as pumice. The remaining amount of the mixture were prepared as 10%bentonite-sand and 20% bentonite-sand. The desired amount of water was added and the mixture were mixed homogenously. Then samples were kept in a closed container for 24 hours in order to supply homogenoity. For each compaction test, total four samples were prepared in different water contents. The Standard Proctor Test was performed according to the ASTM D698 (2012) [8].

Consolidation test samples were prepared at their maximum dry unit weight and 2% wet side of the optimum water content which was obtained from the Standard Proctor tests. The consolidation tests were performed to according to ASTM D2435 (2011) [9]. Consolidation

samples were prepared by compaction with wooden tampers. After preparing the samples were waited for 24 hours under seating pressure (6.86 kPa). The load increment ratio (LIR) was 1.0 (24.5 kPa, 49 kPa, 98 kPa, 196 kPa, 392 kPa and 784 kPa). When there is no negligible change at deformations, the next loading was started. After completion of the loading part of the test, the unloading part was started. The unloading was performed into two steps; 784 kPa to 196 kPa, from 196 kPa to 49 kPa.

3. RESEARCH FINDINGS AND DISCUSSION

In this study, compaction and consolidation behavior of 10% and 20% bentonite-sand mixtures in the presence 10% and 20% pumice were investigated.

3.1. Compaction Test Results

The compaction curves of 10B-90S and 20B-80S mixtures are given in Figure 1 and 2, respectively. As can be seen from Figure 1, the maximum dry unit weight of the 10B-90S mixture is 16.6 kN/m^3, when 10% pumice was added (9B-81S-10P) this value decreased to 16.3 kN/m^3. In the presence of 20% pumice the max. dry unit weight decreased to 15.6 kN/m^3. It was observed that pumice has a maximum dry unit weight reducing effect, however it did not change the optimum water content values significantly. It is seen that, the effect of pumice on the max. dry unit weight is similar for 10B-90S and 20B-80S mixtures.

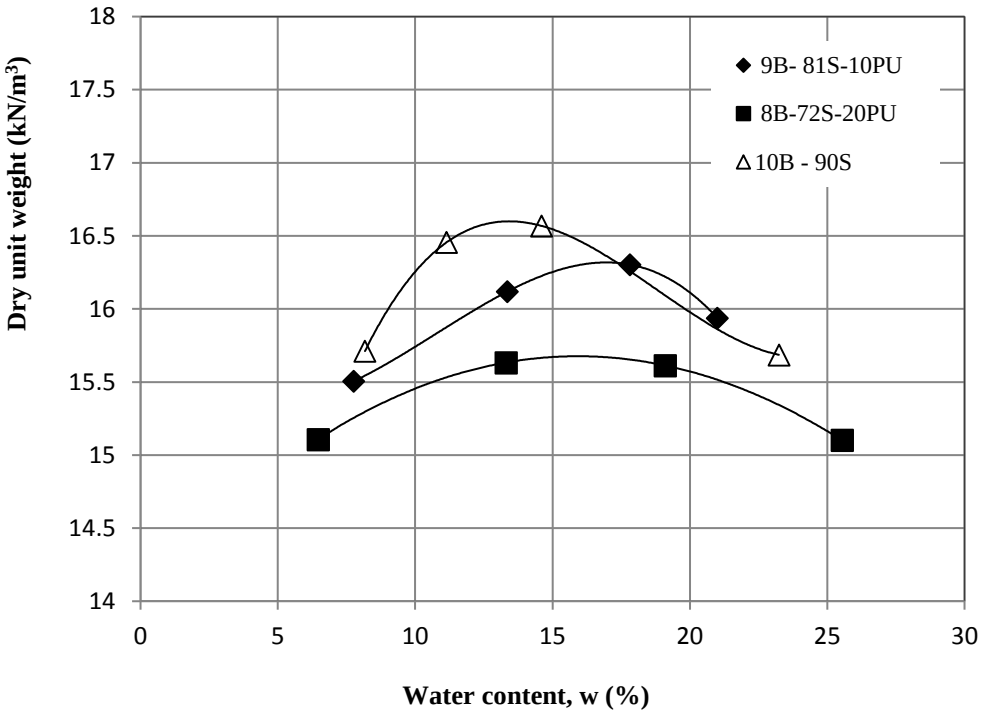

Figure 1. *Pumice addition effect on the compaction behavior of the 10% bentonite-sand mixtures*

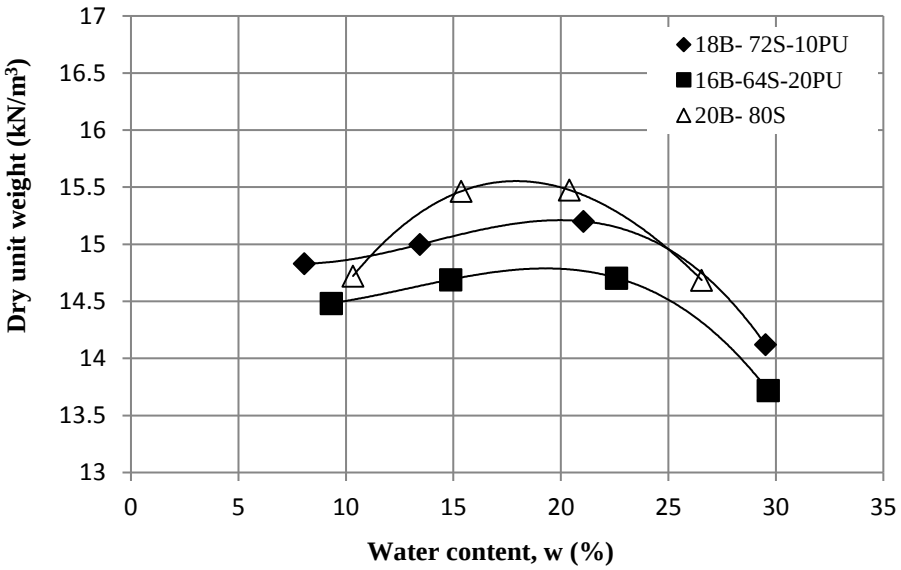

Figure 2. *Pumice addition effect on the compaction behavior of the 20% bentonite-sand mixtures*

3.2. Consolidation Test Results

The compression behavior of 10B-90S and 20B-80S mixtures was determined in the presence of 10% and 20% pumice additives. As shown in Figure 3, the vertical deformation value of 10B-90S mixture in the presence of 10% pumice is 3.4% and in the presence of 20% pumice this value increased to 5.9%. As the pumice content increases, total vertical deformation values of the mixtures increase. For 20B-80S mixture, it was observed that there is no change at the amount of deformation when pumice percentage increased from 10% to 20% (Figure 4). The amount of swelling for 10B-90S mixture in the presence of 10% pumice is 0.2% and in the presence of 20% pumice this value increased to 0.6%. The amount of swelling for 20B-80S mixture in the presence of 10% pumice is 2.0% and in the presence of 20% pumice this value 1.95%. It was observed that there is no significant change at the amount of swelling for 20B-80S mixture when pumice percentage increased from 10% to 20%.

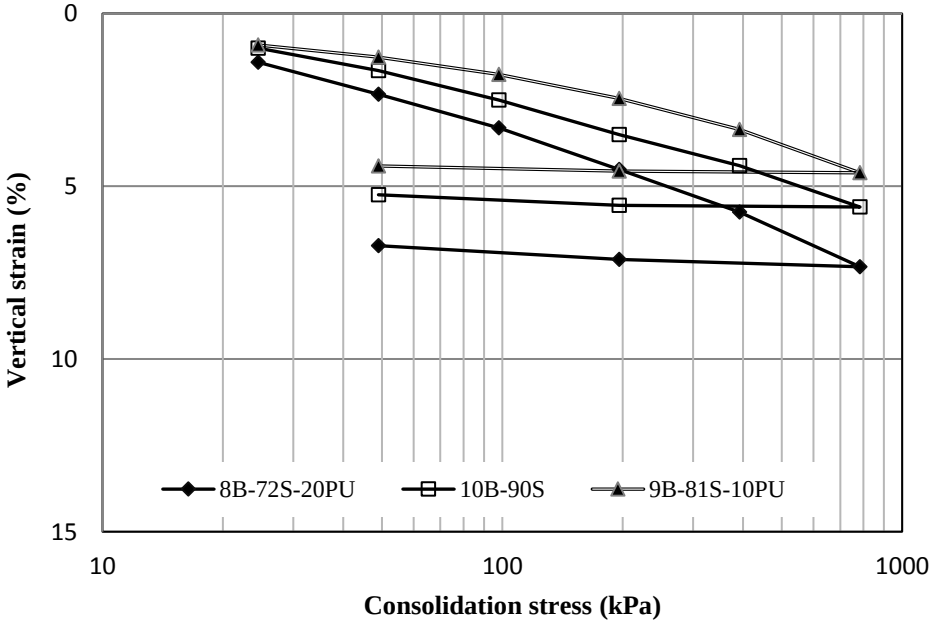

Figure 3. *Compression curves of 10B-90S mixtures with pumice additives*

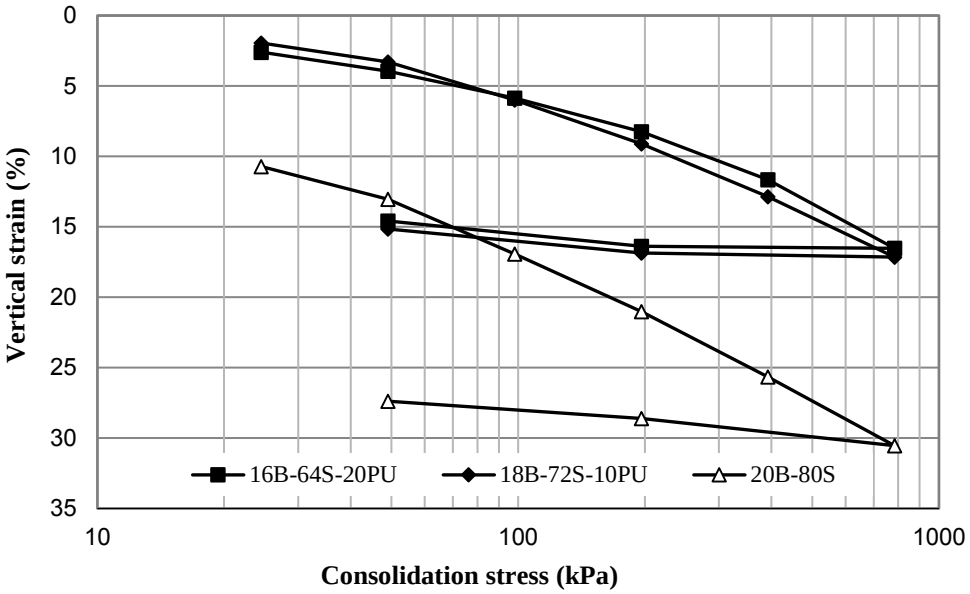

Figure 4. *Compression curves of 20B-80S mixtures with pumice additives*

4. CONCLUSIONS

In this study, the compaction and consolidation behaviors of 10% and 20% sand-bentonite mixtures were investigated in the presence of 10% and 20% of pumice. Generally, it was determined that the presence of pumice decreased the maximum dry unit weight of the mixtures but the water content change vaguely. When the percentage of pumice was fixed and the percentage of bentonite increased from 10% to 20%, it was determined that the maximum dry unit weight decreased. The results of consolidation tests showed that as pumice content increases in the mixture the total vertical strain increased for both mixtures. Even though pumice additive reduces the dry unit weight of the mixtures and increases the total deformation amount, it may increase the strength of the mixtures against thermal changes. For that reason, the same tests will be performed under high temperature as a future study.

ACKNOWLEDGEMENT

This study is supported by The Scientific and Technological Research Council of Turkey (TÜBİTAK) (Grant no: 217M553). The authors are grateful for this support.

REFERENCES

[1] Laloui, L., Cekerevac C., Vulliet L., "*Thermo-Mechanical Modelling of The Behaviour of MC Clay*", Proceedings of the 10th International Conference on Computer Methods and Advances in Geomechanics, ed. C. S. Desai, I: 829-835, 2001.

[2] Fleureau, J.M., 1979. "*Influence d'un Champ Thermique ou Electrique Sur Les Phénomènes D'interaction Solide-Liquide Dans Les Milieux Poreu*", PhD thesis, Ecole Centrale de Paris.

[3] Robınet, J.C., Rahbaou, A., Plas, F. & Lebon, P., 1996. "*A Constitutive Thermomechanical Model for Saturated Clays*", Engineering Geology, 41(1-4):145-169.

[4] Kakali, G., Perraki, T., Tsivilis, S., Badogiannis, E., 2001. *"Thermal Treatment of Kaolin: The Effect of Mineralogy on The Pozzolanic Activity*", Applied Clay Science (20):73–80.

[5] Witham, A.G., Sparks, R.S.J., 1986. "*Pumice*", Bulletin of Volcanology, 48: 209-223.

[6] Liguori, V., Sciorta, R., and Ruisi, V., 1984. "*The pumice aggregates of Lipari Island (Aeolian Isles-Italy)*", Bull. Int. Assoc. Eng. Geol., 30: 431–434.

[7] Chang, L.L.Y., 2002."*Industrial Mineralogy, Minerals, Processes and Uses*", Prentice-Hall, Inc., New Jersey.

[8] ASTM D 698, 2012. "*Standard Test Methods for Laboratory Compaction Characteristics of Soil Using Standard Effort*", ASTM International, USA.

[9] ASTM D 2435, 2011." *Standard Test Methods for One-Dimensional Consolidation Properties of Soils Using Incremental Loading*", ASTM International, USA.

SEISMIC HAZARD ANALYSES IN MICRO SCALE FOR MANISA CITY CENTER

Esra Güneri*, *Dokuz Eylul University, Institute of Science, esra_cetinorgu@hotmail.com*

Ender Başarı*, *Manısa Celal Bayar University, Institute of Science, ender.basari@cbu.edu.tr*

ABSTRACT

In this study, seismic resources around Manisa city center and sub-regions which have the effect potential on the city center were grouped into six different sub-regions. The center of Manisa is spread over a wide area and the distance to the other end of the city center exceeds 20 km. The spread of the city center over a large area also differentiates the distances of points in the city center from the seismic sources. As a result, the earthquake risk probabilities of different points of the city center may vary. Considering this situation, micro-zoning for the city center, Gutenberg-Richter magnitude - frequency relationship, seismic risk estimation and recurrence periods were determined for each micro-zone and seismic sub-regions. In the analyses, earthquake data belonging to both (1900 - 2015) ($m_w \geq 4.0$) and historical ($I0 \geq 5.0$) periods before 1900 were used. The detailed calculation results of the micro-regions are given in this paper and the a and b coefficients calculated for the Gutenberg - Richter magnitude - frequency relationship for the Manisa city center general (3.36 ± 0.13) - (4.90 ± 0.41) and (0.45 ± 0.02) - ($0.68 \pm$) 0.07). The results show that earthquakes in the seismic subregions 2, 4 and 5 for Manisa city center may have devastating effects on earthquakes in seismic sub-regions 1, 3 and 6.

Keywords: Manisa City Center, Poisson Model, Seismic Risk, Source-to-site Distance Probability Distribution.

1. INTRODUCTION

In previous studies, considerable seismic risk determination studies have been performed for many regions including Western Anatolia [1; 2; 3; 4]. Field risk assessments provide general and valid estimates of the earthquake hazard and probability for a given region, but they do not fully reflect the earthquake risk of sites that can be considered as point on a surface such as city center, port, bridge.

In this study, the seismic risk assessment for the province of Manisa was performed using the Poisson model. The historical and instrumental earthquake records were used in seismic risk assessment. The earthquake risk assessments of seismic zones are given together with distance histograms.

2. SEISMOTECTONICS OF THE REGION

Turkey is located in the Alpine Himalayan tectonic belt. Although the tectonism in Anatolia has been defined by different researchers [5; 6] has shaped the tectonism of the region in the north Arap north-west direction of the Arabian plate, and at different speeds in the north of the African plate.

The general seismic activity of Western Anatolia including the leading and aftershocks is given

in Figure 2. When the mechanisms and locations of earthquakes occurred in the region are examined, it is observed that earthquakes are clustered in different characteristic and activity fault systems. The fault systems and seismic activity of the region were grouped into sub-regions with similar characteristics by researchers [3; 4; 7]. In this study, Sayıl and Osmanşahin (2008) considered the lower seismic zone for Western Anatolia Region (Figure 1).

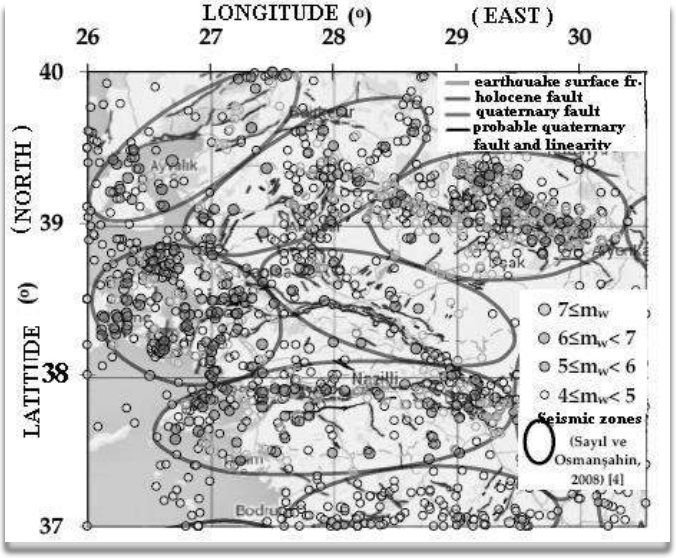

Figure 1.*Fault lines and earthquake center bases in Manisa and its vicinity (Map and fault information:[8], earthquake epicenter and magnitude information:Table 1, Seismic zones: [4]).*

3. MATERIAL

In this study, earthquakes with magnitude (m_w) 4.0 and greater were used in historical and instrumental periods. Earthquakes with a magnitude less than 4.0 are rarely damaged in structures and structures are not damaged in general.

As the greatest moment, the magnitude of the largest earthquake occurred for each sub-seismic zone was taken. Leading and aftershocks are not counted. In the determination of leading and aftershocks earthquake strikes, it has been tried to take into consideration the criteria given in Table 1 [9].

The magnitudes of the earthquakes (different from the magnitude of the moment magnitude) are calculated using the relations proposed in Table 2 for Western Anatolia Region and proposed by Karakostas et al. (2013) [10].

Table 1. *Distance and time intervals used to differentiate leading and aftershocks [9].*

Magnitude	Distance (km)	Time (day)
4.5	35.5	42
5.0	44.5	83
5.5	52.5	155
6.0	63.0	290
6.5	79.4	510
7.0	100.0	790
7.5	125.9	1326
8.0	151.4	2471

Table 2. *Relationships considered for magnitude conversion [10].*

Relationship	b (*)	a (*)	R^2
$m_w=a+bm_s$	0.61±0.003	2.52±0.042	0.95
$m_w=a+bm_b$	0.98±0.006	0.38±0.128	0.90
$m_w=a+bm_l$	0.93±0.003	0.39±0.070	0.94
$m_w=a+bm_d$	1.18±0.010	-0.43±0.182	0.91

The magnitude estimation of historical earthquakes with no knowledge of magnitude and only with the knowledge of violence was made using Equation 1 [11].

$$m_w=3.404+0.355I_0 \quad (1)$$

In the study, the seismic zone boundaries proposed by Sayıl and Osmanşahin (2008) were linearized in terms of ease of calculation of distance histograms (Figure 2).

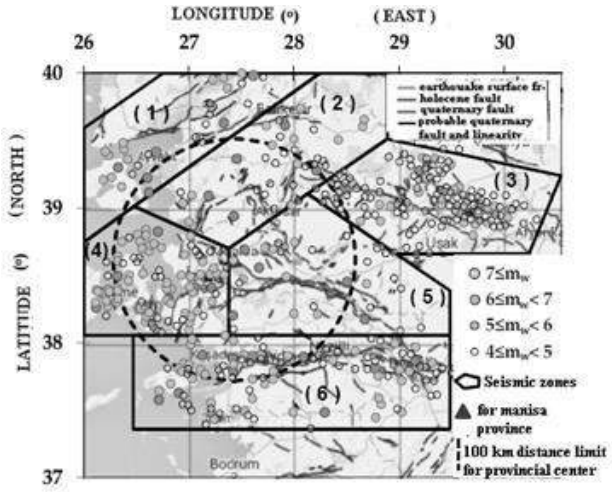

Figure 2. *Seismic zones and earthquakes taken into account in seismic risk analysis. (Map and fault information: [8].*

Number of non-addition and addition of earthquakes of different magnitudes used in the developed s relations to determine the earthquake risk is given in Table 3.

Table 3. *Information on the earthquake data used in eartquake risk analysis*

m_w	1	2	3	4	5	6
4.0-4.4	39	52	148	118	29	105
4.5-4.9	30	30	47	103	18	69
5.0-5.4	19	17	35	83	11	46
5.5-5.9	8	8	8	39	6	20
6.0-6.4	6	5	5	20	4	10
6.5-6.9	5	2	1	8	2	5

7.0-7.4	2	0	1	4	0	2
7.5-7.9	0	0	0	0	0	0
Tg (year)	170	112	111	376	153	169
Observation periods	1845-2015	1903-2015	1904-2015	1639-2015	1862-2015	1846-2015

4. METHOD

The magnitude and frequency relationships of the earthquakes are established in the past and are based on observed earthquakes. Today, one of the widely used methods are Gutenberg and Richter (1954) [12] is proposed by which the general form of Equation 2 given earthquake magnitude-frequency relationship.

$$\log N(m) = a - bm \quad (2)$$

The term N (m), which represents the total frequency in the equation, is the total number of earthquakes with m and greater magnitude. The parameters a and b in equation 2 are the magnitude a frequency relationship coefficients. The coefficient a is dependent on the observation period, the seismic activity of the region and the width of the region. It defines the annual average seismic activity index.The coefficient b is related with the physics of earthquake formation. The coefficients a and b given in Equation 2 are usually calculated by the least squares method [13]. Sayıl and Osmanşahin (2008) proposed Equation 3 for the relationship between n (m) and m.

$$n(m) = 10^{a'-bm} \quad (3)$$

The probability of occurrence of an earthquake in magnitude M within the year T and the period of recurrence D (m) in the magnitude of the observation period Tg year can be calculated by Equation 4 and Equation 5 proposed by Tabban and Gençoğlu (1975) [14].

$$P(m) = 1 - e^{-n(m)T} \quad (4)$$

$$D(m) = \frac{1}{n(m)} \quad (5)$$

The effects of the points at the same distance from the examination area indicated by point A in Figure 4 will be similar with the other conditions being the same, but the effect of the points at different distance r_1, r_2, .., r_i will also be different. Source-field distance histograms are obtained by proportioning and normalizing the total area of the small areas at the same distance to the examination area to the entire source field area (Figure 3).

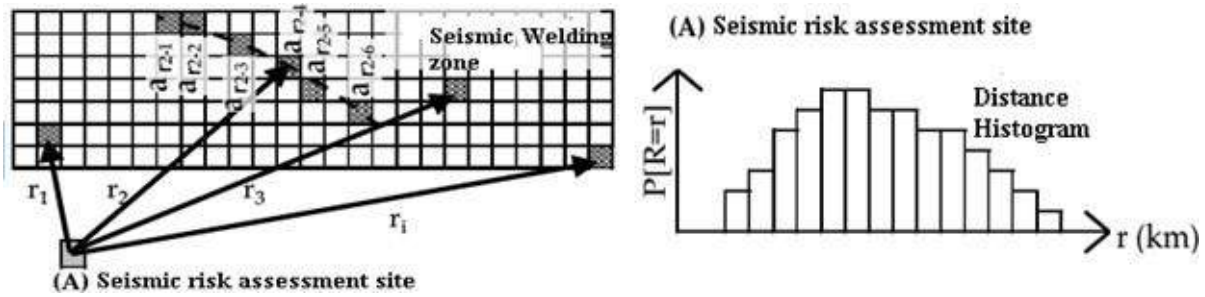

Figure 3. *Source-Distance Histogram*

In this study, the seismic zone zones which can affect the city center of Manisa include 37.36 °North-40.00° North latitudes and 26.00 ° east - 30.54 East longitude bounded area is divided into 16000 small areas with 400 grid. Then, for the distances between 0km and 100km to Manisa city center, normalized histograms were obtained by calculating the source-field distance probability distributions of each seismic source with the source-field distance (Eq.6).

$$P_n[R = r_i] = \frac{1}{A_n}\sum_{j=1}^{k} a_{r_{i-j}} \quad (6)$$

5. ACCOUNT AND ANALYSIS RESULTS

In the study, the correlation coefficients a and b calculated for Equation 2 for the seismic zones (Figure 2) which can affect Manisa city center by applying the least squares method. The magnitudes of the earthquakes considered in the calculation of the a and b coefficients are given in Table 3 above with the addition of earthquake numbers and observation periods. The coefficients a and b were calculated for the seismic regions near Manisa city center (Table 4).

Table 4. *Observations period for seismic zones (Tg), maximum magnitude values (Mmax), total number of eartquakes used for determination of realtionship coefficients and relationship coefficients (a and b).*

Seismic Zone	$m_{w\text{-}max}$	Total number of eartquake	a±(error)	b±(error)
1	7.2	39	3.55±0.17	0.45±0.03
2	6.9	52	3.96±0.17	0.53±0.03
3	7.1	148	4.9±0.41	0.68±0.07
4	7.2	118	4.83±0.36	0.59±0.06
5	6.9	29	3.36±0.13	0.45±0.02
6	7.2	105	4.65±0.16	0.6±0.03

5.1. Seismik Hazard Curves For Manisa City Center

Seismic hazard curves for Manisa city due to six seismic zones which are described in Figure 2 are plotted in Figure 4. According to the results given Figure 2, Seismic zone – 4 has the highest risk for the Manisa city center aspect generating peak horizontal acceleration. On the other hand, seismic zone -3 has the smallest seismic hazard to Manisa city center. In Figure 5 shows the seismic hazard curve due to combination of all seismic zones.

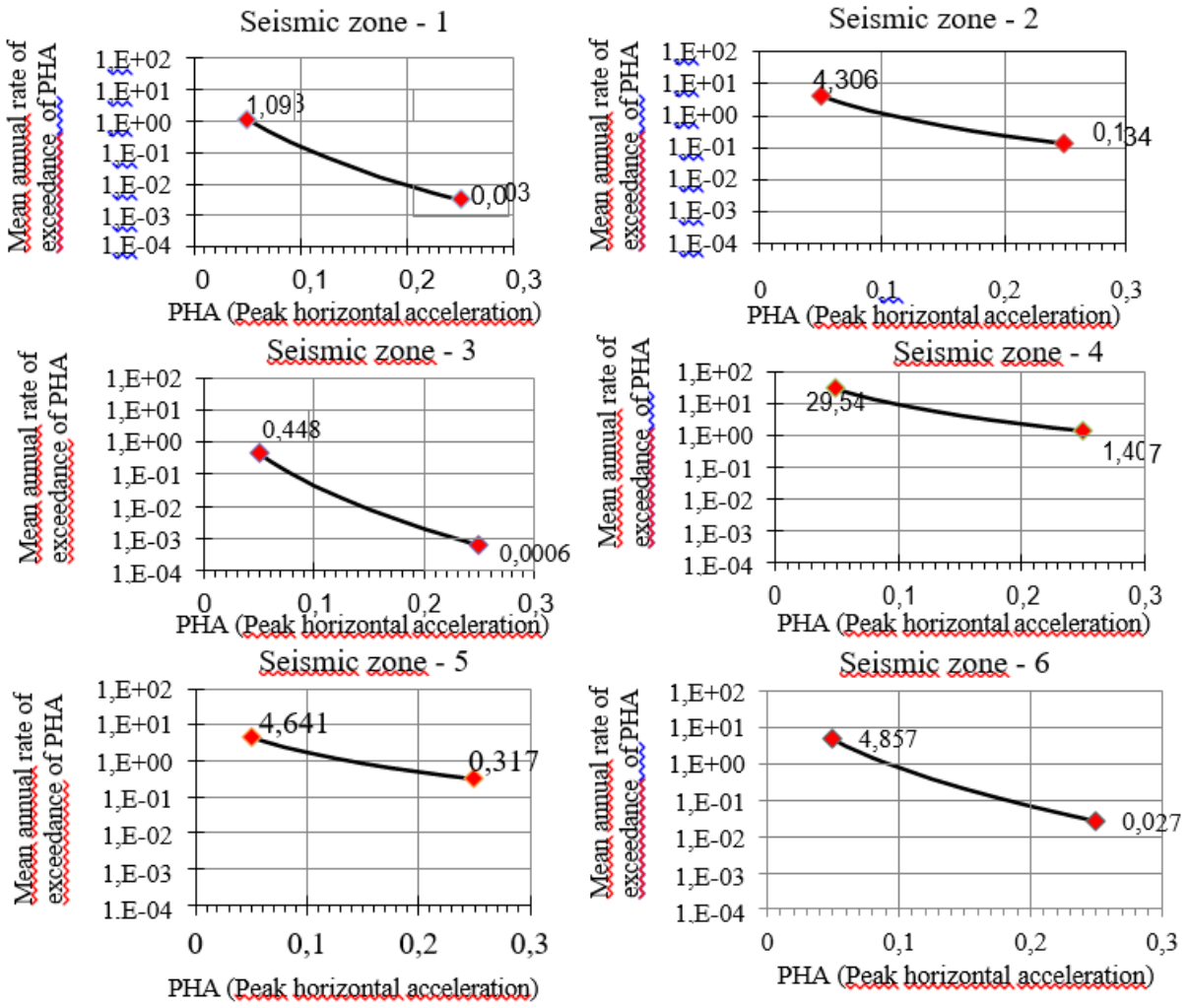

Figure 5. *Seismic hazard curves for source zones 1, 2, 3, 4, 5, 6*

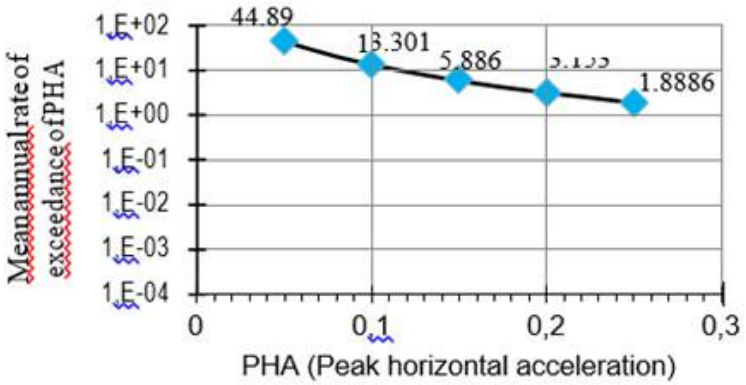

Figure 6. *Total seismic hazard curve for all seismic source zones*

6. CONCLUSION AND DISCUSSIONS

In this study, the seismic risk assessment of the regions that might pose a risk for Manisa city center was conducted. As a result of the analyzes, magnitude - frequency relations, seismic risk values and recurrence periods of the seismic regions in the close distance which could pose a risk for Manisa city center were determined. The magnitude - frequency relationships were determined separately for seismic zones by using different earthquake data ($m_w \geq 4$). The seismic risk assessment of each seismic zone was calculated for earthquakes with 10-year increments, 100-year period and moment magnitude (m_w) of 5.0, 5.5, 6.0, 6.5, 7.0, 7.5. In the risk assessments of the regions and in the calculation of the recurrence periods, the own a and b values of each seismic zone were used.

According to the results given, Seismic zone – 4 has the highest risk for the Manisa citycenter aspect generating peak horizontal acceleration. On the other hand, seismic zone -3 has the smallest seismic hazard to Manisa city center.

In this study, micro zoning was not performed to Manisa city center. It is aimed to establish attenuation relationships for the Manisa city in general form. More detailed attenuation relationships according to local soil properties and detailed seismic hazard mapping for the Manisa city center is planned as a continuation of this study. Literature knowledge related to the Manisa and its neighborhood was selected to connect the different magnitudes and determination of the seismic zones. Although the relations used in the literature have slight differences, relationships which are commonly accepted in the literature have been tried to be selected in order to determine the earthquake risk of Manisa city.

ACKNOWLEDGEMENT

This study is supported by Manisa Celal Bayar University. The authors are grateful for this support.

REFERENCES

[1] Altınok, Y., 1991. "*Assesment of the seismic risk of western Anatolia by Semi-Markow model*", Geophysics, 5:135-140.

[2] Bağcı, G., 1996. "*Earthquake occurrences in western Anatolia by Markov mo*del", Geophysics, 10:67-75.

[3] Firuzan, E., 2008. "*Statistical Earthquake Analysis for Wes-tern Anatolia*", Turkish J. Earth Sci, 17:741-462.

[4] Sayıl, N. Osmanşahin, İ., 2008. "*An investigation of seismicity for western Anatolia*", Nat Hazards 44:51-64.

[5] McKenzie, D.P., 1972. "*Active tectonics of the Mediterranean region*", Geophys J R Astr Soc. 30,:109–185.

[6] Şengör, A.M.C., 1979. "*The North Anatolian transform fault: its age, offset and tectonic significance*", JI geol. Soc. Lond. 136:269-282.

[7] Sözbilir, H., Sümer, Ö., Uzel, B., Ersoy, Y., Erkül, F. İnci, U. Helvacı, C., ve Özkaymak, Ç., 2005. "*17-20 Ekim 2005-Sığacık Körfezi (İzmir) depremlerinin sismik jeomorfolojisi ve bölgedeki gerilme alanları ile ilişkisi*", Batı Anadolu.Türkiye Jeoloji Bülteni. 52(2):217-238.

[8] Emre, Ö., Ere, Ö., Özalp, S., Doğan, A., Özaksoy, V., ve Yıldı-rım, C., 2005. "*İzmir Yakın Çevresinin Diri Fayları ve Dep-rem Potansiyelleri*", Ankara: MTA Raporu no:10754.

[9] Yüceman, M.S. "*Olasılıksal sismik tehlike analizi: genel bakış ve istatistiksel modellemede dikkat edilmesi gerekli hususlar*", 1. Türkiye Deprem Mühendisliği ve Sismoloji Konferansı, ,11-14 Ekim 2011, Ankara, Türkiye.

[10] Karakostas, V., Papadimitriou, E., ve Pabuçcu, Z. A., 2013. "*Homogeneous Earthquake Catalog for Western Turkey and Magnitude of Completeness Determination*", Bulletin of the Seismological Society of America.103(5):2739-2751.

[11] Stucchi, M., Rovida, A., Capera, A.A.G, (2013). Alexandra, P., Camelbeeck, T., Demircioglu, M.B., Gasperini, P; Kouskouna, V., Musson, R.M.W., Radulian, M., Sesetyan, K., Vilanova, S., Baumont, D., Bungum, H., Fäh, D., Lenhardt, W., Zivcic, M., Papaioannou, C., Tatevossian, R., Viganò, D., & Giardini D., The Share European Earthquake Catalogue (SHEEC) 1000–1899. Journal of Seismology. 17(2):523-544.

[12] Gutenberg, B., & Richter, C. F. (1956). "*Magnitude and Energy of Earthquakes*", Annuals of Geophysics. 9(1):1-15.

[13] Güneri, E, 2017. "*Manisa İli Sismik Aktivite Zonları ve Manisa İçin Sismik Tehlike Analizleri*",M.Sc Thesis, Manisa Celal Bayar University, Turkey, 68 pages.

[14]Tabban, A., & Gençoğlu, S., 1975. "*Earthquake and its para-meters"*, Bull Earthq Res Inst of Turk*ey*, 11:7–83.

HYDROLOGICAL AND GEOTECHNICAL MONITORING NETWORK INSTALLED IN SLOPE MOVEMENTS AT FLORES ISLAND

Filipe Marques*, *Laboratório Regional de Engenharia Civil dos Açores, Portugal*, *Filipe.MP.Marques@azores.gov.pt*

Letícia Moniz, *Laboratório Regional de Engenharia Civil dos Açores, Portugal, Leticia.CM.Moniz@azores.gov.pt*

Paulo Amaral, *Laboratório Regional de Engenharia Civil dos Açores, Portugal, Paulo.AP.Amaral@azores.gov.pt*

Ana Malheiro, *Laboratório Regional de Engenharia Civil dos Açores, Portugal, Ana.MM.Malheiro@azores.gov.pt*

ABSTRACT

Located in the western group of the Azores Archipelago, Flores island is a prone zone to slow moving landslides due to its geological, hydrological and morphological context. Over the last 20 years, more attention has been given to this problem. On the other hand, it has been possible to verify that the activity of this phenomenon intensifies when there are periods of long and/or intense precipitation. The present work is developed in two distinct parishes on the Flores Island: Lajedo and Fajãzinha, both located in the southwest of this island. This paper presents the monitoring networks (eg., vibrating wire and Casagrande piezometers, inclinometers, rainfall station and robotic total station) installed in some of the geomorphological instability situations, and the results obtained up to December of 2018. The main goal of the implementation of these monitoring networks is to set an alert and alarm criteria, based on the evolution of the rainfall and the oscillation of the water level in the potential failure surfaces. The work carried out in the Lajedo parish is co-financed by the Azores 2020. Operation ACORES - 01 - 0145 - FEDER - 000055 - DECISIONLARM.

Keywords: Monitoring, Landslides, Risk Management.

1. INTRODUCTION

Despite the geodynamic setting of Azores archipelago [9] [10], rainfall is assumed to be the main triggering factor causing landslides in Azores Archipelago [1], [8]. Whenever the rainfall intensity promotes the reduction of shear strength due to the decrease in apparent cohesion of the soil, or due to the increase of positive pore water pressure in the potential surface failure [2], [5].

In order to better plan and organize the territory, the relationships between water level and displacement velocities exhibited by landslides have been the object of studies, in particular those that present translational and rotational typologies [5].

The monitoring of potentially unstable slopes usually is carried out using various monitoring techniques in order to assess the pressure head, the displacement velocities, the failure depth and types of mechanisms, essential factors for the minimization of geomorphological risk.

With the records obtained from the monitoring, it is possible to predict accelerations and medium-term behavior of geomorphological instabilities, which enables the development of early warning systems, essential for risk management.

These warning and alarm systems are low-cost alternatives for reducing the environmental and economic risk when stabilization measures are not economically viable and/or the rehousing of people entails serious social problems. However, it is necessary to take into account that the prediction of this type of phenomenas exhibits some difficulties, since the deformations that appear within the unstable mass can affect the hydrological and mechanical properties of the materials [11].

In this context, the present work is limited to the study of two situations of geomorphological instability of a slow to very slow kinematic behavior, with a deep failure surface, which develop on the Flores Island (Azores Archipelago). These situations of instability put at risk the urban centers of the Lajedo and Fajãzinha parish.

This work consisted in the implementation of a hydrological and geotechnical monitoring system in the Lajedo parish, using inclinometers, tiltmeters and vibrating wire piezometers and Casagrande piezometers and a rainfall station, and a topographic network in the Fajãzinha parish. It should be noted that it is planned to complement both networks already implemented, with the introduction of a topographic monitoring network in the case of Lajedo and a hydrological and geotechnical network in Fajãzinha.

2. STUDY CASE

Flores Island is located in the western group of the Azores archipelago. Geometrically it presents an elliptical form with a 16.5 km of length and 12.2 km of width, making an area in the order of 143 km^2. The study sites are located in the parish of Lajedo and Fajãzinha, in Lajes das Flores municipality (Figure 1).

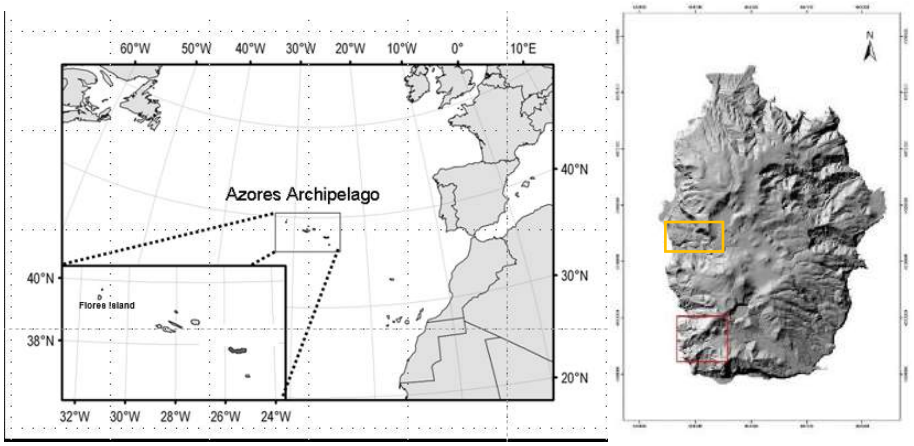

***Figure 1**. Flores Island: Lajedo parish location (red) and Fajãzinha parish (yellow).*

From the geological point of view, the Flores island includes a sequence of highly diversified volcanic products, from Base Complex deposits (lava flows, highly altered tufts) and Upper Complex deposits (lava flows and basaltic pyroclasts) to detrital products resulting from fluvial and geomorphological activity [4].

In Flores Island, particularly in the central zone, a microclimate is developed which includes a rainfall pattern that exceeds the amount of 2000 mm/year, as well as a frequent thick layer of clouds and fog that increase the hidden rainfall and decrease the evapotranspiration [4].

Given the high quantitative of annual rainfall recorded in this island, conditions are created for the recharge of the underground aquifers and also the maintenance of a high water level in the ground surface throughout the year. When the water level reachs a threshold in favorable geological and morphological settings contribute to the landslide activity [6] [7].

2.1. Lajedo

In December of 2010, after a rainy winter, several geomorphological instability situations occurred in the south-west zone of Flores Island, affecting particularly terrains localized in Lajedo parish. Figure 2, on the left, presents the mapping of the three principal landslides observed in Lajedo and the monitoring zones implemented. To the right, we present some evidence of rupture identified in the site # L2.

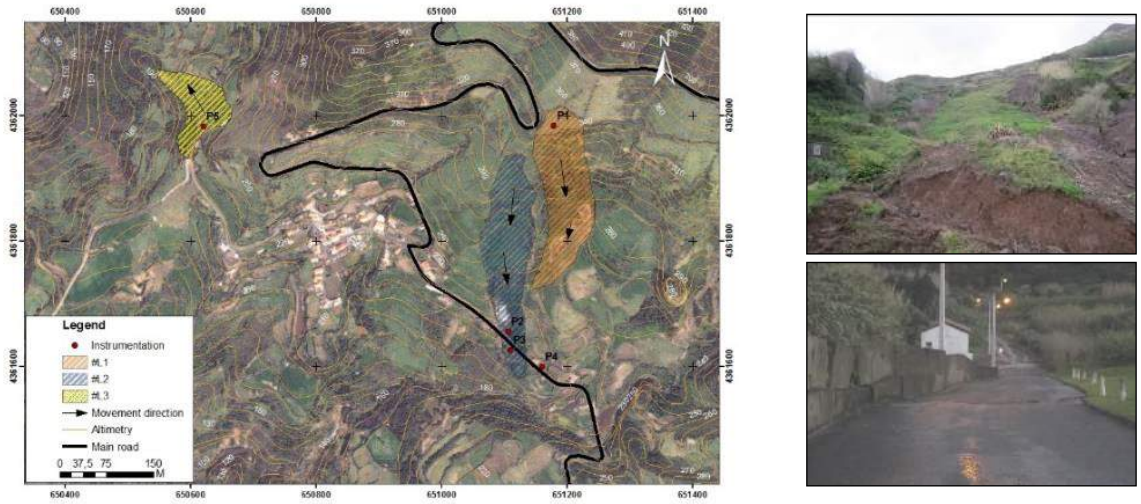

***Figure 2**. On the left, landslides inventory observed in Lajedo and the monitoring zones implemented. On the right, evidence of rupture, in 2010, site #L2.*

The most conditioning geomorphological instability, until now, and the one under analysis in this work corresponds to site #L2 (Figure 2). The #L2 corresponds to a complex movement, of the type of deep-seated earthflow, resulting from the occurrence of a slow deep translational landslide, with flow evolution. The topography surface presents a gradient of 18º. Punctually, gradient variations occurs, coincident with minor scarps of the dislocated mass.

2.2. Fajãzinha

Fajãzinha parish is located on a large coluvionar platform, with slopes ranging from 7 to 20º, and is bordered by imposing escarpments, with sub-vertical slopes, sometimes with heights exceeding 200 m. Several geomorphological indicators of slope movement are identified in the area, such as the presence of concave and convex forms, secondary scars, hummocks, among others.

As a result of the kinematic activity evidenced in the hydrological year of 2012-2013, several indicators of recent geomorphological activity were identified, expressed in the roads and buildings (e.g., ground cracks, echelon cracks, diagonal and longitudinal cracks in masonry walls - Figure 3 on the left).

The geomorphological process corresponds to a complex slope movement, of slide-earthflow type, with a deep failure surface. The foot zone of the geomorphological instability corresponds to the sea cliff, where it is possible to observe the geological nature of the material and the presence of several springs.

Figure 3*. On the left, pathologies verified in housing and streets. On the right, delimitation of the unstable mass of the Fajãzinha and spatial location of the topographic network.*

3. MONITORING NETWORK AND RESULTS

3.1. Lajedo

The first phase of the work carried out in the Lajedo parish consisted of the implementation of the hydrological and geotechnical monitoring network, in the different situations of geomorphological instability verified after the occurrence of 2010. At the site # L2, inclinometer casings (3), Casagrande piezometers (2), vibrating wire piezometer (2) and rainfall stations were installed.

The data acquisition was performed continuously (vibrating wire piezometers and rainfall station) and with punctual measurements (Casagrande piezometers and inclinometers). Regard to continuous measurements, these equipments was connected to a data acquisition unity (datalogger of type CR 800).

Furthermore, this device was linked to a data transmission system of GSM type, realized from LREC – Azores, with a daily cadence. The electrical supply was supported by a 12 volts battery, recharged by solar panels. Concerning to punctual measurements, these were made by the local services of Environment of Flores Island and were executed with an interval of 10 days.

Figure 4 shows the water level fluctuation obtained from the pressure registered by one vibrating wire piezometer installed in #L2 and the accumulated daily rainfall. Between November 2016 and last measurement (March 2019), the water level was near the ground surface, with a fluctuation between 1.0 and 1.6 m.

From this figure, it is possible to conclude that an instantaneous response from the water level to an intense or continuous rainfall period exist. This suggests that materials in this place presents a high to moderated permeability or there are cracks in the soils that allow a quick recharge of water level on the subsoil.

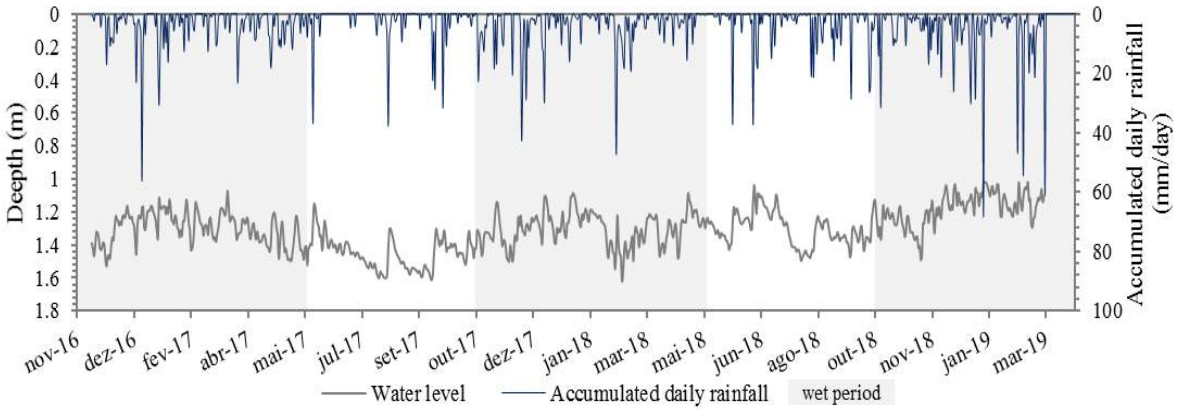

***Figure 4**. Water table variation in P2p1 and daily rainfall from november 2016 to march 2019.*

Figure 5 on the left, shows the more relevant observations performed in P2i inclinometer, during the monitoring period. The results obtained until now show two actives zones in deep, with different displacement rates.

The more superficial zone is situated at approximately 4.5 m. This occurs in the interface between the slope deposit and the weathered lava flow with grey color layer. The second active zone is located at 10.5 m in the transition of a white clay to a basaltic rock, where is located the base of the inclinometer.

The maximum displacement was detected in slope deposit with a quantitative of 13.8 mm, with a mean velocity of 5.7 mm/year. According to Cruden and Varnes (1996) classification, this velocity value indicates an extremely slow movement.

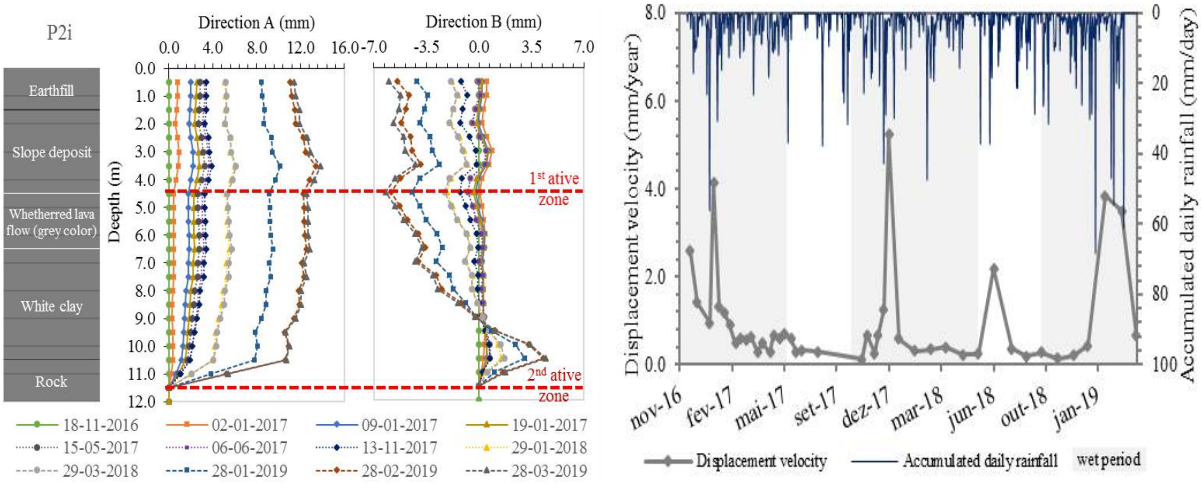

***Figure 5**. On the left, manual inclinometer readings on P2i inclinometer (November 2016 to March 201). On the right, relationship between displacement velocity and accumulated daily rainfall of the P2i.*

Figure 5 on the right, presents a projection of the velocity of the movement and the accumulated daily rainfall. From this figure, it is possible to verify that the test site #L2 consists of an instability with reactivation periods in rainy months (October to May), and deceleration periods in dry months (June to September).

This aspect can also be seen in Figure 5, on the left, where a continuous displacement exists during wet months (e.g. 13-11-2017, 29-01-2018, 28-01-2019, 28-02-2019) in response to rainfall events, ceasing the displacement in dry periods.

3.2. Fajãzinha

In the landslide that affects part of the urban center of Fajãzinha parish, the evaluation of surface deformation of the terrain is carried out with a total station Leica TM50 of 0.5" (0.15 mgon) with angular precision. Distance measurement in precise measuring mode is extremely accurate and has a precision of 0.6 mm + 1 ppm for circular prisms. The equipment used incorporates ATR (Automatic Target Recognition) technology for long reach, which allows the measurement to prisms up to 3000 m, being prepared to work continuously in intense sunlight conditions or total darkness conditions.

Landslide monitoring using total station is generally performed by using three components: (1) a reference network materialized with prisms fixed in a stable position that can be observed from the instrument, (2) one or more stations established on stable ground at locations from which the landslide surface is visible, (3) a group of monitoring prisms at the likely unstable slope zone or area of interest. In this sense, the current monitoring network consists of 2 base stations (PE1 and PE2), 30 control points (C1 to C30) and 4 reference points (PR1, PR2, C15, and C16). All object and reference points are equipped with Leica GPR112 prisms, except PR1 reference point which is equipped with a GMP104 prism. Figure 6 shows the identification and spatial distribution of the monitoring points.

The periodicity of data acquisition is approximately 15 days, and these are assured by the Environmental Services of Flores Islands. In each data acquisition campaign, a minimum of 7 different scans (turns) are made for each observation mark. The atmospheric parameters (pressure, temperature and humidity) were included in the instrument to correct the atmospheric refraction. Taking into account the tolerance of the distances (calculated from the constant part of the accuracy of the equipment (0.6 mm) and from the variable part of the accuracy based on the measured distance (1 ppm)) and the associated error in each measurement, that for 95% confidence interval the maximum obtained was 2 mm, the use of ± 5 mm tolerance was considered for this variable, admitting system changes whenever this value is exceeded.

The geodetic monitoring network was installed in November 2017. The distances between the base station and the observation points vary between 48 to 1137 m.The data presented in this document cover the period between January 2018 and February 2019. During this period, 27 data acquisition campaigns were carried out. Figure 6 shows the variation of the displacements related to the slope distance of some representative benchmarks. In order to understand the movements in planimetry, the absolute deformation vectors obtained, in the campaigns of 25-02-2019 (in purple) and of 22-01-2019 (in black) are projected in the same figure.

It is possible to see that the marks that are outside the unstable zone (PR1, C6, C15 and C16) do not present significant variation for the whole time series, being this variation associated with seasonal and daily fluctuations, caused by atmospheric variations and tidal effects. In contrast, the other points showed a behavior within tolerance variation, with slight oscillations until December 2018, with a significant increase or decrease in displacement values, suggesting a reactivation of the monitored system due to the precipitation quantitative.

In Figure 6, on the left, daily and accumulated rainfall obtained in the meteorological station of Terreiros, located in the area near the parish, is presented. It is possible to see that the months of December 2018, and January and February 2019 were particularly rainy. In the hydrological year of 2017/2018 the accumulated annual precipitation was around 1150 mm. In the hydrological year of 2018/2019, between December 2018 and February 2019, it already rained more than half (620 mm) than in the previous hydrological year, which is why the landslide that affects Fajãzinha has been active. Between December 2018 and February 2019, in 3 different days was registered rainfall values between 50 and 75 mm.

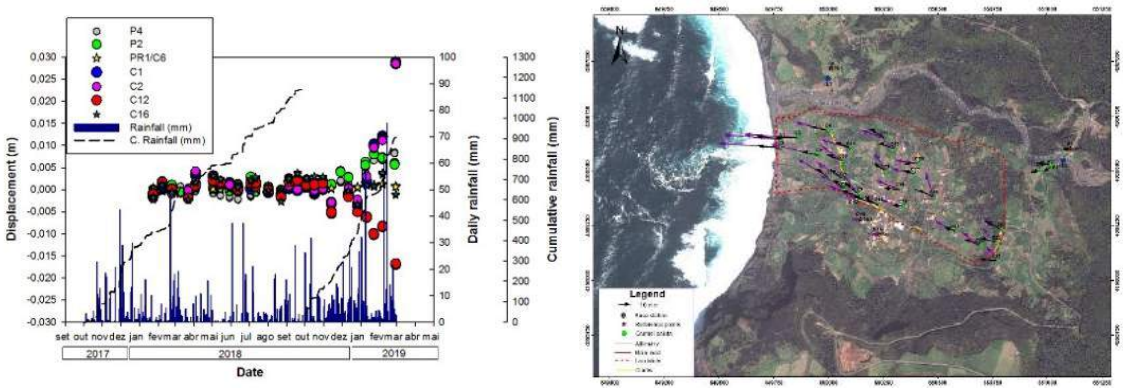

***Figure 6**. (on the left) slope distance variation for some points and daily and accumulated precipitation. (on the right) geometry of the monitoring network, with the identification of the observation marks and projection of the planimetric displacement vectors obtained on 01-22-2019 (black) and 27-02-2019 (purple).*

The maximum displacement observed in the monitoring period showed values of about -57 mm, 16 mm and - 27 mm for the components E, N and Z, respectively. The orientation of the planimetric displacement is compatible with the preferential direction of the movement of the terrain, essentially towards west. The displacement data define an evolution history from the beginning of 2018, as an average annual planimetric velocity of 0.08 m/year. Indicators of movement in relation to references outside the unstable mass in a period of 40 years, obtained by reports of ancient people, allowed to estimate that the unstable terrain presents rates of annual movements in the order of 0.1 m/year, compatible with the registered ones during the monitoring period.

4. CONCLUSIONS

In places prone to the occurrence of geomorphological instability processes, usually are used mitigation measures in order to prevent/attenuate geomorphological hazards. However, in some situations, such as those presented in this paper, the typology and the dimension of the phenomena, the execution of engineering techniques are not feasible, given the high financial cost and/or high environmental impact. Therefore, it is important to use monitoring techniques that allow the monitoring and evaluation of the state of instability situations, as well as the definition of thresholds to originate new reactivations, which are the basis for the development of alarm and alarm systems.With the continuous results of the geotechnical and hydrological monitoring obtained in the Lajedo parish until now, it is possible to identify a practically instantaneous response of the water level with the precipitation, as well as the existence of a relation between movements occurred and the moments of intense precipitation in the place. In this way, it is possible to conclude that, regarding to its state of activity, the landslide process shows an active and intermittent behavior. Furthermore, this paper presented the initial phase of the monitoring network designed for the landslide phenomenon that affects the Fajãzinha, obtaining a vision of the kinematic behavior that occurs, in response to precipitation. The periods of reactivation of the system correspond to moments where rainfall exceeded 50 mm/day, indicating preliminarily a precipitation threshold responsible for the reactivation of the system. The monitoring system designed for Fajãzinha and Lajedo parish is a pilot project for multidisciplinary monitoring. With this type of tool, it is expected to develop a system that allows the decision-making for alert and alarm, based on dynamic models of stability, through the study of the oscillations of the water level in the potential rupture planes and the deformations of the soil.

ACKNOWLEDGEMENT

The implementation of this work was only possible due to the financing of the Operational Program FEDER FSE Açores 2020 to the project designated by: "Desenvolvimento e implementação de um sistema de apoio à decisão para alerta e alarme a movimentos de vertente com o recurso à monitorização cinemática e hidrológica e à modelação hidrológica e geotécnica" (ACORES-01-0145-FEDER-000055- DECISIONLARM).

REFERENCES

[1] Amaral, P., Marques, R., Zêzere, J.L., Queiroz, G., Marques, F., 2009. *"Distributed Transient Modelling of Rainfall Triggered Shallow Landslides for Susceptibility Assessment in Ribeira Quente Valley (S. Miguel, Azores)"*, In: Landslide Processes, from geomorphological mapping to dynamic modelling, Strasburg, France 6-7 February 2009. Strasburg, CERG, France: 29-94.

[2] Amaral, P., 2010. *"Caracterização geotécnica e hidrológica de depósitos vulcânicos: Modelação a estabilidade de taludes no concelho da Povoação (ilha de S. Miguel – Açores)"*, Dissertação de Doutoramento em Geologia especialidade de Vulcanologia. Departamento de Geociências da Universidade dos Açores, pp 277.

[3] Amaral, P., Marques, R., Zêzere, J.L., Queiroz, G., Marques, F., 2010. *"Contribuição da sucção matricial na avaliação dinâmica da estabilidade de vertentes naturais: o caso de estudo do Talude da Estrada Regional no concelho da Povoação (ilha de S. Miguel, Açores)"*, Publicações da Associação Portuguesa de Geomorfólogos, Vol. VII, pp 41 -49.

[4] Azevedo, J., 1998. *"Geologia e Hidrologia da Ilha das Flores (Açores – Portugal)"*, 1º Volume. Dissertação de doutoramento. Departamento de Ciências da Terra. Universidade de Coimbra.

[5] Malet, J.-P., van Asch, TH.W.J., van Beek, R., Maquaire, O., 2005. *"Forecasting the Behaviour of Complex Landslides with A Spatially Distributed Hydrological Model"*, Natural Hazards and Earth System Sciences, Vol. 5, pp 71–85.

[6] Malheiro, A., 1997. *"Algumas considerações sobre a existência de um fenómeno de subsidência na Fajãzinha – Ilha das Flores"*, 6º Congresso Nacional de Geotecnia. Lisboa, 8 p.

[7] Marques, R., Amaral, P., Gaspar, J. L., 2011. *"Considerações sobre fenómenos de instabilidade geomorfológica na freguesia da Fajãzinha (Ilha das Flores)"*: Ocorrências de 2-3 de Dezembro de 2010. Civisa/CVARG.

[8] Marques, R., Amaral, P., Araújo, I., Gaspar, J.L., Zêzere, J.L., 2015. *"Landslides in S. Miguel Island (Azores): Susceptibility Analysis and Validation of Rupture Zones Using A Bivariate GIS-Based Statistical Approach"*, Eds. Gaspar, J.L., Guest, J.E., Ducan, A.M., Barriga, F.J.A. & Chester, D. k. volcanic Geology of São Miguel island (Azores Archipelago). Geological Society, London, Memoirs, 44, 167-184.

[9] Miranda, J. M., Luis, J. F., Lourenço, N., Fernandes, R. M. S., 2015. *"The structure of the Azores Triple Junction: implications for São Miguel Island"*, In: Gaspar, J. L., Guest, J. E., Duncan, A. M., Barriga, F. J. A. S. & Chester, D. K. (eds) Volcanic Geology of São Miguel Island (Azores Archipelago). Geological Society, London, Memoirs, 44, 5–13, http://doi.org/10.1144/ M44.2

[10] Searle R., 1980. *"Tectonic pattern of the Azores spreading centre and triple junction"*, Earth Planet Sci Lett 1980, 51:415–34.

[11] van Asch Th., van Beek, L. e Bogarrd, T., 2006. *"Problems in Predicting the Mobility of Slow-Moving Landslides"*, Faculty of Geosciences. The Netherlands. Engineering Geology 91, pp 46-55.

AN ELASTO-PLASTIC MODEL FOR CLAYS SUBJECTED TO CHANGES IN PORE FLUID CHEMICAL COMPOSITION

Giulia Scelsi*, *DICA, Politecnico di Milano, giulia.scelsi@polimi.it*

Gabriele Della Vecchia, *DICA, Politecnico di Milano, gabriele.dellavecchia@polimi.it*

Guido Musso, *DISEG, Politecnico di Torino, guido.musso@polito.it*

ABSTRACT

Pore fluid composition strongly influences the mechanical behavior of clays, modifying both the volumetric and the shear response of the material. Accounting for this aspect is crucial for engineering applications where changes of the chemical composition of the pore fluid are anticipated, such as engineered barriers for the containment of pollutants.
In this work, a chemo-mechanical model capable of reproducing the response of medium to low activity clays under both mechanical and chemical loading paths is presented. The model is developed in the framework of the theory of elasto-plasticity with generalized hardening: chemo-mechanical coupling is introduced both in terms of stress variables and hardening laws. The general formulation is specialized to the case of medium to low activity clays subjected to variations of the saline concentration of the pore fluid, introducing osmotic suction as a chemical stress variable. The model has then been implemented in a constitutive driver for the integration at the REV level of the incremental constitutive equations. The model is finally tested against literature data.

Keywords: Clay, Osmotic Suction, Elasto-Plasticity, Generalized Hardening.

1. INTRODUCTION

The knowledge of the behavior of clayey soils subject to changes in pore fluid chemical composition is now becoming significant in the practice of civil, energy and environmental engineering. In the framework of elasto-plasticity with generalized hardening [1], a chemo-mechanical model for medium to low activity clays is presented. The static variables are the effective stress tensor $\boldsymbol{\sigma'}$ and the osmotic suction π, which depends on the chemical concentration of the pore fluid.

2. CHEMO-MECHANICAL MODEL

Under the small strain assumption, the total strain increment $\dot{\boldsymbol{\varepsilon}}$ is decomposed into an elastic part, $\dot{\boldsymbol{\varepsilon}}^e$ and a plastic part, $\dot{\boldsymbol{\varepsilon}}^p$. The elastic strain increment is in turn expressed as a sum of two contributions, the one induced by mechanical loading and the one induced by variations of the chemical concentration of the pore fluid. In axi-symmetric conditions, the volumetric and deviatoric strain increments are thus evaluated as:

$$\dot{\varepsilon}^e_{vol,mec} + \dot{\varepsilon}^e_{vol,ch} = \frac{\kappa}{v_0}\frac{\dot{p}'}{p'} + \frac{\kappa_\pi}{v_0}\frac{\dot{\pi}}{\pi+p_{atm}}, \qquad \dot{\varepsilon}^e_{dev,mec} = \frac{1}{3G}\dot{q}$$

where κ is the mechanical elastic compressibility, v_0 is the initial specific volume, κ_π is the chemical compressibility, G is the shear modulus. Null deviatoric chemical strains are assumed.

The yield surface stems from the modified Cam clay model, by introducing the dependence of the internal variable p_c (i.e. the pre-consolidation pressure) on the osmotic suction:

$$f(q,p,p_c) = \frac{q^2}{M^2} + p(p - p_c), \text{ with } p_c = p_0 \mathrm{X}(\pi) = p_0 \left[1 - \gamma_\pi \ln\left(1 + \frac{\pi}{\pi_{ref}}\right)^\beta\right]$$

where M is the slope of the critical state line in p-q plane and p_0 is the pre-consolidation pressure at null osmotic suction. The function X, describing the evolution of p_c with osmotic suction, is set to depend on two material parameters, γ_π and β. The hardening law reads $\dot{\varepsilon}^{pl}_{vol,mec} = \frac{\lambda-\kappa}{v_0}\frac{\dot{p}'_0}{p'_0}$, where λ is the elastic-plastic compressibility. Associativity of the flow rule is finally assumed.

3. MODEL VALIDATION ON EXPERIMENTAL DATA

After calibrating the model parameters (κ , λ , G , M , κ_π , γ_π , β), the model can be used to simulate the behaviour of medium to low activity clays subject to both mechanical and salinization/desalinization paths. As it is shown in Figure 1, the model is capable of reproducing the response of a compacted illitic clay, whose experimental results have been presented in [2], without any dependence of model parameters on the saline concentration of the pore fluid.

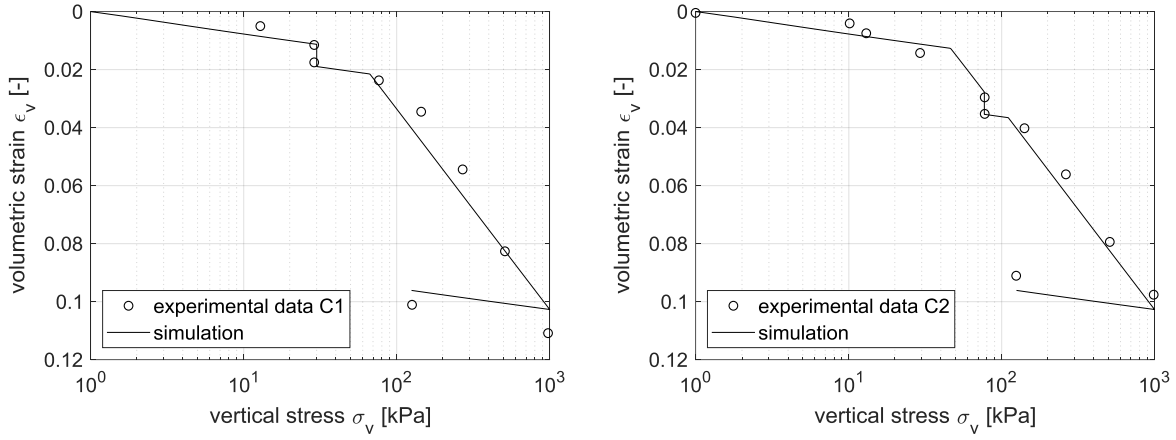

***Figure 1**. Simulation of two experimental tests presented in [2]*

4. CONCLUSION

A simple framework for reproducing the chemo-mechanical response of medium to low activity clays subject to changes in pore fluid chemical composition has been presented. The constitutive model has been validated with experimental data reported in the literature. A limited number of parameters is sufficient to model the chemo-mechanical response of these materials, due to the limited effect of chemical solicitations on material microstructure. When coping with active clays, e.g. bentonites, double-porosity formulations would be more suitable.

REFERENCES

[1] Tamagnini, C., Ciantia, M.O., 2016. "*Plasticity with generalized hardening: constitutive modeling and computational aspects",* Acta Geotechnica, 11:595-623. doi:10.1007/s11440-016-0438-8

[2] Witteveen, P., Ferrari, A., Laloui, L., 2013. "*An experimental and constitutive investigation on the chemo-mechanical behavior of a clay"*, Géotechnique, 63(3):244-255. doi:10.1680/geot.SIP13.P.027

SOCKET ROUGHNESS EFFECT ON SIDE SHEAR RESISTANCE PREDICTION OF ROCK-SOCKETED PILES

Gutiérrez-Ch José Gregorio*, *PhD Candidate, Universidad Politécnica de Madrid, jg.gutierrez@alumnos.upm.es*

Melentijevic Svetlana, *Dr., Universidad Complutense de Madrid, svmelent@ucm.es*

Senent Salvador, *Dr., Universidad Politécnica de Madrid, s.senent@upm.es*

Jimenez Rafael, *Dr., Universidad Politécnica de Madrid, rafael.jimenez@upm.es*

ABSTRACT

Rock-socketed piles have been extensively employed to receive and transmit large concentrated loads to deeper stronger materials. Although the load transfer mechanism combines base and side resistances, the contribution of side shear resistance is often crucial, as it is usually mobilized at much lower strains (or pile settlements) than base resistance. The side shear resistance of rock-socketed piles has usually been estimated using recommendations from codes and standards, or using local knowledge obtained from full-scale static load tests performed in similar ground. There are also empirical formulations as a function of the uniaxial compressive strength of the intact rock. However, this approach neglects the influence of other important aspects such as the effect of roughness at the rock-pile interface, and this factor is not always being considered in current design practices. The aim of this work is to examine the socket roughness effect on side shear resistance of rock-socketed piles. To do that, DEM^{2D} numerical models of direct shear tests, and DEM^{3D} numerical models of rock-socketed piles with different degrees of socket roughness are employed. Numerical results suggest that socket roughness is an important factor that significantly increases the load capacity and stiffness of rock-socketed piles.

Keywords: Rock-socketed Piles, Side Shear Resistance, Socket Roughness, DEM.

1. INTRODUCTION

Usually, the design of axially loaded rock-socketed piles is based on state codes and standards or local knowledge obtained from full-scale static load tests [1]. Depending on the geological conditions, construction techniques, etc., the design is done considering the side shear resistance only, the base resistance only, or the combination of both components [2]; however, it is generally accepted that the side shear resistance is fully mobilized at lower strains (pile settlement of 1% pile diameter) than the base resistance [3,4].

The side shear resistance of rock-socketed piles is frequently estimated as percentage of the uniaxial compressive strength (UCS) of the weaker material (rock or pile) [5], but this empirical formulation neglects the influence of other important aspects affecting the side shear resistance behaviour like the roughness at the rock-pile interface [1,6]. The aim of this work is to examine the socket roughness effect on side shear resistance behaviour of rock-socketed piles through numerical models employing Distinct Element Method (DEM) implementation with $PFC^{2D\&3D}$.

2. NUMERICAL SIMULATION

2.1. DEM Approach with PFC

Particle Flow Code (PFC) is a DEM based package [7] used in this work, in which the materials (e.g., rock or concrete) are simulated as a Bonded-Particle Model (BPM) composed of rigid finite-sized particles –circular (PFC^{2D}) or spherical (PFC^{3D})–. The particles interactions are created or destroyed depending on the proximity between them. The system evolution is computed using DEM approach, in which Newton's second law is employed to determine the motion of each particle and the force-displacement law is used to update the forces at each particle-particle contact [7].

2.2. Small-Scale Numerical Models

In this section, the effect of roughness at the rock-concrete interface has been analyzed using DEM^{2D} models to simulate direct shear tests of rock-concrete interfaces under Constant Normal Load (CNL) and Constant Normal Stiffness (CNS) boundary conditions (see Figure 1). To do that, the micromechanical parameters that reproduce the macromechanical behaviour of each materials –i.e., sandstone and concrete– and the interaction between them –i.e., sandstone-concrete interaction– should be calibrated first. During the calibration procedure, experimental results conducted and presented in [8] corresponding to (i) uniaxial compression strength tests (UCSs) on sandstone and concrete samples, and (ii) direct shear tests (DSTs) on sandstone-concrete planar joints, are employed as a benchmark. The sandstone and concrete samples were simulated with the Flat-Joint Contact Model (FJCM) [9], while the sandstone-concrete interaction was modeled with the Smooth-Joint Contact Model (SJCM) [10]. The methodology of the calibration procedure has been explained with details in [11,12].

The micromechanical properties employed during the calibration procedure of intact DEM^{2D} samples and the comparison of the macromechanical properties resulting from DEM^{2D} and experimental UCTs are summarized in Table 1. As it can be noted, the macromechanical properties obtained from DEM^{2D} are similar to those calculated from laboratory tests.

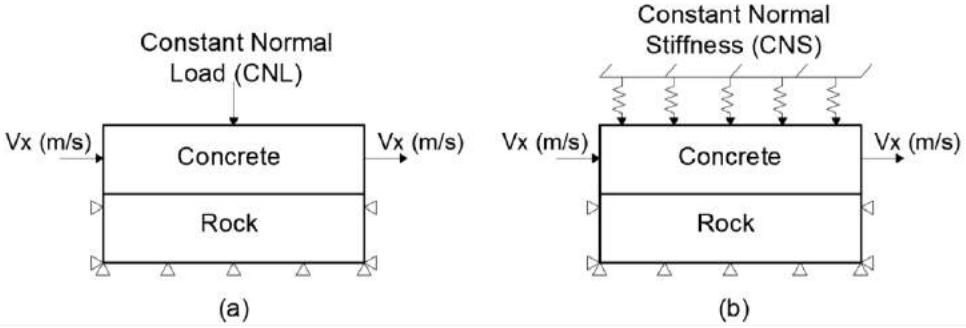

Figure 1. *Idealized sketch of direct shear test: (a) CNL boundary conditions, (b) CNS boundary conditions (modified from [11])*

An illustration of (i) a DEM^{2D} specimen, (ii) the displacement vectors and (iii) the axial stress versus axial strain curve with the corresponding cracks propagations are shown in Figure 2. It can be observed that a few cracks (tension and shear) have been developed at pre-peak stage. As the loading increases, the cracks continue to appear until σ_c is reached, and such cracks increasing rapidly at post-peak stage.

Table 1. *(a) Micromechanical properties fitted from UCSs employed in the calibration of intact DEM^{2D} samples, (b) comparison of macromechanical properties between DEM^{2D} and experimental UCSs (experimental data from [8])*

(a) Micromechanical properties of FJCM	S2-sandstone		S3-sandstone		Concrete	
Effective modulus, E^*, $\overline{E^*}$ (GPa)	1.70		1.90		27	
Normal-to-shear stiffness ratio, k^*, $\overline{k^*}$	1.35		1.45		2.75	
Friction angle, $\emptyset$ (°)	32		35		30	
Ball density, $\rho(kg/m^3)$	2500		2550		2500	
Minimum radius, R_{min} (mm)	1		1		0.8	
R_{max}/R_{min}	1.4		1.4		1.5	
Cohesion, c (MPa)	4.85		7.90		13.55	
Tensile strength, σ_t (MPa)	2.8		3.5		6.0	
(b) Macromechanical properties	Experimental	DEM^{2D}	Experimental	DEM^{2D}	Experimental	DEM^{2D}
UCS (MPa)	11.49	11.59	21.77	21.65	40	39.87
Young's Modulus, E (GPa)	1.98	2.01	3.25	2.32	29.95	30.08
Poisson's ratio, ν	0.10	0.10	0.10	0.11	0.20	0.20

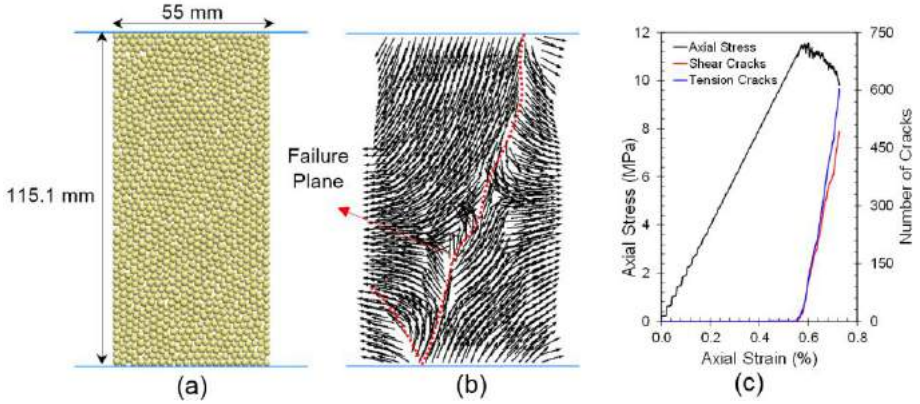

Figure 2. *DEM^{2D} sample: (a) S2-sandstone before the beginning of the UCS test, (b) failure plane and displacement vectors at the end of the UCS test, (c) axial stress, number of cracks (shear and tension) vs axial strain during the UCS test*

On the other hand, the SJCM micromechanical properties calibrated to represent the sandstone-concrete interfaces and the comparison between DEM^{2D} models with laboratory DSTs results conducted on unbonded planar sandstone-concrete joints, are listed in Table 2. Numerical results are similar to those macromechanical properties obtained from laboratory tests performed on unbonded rock-concrete planar joints.

Table 2. *(a) Micromechanical properties calibrated from DEM^{2D} DSTs conducted on unbonded sandstone-concrete planar joints, (b) macromechanical properties of the joints computed from DEM^{2D} and experimental DSTs (experimental data from [8])*

(a) Micromechanical properties of SJCM	Sandstone(S2)-concrete		Sandstone(S3)-concrete	
Joint normal stiffness, $k_{n\,SJ}$ (MPa/mm)	10		10	
Joint shear stiffness, $k_{s\,SJ}$ (MPa/mm)	5		2	
Joint coefficient of friction, μ_{SJ} (tan $\emptyset$ (°))	0.70		0.70	
(b) Macromechanical properties	Experimental	DEM^{2D}	Experimental	DEM^{2D}
System normal stiffness, K_n, (MPa/mm)	-	9.50	-	10.30
System shear stiffness, K_s, (MPa/mm)	1.84	1.81	1.37	1.36
Friction angle, tan $\emptyset$ (°)	35.37	34.99	34.96	34.99

A DEM^{2D} sandstone-concrete joint specimen is presented in Figure 3(a) (grey and yellow balls represent concrete and sandstone materials, respectively; black and red lines represent the network of FJCM and SJCM, respectively). The shear stress (τ) versus shear displacement (δ_s) curves under different normal stress (σ_n) are presented in Figure 3(b). As it can be observed, DEM^{2D} models captured very well the laboratory behaviour.

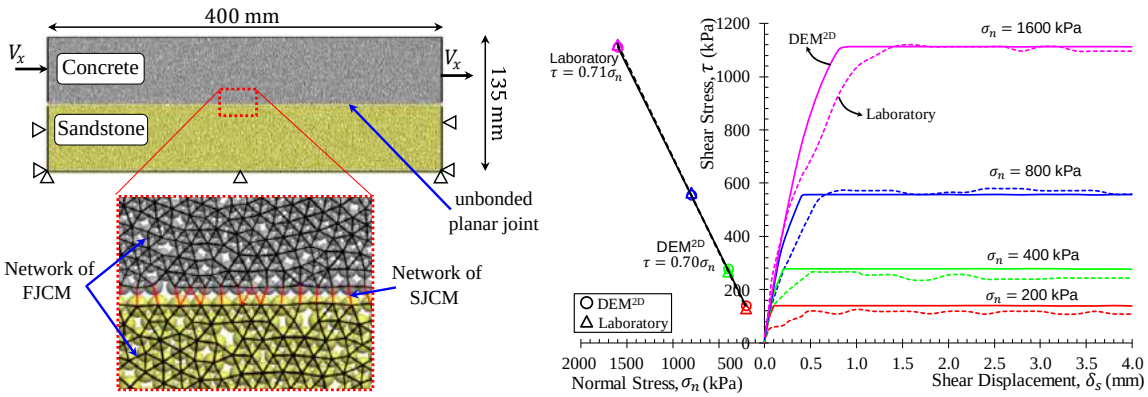

Figure 3. *DEM^{2D} DST sample: (a) sandstone(S2)-concrete unbonded planar joint and details of network of contact (black and red lines represent FCJM and SJCM, respectively), (b) comparison of DEM^{2D} and experimental DSTs with different normal stress (σ_n) (experimental data from [8])*

2.3. Large-Scale Numerical Models

Next, the socket roughness effect on the side shear resistance of rock-socketed piles is examined. To do that, DEM^{3D} numerical models of rock-socketed piles with different degrees of socket roughness are employed (see Figure 4).

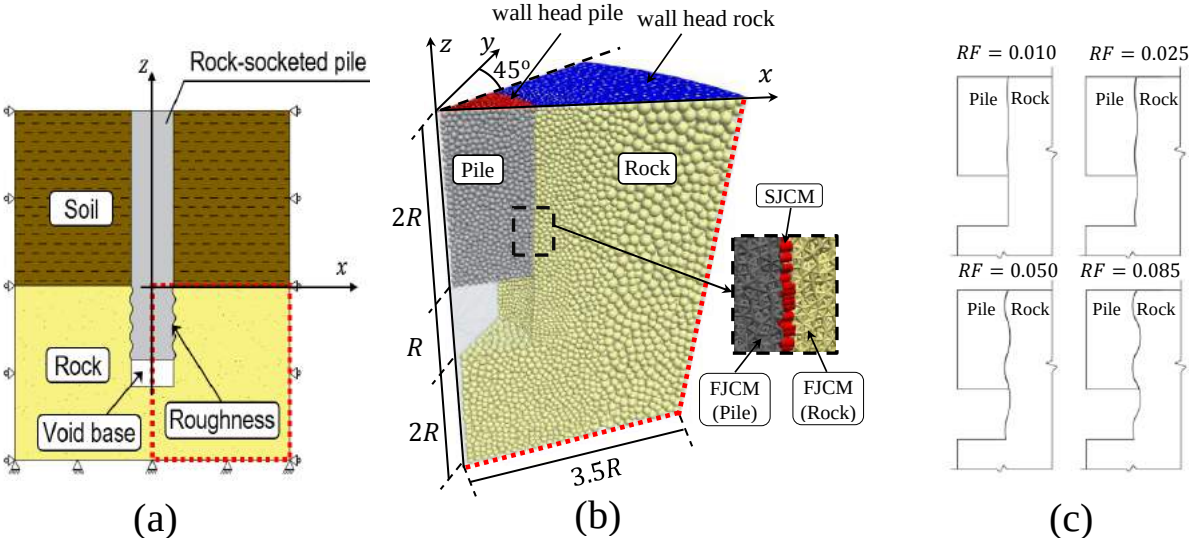

Figure 4. *(a) idealized sub-surface profile (the red dotted line represents the zone modelled), (b) DEM^{3D} rock-socketed pile model, (c) roughness profiles used at the pile-rock interface (RF is the roughness factor define in [14])*

Considering that the computational cost is an important factor of numerical simulations, in particular of DEM models, (i) a section of a pile of 45-degree angle, instead of the whole diameter, is considered, (ii) the rock body was discretized in three zones, increasing the particle size from the pile-rock interface to the boundary wall of model, and (iii) pressure loads to simulate the overlying soil stratum and the corresponding self-weight of the pile embedded in the soil, were applied on the wall head rock and on the wall head pile, respectively (see Figure 4). Thus, the computational time is reduced. The nominal socket radius (R) and the nominal socket length (L) are, 0.4 m and 0.8 m, respectively. The base was made void because only the pile shaft behaviour is analyzed in this work. The rock (S2-sandstone) and the pile (concrete) were simulated using the FJCM, while the SJCM was applied at rock-pile interface. The

micromechanical parameters used in the FJCM and SJCM were those previously calibrated in Section 2.2 (see Table 1 and Table 2). Additional details about the set-up of rock-socketed piles DEM^{3D} models are available in [13].

3. RESULTS

3.1 Small-Scale Numerical Models

The effect of roughness at sandstone-concrete interfaces was investigated through three (3) DEM^{2D} direct shear tests conducted on unbonded symmetric saw-tooth joints (with different base angle, α) under CNL conditions ($\sigma_n = 400$ kPa) with the corresponding micromechanical parameters calibrated in Section 2.1. DEM^{2D} results and the comparison with experimental tests presented in [8] are shown in Figure 5. As it can be noticed, the shear stress increases as the roughness at the sandstone-concrete joint increases. DEM^{2D} results agree well with the laboratory behaviour, in which the peak shear strength and peak shear displacement computed with DEM^{2D} models are very close to those obtained in laboratory summarized in [8]. In addition, Figure 5 shows that a small number of bond breakages –i.e., cracks– take place before reaching the peak shear strength; later, the number of cracks (shear and tensile) increases rapidly, which suggests that there is more degradation of asperities in those models with greater α –i.e., at rougher interfaces–.

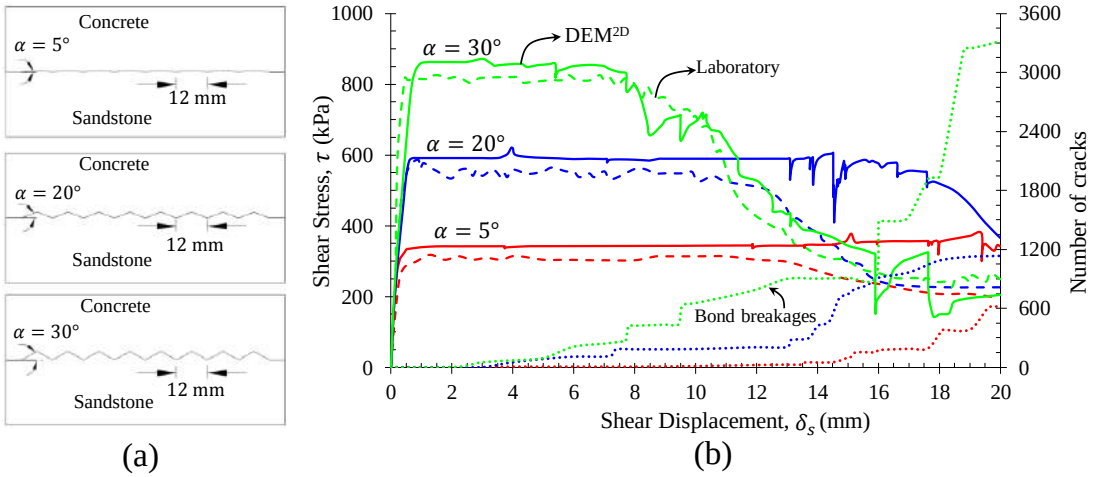

Figure 5. *(a) geometry of the DEM^{2D} DSTs with saw-tooth triangular joints with different base angle: (b) comparison of DEM^{2D} and experimental DSTs conducted on unbonded sandstone(S3)-concrete joints under CNL boundary conditions ($\sigma_n = 400\ kPa$) (experimental data from [8])*

Figure 6(a) compares numerical and experimental results of DSTs conducted on unbonded sandstone(S2,S3)-concrete saw-tooth triangular joints with $\alpha = 20°$ and CNS boundary conditions ($\sigma_n = 400\ kPa$, $K = 800\ kPa/mm$). As it can be observed, DEM^{2D} results agree well with the laboratory behaviour, as well as the CNS boundary conditions increases the shear stress on unbonded roughness joints. Note, that the peak shear stress obtained on sandstone(S3)-concrete unbonded joints with $\alpha = 20°$ under CNS boundary conditions is higher than the peak shear stress obtained on the same sandstone(S3)-concrete specimen under CNL boundary conditions (see Figure 5(b) and Figure 6(a)). In addition, Figure 6(a) presents that the shear stress depends also on the strength of the materials –e.g., the peak shear stress obtained on sandstone(S3)-concrete joint is higher than that computed on sandstone(S2)-concrete–. Finally, the propagations of the number of bond breakages is presented in Figure 6(b); as it can be seen, the number of tension cracks increases faster than shear cracks after the peak shear stress is

reached; later, the number of shear cracks in concrete remains almost constant and the number of shear cracks in S3-sandstone increases slowly compared to the increase of tension cracks of both materials. This results may be due to the concrete is stronger than the S3-sandstone.

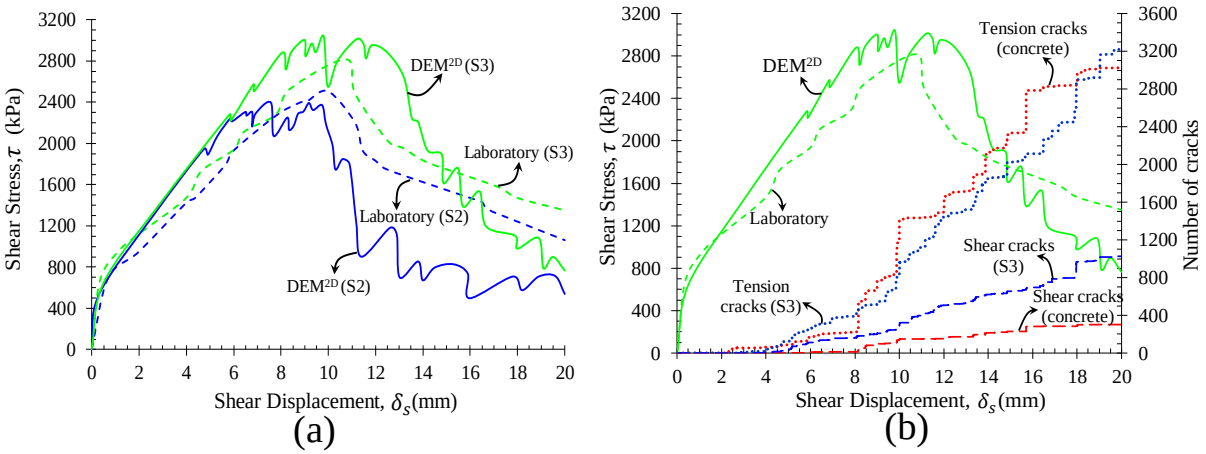

Figure 6. *DSTs conducted on unbonded sandstone(S2,S3)-concrete saw-tooth triangular joints with $\alpha = 20°$ and CNS boundary conditions ($\sigma_n = 400\ kPa$, $K = 800\ kPa/mm$): (a) comparison of DEM^{2D} and experimental results, (b) propagations of bond breakages (experimental data from [8])*

3.2 Large-Scale Numerical Models

Four (4) DEM^{3D} rock-socketed piles testing were conducted to analyze the socket roughness effect on side shear resistance behaviour. All DEM^{3D} models were loading until a limit socket head settlement (δ) of 10% of the socket diameter ($0.1D$) is reached (see Figure 7).

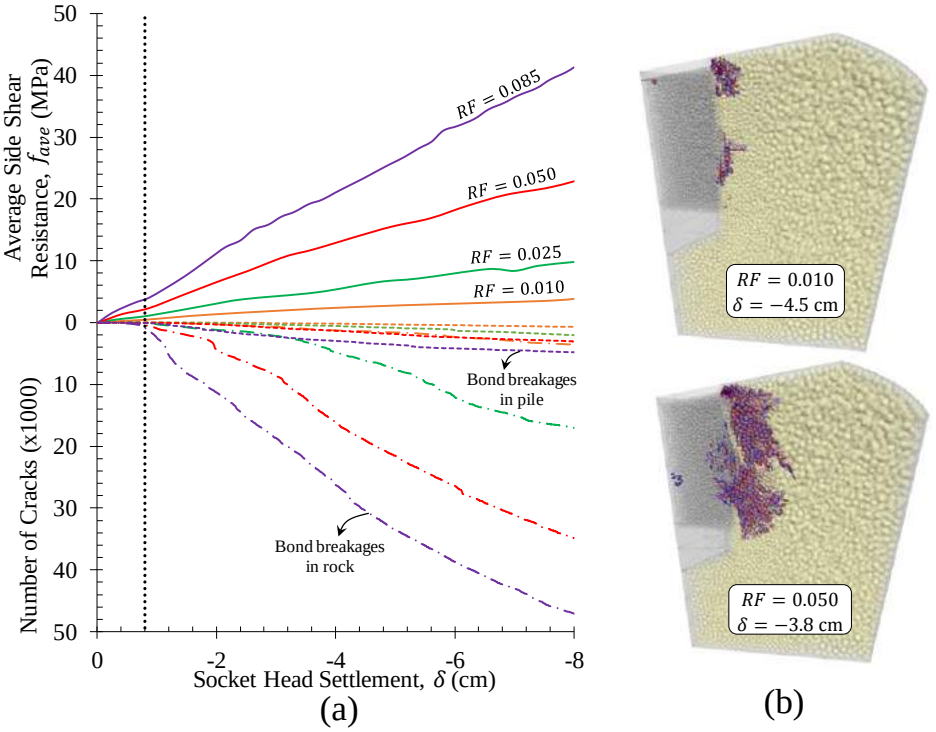

Figure 7. *DEM^{3D} results: (a) average side shear resistance (f_{ave}) and number of cracks versus socket head settlement (δ) for DEM^{3D} simulations of four piles socketed in S2-sandstone (with different roughness profile), (b) cracks propagation for model with $RF = 0.010$ and $RF = 0.050$ (blue and red colors represent bond breakages in shear and in tension, respectively)*

As it can be seen from Figure 7, the average side shear resistance (f_{ave}) increases gradually in the same way that the roughness factor at the rock-pile interface is greater –e.g. f_{ave} of model with $RF = 0.050$ is about 5 times greater than that computed for model with $RF = 0.010$ for a socket head settlement of 0.05*D*, see Figure 7–. This result may be because the rock-pile interface with higher RF is unable to deform sufficiently, thus more dilation and normal stiffness occurs during the loading tests (see Section 3.1). In addition, Figure 7(a)-(b) shows that the number of bond breakages in piles socketed into sandstone-S2 is very small before reaching a socket head settlement of 0.01*D* (i.e., 0.8 cm). After such threshold, the number of cracks (shear and tension) increases, as the socket roughness increases. This behaviour is congrous with that presented in Section 3.1, as well as with previous works by [11,12], suggesting that models with lower socket roughness fail through sliding along the rock-concrete interface, whereas the degradation of asperities and significant bond breakages becomes more relevant at the rock-pile interface with higher RF values. (Note also that the number of bond breakages are greater in S2-sandstone than in pile; this might be as the concrete pile is much stronger than S2-sandstone). According to Figure 7, widely accepted established criterion of the 0.01*D* displacement is an appropriate one in design practices considering that the numerical model presents excessive damage of rock-concrete interface of rock socket piles.

4. CONCLUSIONS

In conclusion, the research findings of this work shows that the degree of roughness is a crucial factor affecting the shear stress behaviour of unbonded rock-concrete interfaces and should be incorporated in current design practice of rock-socketed piles. This paper demonstrates that $DEM^{2D\&3D}$ simulation scheme with their micromechanical parameters calibrated against experimental tests, can adequately simulate the shear behaviour of unbonded rock-concrete interfaces, in particular, (i) the shear stress behaviour of direct shear tests conducted on unbonded planar and saw-tooth triangular joints under CNL and CNS conditions, and (ii) the shear stress resistance of rock-socketed pile testing. Finally, the major advantage of DEM models conducted herein is that employing just a few UCSs and DSTs to calibrate the micromechanical parameters of DEM models there is reduction of costs and time associated to traditional field and laboratory tests to analyze the shear stress behaviour at rock-concrete interfaces.

ACKNOWLEDGEMENT

The first author has received since 2018 the scholarship for PhD research provided by the José Entrecanales Ibarra Foundation and a scholarship to attend to this conference by the Spanish Society for Soil Mechanics and Geotechnical Engineering. The support of both institutions is gratefully acknowledged.

REFERENCES

[1] Seidel, J.P., Collingwood, B., 2001. "*A New Socket Roughness Factor for Prediction of Rock Socket Shaft Resistance*", Canadian Geotechnical Journal, 38(1): 138–153, https://doi.org/10.1139/t00-083.

[2] Zhang, L., 2004. "*Drilled Shafts in Rock: Analysis and Design: Analysis and Design*", CRC Press/Balkema, Netherlands, 396 pages.

[3] Horvath, R.G., Kenney, T.C., 1979. "*Shaft Resistance of Rock-Socketed Drilled Piers*", Symposium on Deep Foundations, ASCE, pp. 182–214, 25 October 1979, Atlanta, USA.

[4] Whitaker, T., Cooke, R.W., 1966. "*An Investigation of the Shaft and Base Resistances of Large Bored Piles in London Clay*", Symposium of Large Bored Piles, pp. 7–49, February 1966, Institution of Civil Engineers and Reinforced Concrete Association, London.

[5] Rezazadeh, S., Eslami, A., 2017. "*Empirical Methods for Determining Shaft Bearing Capacity of Semi-Deep Foundations Socketed in Rocks*" International Journal of Rock Mechanics and Geotechnical Engineering, 9(6): 1140–1151, https://doi.org/10.1016/j.jrmge.2017.06.003.

[6] Pells, P.J.N., Mostyn, G., Walker, B.F., 1998. "*Foundations on Sandstone and Shale in the Sydney Region*", Australian Geomechanics, 33(3): 17–29.

[7] Itasca Consulting Group Inc., 2014. "*PFC Manual, Version 5.0"*, Minneapolis, Minnesota.

[8] Gu, X.F., Seidel, J.P., Haberfield, C.M., 2003. "*Direct Shear Test of Sandstone-Concrete Joints*", International Journal of Geomechanics, 3(1): 21–33, https://doi.org/10.1061/(ASCE)1532-3641(2003)3:1(21).

[9] Potyondy, D.O., 2012. "*A Flat-Jointed Bonded-Particle Material for Hard Rock*", 46th US Rock Mechanics/Geomechanics Symposium, 24-27 June 2012, Chicago, Illinois, USA.

[10] Ivars, D.M., Potyondy, D.O., Pierce, M., Cundall, P.A., 2008. "*The Smooth-Joint Contact Model*" 8th World Congress on Computational Mechanics–5th. European Congress on Computational Methods in Applied Sciences and Engineering, June 30–July 5, 2008, Venice, Italy.

[11] Gutiérrez-Ch, J.G., Senent, S., Melentijevic, S., Jimenez, R., 2018. "*Distinct Element Method Simulations of Rock-Concrete Interfaces Under Different Boundary Conditions*", Engineering Geology, 240: 123–139. https://doi.org/10.1016/j.enggeo.2018.04.017.

[12] Bahaaddini, M., Sharrock, G., Hebblewhite, B.K., 2013. "*Numerical Direct Shear Tests to Model the Shear Behaviour of Rock Joints*" Computers and Geotechnics, 51: 101–115. https://doi.org/10.1016/j.compgeo.2013.02.003.

[13] Gutiérrez-Ch, J.G., Senent, S., Melentijevic, S., Jimenez, R., 2019. "*DEM models to predict side shear resistance of rock-socketed piles considering socket roughness*", 56th US Rock Mechanics/Geomechanics Symposium, 23-26 June 2019, New York, New York, USA.

[14] Horvath, R.G., Kenney, T.C., Kozicki, P.,1983. "*Methods for Improving the Performance of Drilled Piers in Weak Rock*" Canadian Geotechnical Journal, 20(4): 758–772. https://doi.org/10.1139/t83-081.

A METHOD TO DERIVE THE SOIL-NAIL INTERFACE STIFFNESS FROM PULL-OUT TESTS

Jean de Sauvage*, *French Institute Of Science And Technology For Transport, Development And Networks, Marne-la-Vallée, France, jean.de-sauvage@ifsttar.fr*

Frederico Lara Diniz Oliveira, *Ecole Nationale des Ponts et Chaussées, Marne-la-Vallée, France, fred.lara.d@gmail.com*

ABSTRACT

Soil nailing is a technique developed in France during the 70s for the retaining of excavations. The stability of such structures is due to the friction through soil and nails. This friction is often described by a relation between the lateral shear stress and the axial relative displacement. This relation can be complex, but is generally characterized by a slope (k) and a maximal unit skin friction (q_s). Usually, q_s is determined through pull-out tests and k is estimated through correlations with the soil characteristics. However, the behaviour of a soil-nailed wall appears to be strongly dependent on the slope k. Therefore, a method needed to be found to estimate the stiffness of the soil-nail interface through pull-out tests. To achieve this, a numerical study was carried out. A simple one-dimensional model was carried out simulating the influence of a non-uniform grouting section. It was then compared to a finite element model. The numerical results where eventually confronted to experiments. A testing nail was equipped with optic fiber in order to determine the distribution of stresses along its length during a pull-out test. The pull-out test was carried out according to the French standards. The comparison of experimental and numerical results allowed to highlight the role of the slope k. In order to simplify its determination, a method is proposed to derive this value from the tension and the displacement measured at the nail head during a pull-out test.

Keywords: Soil-Nailing, Nail Mobilization, Pull-Out Tests, Interface Stiffness.

1. INTRODUCTION

Soil nailing is a technique developed in France during the 70s for the retaining of excavations. The stability of the retaining wall is ensured through the friction along the nails. When a displacement tends to unsettle the wall, a relative displacement appears between the nail and the soil. This relative displacement generates stresses who tend to retain the soil.

The nails are both submitted to a lateral load and to an axial one. Generally, the axial contribution is the bigger one. Therefore the knowledge of the friction law between nail and soil is crucial in the design of soil-nailed walls. Pull-out tests are the favorite way to determine it [1][2]. Common tests only allow to determine the maximal unit skin friction and give only information on the average behaviour of the interface.

However, the total understanding of the friction law also requires the knowledge of the interface stiffness *k*. As mentioned in [3], the finite element modelling of a soil-nailed wall strongly depends on *k*. The monitoring of pull-out tests using optic fibers along the nail as well as the development of a one-dimensional numerical model allowed us to develop a method to derive the soil-nail interface stiffness.

2. FRICTION ALONG THE NAIL

The whole friction law depends on the way the nail is installed and on the shape of the inclusion since these parameters both influence the grains rearrangements. Therefore, it has to be determined through pull-out tests.

In most of the cases, nails are loaded by the deconfinement of lateral earth pressure during the following excavation. As the nails are subhorizontal, the resulting load is axial. Along the soil-nail interface, a shear stress appears and grows with the relative displacement between the nail and the granular skeleton.

When the stress reaches the maximal unit skin friction q_s, the interface fails and if $q_s$is reached all along the nail, it is pulled out [4]. The determination of q_s through pull-out tests is straight forward. If r is the radius of the nail, L its length and Q the failure load, we have.

When the shear stress is smaller than q_s, a simple assumption considers an elastic behaviour. The shear stress is proportionnal to the relative displacement. Let's say $\tau = ky$. Using experimental observations, Frank and Zhao [5] proposed a bilinear law which is represented on figure 1a.

The coefficient k_β is correlated to the pressuremeter parameters. Most recently, Abchir [6] developed a friction law using an analytical method and assuming that the increase of friction is proportional to the difference between$\tau$and $q_s = \tau_{max}$. It is represented on the figure 1b.

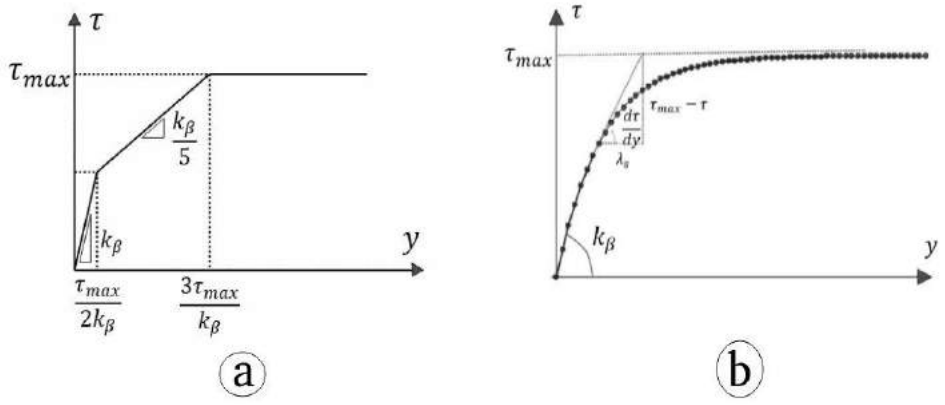

***Figure 1**. Friction laws developed by Frank and Zhao (a) and Abchir (b)*

3. PULL-OUT TEST

Since the friction law depends on the way the nail is installed and on the shape of the inclusion, it has to be determined through pull-out tests.

The common technique is imposing an axial load on the nail head with a hydraulic actuator and monitoring the head displacement.

In order to reduce the flexion effects, the load has to be well aligned with the axis of the nail and in order to minimize the edge effects, the first meter near the facing is not grouted.

The classical monitoring allows to plot the relationship between nail head load and nail head displacement.

Theoretically, the stiffness of the soil-nail interface can be derived from the initial slope of this graph.

However, the set-up conditions of the pull-out test can induce significant errors. In order to increase the precision, the monitoring has to be distributed along the nail.

Such experiments have been carried out using strain gages. Alimi [7] and França [8] did it on reduced scale models and highlighted the influence of soil density on the friction law.

Today a new measurement method allows a cheaper and more integral monitoring of developed shear stresses: the optic fibers [9].

These fibers can be equipped with punctual sensors (Bragg networks) or they can be used as a distributed sensor (Brillouin or Raman diffusion) [10]. The biggest limitation is their huge sensitivity to temperature.

4. NUMERICAL MODELLING

One-dimensional numerical simulations have been carried out to compare to the experimental results of the pull-out tests.

It is based on an analytical formulation but iterations of a numerical program are needed to take into account the non-linearities of the friction laws presented above.

The figure 2 presents the parameters used in this numerical model. Considering an elastic behaviour of the nail, the rate of relative displacement induced by the variation of tension is then given by:

$$\frac{dy}{dx} = \frac{T(x)}{E(x)S(x)} \quad (1)$$

And the static equilibrium of a small part of the nail gives:

$$\frac{dT}{dx} = \tau(y)P(x) \quad (2)$$

Where $S = \pi R^2$ and $P = 2\pi R$.

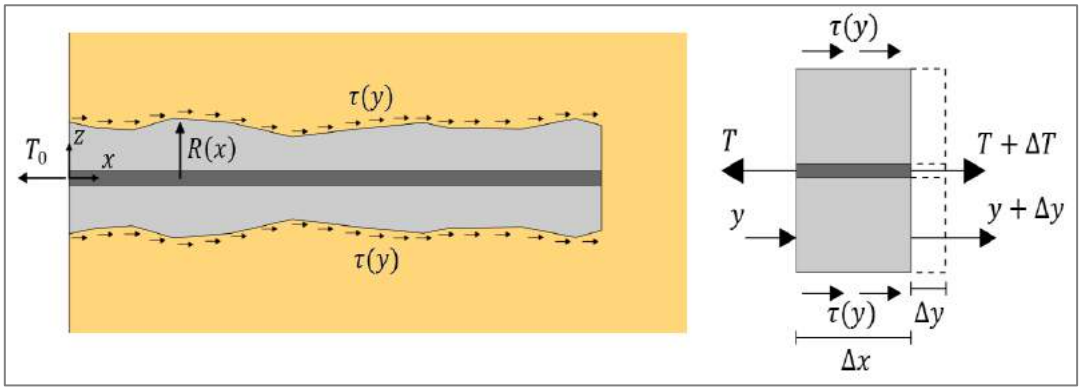

***Figure 2**. Parameters of the one-dimensional model*

The numerical solution of this problem has been computed using Python and a Runge-Kutta algorithm.

In this case, the boundary conditions were the nail head load and the nail tail displacement (equal to zero).

Therefore, a shooting method was used. The figure 3 presents the results obtained for a simple elasto-plastic law.

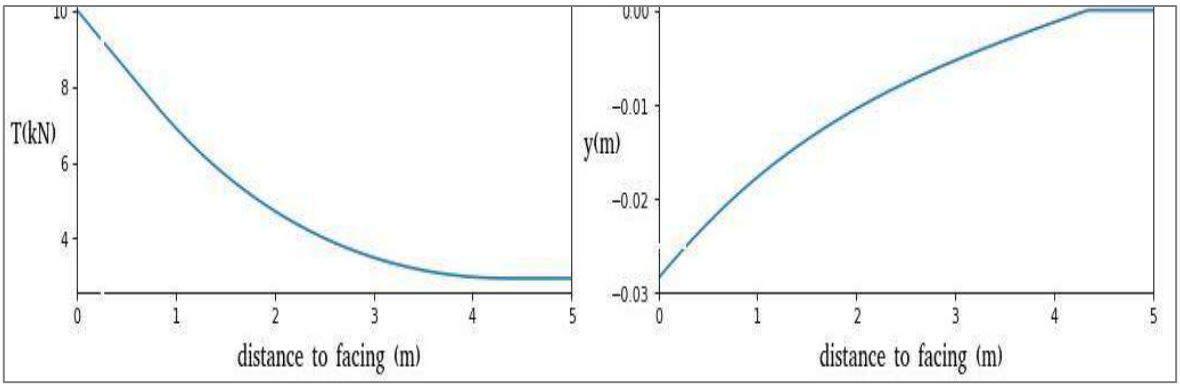

***Figure 3**. Nail head load and displacement obtained with the numerical model for an elasto-plastic law.*

The 1D simulations were then compared to finite element modelling results. The model is 2D and axisymmetric.

It was realized on Plaxis and an example of results can be found on the Figure 4.

Unfortunately, the results strongly depend on the boundary conditions and the confining stress.

Given the uncertainties on the confining stress in a pull-out test, it was decided to use mainly the 1D numerical simulations later on.

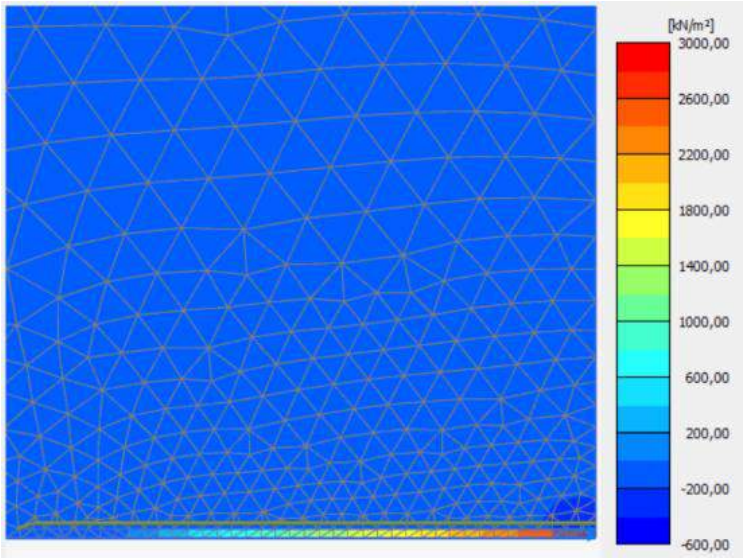

***Figure 4**. Stresses along the axis of the bar computed with the Finite Element Model.*

5. EXPERIMENTAL TEST AND CONCLUSIONS

A pull-out test has been carried out with a 24 mm diameter bar cemented in a 114 mm diameter borehole. The bar was equipped with optic fiber. This allowed to measure the strains along the nail and, therefore, to compute the tension along the nail.

This graph (figure 4) was compared with elasto-plastic numerical 1D simulations obtained for different values of k. The one which fitted at best indicated a value of 5.3 MPa/m, near the one estimated through pressuremeter tests (8 MPa/m).

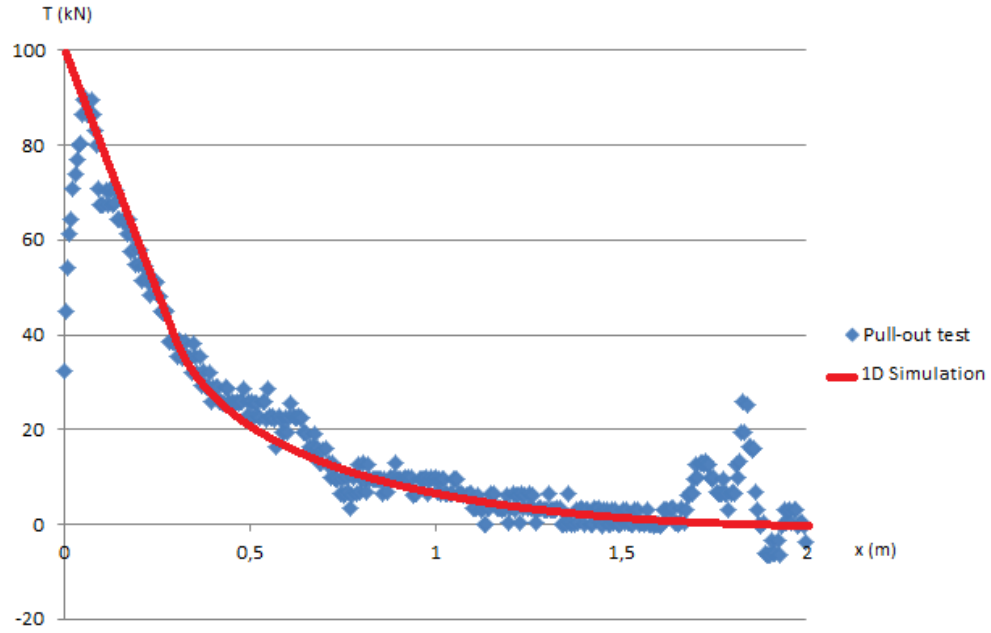

***Figure 5**. Tension along the nail in a pull-out test and comparison with an elasto-plastic 1D simulation for k = 5.3 MPa/m*

A method has been developed and tested to derive the stiffness of the soil-nail interface through a pull-out test. This method involves a distributed measurement of strains along the nail (such as optic fibers) and the comparison with a numerical simulation. It now needs to be validated with more case studies.

Furthermore, the distributed measurement of strains along the nail is quite an expensive monitoring and is not available on all construction sites. Therefore, this method needs to be improved to be applied to classical pull-out tests where only nail head data are available.

ACKNOWLEDGEMENTS

The authors would like to express their gratitude toward NGE Foundation and the French Ministry for Ecologic and Cohesive Transition who allowed this work to be achieved.

REFERENCES

[1] Zhu, H.H., Yin J.H., Yeung A.T., Jin W., 2010. "*Field Pullout Testing and Performance Evaluation of GFRP Soil Nails*", Journal of Geotechnical and Geoenvironmental Engineering. 137(7):633-42.

[2] Zhou, W.H., Yin, J.H., Hong, C.Y., 2011. "*Finite Element Modelling of Pullout Testing on A Soil Nail in A Pullout Box Under Different Overburden and Grouting Pressures*", Canadian Geotechnical Journal, 48(4):557-67.

[3] de Sauvage, J., 2018. "*Etude du comportement des murs de soutènement par clouage des sols en place : Application au dimensionnement du parement*", PhD Thesis, ENTPE, France.

[4] Schlosser, F., Guilloux, A., 1981. "*Le frottement dans le renforcement des sols*", Revue française de Géotechnique, 16:165-77.

[5] Frank, R., Zhao, S.R., 1982. "*Estimation par les paramètres pressiomètriques de l'enfoncement sous charge axiale de pieux forés dans des sols fins*", Bulletin de liaison des Laboratoires des Ponts et Chaussées, 119.

[6] Abchir, Z., Burlon, S., Frank, R., Habert, J., "*T-Z Curves for Piles from Pressuremeter Test Results*", Géotechnique, 66(2), 137-148.

[7] Alimi, I., 1977. "*Etude de l'adhérence sol-armature en place et en laboratoire*", Bulletin de liaison des Laboratoires des Ponts et Chaussées, SPEC VI-F, 40-43.

[8] França, F.A.N., 2007. "*Pullout Tests in Soil Nailed Wall Built in Laboratory*", M.Sc Thesis, Escola de Engenharia de São Paulo, Brazil, 125 pages.

[9] Ferdinand, P., 2018. "*Capteurs à fibres optiques à réseaux de Bragg – Analyse, multiplexage et applications",* Techniques de l'Ingénieur, R6736.

[10] Lanticq, V., 2009. *"Mesure répartie de température et de déformations par diffusion Brillouin : de la fibre optique au capteur pour le génie civil",* PhD Thesis, Telecom ParisTech, France, 169 pages.

AN IMPROVED DESIGN FOR SOIL-NAILED WALLS USING LIMIT EQUILIBRIUM ANALYSIS

Jean de Sauvage*, *French Institute Of Science And Technology For Transport, Development And Networks, Marne-la-Vallée, France, jean.de-sauvage@ifsttar.fr*

ABSTRACT

Soil nailing is a technique developed in France during the 70s for the retaining of excavations. Today, such structures are often designed through Limit Equilibrium based software and their facing is designed to support the maximal tensions admissible in the reinforcements. The professionals generally admit that the service loads in the reinforcements are smaller than the calculated ones, especially at the facing foot because of the construction phasing, from top to bottom. In order to know precisely the facing loads, engineers can use Finite Element Method (FEM) but the results are strongly dependent on the stiffness of soil and of the interface between soil and nail. What is more, the FEM is time consuming. Therefore, Limit Equilibrium based software need to be adapted to take into account the construction phasing to modulate the mobilization of reinforcements. To achieve this, soil nailed walls have been studied through real-scale experiments, centrifuge and numerical modelling. The comparison of this results allowed to propose an improvement of the soil-nailing design using the PROSPER software, developed by IFSTTAR. The PROSPER software choses a failure surface along which the displacement of soil mobilizes the reaction of the nails. This displacement is generally considered as homogenous along the surface but the results of the present work allow the proposition of a better allure. Abacuses have been proposed for the distribution of this displacement and this design approach has been tested on an experimental wall. It provides an efficient and time-saving design of soil-nailed walls.

Keywords: Soil-Nailing, Limit Equilibrium, Nail Mobilization, Design.

1. INTRODUCTION

The technique of soil nailing has been developed in France in the 70's and is widely used to stabilize natural slopes or to create steep excavations. However, its design still raises questions concerning the distribution of loads along the facing. These questions are hidden in the usual design methods based on slope stability analysis and where the inclusions loads are then derived from a multicriteria analysis [1] of nails failure, considering or not the displacements along the potential failure surface.

One problem raised by these methods is that the biggest loads are often found in bottom nail whereas this nail is known to be less loaded. Considering these limitations, the French Organization for Standardization has initiated in 2014 a workgroup dedicated to facing loads in reinforced soil.

The first monitored soil nailed wall was realized in the German National Project called Bodenvernagelung [2] and became a benchmark for the subsequent studies, including the walls built within the French National Project CLOUTERRE. From all these experiments a typical pattern for facing loads has emerged. It induces a resulting force significantly inferior to the active earth pressure. Recent experiments [3] [4] have been led. However, due to their

particular geotechnical contexts (presence of glacial till, rock anchoring), their results cannot be generalized.

2. AN EXAMPLE: THE BÉVENAIS WALL

2.1. Presentation of the Wall

In order to improve the comprehension of these structures, INSA Lyon, the French innovative company GTS and IFSTTAR then set up a collaborative project to monitor an experimental soil nail wall, 7.5m high and 30m long, in a pit located in Bévenais (France). The experimental wall has been divided in half, on one half a facing developed by GTS, on the other half, a usual shotcrete facing, for the purpose of a comparison of their performances.

GTS designed a cost-saving, ergonomic and draining facing for soil nail walls based on precast concrete flakes instead of the usual shotcrete. This process called AD/OC facing does not change the excavation phasing [5].

The structure has been designed using the multicriteria method [1] and the nail lengths were then increased (the final safety factor was 1.68). The total depth of the excavation was reached with five 1.5 m lifts and the horizontal spacing between nails was 2 m. The top nails (level 1 and 2) were 7 m long. The nails 3 and 4 were 6 m long and the last one was 5 m long. Each of them made a 10° angle with the horizon. The wall has been built, then loaded by a 3 m deep trench at the bottom and eventually by a backfill at the top. The water table, located 30 m under the natural ground does not impact the study. The soil is homogenous and constituted of a well graded, unsaturated, clean gravel. The friction angle was 41°.

2.2. Monitoring

The nail loads were monitored using strain gages, but the acquisition was partly defective and therefore poorly harnessed until now. The gages were symmetrically glued on the nails in order to distinguish traction and flexion components. 26 nails have been equipped by a single gage placed at a distance of 20 cm from the facing. 4 nails (located on the levels n° 2 and 4) were equipped by several gages on their whole length. Unfortunately, as only part of these measurements could be harnessed, they eventually did not allow any comparison between the two technologies. The data here presented come indifferently from AD/OC facing and shotcrete.The figure 1 presents the distribution of facing loads and its evolution through time. The loads measured at the end of the construction are very small compared to the 80 kN in the fourth nail announced by the multicriteria method. However, they later increase significantly, yet without reaching the predicted values.

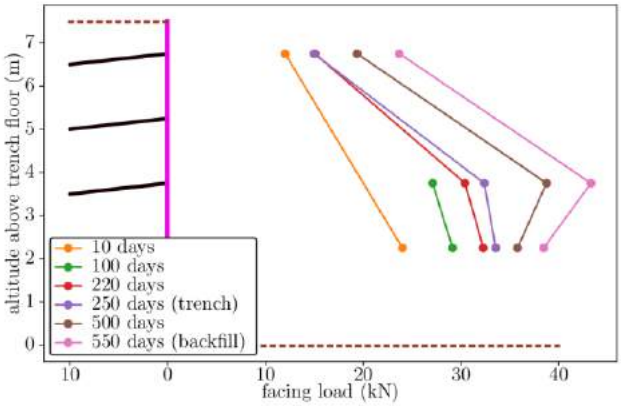

***Figure 1**. Facing loads of the Bevenais wall at different dates*

3. DESIGN USING PROSPER

3.1. The PROSPER Software

The traditional design tools for soil nailed walls are based on the classical slope stability analysis methods: a failure surface has to be chosen and the factor of safety is obtained comparing disturbing forces with resisting ones. The latter are increased by the stabilizing efforts due to the nails. These stabilizing efforts are commonly worked out through multicriteria analysis or through the so-called displacement method which considers the same type of nail failure.

This last approach is the one used in the PROSPER software, developed by LCPC (Laboratoire Central des Ponts et Chaussées) [6]. A displacement of the sliding mass is supposed and the loads induced in the nails are then calculated by integrating the beam equation. This displacement is iteratively increased until the desired factor of safety is reached. The integration of beam equation also gives access to the facing loads.

This method assumes a movement along the failure surface which is, by default, taken homogeneous and therefore neglects the soil's deformability. Moreover, the construction phasing is not taken into account even though it has consequences on the relative mobilization of each inclusion. Notably, the loads developed in the bottom nail are generally highly overestimated because this nail is mobilized by no further excavation.

3.2. Introduction of Relative Displacements

In order to improve the analysis, the PROSPER software allows the introduction of displacement varying between the top and bottom of the failure surface. For each nail, it is possible to define a ratio between the displacements along the failure surface and the maximal displacement at the wall top.

The distribution of this ratio can be estimated using the results presented in [7]. In this case the ratios imposed into PROSPER are the following : 100% for the top nail, 54% for the second, 44% for the third, 29% for the fourth and 1% for the bottom one. The figure 2 presents the facing loads obtained for a homogeneous displacement of the sliding mass and the ones obtained considering a variation of this displacement. In both cases, the computation was made with and without cohesion. The pattern of facing loads obtained using these corrected displacements is more conform to experimental observations.

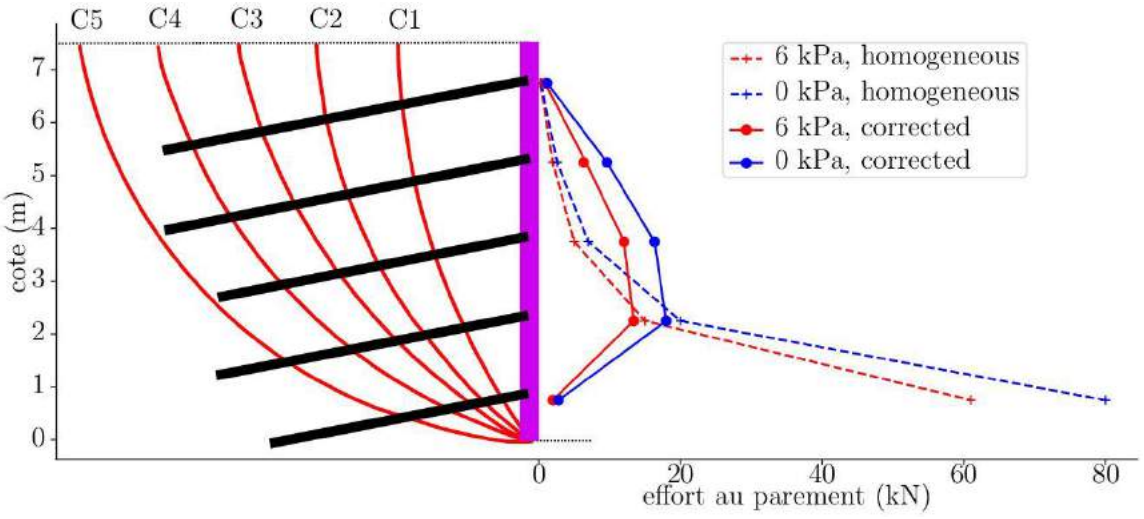

***Figure 2**. Facing loads of the Bévenais wall obtained with Prosper*

4. CONCLUSION

It has been showed that the introduction of a non-homogeneous relative displacement along the failure surface leads to a distribution of facing loads more conform to the observations. It is then crucial to develop abacus for relative displacement in order to significantly improve the design of soil nailed walls and their facing.

ACKNOWLEDGEMENT

The authors want to thank the company GTS and its research manager Philippe Robit as well as INSA Lyon and Ali Limam for the provision of their experimental data. Eventually, we want to thank the french ministry for Ecologic and Cohesive Transition for the funding of the PhD in which this work has been made possible.

REFERENCES

[1] Schlosser, F., Guilloux, A., 1981. "*Le frottement dans le renforcement des sols*", Revue française de Géotechnique, 16:165-77.

[2] Gassler, G., 1987. "*Vernagelte Gelandesprunge – Tragverhalten und Standsicherheit*", PhD Thesis, University of Karlsruhe, Germany.

[3] Menkiti, C.O., Long, M., 2008. "*Performance of soil nails in Dublin glacial till*", Canadian Geotechnical Journal, 45(12):1685-1698

[4] Jacobsz, S.W., Phalanndwa, T.S., 2011. "*Observed axial loads in soil nails*", African Regional Conference on Soil Mechanics and Geotechnical Engineering, 18-21 July 2011, Maputo.

[5] Robit, P., Rajot, J.P., Limam, A., 2014, "*Paroi clouée AD/OC – une alternative au béton projeté qui renforce le drainage et limite les émissions de CO2*", Journées Nationales de Géotechnique et de Géologie de l'Ingénieur, 13-15 July 2014, Beauvais.

[6] Delmas, P., Cartier, G., Abdelhedi, A., 1986. "*Une nouvelle méthode de dimensionnement du clouage des pentes : programme Prosper*", Bulletin de liaison des Laboratoires des Ponts et Chaussées, 141.

[7] Sauvage (de), J., 2018. "*Etude du comportement des murs de soutènement par clouage des sols en place. Application au dimensionnement du parement*", PhD Thesis, ENTPE, France.

TREATMENT OF STRUCTURAL DAMAGES OF AN INDIVIDUAL HOUSE BY HUMIDIFYING ITS CLAYEY FOUNDATION SOIL – THE MACH PROJECT

Lamine Ighil Ameur*, *Cerema Blois - Direction Territoriale Normandie-Centre, Blois – France, lamine.ighil-ameur@cerema.fr*

Lucile Saussaye, *Cerema Blois - Direction Territoriale Normandie-Centre, Blois – France*

David Mathon, *Direction Départementale des Territoires du Loir-et-Cher, Blois – France*

ABSTRACT

Damages induced by shrinkage-swelling phenomenon of clayey soils are well known as major natural disaster in France and more generally in the world. Thus, the volumetric change of soils below existing buildings (such us: houses, road infrastructures …) that happens with water content variations and provokes a significant foundation settlement. Therefore, Cerema Blois has decided to be part of important projects in order to develop innovative technical solutions to overcome this current environmental issue. Affecting an individual house, soil shrinkage-swelling causes important and expensive structural damages. For this case, Cerema Blois has tested an innovative and environmental solution on one damaged-house localized at center region in France. It is based on stocking rainwater into two tanks of 800 liters volume capacity of each one and the principle is to humidify the foundation soil during high drying period. Now, this solution highlights satisfying results in terms of closing cracks. The supervision of this experience started in 2017 and has a duration of four years.

Keywords: Clay, Shrinkage, Swelling, Rainwater, Damages, Suction, Desiccation Cracking.

1. INTRODUCTION

The shrinkage-swelling of clays (SSC) phenomenon, also known as a geotechnical drought, causes important movements of soils affecting the foundations of structures on the surface. Indeed, the volume of these clayey soils varies according to their water content; this leads to differential settlement phenomena that are particularly harmful for buildings (individual houses, buildings and road infrastructures) [1], [2].

In France, the SSC hazard is ranking second as the natural risk in terms of financial impact and disorders, with an average of 20,000 individual houses affected per year [3]. The impulse of climate change will not stop growing the SSC phenomenon and will bring the cost of average annual losses generated up to +23% by 2050 [4].

In this context, the Cerema[1] has invested heavily in the search for innovative techniques through national and international projects to overcome this major problem. To this end, the Cerema has conducted since 2016 an experiment that consists in instrumenting a house degraded by geotechnical drought under the MACH project. The objective is to control the SSC phenomenon by injecting the rainwater, recovered and stored, directly in the ground of foundation.

[1] Centre d'études et d'expertise sur les risques, l'environnement, la mobilité et l'aménagement

The MACH project has a supervision duration of four years. Full project description and experimental results of 2017 have been published in [5] and [6] conferences. In this study, the continued follow-up operations and its results during 2018 are presented and compared with those of 2017.

2. THE MACH ECOLOGICAL PROCESS

2.1. Rainwater Storage and Injection System

The rainwater storage and injection device are shown in Figure 1. First, rainwater is collected and stored into two tanks of total volume of 1,600 liters. Then, the injection action needs a preparation of a fixed volume of 300 liters by opening the filling valve by the house owner. The humidification of the foundation soil is performed when the injection valve is opened and the water is gravity flowed through the injection system.

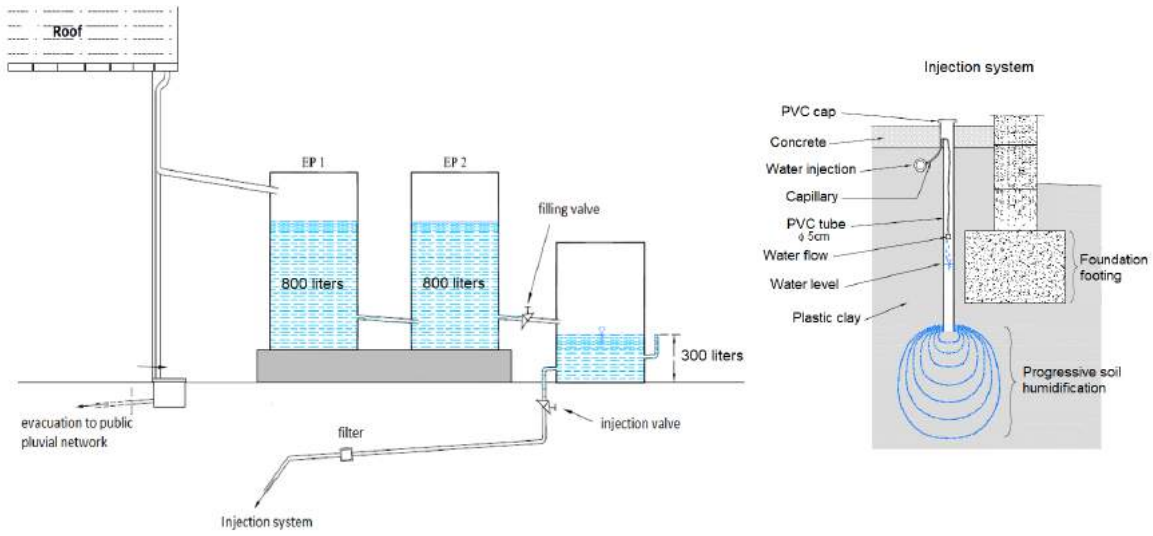

***Figure 1**. Rainwater storage and injection device*

2.2. MACH Follow-Up Operations

There is three principal operations to follow-up during the MACH process summary illustrated in Figure 2:

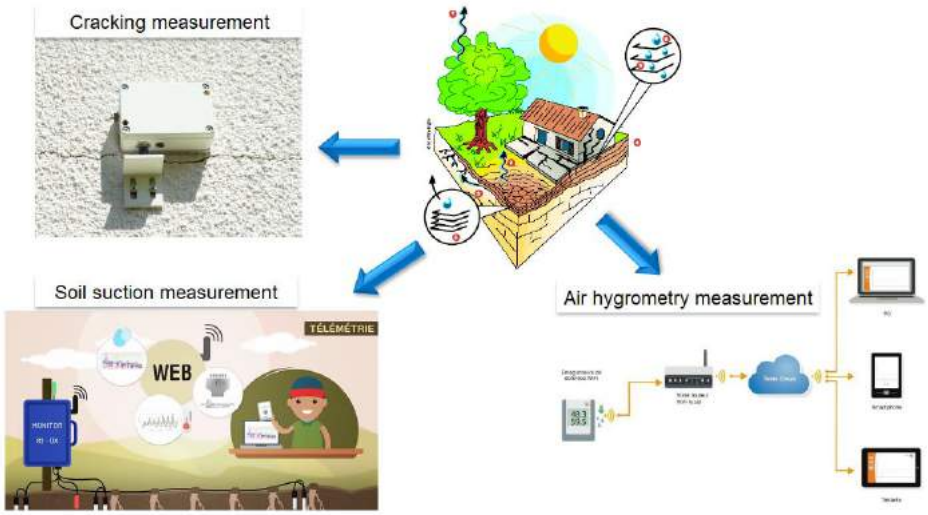

***Figure 2**. The MACH follow-up operations*

(1) The soil suction monitoring available online, which is essential to the injection process by giving the injection instructions to the house owner. This operation allows recording the soil suctions related to water content conditions, and can reach a maximum suction of 239 kPa which represents the limit of measuring sensors.
(2) The monitoring of the cracking consists of measuring the opening or the closing of the cracks appeared in the house by the disorders observed during summer 2015.
(3) Since the end of 2018, a connected device has been installed in the house to measure in real time and continuously the hygrometry (relative humidity and temperature) of the outside atmosphere. This data is automatically saved on a cloud reachable at any time and from anywhere.

The results of all these operations allow writing an annual report each year along the duration of the MACH project.

3. MACH EXPERIMENTAL RESULTS: 2017 vs 2018

Figure 3 shows the soil suction results of the years 2017 and 2018 as well as the evolution of crack 1 (street side facade). The annual report of rainwater injections is also reported.

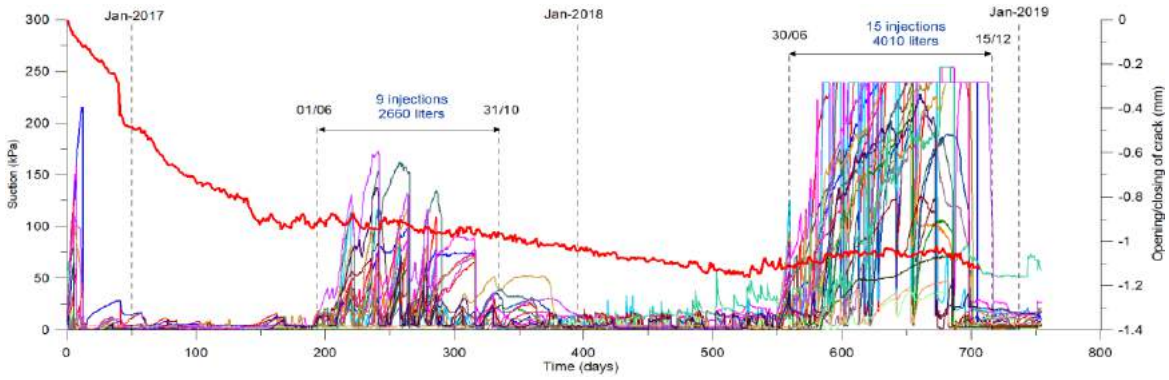

***Figure 3**. Comparison of MACH experimental results during 2017 and 2018*

In terms of suction, the results show very high values recorded from June 30 to December 15, 2018 and having reached the limit of Watermark® probes (239 kPa) for several weeks. These values are significantly higher than those known in 2017 with peaks below the limit of probes and shorter durations.

In terms of rainwater injections, this is consistent with the soil suction with more than 15 injections (4010 liters) applied in 2018 against 9 injections (2660 liters) in 2017.

In terms of cracking (red curve), the results highlight a positive effect of control following the application of rainwater injections. Indeed, the opening crack 1 has stabilized during critical periods of high suction values thanks to water injections.

4. CONCLUSION

This study summarizes the monitoring operations during 2018 through the installation of new equipment and performing the follow-up operations. The summer of 2018 was considered like one of the hottest and comparable to that of 2003, resulting in a particularly severe drought. This made it possible to test the MACH process under extreme demands of rainwater and strong suctions in the soil. The results obtained confirm the effectiveness of the MACH process for the stabilization of cracks during the period of high temperatures and very low rainfall.

ACKNOWLEDGEMENT

This work is funded by la Direction Générale de la Prévention des Risques of Ministère de la Transition Écologique et Solidaire. The authors would like to thank the MACH house owner, Mr. Noblecourt, for his availability to do the rainwater injections. Then, additional thanks to the industrial partners for their contribution to the instrumentation of the house and to take part to the follow-up phase: Agence Qualité Construction (AQC); ELEX expert society and Challenge Agriculture society.

REFERENCES

[1] ARGIC, 2009. "*Analyse du Retrait-Gonflement et de ses Incidences sur les Constructions*", Final report: BRGM/RP-57011-FR, p 92.

[2] ARGIC 2, 2015. "*Analyse du Retrait-Gonflement et de ses Incidences sur les Constructions 2*", Final report, IFSTTAR, p 29.

[3] BRGM, 2019. "*Géosciences et risques naturels*", the BRGM review for sustainable land No: 23, pp50-57.

[4] CCR, 2018 "*Impact du changement climatique sur les dommages assures*", Scenario RPC 8.5, Report of a study available online: www.catastrophes-naturelles.ccr.fr.

[5] Mathon D., Dore L., Ighil Ameur L., 2018. *"Réparer une maison en arrosant ses fondations – Le projet MACH"*, JNGG, 13-15 June 2018, Champs-sur-Marne, France.

[6] Mathon D., Ighil Ameur L., Dore L., Saussaye L., 2018. *"Réparer une maison en arrosant ses fondations – Projet MACH"*, Fourth International Conference UNSAT, 29-31 October 2018, Oran, Algeria.

INFLUENCE OF BASE GROUTING ON LOAD DISTRIBUTION IN A BORED PILE

Adam Krasiński, *Faculty of Civil and Environmental Engineering, Gdansk University of Technology, Poland, adam.krasinski@pg.edu.pl*

Mateusz Wiszniewski*, *Faculty of Civil and Environmental Engineering, Gdansk University of Technology, Poland, mateusz.wiszniewski@pg.edu.pl*

ABSTRACT

Pile base grouting is generally carried out to reduce pile settlement and improve its bearing capacity. Example of two static load tests on instrumented bored piles installed with and without grouting is presented. The interpretation and comparative analysis of both piles showed that grouting primarily activates and increases the pile shaft resistance and therefore improves the characteristics of bored pile interaction with the soil. The grouting 'work principle' was characterized in the paper.

Keywords: Pile Base Grouting, Pile Instrumentation, Pile Foundation, Bored Pile

1. INTRODUCTION

The side shear of bored shafts fully develops at displacement of between 0.5 and 1.0% of the shaft diameter (D), whereas, the end bearing is fully mobilized at displacements of 10 - 15% D. Therefore, the end bearing requires 10-30 times more displacement to mobilize the same percentage of its ultimate value. This forces engineers to reduce the end bearing contribution to the capacity of bored shafts to fulfill settlement limits [1].

Base grouting technology is used to prestress the soil underneath the pile base and to mobilize shaft friction before the 'real' load is applied, that allows to reduce mentioned above limitations. In Poland mostly used and well known are four technological solutions that were described in [2].

2. GROUTING WORK PRINCIPLE

Purpose of the pressure grouting is to introduce initial compressive force between pile base and the subsoil. On the pile side, this force is absorbed by pile weight and by the soil friction along the pile shaft, which acts downwards (f_{s1} in Fig. 1). With respect to the soil underneath the pile base, strength of the injection causes its pre-stressing and consolidation. At the same time, relaxation and disturbance of the soil structure created during the drilling are also reduced.

In non-cohesive soils, a certain volume of soil is additionally cemented and the effective area of the pile base increases. The injection pressure p_{in} should be adjusted, so that it causes the pile to be moved up (s_{p1}), however, but not more than 5 mm. In addition, the maximum pressure should be sustained for a specified period of time and held until the cement grout has hardened. The value of a pre-generated force in the pile base cannot be calculated directly from the injection pressure.

As a result of various pressure losses and as a result of soil consolidation under the pile base, the permanent force value in the base (Q_{b1}) is 30% to 50% lower than the initial value (calculated on the basis of the injection pressure p_{in}).

In Fig. 1, values of resistance and displacement corresponding to the moment of injection activation are marked on the graphs by points *A*, and stabilized values (permanent) - by points *B*. The points *A'* and *B'* indicate the displacement (settlement) of the soil under the pile base, caused by the injection pressure, which are in fact not measurable.

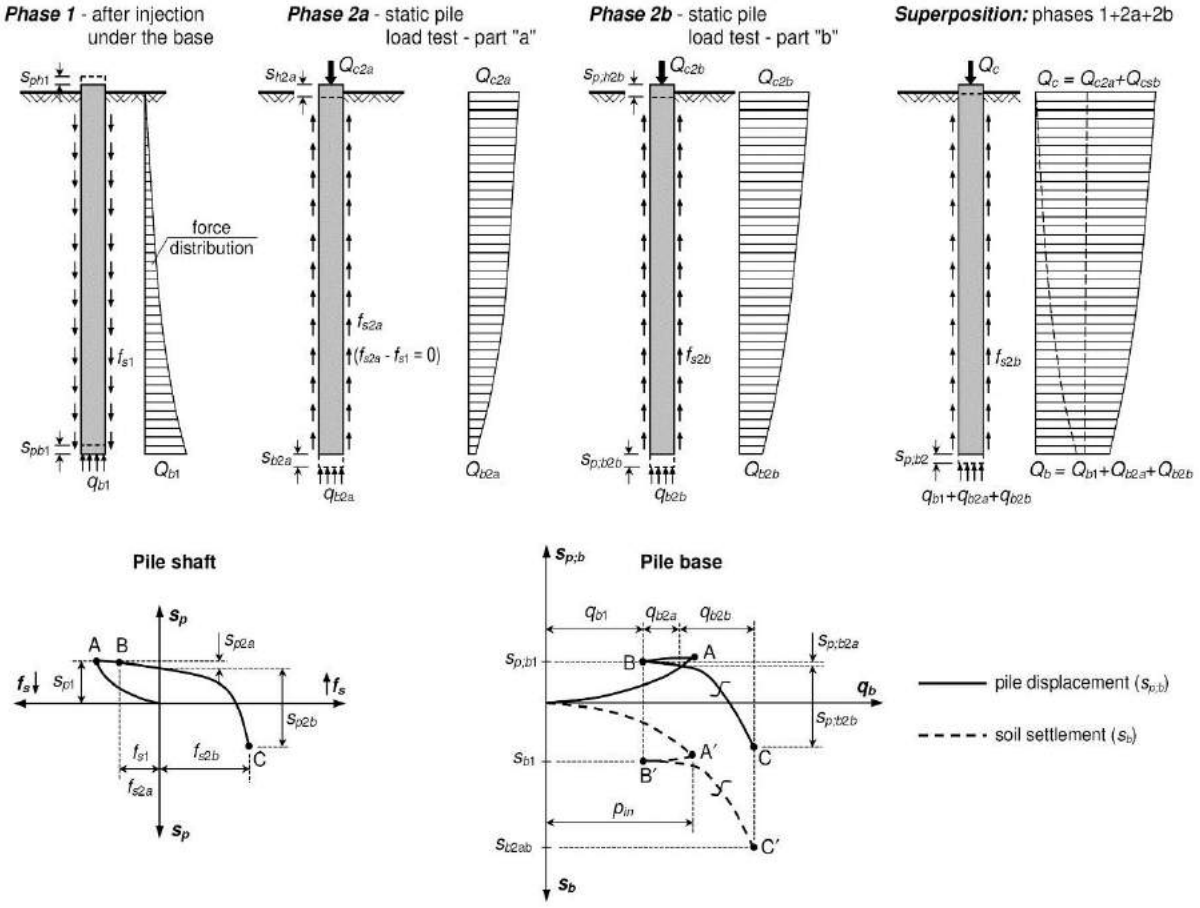

Figure 1. *Schematic work idea of the pressure grouting under the pile base*

During the transfer of external loads (eg. during a load test), a significantly smaller settlement of the pile with injection than the pile without injection is observed. From the schematic diagram in Fig.1, it follows that the decrease in pile settlement value is primarily the result of the specific work of the pile shaft.

When loading a pile, firstly shaft friction f_{s1} induced by the injection (directed downwards) is reduced to zero by friction f_{s2a}, and then the friction direction is reversed upwards and continuously mobilized to the value f_{s2b}. As a result, the resistance of the pile shaft, reaching in the final phase to point *C*, can even be doubled ($f_{s1} + f_{s2b}$).

Additionally, when taking into account that soil during reloading behaves much stiffer then during primary loading, it results in greater stiffness of the pile in the initial load stages. Pile base resistance, during a static load test achieves a relatively small value ($Q_{b2a} + Q_{b2b}$) and also shows reduced stiffness, but it must be noted that this resistance is added to the already existing force generated by the injection (Q_{b1}).

3. PILE LOAD TESTS - EXPERIMENTAL DATA

Two piles (bored in casing) No. 62 and No. 99 with diameter D = 1500 mm and effective length of 19.7 m were analyzed. For pile No. 62 base grouting was injected, while pile No. 99 was executed without injection. For comparative study, static load test on both piles were performed (using additional strain gauges for load distribution along pile shaft) and the results are presented in figures below (Fig 2, Fig. 3 and Fig. 4). A detailed description of foundation, ground conditions, calculation analysis and the basic results of pile load tests are presented by Dembicki et al. in [3]. To calculate the load distribution along shaft (based on strain gauges measurements), it was necessary to adopt an appropriate longitudinal pile core stiffness *EA*. The value of this stiffness, however, may change with strain and depth (eg. due to even small changes in the pile diameter. Constant concrete stiffness modulus value *E* and its determination on the basis of general recommendations, e.g. from tables based on concrete class, is not very precise and leads to erroneous results interpretation [4]. In the analysis, the *EA* value was determined as strain and depth dependent.

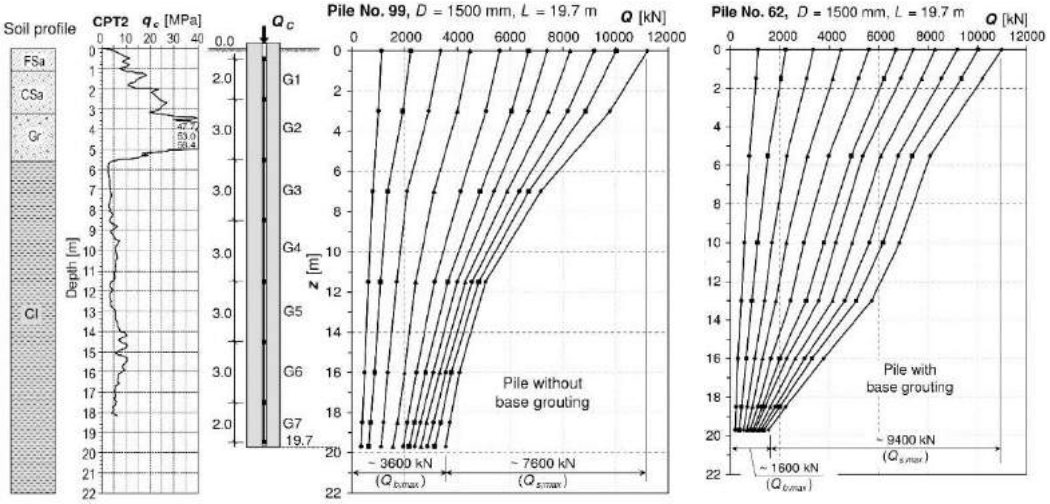

Figure 2. *The axial force distribution in both piles.*

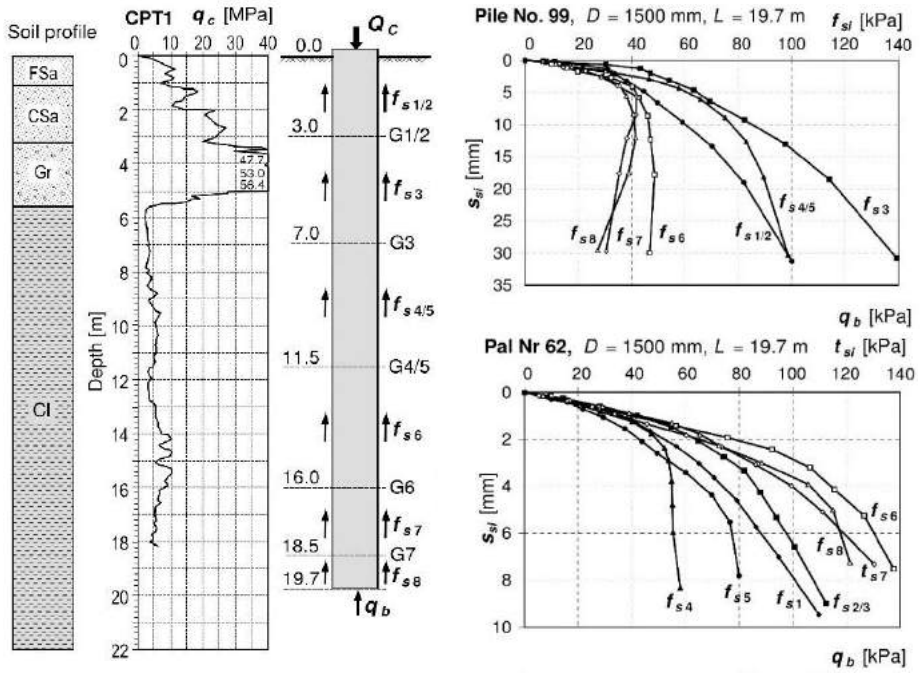

Figure 3. *Plots of soil resistance along the shaft for piles No. 62 and 99.*

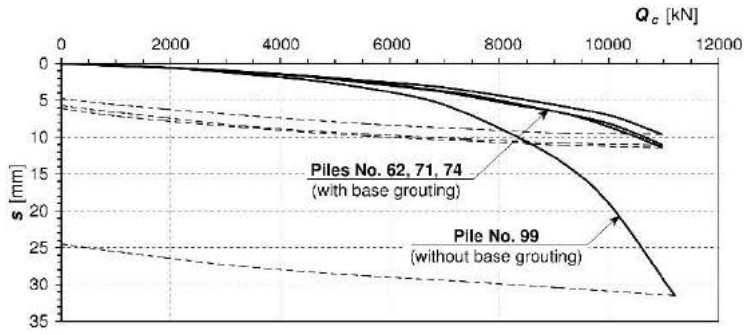

Figure 4. *Plots of foundation piles settlement from static load tests.*

4. RESULTS AND CONCLUSIONS

- ✓ Figure 4 shows a very clear and positive effect of grouting. After exceeding the force value $Q \approx 4000$ kN, larger settlement growth in the pale without injection is observed. For $Q_{max} \approx 11000$ kN pile without injection showed about three times greater settlements ($s \approx$ 31,5 mm) than pile with injection ($s = 10 \div 12$ mm).

- ✓ It is believed, that the grouting injection increases the initial pile stiffness, but does not increase the load-bearing capacity of the pile R_{ult}. However, determining the design pile load capacity R_d, according to the criterion of allowable settlements, it can be concluded that the injection certainly increases the pile bearing capacity. On the other hand, the pile bearing capacity increases when as the injection result soil is cemented and the effective area of the pile base is increased.

- ✓ Practical example indicates that it is very expedient to perform pile testing with the measurement of axial force distribution along pile shaft. Such a measurement not only allows to more accurately verify the effectiveness of grouting injection, but also to get to know the essence of its operation and the characteristics of soil structure interaction.

- ✓ Although the primary purpose of base injection is to pre-stress its substrate, it has been found that this treatment also activates increased soil resistance along the pile shaft. According to theoretical analysis, the soil resistance along shaft can increase twice and according to the research - even three times, especially in the lower pile sections.

REFERENCES

[1] Mullins G., Winters D., Dapp S., 2006. *"Predicting End Bearing Capacity of Post-Grouted Drilled Shaft in Cohesionless Soils"*, Journal of Geotechnical and Geoenvironmental Engineering, 132 (4), https://doi.org/10.1061/(ASCE)1090-0241(2006)132:4(478).

[2] Gwizdala K., Pinkowski A., 2007. *"Wpływ iniekcji pod podstawą na osiadanie pali wierconych w piaskach" [The influence of Grouting Under the Base on Bored Piles Settlement in Sands]*. Inzynieria i Budownictwo, 63.

[3] Dembicki E., Cudny M., Krasinski A., Zaleski K., 2013. "*Pylon Foundation of a Cable Stayed Bridge at The Motorway Rig Road of Wrocław"*. 18th International Conference on Soil Mechanics and Geotechnical Engineering, pp. 2715-2718, 2-6 September 2013, France.

[4] Fellenius B.H., 2001. *"From Strain Measurements to Load in an Instrumented Pile"*, Geotechnical News Magazine, 19(1):35-38.

DEVELOPMENT OF DIRECT SHEAR AND TRIAXIAL TEST PROCEDURES ON MICROBIALLY TREATED SAND SPECIMENS

Mert Tunalı, *Civil Engineering Department, Middle East Technical University, mert.tunali@metu.edu.tr*

Emre Duman, *Civil Engineering Department, Middle East Technical University, emre.duman@metu.edu.tr*

Yılmaz Emre Sarıçiçek, *Civil Engineering Department, Middle East Technical University, yilmazs@metu.edu.tr*

Onur Pekcan*, *Civil Engineering Department, Middle East Technical University, opekcan@metu.edu.tr*

Rafig Gurbanov, *Molecular Biology and Genetics Department, Bilecik Seyh Edebali University, rafig.gurbanov@bilecik.edu.tr*

Ayşe Gül Gözen, *Biological Sciences Department, Middle East Technical University, agozen@metu.edu.tr*

ABSTRACT

In the last decade, biology-based ground improvement method known as microbially induced calcium carbonate precipitation (MICP) has attracted the attention of the researchers seeking environmentally friendly solutions to the challenging problems of Geotechnical Engineering field. Within this scope, a group of researchers from interdisciplinary fields in the Middle East Technical University also have aimed at contributing to the literature for the last few years. Previous deductions of the authors especially in micro-scale paved the way for macro-scale mechanical tests, which form the engineering basis of practical MICP implementations. The mechanical test program included both direct shear and triaxial tests. The test procedures were formed in a progressive way such that the problems encountered during the trials were eliminated in the further tests. Accordingly, challenges and inferences throughout the development of test procedures are presented in this study.

Keywords: Microbially Induced Calcium Carbonate Precipitation, Direct Shear Test, Triaxial Test.

1. INTRODUCTION

Increasing population and migration to the cities result in growing infrastructural demand and lead to necessity of construction within ground conditions that are normally not desirable. The solution for undesirable ground conditions lay in the application of ground improvement techniques. For this purpose, conventional ground improvement methods have been successfully used for many decades. However, increasing environmental awareness, the expectations, and most importantly the regulations force people question the feasibility of existing methods. At that point, the quest for better applications brought about bacteria-based methods considering their advantages. As the bacteria already live in the ground, the external interferences are minimized. Bacteria can function even under extreme conditions.

Providing the necessary nutrition for bacteria to the soil, formation of calcium carbonate takes place inside the pores. Formed calcium carbonate particles are effective in improving strength and deformation characteristics of soils, especially sands. The whole procedure is known in the literature as microbially induced calcium carbonate precipitation (MICP).

The authors of this proceeding have been working on the subject for the recent years. Accordingly, the authors initially intended to comprehend the subject in the micro level. Experiments in syringes demonstrated the viability of the calcium carbonate precipitation under various conditions in sands. Specimens extracted from syringes were monitored through SEM, EDS and XRD techniques. The results and discussions about the subject were previously published by some members of the research group [1].

In geotechnical engineering, one of the optimum ways for understanding the strength characteristics of soils is to perform mechanical tests in laboratory conditions, alternative to field tests. The frequently used mechanical tests on bacteria-treated specimens include unconfined compression test [2,3,4], direct shear test [5, 6] and triaxial test [7, 8, 9, 10]. The authors of this publication also emphasized on the importance of above-mentioned mechanical test in their studies. Accordingly, a publication revealing the results of unconfined compression tests is to be published in the upcoming months. Furthermore, the objective of the researchers is to extend the knowledge by employing direct shear and triaxial tests. Therefore, this paper aims at contributing to the literature of MICP through summarizing the approaches adopted while performing direct shear and triaxial tests on improved sands.

2. METHODOLOGY

2.1. Direct Shear Test

One of the fundamental challenges for the evaluation of the geomechanical properties of the microbially treated soils is specimen preparation stage. As there exists no standard specimen preparation procedure, researchers have followed many different procedures. Within the concept of this study, a specimen preparation procedure was designed by assessing these options emerged in the literature.

The design process started with the question of “How to apply the cementation solution?”. There are two alternatives appearing in the literature: Submersion of the mold into the medium [5, 11] and injection of the medium through the soil matrix by producing a head difference or using a peristaltic pump [12, 13, 14, 15]. In the current study, the researchers opted for injection through use of peristaltic pump. The reasons for this selection are resembling the grouting methods in the field and having more control on injected fluid.

The next decision was related to the properties of the mold in which the specimens were prepared. Hence, first, two options were considered: Either preparation of the specimens in the direct shear box or preparation in a mold and then transferring into the direct shear box. Mold made of geotextile material is an example for the latter case [11]. In this study, to eliminate the possible disturbances during the transferring stage, the specimens were prepared in the direct shear boxes. However, the risk of corrosion emerged with this selection as it could ruin the reactions. Therefore, boxes produced from stainless steel were used. The boxes had the same dimensions with the conventional direct shear boxes available in the market (60 mm in diameter).

The pilot tests were performed after production of the direct shear boxes. In order to get the drained parameters quickly, the pilot tests were performed under dry conditions. The specimens were kept under 60 ^{o}C until no mass change was observed.

Following the drying process, a stiff crust layer was observed on the top of the specimens (Figure 1). The direct shear test results under this condition were unreliable. An example for the pilot tests illustrating the shear and displacement behavior is given in Figure 2. At the end of the tests, it was noticed that the observed stiff crust layer was strongly bonded to the upper half of the direct shear box.

That probably limited the transfer of the normal load given to the specimen by not allowing the formation of shear plane at the joint of two halves of the box. This condition is probably valid especially for the case of relatively low normal loads. Eventually, the idea of such a drying process was leaved. Air drying could be considered as another option, but considering the long time required to get fully dry specimens, the idea was also eliminated. As a result, the strategy was shifted to testing specimens under saturated conditions.

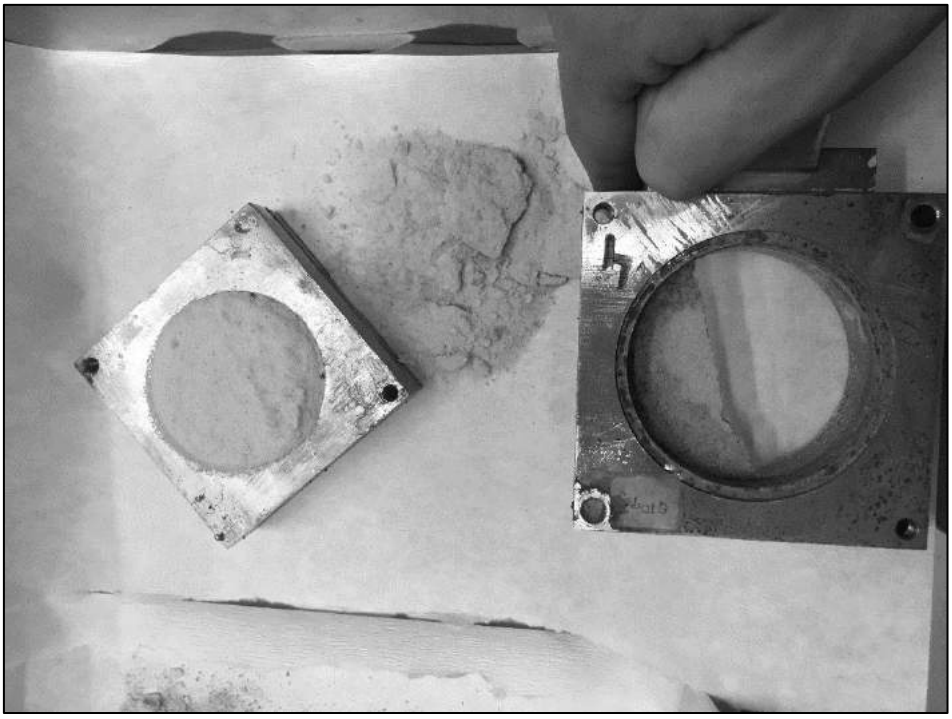

Figure 1*. Crust layer observed after drying process*

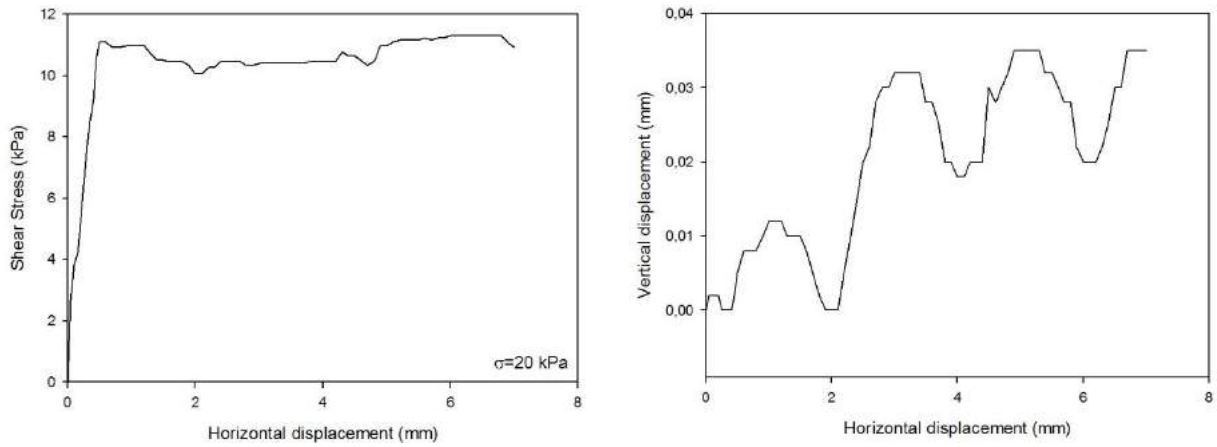

(a) (b)

Figure 2. *An example of pilot experiment results*

In the literature, researchers have mainly focused on two main injection strategies: Continuous-flow where the medium flows through the specimen without any interruption and stopped-flow where the injections were performed in a periodical manner and the system was left for reaction between two consecutive injections. The researchers obtained better results when stopped-flow strategy was applied [16, 17].

In order to function under maximum efficiency, it is essential to have a closed system that prevents any leakage. Thus, it was required to take precaution against possible leakage from the joint of the two halves of the box. Application of silicone would be a solution. However, the remainings of the silicone after removal for shearing process would affect the test results. Finally, it was decided to use a special tape around the joint that provides leakage protection. To ensure a watertight mold, silicone was also applied to the two edges of the tape (Figure 3).

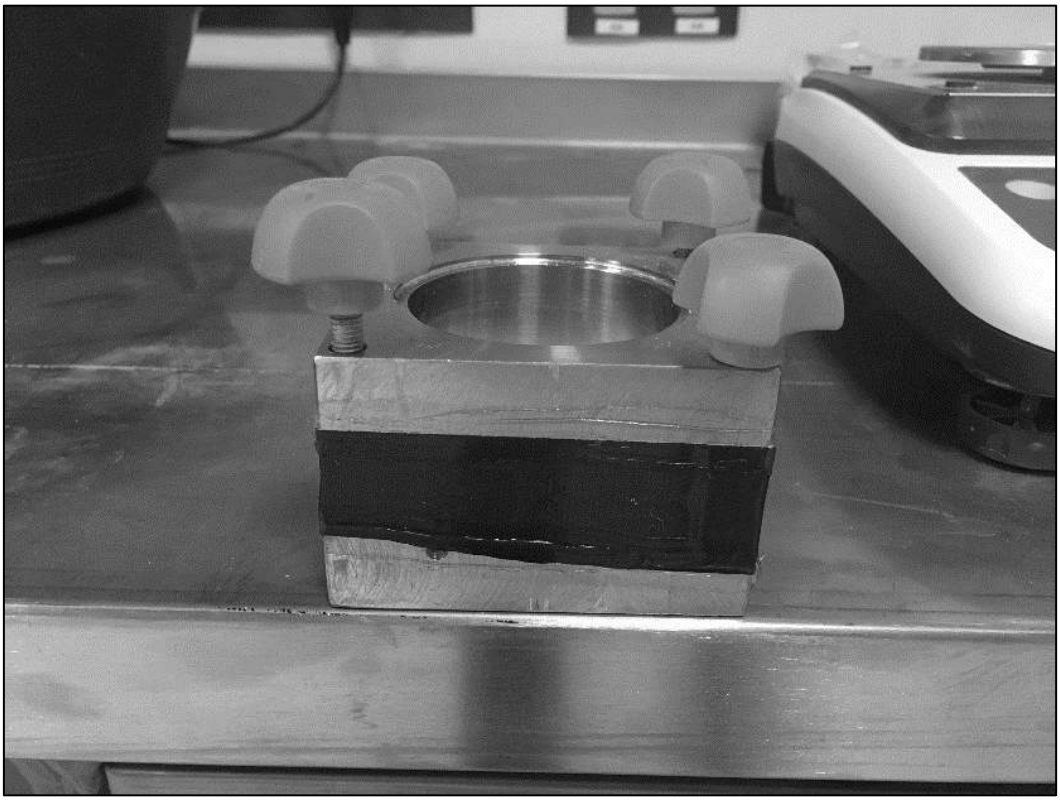

Figure 3. *Watertight mold with silicone application*

In conclusion, thanks to improvements in experimental procedure, at the end reliable results were obtained. The results revealed that improvements in mechanical characteristics with certain type of bacteria are highly possible.

2.2. Isotropically Consolidated Drained Triaxial Test

In this section, the test procedure for already planned isotropically consolidated drained triaxial test (CD) is introduced. In general, the conventional triaxial test procedure together with some required minor changes is followed and the main reason for conducting CD test out of other possible triaxial tests is the fact that drainage conditions in CD test are similar to drainage conditions of sands for most of the cases. However, as mentioned above some modifications for triaxial testing of MICP treated sands were inevitable and those modifications are going to be discussed.

The first step is initial calibrations and specimen preparation. Following the end of the previous experiment, before preparing a new specimen, initially each drainage line of triaxial base is controlled for investigating possible clogging occurrence.

Compatibility of porous stones is checked by injecting biological solutions from bottom drainage line to porous stones. No specimen is placed on top of the stones at that stage. Effluents are collected and optical density (OD) of the solution is measured. For specimen preparation, undercompaction method is adopted as suggested by Ladd [18]. The method allows specimen to have uniform density along the height of the specimen. During the compaction of upper layers with tamping rod, lower layers are also compacted as expected.

Yet, in undercompaction, height of layers is adjusted based on the principle that each layer is going to be compacted equally at the end. In this study, specimens are prepared in 8 layers and with 4% water content which is mentioned as reasonable value for most of the soils [19]. Before compacting the specimen, vacuum is applied to split mold to ensure full contact of membrane with split mold. After completing compaction, vacuum is utilized for specimen from top cap and split mold is removed. Then, cell pressure is gradually applied while decreasing the vacuum slowly, in order to avoid overconsolidation of specimen.

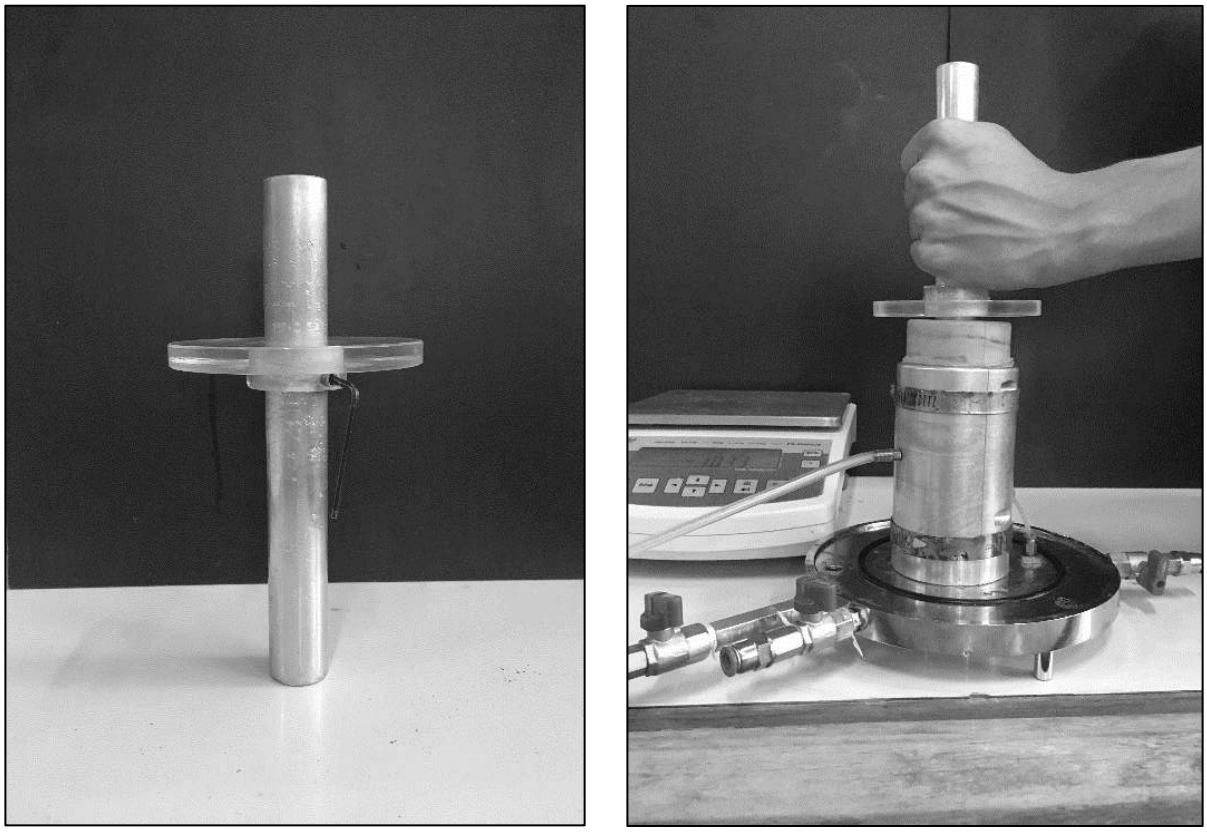

a. Tamping rod with adjustable height

b. Compaction of layers

Figure 4. *Specimen preparation with undercompaction method*

The next step is injection of biological and cementation solutions after application of seating cell pressure. At that point, at the same time multiple triaxial test cells are to be used during specimen nutrition for time saving. Providing nutrition inside the cell appears to be more appropriate for reflection of practical applications. The reason for this is that the soil is under certain confinement conditions in the ground with depth. The cell pressure value is determined by considering target improvement depth of soil which might vary depending on

different uses such as liquefaction mitigation, slope stabilization, bearing capacity improvement, settlement reduction, erosion and seepage control etc. Variables such as injection rate and retention time are kept same as in the direct shear tests for consistency.

Depending on the expected cementation levels, the number of injections might be increased or decreased as given in the study of Feng and Montoya [7] to obtain lightly/moderate/heavily cementation levels. In this case, a reverse injection scheme is employed. While biological solution is injected from bottom drainage line, cementation solution is injected from top drainage line to reduce clogging possibility in the drainage lines [20]. Each stage requires detailed and careful maintenance of the equipment used in the experiment.

At the next stage, saturation process is completed. Initially, carbon dioxide is flushed through the specimen for certain time until a rate of three bubbles per second is observed at the output. Rate of flushing is measured by connecting effluent line to a bowl filled with water. The reason for flushing CO_2 is basically replacing soluble air with a gas of better solubility in water [21]. This process is continued for 20-30 min and de-aired water is flushed subsequently.

The rate of flushing should be carefully determined in order to prevent disturbance of the specimen. Pressure volume actuators might be discharge controlled and, in this case, very low discharge values can be chosen. If this is not the case, flushing of de-aired water can be done with very low-pressure values. Producing a head difference is another option for flushing of de-aired water. After flushing, the specimen is saturated until Skempton's B value is reached to 0.95.

As a final step, specimen is consolidated to desired effective stress and sheared. After completing shearing, cell and backpressures are gradually decreased. Together with a partial vacuum from top cap, specimen is removed from pedestal.

3. CONCLUSION

In this publication, the primary aim is to introduce the steps that were followed and currently being followed in MICP based experiments. Following the end of testing program, results are going to be revealed in forthcoming studies. The experience gained so far indicate that in overall, the procedure followed in operation of direct shear test and triaxial test on improved sands are promising. Eliminating the possible drawbacks require hands-on experience and detailed investigation at every step.

REFERENCES

[1] Saricicek, Y. E., Gurbanov, R., Pekcan, O., Gozen, A. G., 2019. "*Comparison of Microbially Induced Calcium Carbonate Precipitation Eligibility Using Sporosarcina Pasteurii and Bacillus Licheniformis on Two Different Sands"*, Geomicrobiology Journal, 36(1): 42–52, http://doi.org/10.1080/01490451.2018.1497732.

[2] van Paassen, L. A., Ghose, R., van der Linden, T. J. M., van der Star, W. R. L., van Loosdrecht, M. C. M., 2010. "*Quantifying Biomediated Ground Improvement by Ureolysis: Large-Scale Biogrout Experiment*", Journal of Geotechnical and Geoenvironmental Engineering, 136(12): 1721–1728, http://doi.org/10.1061/(ASCE)GT.1943-5606.0000382.

[3] Al Qabany, A., Soga, K., 2013. "*Effect of Chemical Treatment Used in MICP on Engineering Properties of Cemented Soils*", Geotechnique, 63(4): 331–339. http://doi.org/10.1680/geot.SIP13.P.022.

[4] Montoya, B. M., Feng, K., Shanahan, C., 2013. "*Bio-Mediated Soil Improvement Utilized to Strengthen Coastal Deposits*", 18th International Conference on Soil Mechanics and Geotechnical Engineering, pp. 2565–2568, 2-6 September 2013, France.

[5] Chou, C. W., Seagren, E. A., Aydilek, A. H., Lai, M., 2011. "*Biocalcification of Sand through Ureolysis*", Journal of Geotechnical and Geoenvironmental Engineering, 137(12): 1179–1189, http://doi.org/10.1061/(ASCE)GT.1943-5606.0000532.

[6] van Paassen, L. A., van Hemert, W. J., van der Star, W., van Zwieten, G., van Baalen, L., 2012. "*Direct Shear Strength of Biologically Cemented Gravel*", GeoCongress 2012: State of the Art and Practice in Geotechnical Engineering, pp. 968-977, 25-29 March 2012, the USA. http://doi.org/10.1061/9780784412121.100.

[7] Feng, K., Montoya, B. M., 2016. "*Influence of Confinement and Cementation Level on the Behavior of Microbial-İnduced Calcite Precipitated Sands Under Monotonic Drained Loading*", Journal of Geotechnical and Geoenvironmental Engineering, 142(1): 04015057-1-9, http://doi.org/10.1061/(ASCE)GT.1943-5606.0001379.

[8] Lin, H., Suleiman, M. T., Brown, D. G., Kavazanjian, E., 2016. "*Mechanical Behavior of Sands Treated by Microbially Induced Carbonate Precipitation*", Journal of Geotechnical and Geoenvironmental Engineering, 142(2): 04015066-1–13. http://doi.org/10.1061/(ASCE)GT.1943-5606.0001383.

[9] Montoya, B. M., Dejong, J. T., 2015. "*Stress-Strain Behavior of Sands Cemented by Microbially Induced Calcite Precipitation*", Journal of Geotechnical and Geoenvironmental Engineering, 141(6): 04015019-1-10, http://doi.org/10.1061/(ASCE)GT.1943-5606.

[10] Ozdogan, A., 2010. "*A Study on the Triaxial Shear Behavior and Microstructure of Biologically Treated Sand Specimens*", M. Sc. Thesis, University of Delaware, the USA, 132 pages.

[11] Zhao, Q., Li, L., Li, C., Zhang, H., Amini, F., 2014. "*A Full Contact Flexible Mold for Preparing Samples Based on Microbial-İnduced Calcite Precipitation Technology*", Geotechnical Testing Journal, 37(5): 917-921, http://doi.org/10.1520/GTJ20130090.

[12] Harkes, M. P., van Paassen, L. A., Booster, J. L., Whiffin, V. S., & van Loosdrecht, M. C. M., 2010. "*Fixation and Distribution of Bacterial Activity in Sand to Induce Carbonate Precipitation for Ground Reinforcement*", Ecological Engineering, 36(2): 112–117. http://doi.org/10.1016/j.ecoleng.2009.01.004.

[13] Al Qabany, A., Soga, K., M., Santamarina, C., 2012. "*Factors Affecting Efficiency of Microbially Induced Calcite Precipitation*", Journal of Geotechnical and Geoenvironmental Engineering, 138(8): 992–1001. http://doi.org/10.1061/(ASCE)GT.1943-5606.0000666.

[14] Canakci, H., Sidik, W., Kilic, I. H., 2015. "*Bacterail Calcium Carbonate Precipitation in Peat*", Arabian Journal for Science and Engineering, 40(8): 2251–2260. http://doi.org/10.1007/s13369-015-1760-4.

[15] Jiang, N., Soga, K., Kuo, M., 2017. "*Microbially Induced Carbonate Precipitation for Seepage-Induced Internal Erosion Control in Sand–Clay Mixtures*", Journal of Geotechnical and Geoenvironmental Engineering, 143(3): 96-104, http://doi.org/10.1061/(ASCE)GT.1943-5606.0001559.

[16] Martinez, B. C., Barbouki, T. H., Dejong, J. D., Ginn, T. R., 2011. "*Upscaling of Microbial Induced Calcite Precipitation in 0.5m Columns: Experimental and Modeling Results*", Geo-Frontiers 2011, pp. 4049–4059, 13-16 March 2011, the USA.

[17] Ng, W., Lee, M., Hii, S., 2012. "*An Overview of the Factors Affecting Microbial-İnduced Calcite Precipitation and its Potential Application in Soil İmprovement*", International Journal of Civil and Environmental Engineering, 6(2), 188-194.

[18] Ladd, R.S., (1978). "*Preparing Test Specimens Using Undercompaction*", Geotechnical Testing Journal 1, 1(1): 16-23. https://doi.org/10.1520/GTJ10364J.

[19] Germaine, J. T., Germaine, A. V., 2009. "*Geotechnical Laboratory Measurements for Engineers*", John Wiley & Sons, the USA, 354 pages.

[20] Martinez, B. C., DeJong, J. T., Ginn, T. R., Montoya, B. M., Barkouki, T. H., Hunt, C., Tanyu, B., Major, D., 2013. "*Experimental Optimization of Microbial-Induced Carbonate Precipitation for Soil Improvement*", Journal of Geotechnical and Geoenvironmental Engineering, 139(4), 587–598. http://doi.org/10.1061/(ASCE)GT.1943-5606.0000787.

[21] Donaghe, R. T., Chaney, R. C., Silver, M. L., 1988. "*Advanced Triaxial Testing of Soil and Rock*", American Society for Testing and Materials, the USA.

BEHAVIOR OF STRIP FOOTING NEAR SLOPE UNDER ECCENTRIC LOADING

Baazouzi Messaoud*, *Département of Civil engineering/University of Blida 1, Blida, Messaoud.baazouzi@gmail.com*
Badis Mazouz, *Laboratory of Research in Hydraulic Applied LARHA /University Of Batna 2, Batna, Algeria*
Abech. Khalifa, *Laboratory of Research in Hydraulic Applied LARHA /University Of Batna 2, Batna, Algeria*
BOUDIAF. Khaoula. *laboratory of research in Civil engineering LRGC/University of Biskra, Biskra, Algeria*

ABSTRACT

The bearing capacity of shallow foundation near slope has always been one of the subjects of major interest in geotechnical engineering for researchers and practical engineers. This paper presents the results of laboratory model tests of an eccentrically loaded capacity of foundations on slopes. In order to achieve this objective several tests were carried out with an eccentrically loaded model footing under various positive and negative eccentricity ratio ±e/B and various normalized footing distance d/B. The results have been compared with those available in the literature. The results of the experimental study proved that the load eccentricity, and the normalized footing distance had considerable effects on the drained bearing capacity. Failure mechanism were not symmetrical, the higher length it can be developed on the slope side and the lengths of failure surfaces decreased with the increasing eccentricity.

Keywords: Bearing Capacity, Eccentric Loading, Failure Mechanism, Shallow Foundation Slope.

1. INTRODUCTION

The prediction of the bearing capacity of a shallow foundation is a very important problem in Geotechnical Engineering. There is an extensive literature dealing with drained bearing capacity of foundation during the last century through different methods; experimental investigations, numerical and theoretical analyses. Under eccentric loading is the effective width method is broadly accepted in foundation design [1]. [2] proposed empirical modifications to [3] expressions who proposed to take account the effect of moment loading by introducing effective foundation dimensions, which consists of replacing the actual footing B by an effective footing with width B' [4].

$$q_u = \frac{1}{2} B' \gamma N_\gamma$$

Recent decades, the approach of multiplicative factors is being replaced by the use of a failure envelope (V–H–M) space, various studies can be found in the literature (e.g., [5]; [6]; [7]; [8]; [9]; [10]; [11]; [12]; [13]), have been proposed expression for the load interaction diagram and failure surface for strip, circular and rectangular surface footings on horizontal ground. However, contrary to the horizontal flat soil case, very limited work has been done on the

eccentric loading capacity of strip foundations on slopes, due to land limitation and some other specific reason, such as bridge abutments, towers footings of electrical transmission lines and buildings that are located next to a ravine [14]. In these cases, the bearing capacity may be significantly reduced depending on the location of the footing with respect to the slope. However, the difficulty in solving a footing on slope problem is that the ultimate bearing capacity is affected by either the local foundation failure or the global slope failure, which has negative consequences on the environment in general. [15] When the foundation is constructed near slope, the length of failure mechanism has been much shorter than that of the same footing on horizontal ground surface due to lack of on the side of the slope of the strip footing, the bearing capacity is decreases ([16]; [17]; [18]; [19]).

Different studies have been devoted for the calculation of the bearing capacity of shallow footings under eccentric, the limit equilibrium method of the same problems was presented by [20], who also developed a theory for calculated the problem of footings near cohesionless slopes subjected to eccentric vertical loads. They conclude that the position of the load to the center of the footing is highly considerable effect. [21] used the finite element FE method to investigate the stability of footing rest on the crest of the slope under eccentric loads. The results show effect of eccentric loads is differs considerably depending the position of the loads versus the middle of footing and the crest of the slope. [22] have been used linear and non-linear FEM analysis to investigate effect of load eccentricity and soil reinforcement on the bearing capacity and the failure mechanism of the footing. Furthermore, some experimental works on the bearing capacity of foundation near slope under eccentric loads have been conducted by [23] were used full-scale model tests on very dense sand to investigate the ultimate bearing capacity depending to the eccentric loads for strip footings stay in the for sloping ground ($D_f/B=0$) and embedded in soil ($D_f/B=0.25$). They found that the ultimate bearing capacity decreases with increase of the eccentric loads and the slope inclination. Also, they found that the failure mechanism for the footing on the top of the slope decrease with increase of eccentric of the load. [24] who investigated an artificial neural networks (ANNs) and multi-linear regression model for the prediction of ultimate loads of eccentric and eccentric-inclined loaded of strip footings. In addition, [25] and [26] have been employed the experimental investigation with numerical analysis to estimate the stability of uniformly reinforced slopes under eccentric loads. They show that the bearing capacity increases by reinforcing the soil zone immediately beneath the footing with footing size reinforcing layers up to depth. According to literature review, none of the published studies pointed out the experimental analyses of eccentric loaded strip footings without reinforced considering varieties of positive and negative eccentricity ratio ±e/B and various normalised footing distance d/B. This study tries to point a good understanding of the behavior strip footing resting on sand soil under eccentrically loads. For this purpose, experimental studies have been carried out to define the ultimate load, and then, the load-settlement curves have been plotted. A total of 28 laboratory model tests were carried out with different footings distance, the eccentricity ratio (e/B) changed from 0 to ±0.3.

2. EXPERIMENTAL STUDY

2.1. Experimental Model Test

A series of laboratory model tests was conducted in a test tank made of a rigid steel, with inside dimensions of 1.8 × 0.5 m in plan and 0.6 m in high as shown in Fig.1. One of the two sidewalls of the tank are made of 10 mm thick transparent Plexiglas plate allows the sample to be seen during preparation and to observe the failure mechanism during the tests and the other sides consist of 3 mm steel plate. The horizontal lines with equal 50mm spacing were also marked on the inner surfaces of the test tank to make easy the preparation of the sand bed in layers.

Plane strain conditions during all tests are ensured by construction the test tank walls rigid with melted steel. All tests were conducted with an artificially made slope of β=33.69°. The different parts and apparatus of the model test are shown in Fig. 1. The loading system is a moving lever mechanism consisting of a rigid metal beam. The load is applied to the footing by placed masses sequentially on the lever and measured by a load sensor (load sensor 20KN). The displacements were measured by a sensor placed on the load point application as shown in Fig. 1.

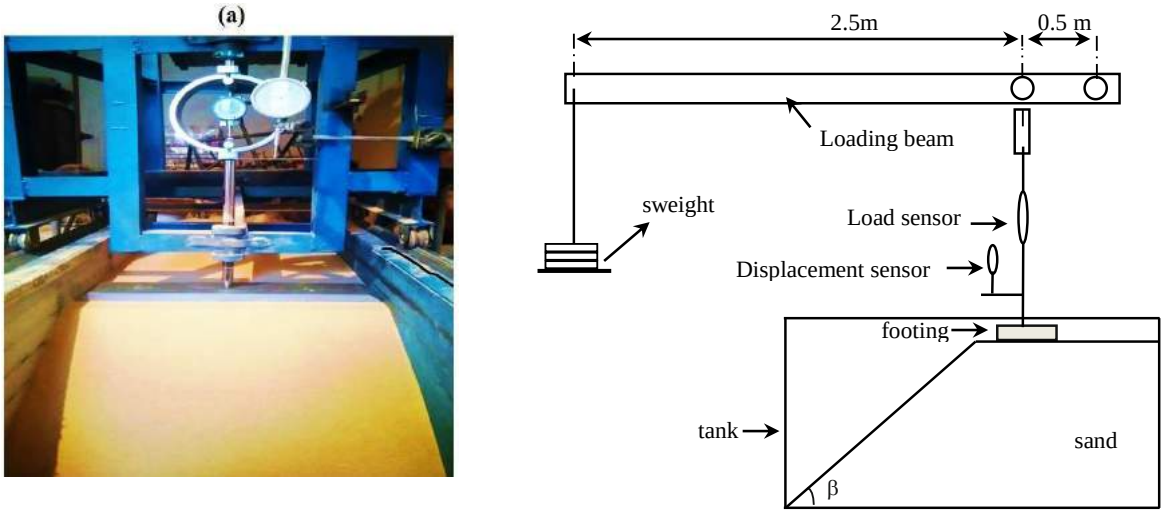

Figure 1. *Schematic view of the experimental apparatus.*

2.2. Test Materials

2.2.1. Footing

The model strip footing used was made of a rigid steel plate with Several holes are created on the upper side of the footing, considered as loading points during the application of different eccentric loads. (see Fig. 2). The footing was 499 mm in length, 100 mm in width, B, and 20 mm in thickness, with the length of the footing was made almost equal to the width of the tank in order to maintain the plane strain conditions. The tow ends of footing have been polished to minimize all efforts resulting from the friction with the tank walls. A rough base condition was provided by using rough sandpaper on the base of the model footing.

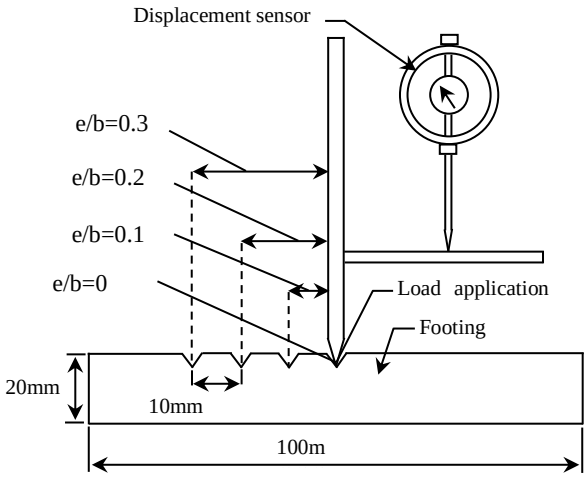

Figure 2. *Schematic view of the tested footing and load point application*

2.2.2. Sand

The sand used in this research is "Pit Sand", whose particle size distribution is shown in Fig.3. It has a coefficient of uniformity (Cu) of 3.08, coefficient of curvature (Cc) of 1.29, effective particle size (D10) of 0.36 mm, and specific gravity of 2.63. The maximum and minimum dry unit weights of the sand are found to be 14.1 and 19.3 kN/m. The sand was dried until the moisture content was almost zero (dry condition) throughout all tests. In all tests the total (dry) unit weigh and relative density (ID) of sand was kept at 16.2 kN/m3 and 60% respectively. The internal friction angle of compacted sand at relative density of 60% measured from a series of direct shear tests is approximately 38° which correspond to dense sand. The properties of this soil are given in Table1.

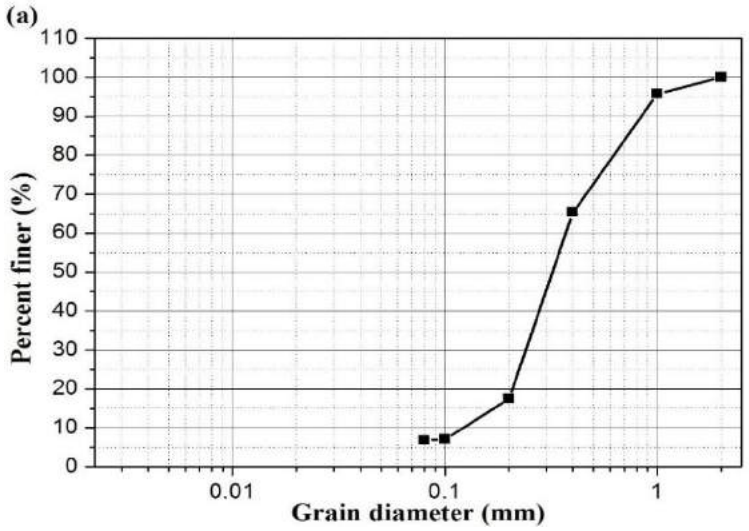

Figure 3. *Particle size distribution curve for the sand*

Table1. *Soil Parameters.*

Parameter	Value
Cohesion, c (kPa)	0.0
Angle of internal friction (°)	38.00
Unit weight, γ (kN/m3)	16.20
Maximum dry density (kN/m3)	19.30
Minimum dry density (kN/m3)	13.92
D10 (mm)	0.12
D30 (mm)	0.24
D60 (mm)	0.37
Coefficient of uniformity, Cu	3.08
Coefficient of curvature, Cc	1.29

2.3.Slope Preparation and the Test Program

The procedure adopted for the slope preparation was the same as those used by [27] and [28] as in the figure 5. The sand slope model is made by pouring and compacting in 50 mm thick sand layers to cover the entire plane surface of the test tank. For the construction of the slope model, the sand was poured in 50 mm thick layers up to a height of 500 mm from the bottom of the test tank and covering its entire area. The geometry of the slope was drawn on both sides of the test tank and the sand was excavated, accordingly. The desired slope angle was achieved by using a rigid metal blade. Three tests were conducted to investigate the effect of slope in the behavior of bearing capacity of strip footing under eccentric loads. The figure 5 shows three different methods of the load test: (1) centric load; (2) positive eccentrically (Eccentric load towards slope face) and (3) negative eccentrically (Eccentric load far away from slope face). Each series of tests was conducted to study the response of one parameter while the other ones remained constant. The varied conditions include the eccentricity value and the normalized distance d/B.

Table 2. *Model Tests Program*

Test reference	d/B	e/B	tg β
000, 001, 002, 003	0	0	
050, 051, 052, 053	0.5	0.1	
100, 101, 102, 103	1	0.2	
150, 151, 152, 153	1.5	0.3	2/3
200, 201, 202, 203	2	-0.1	
250, 251, 202, 253	2.5	-0.2	
300, 301, 302, 303	3	-0.3	

3. RESULTS AND DISCUSSION

In total three series consisting of 49 model tests were performed to study the effect of various parameters of positive e/B = 0, 0.1, 0.2, 0.3, negative (e/B) = 0, -0.1, -0.2, -0.3 eccentric loads and normalised slope/footing distance d/B of 0, 0.5, 1.0, 1.5, 2.0, 2.5, 3 are considered. Typical load-settlement curve for footing under eccentric load is illustrated in Fig.6, for e=0.1B. In this curve, the ultimate bearing capacity was determined by tangent intersection method [29] and [30], this method based drawn from the initial and the end points of the load– settlement curve and the ultimate load corresponding to the intersection point of these two lines.

A reduction factors are expressed in non-dimensional form in terms of bearing capacity of strip footing under eccentric loads and near of the slope. The first is i_e = eccentric factor, $q_{u(eccentric)}$ = ultimate bearing capacity (eccentrically load per unit area) and $q_{u(centric)}$ = ultimate bearing capacity (vertical centric loading).

$$i_e = \frac{q_{u(eccentric)}}{q_{u(centric)}}$$

The results of this study are compared with the results of [2]; [23] and [25].

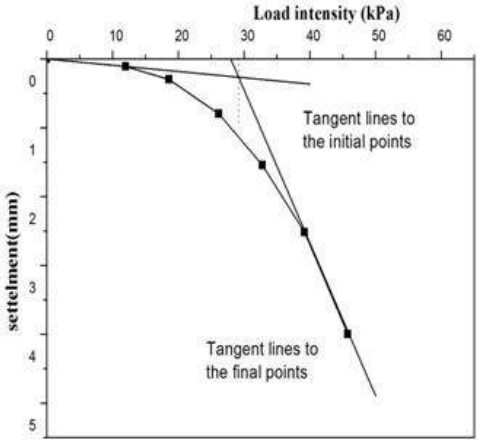

Figure 6. *Interpretation of Load Test Data*

3.1.Effect of the Load Eccentricity Location Relative to the Slope Face

The influence of the eccentrically loads is investigated for various eccentricity ratio ±e/B and normalized slope/footing distance d/B as mentioned in the table 2. Fig.7, shows the load–settlement curves at different e/B ratios for d/B=0.5, 1.5 and 3 respectively. As seen, the ultimate bearing capacity under eccentrically loads increase with increases of the normalized slope/footing distance d/B. in the cases of d/B=0.5 and 1.5 the ultimate bearing capacity in the he positive case smaller than the negative eccentric load, this is the failure mechanism extends to the slope, However, in the case of d/B=3 the same ultimate bearing capacity for two cases of eccentricity ratio, this correspond that the failure mechanism extend in the horizontal ground surface or in other meaning that the slope not effected in ultimate bearing capacity for two sing eccentricity loads. a similar trend case was reported by [31] has been observed that the ultimate bearing capacity remains nearly constant when the normalized distance in excess of about d/B>3. The same observation was signaled by [32] that the slope not effected in the ultimate bearing capacity when the normalized distance greater than the d/B>3. Concerning the centric loading always greater than the eccentric loading in the two cases of eccentrically loads ratio e/B.

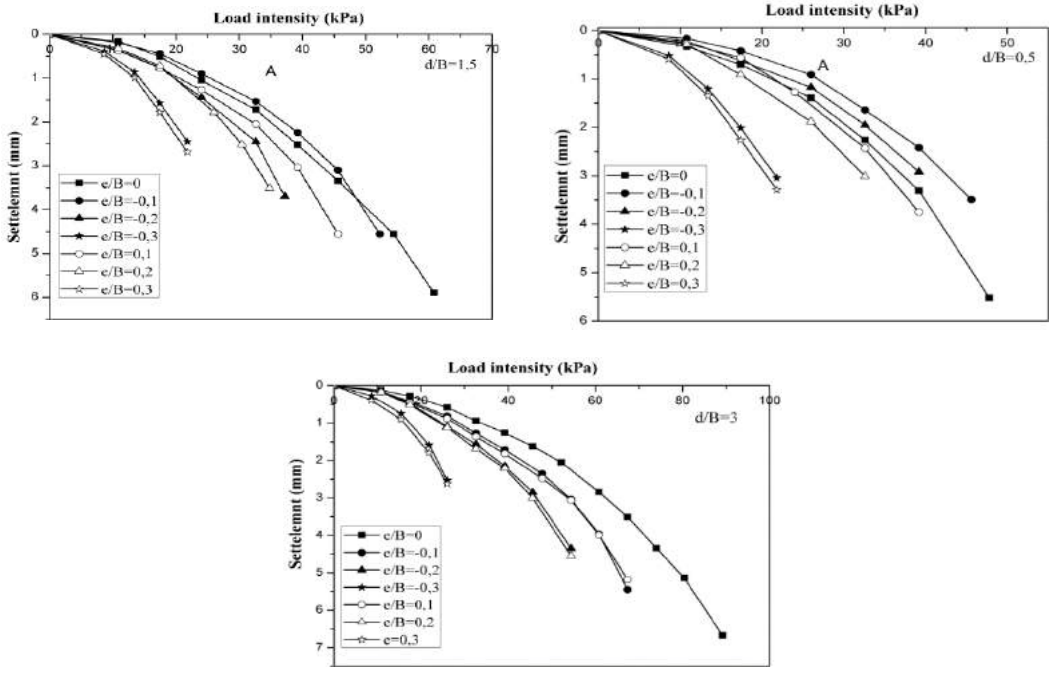

Figure 7. *Summary of load–settlement curves at different e/B ratios (model test).*

4. CONCLUSION

The experimental study of an eccentrically loaded strip footing near slope have been conducted. Various geometries were considered, the results of the analyses were compared to other available solutions. It was found that the ultimate bearing capacity depends the eccentric ration e/B and normalized distance d/B also the inclination slope β. Based on the laboratory tests, the following main conclusions are drawn:

- The bearing capacity increased when the footing located so far to the top of the slope.
- Loading the bearing capacity under centric loading is greater than under eccentrically loading.
- The effect of eccentric loading in the ultimate bearing capacity.

REFERENCES

[1] Sieffert, J.-G. and C. Bay-Gress (2000). "*Comparison of European bearing capacity calculation methods for shallow foundations*", Proceedings of the Institution of Civil Engineers-Geotechnical Engineering 143(2): 65-74.

[2] Meyerhof, G.T. (1953). "*The bearing capacity of foundations under eccentric and inclined loads*", Proc. of 3rd ICSMFE, 1, 440-445

[3] Terzaghi, K. (1943). "*Theory of consolidation*". Theoretical Soil Mechanics: 265-296.

[4] Loukidis, D. and R. Salgado (2008). "*Analysis of the shaft resistance of non-displacement piles in sand*". Géotechnique.

[5] Georgiadis, M. and R. Butterfield (1988). "*Displacements of footings on sand under eccentric and inclined loads*". Canadian Geotechnical Journal 25(2): 199-212.

[6] Gottardi, G. and R. Butterfield (1993). "*On the bearing capacity of surface footings on sand under general planar loads*". Soils and Foundations 33(3): 68-79.

[7] Bransby, M. and M. Randolph (1998). "*Combined loading of skirted foundations*". Geotechnique 48(5): 637-655.

[8] Taiebat, H. and J. Carter (2000). "*Numerical studies of the bearing capacity of shallow foundations on cohesive soil subjected to combined loading*". Geotechnique 50(4): 409-418.

[9] Bransby, M. and G.-J. Yun (2009). "*The undrained capacity of skirted strip foundations under combined loading*". Geotechnique 59(2): 115-125.

[10] Taiebat, H. and J. Carter (2010). "*A failure surface for circular footings on cohesive soils*". Geotechnique 60(4): 265-273.

[11] Gourvenec, S. and S. Barnett (2011). "*Undrained failure envelope for skirted foundations under general loading*". Géotechnique 61(3): 263-270.

[12] Shen, Z., X. Feng, et al. (2016). "*Undrained capacity of surface foundations with zero-tension interface under planar VHM loading*". Computers and Geotechnics 73: 47-57 %@ 0266-0352X.

[13] Feng, X., S. Gourvenec, et al. (2017). "*Shape effects on undrained capacity of mudmat foundations under multi-directional loading*". Ocean Engineering 135: 221-235 %@ 0029-8018.

[14] Shields, D. H., Chandler. N., Garnier. J. (1990). "*Bearing capacity of foundation in slopes*". J Geotech Eng., ASCE. 116 528-537.

[15] Azzouz, A. S. and M. M. Baligh (1983). "*Loaded areas on cohesive slopes*". Journal of geotechnical engineering 109(5): 724-729.

[16] Uzuner, B. (1975). "*Centrally and Eccentrically Loaded Strip Foundations on Sand*". University of Strathclyde.

[17] Moroglu, B., B. A. Uzuner, et al. (2005). "*Behavior of the model surface strip footing on reinforced sand*".

[18] Sadoglu, E., E. Cure, et al. (2009). "*Ultimate loads for eccentrically loaded model shallow strip footings on geotextile-reinforced sand*". Geotextiles and Geomembranes 27(3): 176-182.

[19] Cure, E., E. Turker, et al. (2014). "*Analytical and experimental study for ultimate loads of eccentrically loaded model strip footings near a sand slope*". Ocean Engineering 89: 113-118.

[20] Saran, S. and B. Reddy (1990). "*Bearing capacity of eccentrically loaded footings adjacent to cohesionless slopes*". Indian Geotechnical Journal 20(2): 119-142

[21] Jao, M., F. Ahmed, et al. (2008). "*Stability of eccentrically loaded footings on slopes*". Geomechanics and Geoengineering: An International Journal 3(2): 107-111.

[22] Sahu, R., Patra, C.R., Sethy, B.P. (2017). "*Experimental and numerical studies of eccentrically Loaded strip footing by using Plaxis"*. Indian geotechnical conference, GeoNst.

[23] Cure, E., E. Sadoglu, et al. (2014). "*Decrease trends of ultimate loads of eccentrically loaded model strip footings close to a slope*". Geomechanics and Engineering 6(5): 469-485.

[24] Ornek, M. (2014). "*Estimation of ultimate loads of eccentric-inclined loaded strip footings rested on sandy soils*". Neural Computing and Applications 25(1): 39-54.

[25] Turker, E., E. Sadoglu, et al. (2014). "*Bearing capacity of eccentrically loaded strip footings close to geotextile-reinforced sand slope*". Canadian Geotechnical Journal 51(8): 884-895.

[26] Sawwaf, M.A. (2007). "*Behavior of strip footing on geogrid-reinforced sand over a soft clay slope*". Geotext. Geomembrane 25:50-60.

[27] Selvadurai, A. and C. Gnanendran (1989). "*An experimental study of a footing located on a sloped fill: influence of a soil reinforcement layer*". Canadian Geotechnical Journal 26(3): 467-473.

[28] Lee, K. and V. Manjunath (2000). "*Experimental and numerical studies of geosynthetic-reinforced sand slopes loaded with a footing*". Canadian Geotechnical Journal 37(4): 828-842.

[29] Adams, M. T. and J. G. Collin (1997). "*Large model spread footing load tests on geosynthetic reinforced soil foundations*". Journal of Geotechnical and Geoenvironmental Engineering 123(1): 66-72.

[30] Trautmann, C. H. and F. H. Kulhawy (1988). "*Uplift load-displacement behavior of spread foundations*". Journal of geotechnical engineering 114(2): 168-184.

[31] Choudhary, A., J. Jha, et al. (2010). "*Laboratory investigation of bearing capacity behaviour of strip footing on reinforced flyash slope*". Geotextiles and Geomembranes 28(4): 393-402.

[32] Graham. J, Andrew. M, Shields. D.H. (1988). "*Stress characteristics for shallow footing in cohesionless slopes*". Canadian Geotechnical Journal. 25 238-249.

THERMAL CONDUCTIVITY BEHAVIOR OF TINCAL ADDED SAND-BENTONITE MIXTURES

Mesut Şahin Irgat*, *Dokuz Eylul University, Inst. of Natural and Appl. Sci., mesutsirgat@gmail.com*

Yeliz Yukselen Aksoy, *Dokuz Eylul University, Dept. of Civil Eng., yeliz.yukselen@deu.edu.tr*

ABSTRACT

In the last decade there has been a rapid increase in the number and type of energy structures due to increasing energy requirements. The energy geostructures are into direct contact with the soil, causing thermal changes in the soil. Recent studies have shown that thermal cycling and high temperature lead to changes in engineering properties such as hydraulic conductivity, volumetric change and shear strength. There is a need for thermally resistive and durable soil layers at the nuclear waste landfills and under energy structure foundation systems. In this study, boron additive namely; tincal was added to sand-bentonite mixtures in order to develop heat resistant soil material which can maintain the resistance against heat effects. The 10% and 20% bentonite was used in the sand-bentonite mixtures. The mixtures were compacted at maximum dry unit weight and optimum water content in the specificially manufactured wooden boxes. Boron mineral tincal added at the percentages of 5%, 10% and 15%, and thermal resistivity measurements were performed. When the results are examined, it has been found that the tincal mineral improve the thermal resistivity of the sand-bentonite mixtures.

Keywords: Boron minerals, Sand-Bentonite Mixtures, Thermal Conductivity, Tincal

1. INTRODUCTION

In the last two decades with increase in number and type of thermos-active geostructures due to increasing energy requirements. These structures are directly contact with the soil and causing thermal changes in the soil. Recent studies have shown that temperature variations lead to changes in engineering properties such as hydraulic conductivity, volumetric change and shear strength. The temperature increase may cause harmful effects under some circumstances. For example, the hydraulic conductivity increase in nuclear waste isolation landfills may cause irreversible environmental contamination. The volume changes and strength loss may cause structural deformations at energy structures.

A huge number of engineering projects are related to the heat transfer. Heat transfer take place through the soil mass. Some places such as high voltage buried power cables, oil and gas pipe line, energy piles, storage and utilization of geothermal energy, nuclear waste disposal facilities, ground improvement techniques by using heating and freezing and subway and tunnel fire prevention design which are influenced by heat transfer. Around the buried high voltage electric cables, the thermal conductivity of soil is important. In order to maintain heat flux around the cable the thermal conductivity of soil should be high. At nuclear waste repositiries the buffer should transmit the heat from canister surface to the other layers. According to direction of vector of heat transfer, angle of internal friction (Ø) and cohesion (c) of soils will change and ultimate bearing capacity and shear strength of soil also will change. Protection of soils from the heat flux is a very important process where the flux is exist.

Thermal conductivity (or resistivity) is one of the most difficult parameters to estimate. Because it can be influenced easily by degree of water content, mineral content, organic matter, shape of grain and porosity and grain size distribution. Many laboratory tests must be done to be able to understand effect of water content, grain size distribution, mass density on thermal resistivity in soil. The magnitude of the effect of thermal resistance on internal friction angle and cohesion is a important problem during geotechnical designing. In order to characterize soil thermal behavior the thermal conductivity or thermal resistivity values are used [1].

The boron minerals are used in order to increase the thermal resistivity of materials in industry. The challange of this study is boron mineral added sand-bentonite mixtures may show more resistance against high temperature. In this study, boron additives namely; tincal were added to sand-bentonite mixtures in order to develop heat resistant soil material which can maintain the resistance against heat effects.

In this study, the thermal condcutivity values of the 10% bentonite-sand and 20% bentonite-sand mixtures were determined in the presence of boron mineral; namely tincal. The relationship between the some soil properties and thermal conductivity values were also reported.

2. MATERIAL CHARACTERIZATION AND METHODS

2.1. Material Characterization

Sand, bentonite, tincal samples were used in all experiments. The bentonite samples were gathered from Eczacıbaşı Esan Company and it is Na-bentonite. Boron mineral was supplied from Eti Mining General Directorate of Turkey. The bentonite samples were oven dried (105°C), crushed and sieved through 0.425 mm. Grain size distribution, liquid limit, plastic limit and specific gravity values of soil samples determined in accordance with [2], [3] and [4] standards. Sand was sieved through No.6 sieve. Tincal sample was sieved through No.40 sieve. The physico-chemical properties of the sand, bentonite and tincal samples are given in Table 1 and Table 2, respectively.

Table 1. *The properties of sand and bentonite samples*

Property	**Sand**	**Bentonite**
Specific gravity	2.65	2.697
Liquid limit (%)	---	468
Plastic limit (%)	---	53.7
Clay(%)	12	60

Table 2. *Properties of the used boron minerals*

Property	**Tincal**
Specific gravity	1.73
Molecular weight (g/mol)	381.37
Heat capacity (J/g°C)	4.00
Thermal conductivity (W/mK)	0.704
Specific surface area (m^2/g)	13.55

2.2. Laboratory Tests

The sand-bentonite mixtures were prepared with the ratio of the amount of bentonite to the amount of sand-bentonite was 0.10 and 0.20. Tincal additive was added to the bentonite-sand mixture to be 5%, 10% and 15% respectively. As the thermal conductivity coefficient of the air is very low, the void ratio in a composite material directly changes the thermal conductivity. For this reason, the void ratio of all samples was tried to be kept the same. Throughout the experiments, the void ratio of the sand-bentonite mixture, 0.74, was used.

The optimum water content and maximum dry unit weight values were determined by the Standard Proctor tests. The specific gravity (G_s), optimum water content (ω_{opt}) and dry unit weight (γ_{dry}) of the samples were used in the calculations to maintain the same void ratio. As an example, the specific gravity and water content values were given in Table 3.

Table 3. *The maximum dry unit weight, optimum water content and specific gravity values of the 10B-90S and 20B-80S mixtures*

Sample	Tincal content (%)	Specific gravity (G_s)	Max. dry unit weight (γ_{drymax})	Water content (w) (%)
10B-90S	0	2.636	1.722	14.0
	5.0	2.683	1.542	16.2
	10.0	2.697	1.550	18.5
	15.0	2.727	1.567	19.0
20B-80S	0	2.579	1.722	14.0
	5.0	2.601	1.535	16.9
	10.0	2.685	1.545	18.5
	15.0	2.742	1.550	20.5

All samples were compacted in the wooden mold (12 cm x 12 cm x 4 cm) as shown in Figure 1.

Figure 1. *The compacted sample in the wooden mold*

The compaction process was carried out manually. By doing some trials, the number of hammer drops were determined. After that, all samples were compacted under same energy level. The mixtures were compacted at maximum dry unit weight and optimum water content in the specificially manufactured wooden box. Boron mineral tincal was added at the percentages of 5%, 10% and 15% and thermal resistivity measurements were done.

Thermal conductivity of each samples were measured by using hot-wire methods. All measurements were made by using shotherm QTM device (Figure 2). A total of five measurements were taken from each sample and average of these measurements were reported as thermal conductivity value. Figure 3 shows these five measurements positions on the sample.

Figure 2. *Shotherm QTM device*

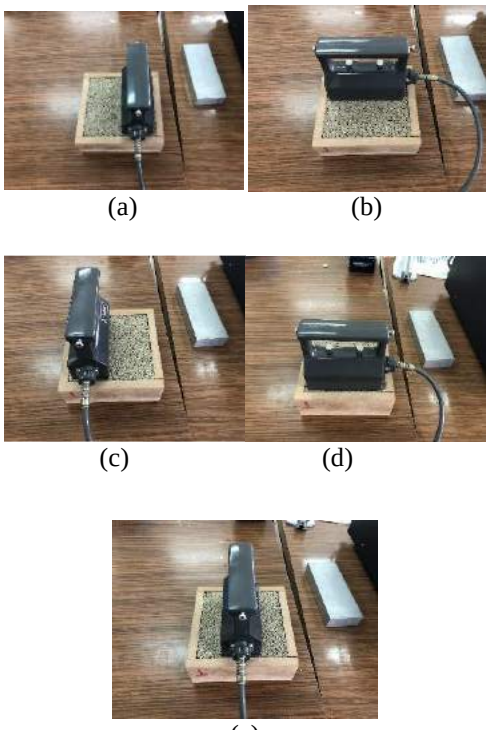

(a) (b)

(c) (d)

(e)

Figure 3. *The measurement positions on the sample*

3. RESULTS AND DISCUSSIONS

The termal conductivity of sand-bentonite mixtures were determined in the presence of boron minerals tincal. The thermal conductivity values of 10% bentonite-sand and 20% bentonite-sand mixtures are given in Table 4.

As seen from the results in Table 4, the reference value of the in the additive-free 10% bentonite was found to be 1.450 W/m-K, while it was 1.048 W/m-K in the 20% bentonite mixture. In other words, when considering the additive-free samples, the thermal conductivity value decreases with increasing bentonite percentage in sand–bentonite mixtures. Considering the effects of tincal additive on the thermal conductivity values of sand–bentonite mixtures, when 5%, 10% and 15% tincal additives were added into the 90S-10B mixture, the thermal conductivity values were 1.118, 1.240 and 1.417 W/m-K in the samples. When 5%, 10% and 15% tincal additives were added into the 80S-20B mixture, the thermal conductivity values were 0.844, 1.041 and 1.489 W/m-K in the samples.

Table 4. *Thermal conductivity of sand-bentonite mixtures in the presence of tincal*

Sample	Tincal (%)	Thermal Conductivity (W/m.K)
10% Bentonite	0	1.450
	5	1.118
	10	1.240
	15	1.417
20% Bentonite	0	1.048
	5	0.844
	10	1.041
	15	1.489

Measurement results indicate that the lowest thermal conductivity coefficient (0.844 W/m-K) was found in the 5T-76S-19B sample while the highest value (1.489 W/m-K) was measured in 15T-68S-17B sample. On the other hand, the thermal conductivity value increased proportionally when the amount of boron additive was increased from 5% to 15%. In the 20% bentonite group, the lowest value (0.844 W/m-K) was measured in the sample with 5% tincal. This result showed that the thermal conductivity coefficient could be decreased by 19.5% with the addition of 5% tincal in the sample group containing 20% bentonite.

Examining the effect of tincal in both main groups, the tincal additive decreased the thermal conductivity values in the 90S-10B mixtures, while it first decreased the thermal conductivity values in the 80S-20B mixtures, but a thermal conductivity value higher than that of the additive-free sample was obtained with the addition of 15% tincal. The increase in thermal conductivity is about the fine content increment in the mixture. It should be noted that the optimum boron mineral content is 5%. The Figure 5 shows the relationship between the moisture content and thermal conductivity of the samples.

As water content increases, the air in the voids replaces with water. It is known that the thermal resistivity of air (about 4000 K·cm/W) is higher than that of water (about 165 K·cm/W). When more water is added to the soils, there is a thin water film formed around the particles which allows the transfer of heat more easily. According the results of this study, as water content increases, the thermal conductivity of the samples increases. The Figure 6 shows the relationship between the dry unit weight and thermal conductivity of the samples. The results have shown that as dry unit weight increases the thermal conductivity value increases almost linearly. As dry unit weight increases, the contacts between the samples increase [5]. Therefore, the thermal conductivity increases as well.

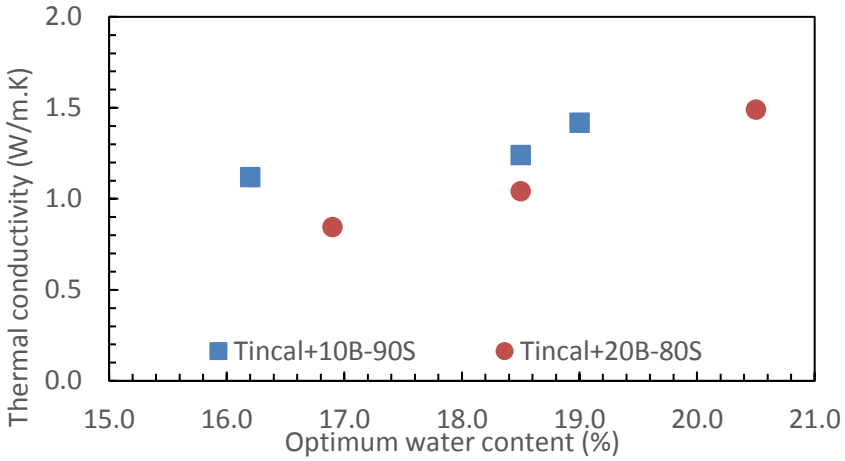

Figure 5. *The relationship between the moisture content and thermal conductivity*

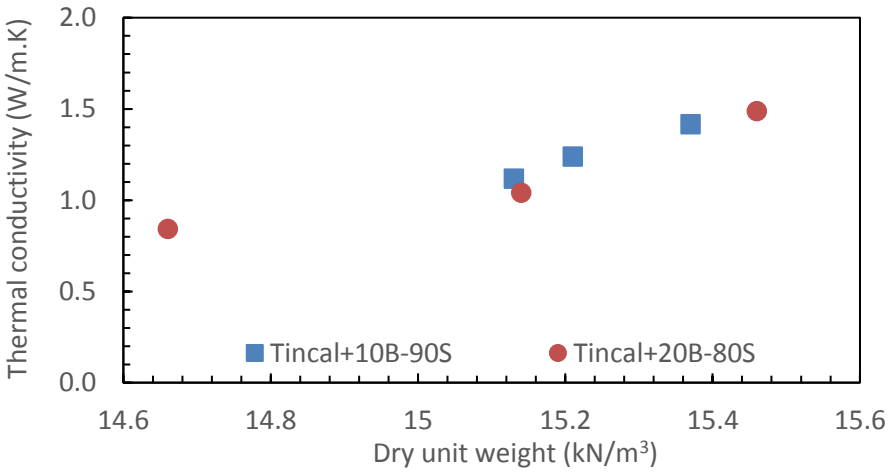

Figure 6. *The relationship between the unit weight and thermal conductivity*

4. CONCLUSIONS

The thermal conductivity values of the 10% bentonite-sand and 20% bentonite-sand samples were determined in the presence of tincal. Generally, the thermal conductivity values of the 10% and 20% bentonite-sand mixture decreased in the presence of tincal. The results have shown that as dry unit weight increases the thermal conductivity value increases. In some projects, the thermal conductivity of the soil is high and in some projects it is desired to be low. It can be concluded that according to the desired value tincal addivite can be used as a temperature resistance increasing admixture.

ACKNOWLEDGMENTS

This study is supported by The Scientific and Technological Research Council of Turkey (TÜBİTAK) (Grant no. 217M553). The authors are grateful for this support. The authors would like to thank Ezcacıbaşı Esan Mining Company and Eti Mining General Directorate for supplying samples which are used in this study.

REFERENCES

[1] Wang, M., Chen, Y-F., Zhou, S., Hu, R., Zhou, C-B., 2015. *"A homogenization-based model for the effective thermal conductivity of bentonite-sand-based buffer material"*, International Communications in Heat and Mass Transfer, 68: 43-49.
[2] ASTM D 422, 1999a. *"Standard test method for particle-size analysis of soils*", ASTM International, USA.
[3] ASTM D 4318, 1999b. *"Standard test method for liquid limit, plastic limit, and plasticity index of soils*", ASTM International, USA.
[4] ASTM D 854, 1999c. *"Standard test method for specific gravity of soils",* ASTM International, USA.
[5] Cai, G., Zhang, T., Puppala, A.J., Liu, S., 2015. "*Thermal Characterization and prediction model of typical soils in Nanjing area of China*", Engineering Geology**,** 191: 25-30.

BEHAVIOR OF ROCKS UNDER THERMAL EFFECT – A REVIEW

M. Sobhey [1*], *A. Lecturer in Structural Engineering Department, Tanta University, Tanta, Egypt*
E-mail: m.sobhey@f-eng.tanta.edu.eg
M. El Sawwaf [2], *Professor in Structural Engineering Department, Tanta University, Tanta, Egypt*
E-mail: mos_sawaf@hotmail.com
M. Shahien[3] *Professor in Structural Engineering Department, Tanta University, Tanta, Egypt*
E-mail: marawan.shahin@f-eng.tanta.edu.eg
A. Farouk [4] *A. Professor in Structural Engineering Department, Tanta University, Tanta, Egypt*
E-mail: drafarouk@f-eng.tanta.edu.eg

ABSTRACT

The effect of under/after high temperature conditions on the thermo-mechanical behaviour of different rocks is extremely important issue for several engineering applications. Changes in the properties of rock after undergoing high temperature may affect stability and even induce engineering disasters. In General, the scope of high temperature ranges from normal temperatures (10-50 ^{0}C) to high temperatures (1000-1500 ^{0}C). Temperature is one of the key factors that influence the microstructure, the physical and mechanical properties for variety of rocks as Granite, Sandstone, Limestone, Mudstone, Marble and Diorite. A review study for vast majority of previous experimental investigations was carried out for some mechanical, physical and thermal properties of rocks, including deformation modulus, Poisson's ratio, tensile strength and compressive strength all vary considerably with increasing temperatures. Therefore, the results of experimental studies indicated that, behavior of rocks that exposed to high temperatures is different from those under normal temperature conditions. It has been known that rock strength and deformation modulus generally declined with the elevated temperature, especially beyond a certain temperature. Moreover, new correlations for the uniaxial compressive strength (UCS) with Tensile strength (TS) and for Young's modulus (Es) with uniaxial compressive strength (UCS) due to the elevated temperatures for different types of rocks were presented.

Keywords: Experimental Investigations, Thermal Effect, Behavior of Rocks.

1. INTRODUCTION

The impact of thermal effect on rocks is a topic of growing importance in geotechnical engineering because of its relevance to several engineering applications such as hot dry rock (HDR), deep geological disposal of nuclear waste, (Granitic rocks such as granite and diorite are a widely acceptable site for nuclear waste disposal and are also main rock types of HDR reservoir) (at temperatures which generally vary from 100 to 300 ◦C and will rise over the storage interval), geothermal energy resource extraction, solar heating of rock monuments and buildings, Fires in tunnels, mines and buildings and underground coal gasification (UCG). (Sellin and Leupin 2013; Verma et al. 2015), (Brown et al. 2012; Gelet et al. 2012), (Burton et al. 2006; Otto and Kempka 2015). The process of underground coal gasification (UCG) is based on in situ, sub-stoichiometric coal combustion for production of a high-calorific synthesis gas, which can be applied for electricity generation. Fig. 1 presents a schematic view of the in-situ coal gasification principle.

However, UCG can induce impacts such as high thermal effects on the surrounding rocks of the coal layer. Temperatures above 1,000 °C can be achieved in the UCG reactor and its close vicinity (Otto and Kempka 2015). The impact of high temperature on the physical and mechanical properties of rocks has been largely investigated using laboratory studies since the 1970s over the last several decades. (Francois, 1980; Bauer et al., 1981; Paquet et al., 1981; Heuze, 1983; Hirth and Tullis, 1989). Exploration of geothermal activities has posed new challenges for geotechnical engineers to counter rock engineering problems at high temperatures. Laboratory testing is an important aspect of rock mechanics, which provides essential input data for the design of engineering structures in the Earth's crust and mantle subjected to tectonic forces. Heuze, 1983; Wang et al., 2002; Dwivedi et al., 2008; Xu et al., 2008).

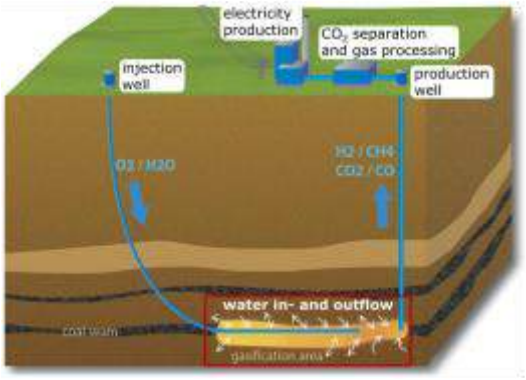

Fig. 1. *Principle of in situ coal gasification method (Otto and Kempka 2015)*

In the case of a high-temperature impact on rock, an additional factor which influences its strength is the thermal expansion of minerals included in the composition of the rock. The temperature induces micro cracks due to the different natures of the constituent minerals (intergranular). These cracks are due to the different expansion coefficients of the component minerals as shown in Table. 1, causing a differential expansion, generating internal stresses resulting in the creation of cracks in the transition phase between components. When temperature changes occur in a very short time, intergranular cracks occur by another different process than the previous ones: high temperature gradients in the material. These temperature gradients act by amplifying the differential dilation effects by different coefficients of expansion, which causes volumetric increase, and thermal crack opening. (Jansen et al., 1993). Moreover, chemical changes take place, the result of which is polymorphic transformation, melting and the disappearance of certain minerals in rocks (Dengina, Kazak, Pristash 1993; Pinińska 2007; Małkowski, Skrzypkowski, Wu et al. 2013).

Table. 1: *Linear thermal expansion coefficients for rock minerals (Siegesmund et al. 2011)*

Mineral	Linear thermal expansion coefficient		Temp. range [°C]
	Parallel to c-axis [K^{-1}]	Perpendicular to c-axis [K^{-1}]	
Calcite	25.1×10^{-6}	-5.6×10^{-6}	0-85
Dolomite	25.8×10^{-6}	6.2×10^{-6}	24-700
Quartz	7.7×10^{-6}	13.3×10^{-6}	0-80
Albite	10.5×10^{-6}	5.6×10^{-6}	25-970
Gypsum	54×10^{-6}	$7\text{-}117 \times 10^{-6}$	25-42
Micas	8.7×10^{-6}	17.8×10^{-6}	unknown
Clay	6×10^{-6}	15×10^{-6}	25-350

Based on the characteristics of the axial stress‑axial strain and axial stress‑lateral strain curves of uniaxial compression tests, Hoek and Bieniawski (1965) found that the crack propagation process of brittle materials consists of three main stages: (1) crack of pre-existing micro-cracks closure followed by an elastic region; (2) crack initiation followed by a stable crack propagation region; (3) crack damage followed by unstable crack propagation until ultimate failure. Brittle to plastic transition in response to increasing temperature has been studied for different types of rocks.

Tullis and Yund (1987) studied the Brittle to plastic transition in response to increasing temperature for different types of rocks. Xu et al. (2008) had used different temperatures ranging from room temperature to 1200 ◦C for different granite samples. The results showed that the phase-changing behaviour of brittle–plastic transition appears around 800 ◦C and the mechanical properties of samples did not significantly vary before that.

Moreover, a mix trend of the maximum unconfined compressive strength of the granite rocks with the elevated temperature was appeared until it reaches 8000C; the trend significantly decreases after that. The normalized elastic modulus decreases with the elevated temperature as shown in Fig. 2.

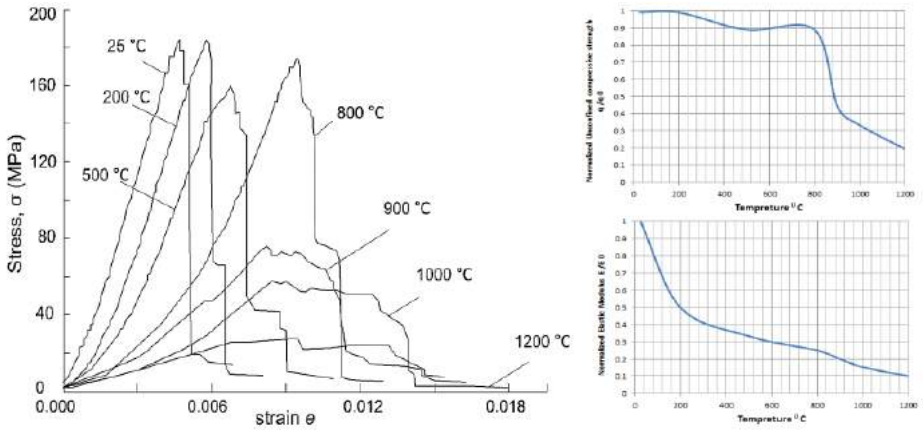

Fig. 2. *Stress‑strain curves of rock after high temperature (Data from Xu et al., 2008).*

The experimental procedures of ‘‘after/under high-temperature treatment’’ in the reviewed references are basically identical, taking into account heating the samples at a certain rate to prevent occurring heat shock in the rock samples under atmospheric pressure in a furnace until a predetermined temperature is reached. Then, the temperature is maintained for a given period (several hours), followed by cooling down the samples in the furnace chamber or under normal ambient conditions (room temperature cooling). Varieties of Lab. Tests were conducted on rock samples either under or after high-temperature treatment. The detailed testing parameters for each reference reviewed are summarized in Table 2.

2. VARIATIONS OF MECHANICAL PROPERTIES

Normalized values of bulk density, elastic modulus, passion ratio, compressive strengths and tensile strengths for different rocks at various temperatures were collected from literature.

2.1. Bulk Density (Υ_b)

Unit weight of rocks declines with raising the thermal effects on rock samples from the room temperature to the high temperature due to volumetric expansion of the constitution minerals and mass loss of rock sample (Otto and Kempka 2015).

Fig. 3 shows the variation of normalized bulk density versus temperature up to 1000 °C for different sandstone samples, the decrease of sandstone samples density is slightly little compared with initial room temperature. Only above 1000 °C a significant decrease is noticed.

Table. 2: *Testing parameters of thermal effects*

References	Testing type[a]	Heating rate (°C/min)	Constant temp. period (h)	Cooling down ways	Sample size[b] D × H	Sample shape
Araújo et al. (1997)	Under	1.5	–	–	50 × 100	Cylinder
Chen et al. (2013)	After	10	2	F	50 × 100	Cylinder
de Pater and Wolf (1992)	Under	u	u	–	40 × 80	Cylinder
Hajpál and Török (1998)	After	c	6	F	40 × 80	Cylinder
Lan (2009)	After	5	1	F	36 × 80	Cylinder
Meng et al. (2006)	Under	u	–	–	25 × 50	Cylinder
Qin et al. (2009)	After	5–10	1	F	50 × 50	Cube
Rao et al. (2007)	Under	30	2	–	50 × 50	Cube
Su et al. (2008)	After	10	4	F	50 × 100	Cylinder
Wu (2007)	After	30	5	F	50 × 40	Cylinder
Wu et al. (2005)	Under	u	0.5	–	50 × 100	Cylinder
Wu et al. (2005)	After	u	1	F	50 × 100	Cylinder
Wu et al. (2007)	After	5	2	F	50 × 100	Cylinder
Yin et al. (2009)	After	20	5	F	50 × 100	Cylinder
Yin et al. (2012)	After	10/3	4	F	50 × 100	Cylinder
Zhan and Cai (2007)	Under	u	6	–	50 × 50	Cylinder
Zhang et al. (2010)	Under	120	2	–	20 × 45	Cylinder
Zhao et al. 2010	After	30	5	F	50 × 100	Cylinder

Samples were cooled down in the furnace chamber ‘F’, or under normal ambient conditions ‘A’ the unit is mm, D is short for diameter and H for height

2.2. Uniaxial Compressive Strength (UCS)

UCS is one of the most important parameters reflecting the basic mechanical properties of rocks. It is extremely essential in the fields such as rock mass classification and development of rock and rock mass failure criteria (Jaeger et al. 2007).

The trend of UCS change is complex due to the variety of minerals compassion in different rock samples at elevated temperatures, although it is more likely to decrease with increasing temperature in almost cases.

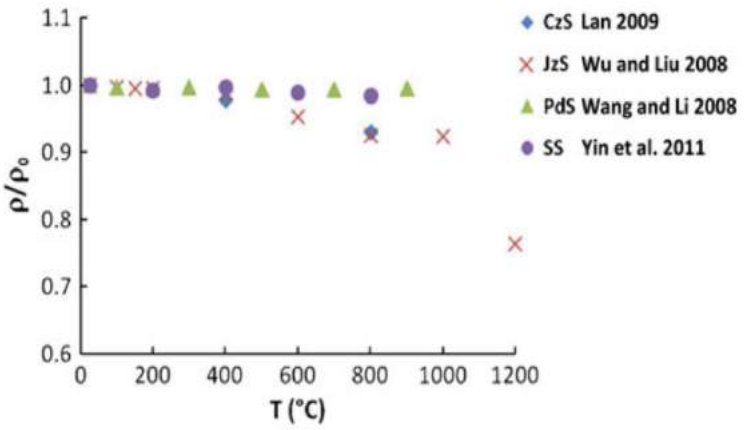

Fig. 3: *Variation of normalized bulk density versus temperature for different sandstone samples (Tian et al., 2012)*

Numerous experiments in literature have shown that apart from the temperature, acting pressure is also significant in the change of rock strength parameters. Ferrero and Marini (2001) tested 15 samples of two types of marble which were previously heated to temperatures up to 600 °C and later cooled applying a very low gradient of temperature.

Koca et al. (2006) studied nine samples of intact marble, under different temperatures observing important descents of the rock strength. These authors also tested five rock samples obtained from building elements previously exposed to fire (subjected to an estimated temperature of 500 °C) using temperatures from room temperature to 300 °C which caused a very high elastic modulus decrease beyond 200 °C. A noteworthy aspect in the work from Koca et al. (2006) is that the uniaxial compressive strength of the material exposed to 500 °C and then cooled to room temperature exhibits very similar uniaxial compressive strength values than the intact material tested at 500 °C.

Rao et al. (2007) tested eight sandstone samples and observed a strong initial increase of resistance to 250 °C, and then a decline to 300°C, however at this temperature, resistance is 138% higher than the initial. Ranjith et al. (2012) tested sandstones until 950 °C obtaining different results than in other works, highlighting the significant increase in strength with temperature, reaching 180% of the initial strength at 600 °C, then lowering until the maximum test temperature is reached, remaining above the initial strength.

Sygała et al. (2013) introduce the changes in the values of uniaxial compression of several types of rocks, subjected to high temperatures. Liu and Xu (2014) discovered the threshold temperature is 400 °C. They found granite UCS changes slightly from room temperature to 400 °C, but dramatically decreases with temperature from 400 °C onward, by means of testing on granite sample after high-temperature treatment.

Shao et al., (2015) studied the Fracturing behaviour of Australian Strathbogie granite test specimens such as the crack propagation at high temperatures up to 800 using electron microscopy scanning (SEM) and unconfined strength test. Specimens were heated at a rate of 5 °C /min with a 1 h holding period before testing. The results of stress–strain and SEM reveal that the failure modes of Strathbogie granite specimens changed from brittle fracturing to quasi-brittle shear fracturing and eventually to ductile failure with increasing temperature.

Fig. 4 graphically summarizes the all previously described results. The results show that a mixed trend in the values of the normalized UCS q / qo, where qo is the value of the UCS at the room temperature= 25 °C in all cases with the elevated temperature generally occurs until reaches to 800 °C, after that steeply decreases.

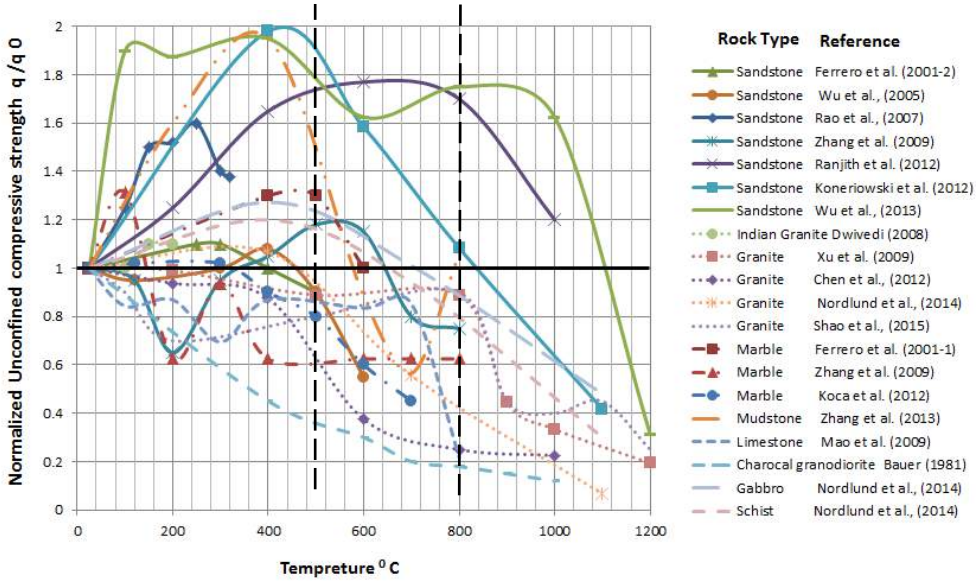

Fig. 4: *Variation of normalized UCS for different types of rocks versus temperature Data from (Brotóns et al., 2013) and (Sygała et al. 2013)*

2.3. Young's Modulus and Poisson's Ratio (E_s and ν)

Elastic properties of isotropic rocks are determined by Young's modulus and Poisson's ratio. This is the factor of proportionality between stress and the corresponding elastic strain. Similarly, as strength, elasticity of rocks depends mainly on the elasticity of composing minerals, the density, porosity and other factors.

Young's modulus is determined for the entire height of the sample or at a center section as the tangent of the angle of inclination to the x-axis of the straight line approximating the post-failure curve in the ascending part of the stress-strain characteristics of compressed rock sample or as a tangent of secant inclination (Bukowska 2012). Changes of the value of Young's modulus of selected rock subjected to heating at various temperatures. In the case of granites studied by Chen et al. (2012), to a temperature of 400°C, Young's modulus is generally not changed significantly.

For samples heated at higher temperatures there was a sharp decline in the value of Young's modulus, reaching a temperature of 1000°C, only 10% of the value obtained at room temperature. Some rocks exhibit a clear decrease in elastic modulus at elevated temperatures, while some rocks firstly experience a slight increase within a certain temperature range (from 25 to 200 °C). But for all rocks, elastic modulus will finally decrease to a much lower level after critical temperatures equals to (600 °C).

Fig. 5 graphically summarizes the all previously described results. (Yang et al. 2017) presented the variation of Poisson's ratio versus temperatures for different granite samples. Poisson's ratio reduces slightly with raising the temperature between 50 °C and 400 °C. He mentioned also that this trend is not yet profound due to limited available experimental data beyond 600 °C and might be different for the variety types of rock.

Brotons et al. (2013) introduce Poisson's ratio values for calcarenite stone samples before and after the specimen heating obtained by ultrasonic propagation velocity tests. This parameter decreases inversely proportional to the temperature. Fig. 6 graphically summarizes the all previously described results.

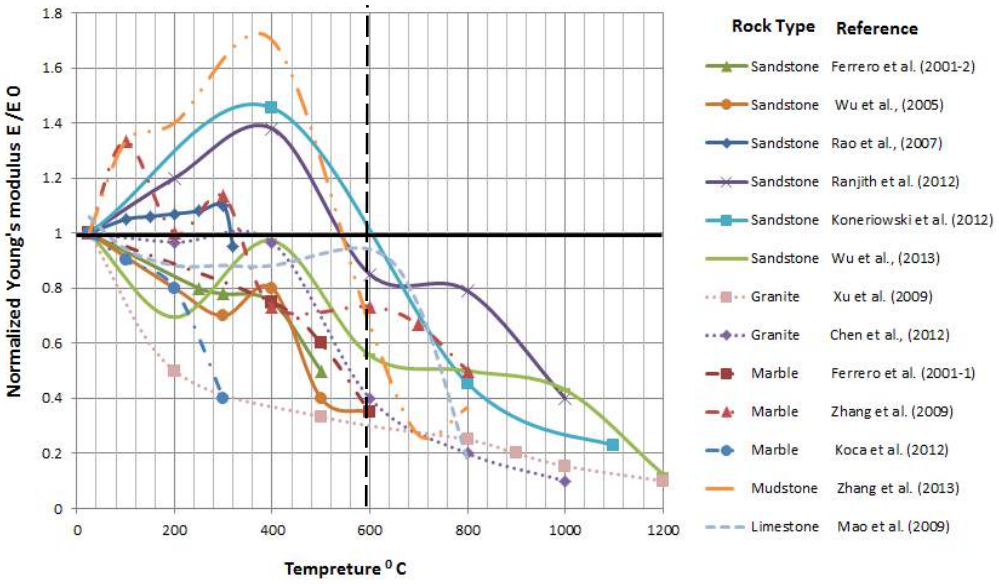

Fig. 5: *Variation of normalized Young's modulus for different types of rocks versus temperature Data from (Brotóns et al., 2013) and (Sygała et al. 2013)*

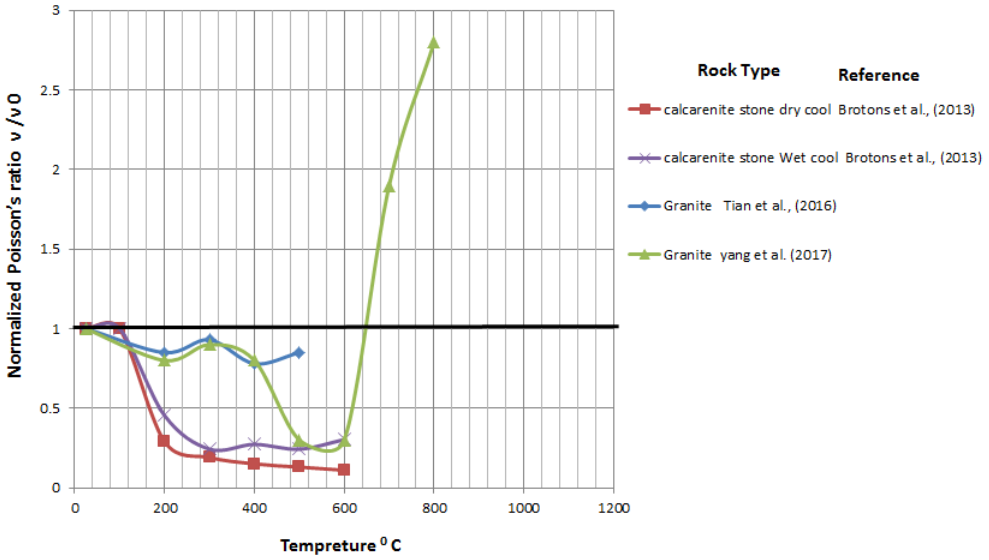

Fig. 6: *Variation of normalized Poisson's ratio for different types of rocks versus temperature Data from (Brotóns et al., 2013) and (Yang et al. 2017)*

2.4. Tensile Strength (TS)

Almost different types of rocks, tensile strength parameter (TS) declines with increasing the temperature, especially after 400°C where the decreasing rate will become much higher. (Dwivedi et al., 2008) presented Variation of normalized tensile strength of granite samples versus different temperature up to 1200 °C.

(Roy and Singh, 2016) showed that the decrease of tensile strength of granite is negligible below 250 °C. (Liu et al., 2016) study falls in the context of underground coal fires (UCF). The objective of the research is to experimentally characterize the change in mechanical behavior using tensile strength test of two Australian mudstone rocks when subjected to temperatures up to 1200 °C for 24 hours.

Results show that, when the heating temperature increases, the normalized tensile strength significantly decreases. (Tian et al., 2015) presented the values of normalized tensile strengths for different sandstones samples. Similar to the relations of normalized tensile strengths with temperature, the values of normalized tensile strengths can also be increasing, decreasing or remain constant with temperature up to a certain temperature which may be about 500 °C for most sandstone samples.

Fig. 7 graphically summarizes the all previously described results. It is generally accepted that elastic modulus and strength of rocks decrease with increasing temperature. Experimental results in the literature have indicated that the nature of changes of the strength properties with increasing temperature is not consistent for all the rocks. Below 500–800 °C, the trend of strength with temperature can be increasing, decreasing or unchanged.

Above that, a decreasing trend is always observed due to the variety of minerals compassion, initial micro-cracks for different rocks and experimental conditions Tian et al. (2015). Rao et al. (2007) reported that increase in the strength and mechanical properties of rocks from 20°C to 400°C due to the free moisture content in rock and the applied heat reduced the moisture content, thereby making the rocks to be stronger.

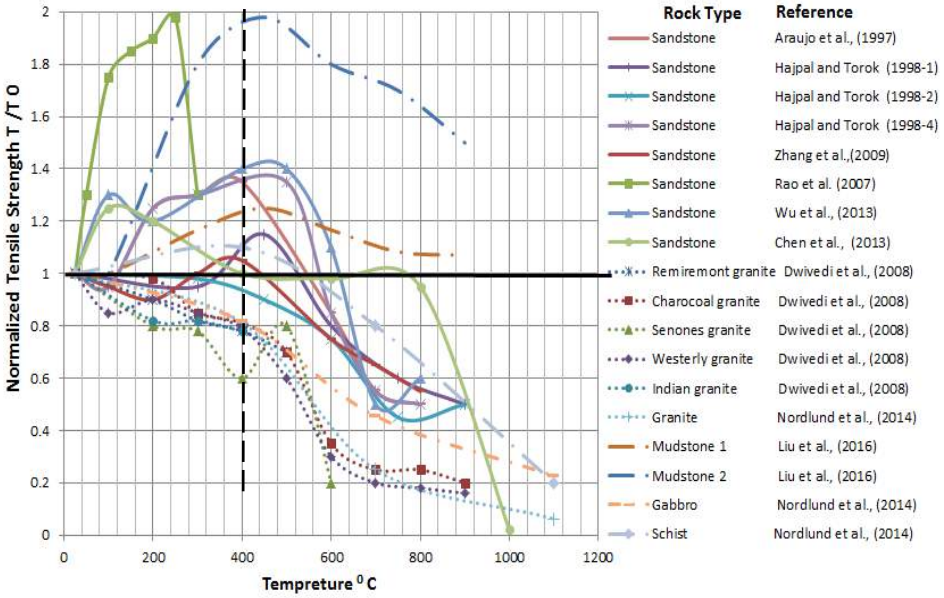

Fig. 7: *Variation of normalized tensile strength of rock samples versus different temperature Data from (Tian et al., 2015), (Dwivedi et al., 2008) and (Liu et al., 2016)*

3.1. Relation between the Uniaxial Compressive Strength (UCS) and Tensile Strength (TS) with the Elevated Temperatures for Rocks

To develop a new correlation between UCS and TS with the elevated temperatures for different types of rocks, comparisons of vast majority of previous experimental investigations were reviewed.

Fig. 8 shows the ratio between the uniaxial compressive strength (UCS) and Tensile strength (TS) for rocks versus different temperature Data from (Tian et al., 2015), (Dwivedi et al., 2008) and (Liu et al., 2016).

The results show that at the room temperature the ranged of the correlation between the uniaxial compressive strength (UCS) and Tensile strength (TS) was between (7 to 15) % for different rocks.

This coloration sharply decreases with the elevated temperature, until the temperature reach 1000 °C the correlation finds to be from 9 to 2%.

3.2. Relation between the Young's Modulus (E_s) and Uniaxial Compressive Strength (UCS) with the Elevated Temperatures for Rocks

The uniaxial compressive strength and static Young's modulus E_s of intact rocks are the most important geotechnical parameters for stability analysis of surface and underground structures. These parameters are obtained by the uniaxial compressive test.

Fig. 9 shows the ratio between the Young's modulus (Es) and uniaxial compressive strength for rocks versus different temperature Data from (Tian et al., 2015), (Dwivedi et al., 2008) and (Liu et al., 2016).

The results show that at the room temperature the ranged of the correlation between the Young's modulus (E_s) and uniaxial compressive strength was between (15 to 35) % for different rocks. This coloration sharply decreases with the elevated temperature, until the temperature reach 1100 °C the correlation finds to be from 13 to 5%.

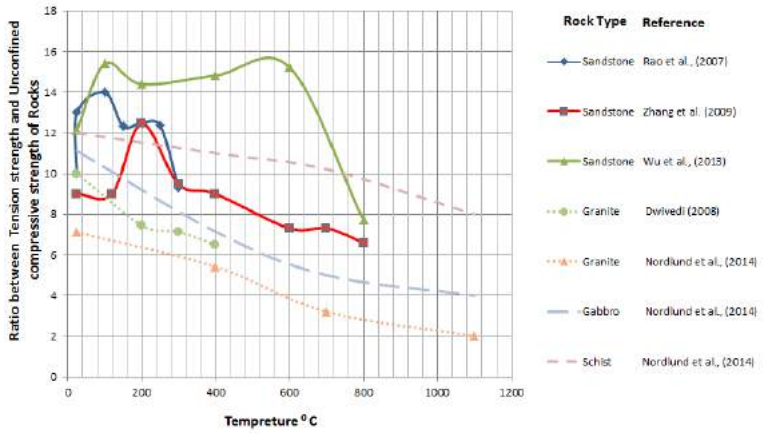

Fig. 8: *Ratio between the (UCS) and (TS) for rocks versus different temperature Data from (Tian et al., 2015), (Dwivedi et al., 2008) and (Liu et al., 2016)*

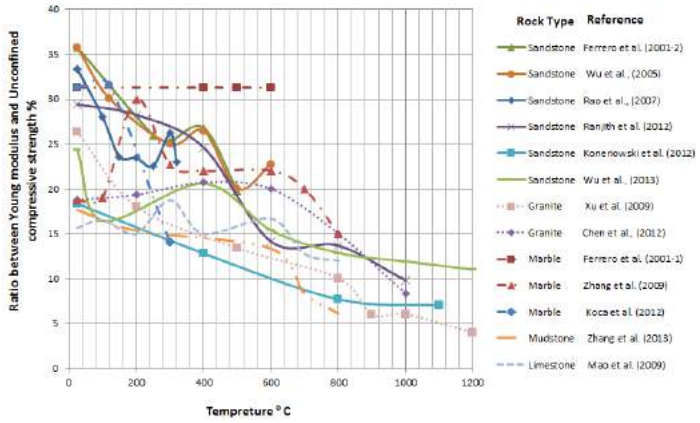

Fig. 9: *Ratio between the (Es) and (UCS) for rocks versus different temperature Data from (Tian et al., 2015), (Dwivedi et al., 2008) and (Liu et al., 2016)*

4. CONCLUSION

The presented reviewed data are expected to support analytical calculations and numerical simulations of thermo-mechanical processes for different rocks. Based on the extensive review on mechanical rock properties during and after high-temperature treatment, the following conclusions are drawn:

- The decrease of rocks samples density is slightly little compared with initial room temperature. Only above 1000 °C a significant decrease is noticed.
- The trend of UCS change is complex at the elevated temperatures, although it is more likely to decrease with increasing temperature after (500 °C to 800°C) in almost cases.
- A mixed trend for normalized elastic modulus and normalized tensile strength were obtained up to about 500 °C. Beyond the temperature, normalized elastic modulus and normalized tensile strength decrease with increasing temperature up to 1000 °C.
- Poisson's ratio reduces slightly with raising the temperature between 50 °C and 400
- The coloration between the uniaxial compressive strength (UCS) and Tensile strength (TS) sharply decreases with the elevated temperature, until the temperature reach 1000 °C the correlation finds to be from 9 to 2%.
- The coloration between the Young's modulus (Es) and uniaxial compressive strength was decreases with the elevated temperature, until the temperature reach 1100 °C the correlation finds to be from 13 to 5%.

ACKNOWLEDGEMENT

This study was supported by Geotechnical lab. in Tanta University and this support was gratefully acknowledged.

REFERENCES

[1] Sanchez, M., Gens, A., Guimaraes, L., 2012. *"Thermal-Hydraulic Mechanical (THM) Behaviour of A Large-Scale In-Situ Heating Experiment During Cooling and Dismantling"*, Canadian Geotechnical Journal, 49(10):1169–1195.
[2] Ringwood, A.E., 1985. *"Disposal of High-Level Nuclear Wastes—A Geological Perspective"*, Mineralogical Magazine, 49(351):159–175.
[3] Hokmark, H., Claesson, J., 2005. *"Use of An Analytical Solution for Calculating Temperatures in Repository Host Rock"*, Engineering Geology, 81:353–364.
[4] Gibb, F.G.F., Travis, K.P., McTaggart, N.A., Burley, D., 2008. *"A Model for Heat Flow in Deep Borehole Disposals of High-Level Nuclear Waste"*, Journal of Geophysical Research, 113:BO5201. doi:10.1029/2007JB005081.
[5] Zhao, Y.S., 2000. *"Rock Mechanics Problems in Geothermal Exploitation of Hot Dry Rocks"*, In: Proceedings of the 6th academy conference of Chinese rock mechanics and engineering, Wuhan, pp 361–364.
[6] Gelet, R., Loret, B., Khalili, N., 2012. *"A Thermo-Hydro-Mechanical Coupled Model in Local Thermal Non-Equilibrium for Fractured HDR Reservoir with Double Porosity"*, Journal of Geophysical Research, 117:B07205. doi:10.1029/2012JB009161.
[7] Cherubini, Y., Cacace, M., Scheck-Wenderoth, M., Moeck, L., Lewerenz, B., 2013. *"Controls on The Deep Thermal Field: Implications From 3-D Numerical Simulations for The Geothermal Research Site Gro Schonebeck"*, Environmental Earth Sciences, 70(8):3619–3642.
[8] Burton, E., Friedmann, J., Upadhye, R., 2007. *"Best Practices in Underground Coal Gasification"*, Lawrence Livermore National Laboratory, USA.
[9] Younger, P.L., 2011. *"Hydrogeological and Geomechanical Aspects of Underground Coal Gasification and Direct Coupling to Carbon Capture and Storage"*. Mine Water and the Environment, 30(2):127–140.

NUMERICAL STUDY ON REDUCING THE GROUND BORNE VIBRATIONS USING OPEN TRENCH AND RUBBER-CHIPS FILLED TRENCH WAVE BARRIERS

Mohammad Mouaz Hassoun, *Muğla Sıtkı Koçman University, mouazhassoun93@gmail.com*

Deniz ÜLGEN, *Muğla Sıtkı Koçman University, denizulgen@gmail.com*

Onur Toygar, *Muğla Sıtkı Koçman University, onurtoygar@mu.edu.tr*

Selda Durmaz, *Muğla Sıtkı Koçman University, seldadurmaz@mu.edu.tr*

ABSTRACT

Ground borne vibrations generated by construction works, vehicle traffic and machines have begun to create problem to dwellers and environment with rapid urbanization. Isolation of the source or wave barriers is commonly preferred by engineers to reduce the effect of those vibrations. In the present study, isolation performance of open and rubber chip filled trench are investigated by numerical modeling.

The vibration isolation performance of trench type wave barriers is assessed based on those measurements. As a result of the assessment, it is determined that the trench depth and vibration source working frequency are the main parameters affecting the efficiency of wave barrier. Besides, numerical analyses show that the isolation performance decreases as away from the trench. Moreover, even though open trench is more effective on reducing ground borne vibrations, as the normalized trench depth increases isolation performance of rubber chip filled trench barrier approaches the performance of open trench barrier.

Realistic scale study is modeled and validated by using finite element method for making a parametric study. Numerical analyses are applied for different source working frequencies to clarify the effect of normalized trench depth on isolation efficiency of trench type wave barriers.

Keywords: Vibration Isolation, Wave Barrier, Wave Propagation, Rubber Chips. Attenuation.

1. INTRODUCTION

The concept of isolation is obstructing these propagated waves within the soil medium before they reach isolated region. Obstruction in a soil medium can be achieved through creating a discontinuity in the wave path using a wave barrier; where the wave loses the accessibility to isolated region. Filled-in wave barriers and open trenches are the direct application of screening vibrations in soil mediums. This study concentrates on studying the screening efficiency of open and rubber chip-filled trenches numerically.

In this study, a series of numerical analyses for the vibration-to-trench system have been performed using Quake/W software. The analyses are done considering open trenches and filled-in rubber chips wave barriers. The main goal of performing those analyses was to make an initial evaluation for the benefit of conducting such experiments using a rarely-used material in field which are rubber chips.

2. NUMERICAL ANALYSES

In favour of verifying and validating the numerical analysis of results, series of analyses have been performed regarding the case of open trench for a frequency range of 10-100 Hz. The obtained results were compared with results of other experimental studies including the Toygar [6]. Procedure of modelling started with defining two systems of definition; first system simulates the static case of the profile, which means before starting motion. The second defining system expresses the dynamic case after starting the vibration motion. Thereafter, the analysis started for each frequency separately; starting by 10 Hz and ending with 100 Hz. The analyses are performed for the case of no trench and open trench. The numerical model is given in Figure 1.

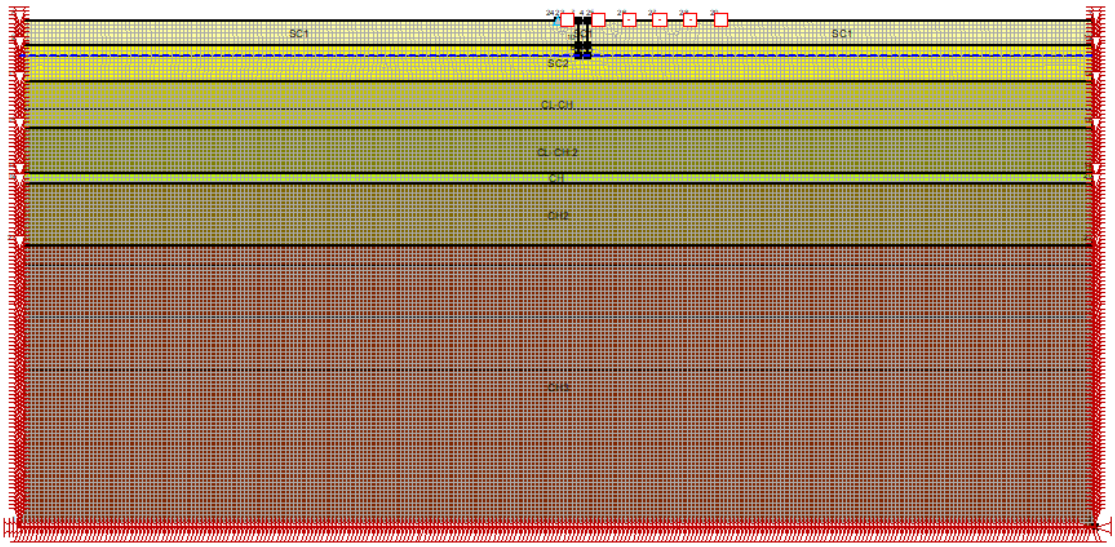

***Figure 1**. QUAKE/W 2D Numerical model*

Figure 2 shows the variation of amplitude reduction ratio with normalized depth for open trench isolation. Amplitude reduction ratio is defined as the ratio of amplitudes before and after isolation and normalized depth is the ratio of trench depth to Rayleigh wave length. Obtained results of the open trench numerical analyses were found consistent with the experimental studies of Wood [4], Alzawi & El nagger [3], Haupt [1], and Toygar [6]. Herein, further numerical modelling and analyses regarding a rubber chip-filled trench have been performed.

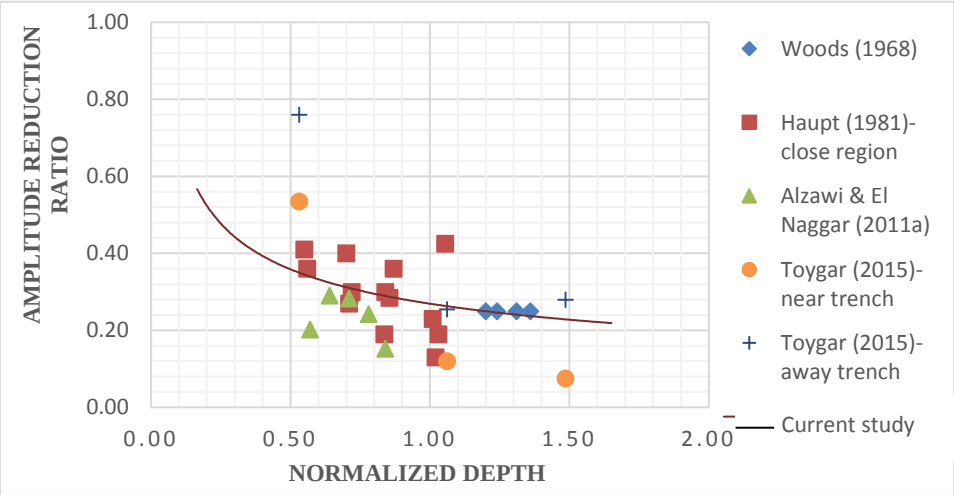

***Figure 2**. Comparison of Numerical analysis with some experimental studies.*

3. RESULTS

The numerical analysis regarding the rubber chips-filled trench has been performed after validating the model for the open trench case. Results obtained for the rubber chip-filled trench case were drawn in a graph to evaluate their efficiency (Figure 3).

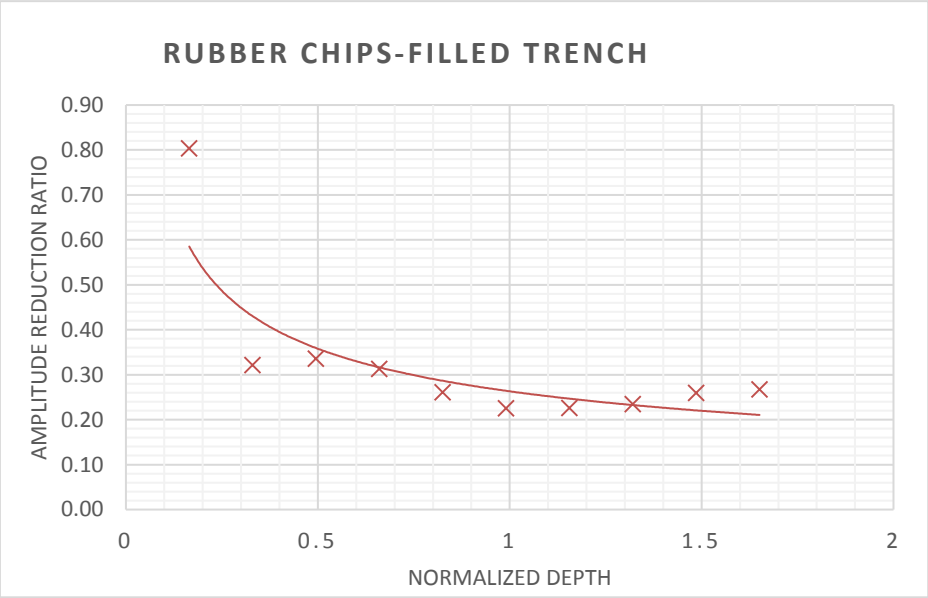

***Figure 2**. Efficiency chart of the rubber chips-filled trench Numerical analysis.*

Based on obtained amplitude reduction ratios variations with respect to normalized depth of trench, it is found that both open trench and rubber chip-filled trench provide good levels of vibration isolation majorly. Furhtermore, vibration isolation efficiencies of open trench and rubber chip-filled trench vary with respect to excitation frequency and distance.

Results also show that for a normalized depth of D = 1 (see Figure 3), a kind of isolation optimization occurs; where the amplitude reduction ratio reaches its minimum limits. This expresses a high isolation level exceeds 75%. Herein, an initial recommendation value for preliminary design of rubber chips-filled trench is suggested to be D = 1.

4. CONCLUSION

The main purpose of the current study is to investigate –numerically- the efficiency of rubber chips (shredded tyres) as vibration isolation fill-in material for wave barriers. Besides, the study targeted evaluating the vibrational screening efficiency of open trench wave barriers.

In the analysis, vibrations have been generated at different levels of intensity in order to generate multi frequencies 10 Hz - 100 Hz. This range is repeatedly produced by highway traffic, railways, and construction activities (piling, excavating, etc.).

The major findings of the analyses were as follows:

-The amplitude reduction ratios obtained from the case of open trench have had a good consistency with the published experimental studies.

- Rubber chips are abundant, easy to handle, sustainable, and effective isolator when filled-in trenches for the sake of isolating soil mediums against vibrations. From technical point of view, rubber chips provide good vibration isolation for normalized depths close to one.

REFERENCES

[1] Haupt, W.A., 1981. "*Model tests on screening of surface waves*." 10th International Conference on Soil Mechanics and Foundation Engineering. 3: 215-222, 15-19 June 1981, Stockholm.

[2] Haupt, W.A., 1995. "*Wave propagation in the ground and isolation measures*." 3rd International Conference on Recent Advances in Geotechnical Earthquake Engineering and Soil Dynamics. 2: 985-1016. 2-7 April 1995, Missouri.

[3] Alzawi, A. and El naggar, M.H., 2011a. "*Full scale experimental study on vibration scattering using open and in-filled (Geofoam) wave barriers*." Soil Dyn Earthq Eng 31: 306-317.

[4] Woods, R.D., 1968. "*Screening of surface waves in soils"*. Detroit: Ph.D Thesis University of Michigan, United States of America, 57 pages.

[5] Toygar, O., 2015. *"Investigation of Vibration Isolation Performance of Trench Type Wave Barriers by Field Tests*", M.Sc Thesis, Mugla Sitki Kocman University, Turkey, 95 pages.

[6] Ulgen, D. and Toygar, O., 2016. "*Screening effectiveness of open and in-filled wave barriers*." Const. Building Mater. 86: 12-20.

[7] Rayleigh, J.S., 1885. "*On waves propagated along the plane surface of an elastic solid*." London Mathimatical Society, Oxford Journals 17 : 4-11. 1 November.

NUMERICAL EVALUATION OF THE PIPE-PILE BUCKLING DURING VIBRATORY DRIVING IN SAND

Montaser Bakroon*, *Chair of Soil Mechanics and Geotechnical Engineering, Technische Universität Berlin, r.daryaei@campus.tu-berlin.de*

Reza Daryaei, *Chair of Soil Mechanics and Geotechnical Engineering, Technische Universität Berlin, m.bakroon@campus.tu-berlin.de*

Daniel Aubram, *Chair of Soil Mechanics and Geotechnical Engineering, Technische Universität Berlin, daniel.aubram@tu-berlin.de*

Frank Rackwitz, *Chair of Soil Mechanics and Geotechnical Engineering, Technische Universität Berlin, frank.rackwitz@tu-berlin.de*

ABSTRACT

The buckling of steel pipe piles during vibratory driving is numerically studied using the Multi-Material Arbitrary Lagrangian-Eulerian (MMALE) method. This method handles the large soil deformations that occur during pile driving and other geotechnical installation processes. The Mohr-Coulomb and an elastic-perfectly plastic material model are used to model the soil and the pile mechanical behavior, respectively. The result of a small-scale pile driving experiment is used to validate the numerical model. The penetration trend agrees well with the experimental measurements. Thereafter, four case scenarios and their possible effects on pile buckling, namely the presence of heterogeneity in the soil (a rigid boulder inside the soil) and the existence of geometrical imperfection modes in the pile (ovality, out-of-straightness, flatness) are investigated. This study shows that a combination of local and global buckling initiates at the pile tip and the pile shaft, respectively. During the initiation of buckling, a decrease in the penetration rate of the pile is observed compared to the case where no or minimal buckling occurs. It is shown that a less portion of the driving energy is spent on the pile penetration and the rest is spent on other phenomena such as buckling, resulting in less pile penetration. The cross section of the pile tip after buckling takes a form of a "peanut", yet with a different geometry for each case. In cases where the model was initially symmetric, an asymmetric shape in cross section of the pile tip was obtained at the final stage which can be attributed to complex soil-structure interaction. The results of the numerical approach provide promising results to be used as an evaluation tool to reach reliable predictions in pile installation practice.

Keywords: Pipe-Pile Buckling, Imperfection, Pile Installation, Soil-Structure Interaction, Multi-Material Arbitrary Lagrangian-Eulerian, Large Deformations.

1. INTRODUCTION

One of the dominant pile failure modes is pile buckling where a sudden increase in pile deformation is observed. Buckling usually occurs in slender structures subjected to an axial compressive force as a mechanical instability. It is mostly investigated in the field of structural and mechanical engineering but not thoroughly in geotechnical engineering. The focus of this study is the evaluation of pile buckling during the installation process of the pile. Several scenarios are considered such as the presence of heterogeneity in the soil and penetration using initially imperfect piles.

In the literature regarding pile buckling, the support condition of the pile is idealized, i.e., the pile is considered either with no lateral supports or as completely embedded ("wished-in-place") without simulation of the installation process. However, as the pile penetrates during installation, lateral support from the soil evolves because of its particular nonlinear, path-dependent mechanical behavior. Therefore, the pile can be divided into two distinct parts with different buckling characteristics, namely, an embedded part and an upper part which is not yet laterally supported. The motivation of this study is to investigate buckling during the installation process under semi-embedded pile condition which is frequently observed in offshore geotechnical engineering.

Conventionally, buckling is classified into two main groups: Global buckling and local buckling. In global buckling, the pile deforms somewhat similar to the Euler's buckling problem mainly due to an instability associated with the axial load and the pile as a whole. In local buckling, on the other hand, significant permanent deformations occur in the cross-section of the pile with no direct correspondence to an overall instability [1].

The global buckling phenomenon in geotechnical engineering design codes for pile performance is characterized by defining a critical stress/load depending on the slenderness ratio (Length/radius of gyration) and structure stiffness as well as the soil stiffness [1]. In contrast, the local buckling is generally characterized as localized damage which is often encountered at the pile tip (so-called pile tip buckling) and can occur at any stage of driving to the pile. Several reasons are suggested in the literature for the local buckling including initial pile imperfection, soil heterogeneity, induced forces from the soil, etc. Increased driving resistance, pile deviation from its longitudinal axis, and different pile response against lateral loads are some of the effects of the local buckling [2].

The local or pile tip buckling was observed in several offshore practices such as the pile installation project is the Goodwyn-A platform construction project in Australia. It was reported that the occurrence of local buckling caused many piles to fail during installation [3].

Due to many challenges to evaluate the pile installation on-site, the numerical simulation of such processes has gained attention during the last decades. However, the simulation of pile installation has posed several challenges, which generally involve large deformations and material flow when conventional numerical methods are used.

In this study, a robust numerical approach is suggested facilitating the study of pile buckling during installation in the soil. By using this method, the occurrence of local buckling can be observed due to various scenarios such as initial pile imperfection. To the best knowledge of the authors, numerical evaluation of buckling behavior of perfect or imperfect piles during installation in soil has not been extensively studied in the literature.

The structure of the paper is as follows: in section 2, a brief description of the employed numerical method, the developed numerical model, as well as its validation against the experiment is presented. In section 3, the results of the different scenarios are shown and discussed. The concluding remarks are presented in section 4.

2. METHODOLOGY

2.1. Description of the MMALE method

Pile installation belongs to the group of large deformation problems, the numerical analysis of which via the conventional numerical approaches is often challenging [4]. Concerning methods which are capable of handling such problems, one of the most promising approaches is the Multi-Material Arbitrary Lagrangian-Eulerian (MMALE) method [5].

The general strategy of MMALE is to generate a mesh not necessarily aligned with material boundaries. Therefore, a number of so-called multi-material elements might be present holding a mixture of two or more materials. A zone free of any material known as the void zone with neither mass nor strength must be introduced in the mesh. Such zones are essential for non-Lagrangian calculation step to capture material flow into initially unoccupied (i.e., void) regions of the physical space. After one or several Lagrangian steps are performed, a new arbitrary mesh is developed which may not be identical to the initial mesh configuration (rezoning/remeshing step). Subsequently, the solution is transported from the previous mesh to the new mesh (remapping/advection step). The sub-steps are not performed in parallel but in a sequential routine using the operator-splitting technique [5], [6].

Despite its popularity in fluid dynamics and computational physics, the MMALE application in geotechnical problems is limited. A series of works conducted by Bakroon et al. [7], [8] assesses the capabilities of MMALE in the simulation of complex large deformation problems. Compared to classical Lagrangian methods, the MMALE showed promising performance.

2.2. Soil-Structure Interaction

The penalty contact scheme is employed in the numerical model where the momentum is maintained [9]. The contact force is measured based on the arbitrary penetration of the parts. This is considered by adding a penalty term to the energy equation as follows [10]:

$$\Pi = \mathrm{E_p} + E_k + \frac{1}{2}k\Delta u^2 \qquad \textbf{(1)}$$

Where E_p and E_k are potential and kinetic energy, respectively, k is the spring stiffness representing the contact interface, and u is the arbitrary penetration of two contact parts.

2.3 Description of the Model

A model based on MMALE formulation is developed, where a pile is installed in the soil using vibratory force. The model has been developed to back-calculate a small-scale experimental test at TU Berlin. The model configuration and the load history curve is shown in Figure 1a and Figure 1b, respectively.

The pile has 1.5 m height, 0.2 m diameter, and 0.005 m thickness. The conventional shell element formulation with reduced integration point is used. A uniform element size of 2-cm is assigned. An elastic-perfectly plastic material model based on von Mises failure criterion is used (see Table 1).

Table 1. *General properties of the pile used in benchmark models*

Density ρ (kg/m³)	**Elastic Modulus E (MPa)**	**Yield Stress σ_y (MPa)**	**Poisson ratio υ**	**Thickness t (m)**	**Radius R (m)**
7850	2.1E5	250	0.3	0.005	0.1

Table 2. *Mohr-Coulomb material constants for Berlin sand* [11]

Density ρ (kg/m³)	**Friction angle ϕ**	**Dilatancy angle ψ**	**Cohesion c (MPa)**	**Poisson ratio υ**	**Elastic Modulus E (MPa)**
1900	35°	1°	0.001	0.2	20

For the soil, a mesh with 2 m height and 1 m radius with the one-point integration MMALE element formulation is generated. A mesh, with varying element width from 0.6 – 8 cm is used in the horizontal direction, whereas a uniform mesh in the vertical direction with 2.5 cm is considered. The mesh is filled with the soil up to the height of 1.8 m. The rest is kept as unfilled/void domain above the soil material to enable the soil to move to this domain after penetration starts.

The Berlin sand is used with the Mohr-Coulomb constitutive equation parameters listed in Table 2. The initial stress in the soil is defined with assigning the gravity acceleration as 10 m/s^2.

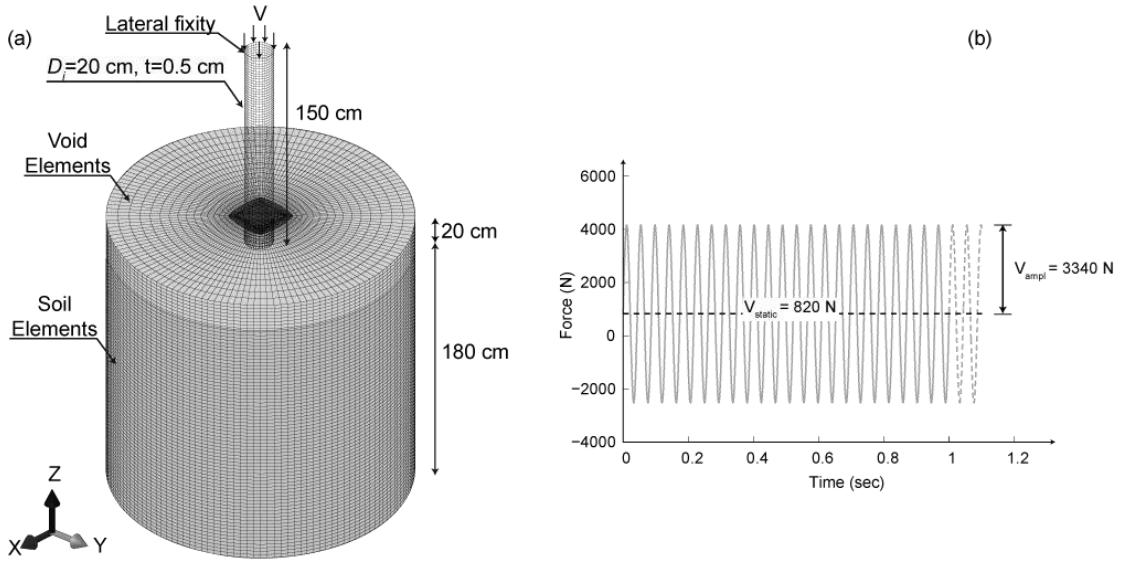

Figure 1. *Schematic diagram of the (a) isometric view of the numerical model configuration and (b) vibratory load history curve*

A penalty contact with a tangential friction coefficient of 0.1 is defined. The pile is fixed at the top against horizontal movements. Conventional fixities are applied to the soil boundary.

2.4. Validation Against Experimental Results

The proposed numerical model is validated against a small-scale experimental test conducted at the laboratory of the Chair of Soil Mechanics and Geotechnical Engineering at Technische Universität Berlin (TU Berlin). The test consists of a half-cylindrical pile with 1.5 m length, 0.005 m thickness, and 0.2 m outer diameter place above the Berlin sand. Using pile guides, the pile is constrained in the horizontal direction. A vibratory motor with the driving force of 1670 N using the frequency of 23 Hz is employed. The mounting parts and the motor weigh about 410 N.

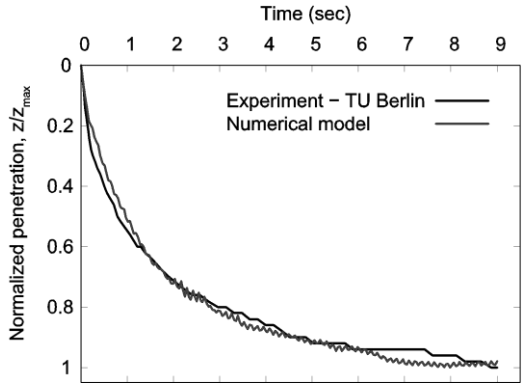

Figure 2. *Penetration depth vs. time curve obtained from the numerical model and experimental measurement*

A quarter model is developed based on the descriptions in section 2.3, with assuming the pile acting as a rigid part. Figure 2 shows the pile displacement curve from the numerical model compared with experimental measurement. Since the focus of this study is to reach the same penetration trend, the curves are normalized by their maximum value.

The numerical result is in good agreement with the one measured in the experiment. Initially, the penetration rate is significant due to less soil resistance and confining pressure. Subsequently, the confining stress in the soil around the pile skin increases, causing an increase of the frictional force and thus a decrease in the penetration rate.

The vertical and horizontal stress contours at the designated time during the vibratory loading is shown in Figure 3. The areas around the pile are disturbed during the installation up to a distance horizontal distance of 2D, where D is the pile diameter (Figure 3a). In a lateral distance far enough from the pile, say 5D, the lateral stress in the soil reaches its in-situ value, which verifies that the boundary distance is far enough from the dynamic source to have substantial effects. A relatively large vertical stress is noted in the soil under the pile tip until the depth of 4D (Figure 3b). At a depth of about 6D from the soil surface, the stress isolines become almost horizontal, determining the influence region of the vibration caused by driving which is reasonably far from the boundary.

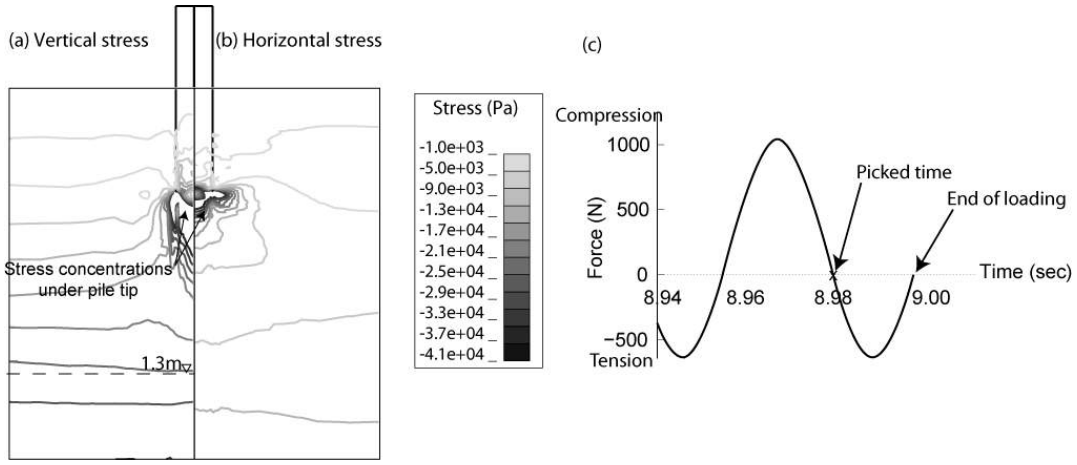

Figure 3. *Isolines of the induced (a) vertical and (b) horizontal stress in the soil, and (c) the corresponding loading at 8.98 sec*

3. RESULTS AND DISCUSSION

In this section, the pile buckling phenomenon during installation is evaluated by using the model described in section 2.3. Here, five different scenarios are presented. In the first case, a model is developed the pile is geometrically assumed perfect. This case is referred to as the reference model. In addition, three models are developed where the pile initially holds an imperfection, namely a pile with an oval shape in cross-section, a flat side, and out-of-straightness. In the last case, heterogeneity is introduced by defining a boulder in the soil. To reach a more noticeable buckling in the model after a short amount of penetration, a lower elastic modulus (1% of the one in Table 1) was assigned to the pile.

The comparison criteria are the mean strain, internal energy, and load-penetration curve. The mean strain is defined as one-third of the strain tensor trace based on the infinitesimal theory. The internal energy is defined as the work done to induce strain in a unit volume of the shell part (taking into account the shell thickness). This criterion is used here to evaluate the accumulated strain in a pile during installation.

In Figure 4a, the vertical displacement of the pile head is plotted against time. In the case of the reference model, the pile did not exhibit any significant buckling until about 8 seconds of the simulation or 0.65 m penetration depth.

Afterward, a localized buckling was observed. The other four models (ovality, flatness, straightness, and heterogeneity), the final penetration is less than the reference model. Initially, the penetration rates are mostly identical. In case of heterogeneity, the penetration rate decreases significantly after it hits the boulder at 1.5 seconds. The final depth of this case is half of the reference model. After about 2 seconds, the penetration rate of the oval-shaped pile starts to decrease as well. In the case of the other two imperfect piles, namely the piles with flatness side and out-of-straightness, the penetration rate decrease at the same time after about 4 seconds.

In Figure 4b, the accumulated internal energy for all cases is plotted. Knowing that the same driving force was used for all models, one can conclude that the same driving energy is utilized in all models. According to the energy conservation law, this energy must have been spent on other phenomena such as additional strains and/or buckling in the pile. Therefore, to assess this point, the internal energy of each pile, is compared in Figure 4b. The curves in are cut to the value of 40 J. In case of a further increase in energy curve, a cross sign is replaced. In all cases, as the penetration curve deviates from the reference model, the corresponding internal energy of the pile starts to increase considerably. Thus, the remaining driving energy is spent on buckling. On the other hand, a decrease in the internal energy value is noticed after significant jumps in some cases which can be attributed to the induced elastic strains in the pile which after further penetration the pile springs back elastically. The possibility of the occurrence of this behavior has also been reported by Aldridge et al. [2]. As a result, it can be argued that the driving energy for the pile installation is reflected in the model in other forms, such as pile buckling.

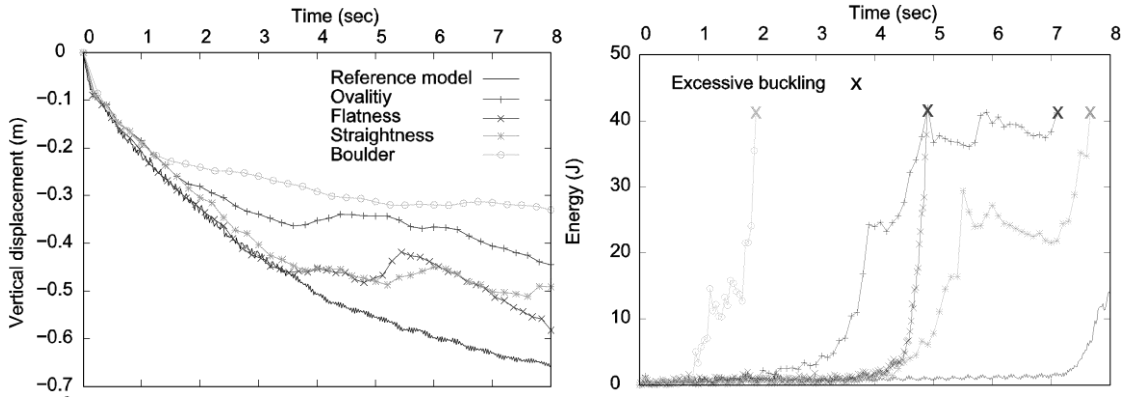

Figure 4. *Comparison of the imperfect piles with the reference model based on the (a) vertical displacement (b) the internal energy*

The deformed shape of the pile in length and pile tip section and the mean strain contour plots are shown in Figure 5. The results correspond to the time stamps, where maximum internal energy was measured. In the case of the reference model, a minor strain is induced in the pile which is less than 0.05%. Also, the initial cross-section is maintained during the penetration.

In comparison to the reference model, a relatively significant strain/buckling is induced by the piles in the models, which is mostly accumulated at the pile tip. This points out the parts where the pile is damaged. Furthermore, the progressive pile deformation is non-symmetric even for the case of ovality and reference model where the piles have an initial symmetric shape. Besides, each model shows a different buckling mode due to the different initial condition. Also, the cross sections of the pile tip in the studied cases tend to contract in one side direction and take a so-called “peanut-shaped”. This phenomenon has also been reported in the literature [2], [3].

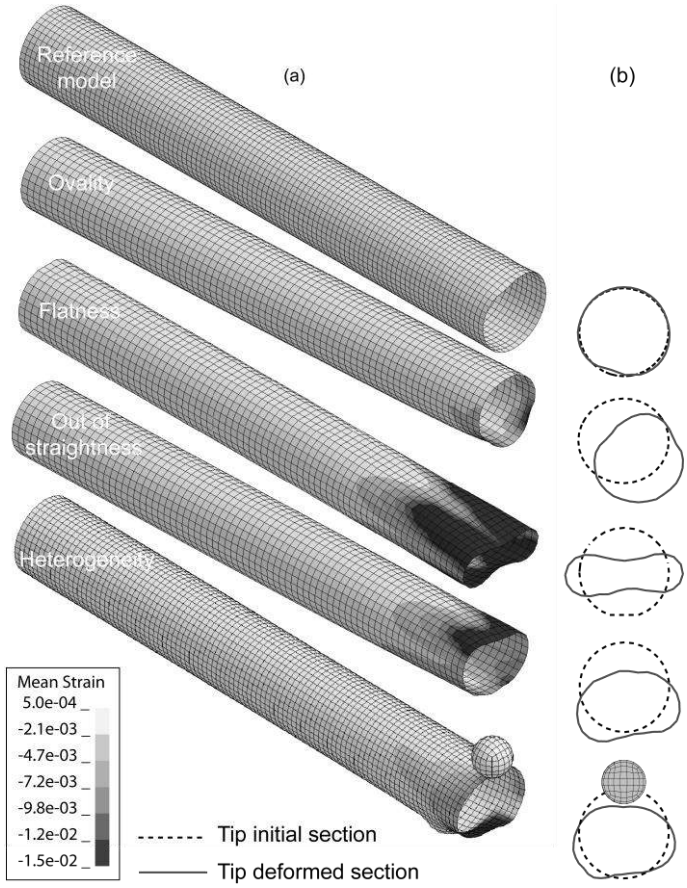

Figure 5. *(a) Contours of induced mean infinitesimal strain in the imperfect piles and the reference model and (b) the pile tip cross section compared to its initial*

Concerning the above discussion, the proposed numerical model is shown to consider the complex site conditions such as the effects of soil resistance, pile imperfection, and heterogeneity during pile driving. In addition, the model provides reliable measures to assess pile buckling.

4. CONCLUSION

The focus of this study is to evaluate pile buckling during pile driving taking various complex conditions into account, such as the presence of heterogeneity in the soil and existence of initial geometrical imperfections in the pile. To this extent, a robust MMALE numerical approach, in conjunction with a soil-structure interaction scheme, was used to improve the numerical analysis of pile buckling during the installation process.

The results are compared to a reference model where the pile has a perfect cylindrical shape with no heterogeneity in the soil. The buckling modes varied for each scenario. Interestingly, before the initiation of a significant buckling, a decrease in the penetration rate was observed. Simultaneously, the internal energy started to increase. This study shows that the driving energy used for pile driving is consumed on other phenomena such as pile buckling. Consequently, less penetration will be observed in the case of buckling. The initial imperfection not only accelerates the buckling process but also changes the buckling mode of the pile.

The presented work focused on a specific area, i.e. pile imperfection and soil heterogeneity. There are numerous affecting parameters on pile buckling which cannot be summarized in one study. Following points may also be considered in future works:

- Evaluation of the effects of varying pile thickness in length on reducing the buckling
- Determination of the occurrence of the plugging during installation
- Evaluation of the pile bearing capacity

ACKNOWLEDGMENT

The authors are thankful for the partial financial support obtained from Deutscher Akademischer Austauschdienst (DAAD) with grant number 91561676 and the Elsa-Neumann scholarship of city Berlin (NAFOEG) with grant number T68001.

REFERENCES

[1] DIN EN 1993-1-6:2007, *Design of Steel Structures - Part 1-6: Strength and Stability of shell structures*, Eurocode 3. 2007.

[2] Aldridge, T. R., T. M. Carrington, and N. R. Kee, 2005. "*Propagation of Pile Tip Damage During İnstallation*," Frontiers in Offshore Geotechnics, ISFOG 2005 - Proceedings of the 1st International Symposium on Frontiers in Offshore Geotechnics, pp. 823–827.

[3] Kramer, G., 1996. "*Investigation of the Collapse Mechanism of Open Ended Piles during Installation*," TU Delf.

[4] Bakroon, M., R. Daryaei, D. Aubram, and F. Rackwitz, 2017 "*Arbitrary Lagrangian-Eulerian Finite Element Formulations Applied to Geotechnical Problems*," in *Numerical Methods in Geotechnics*, J. Grabe, Ed. Hamburg, Germany: BuK! Breitschuh & Kock GmbH, pp. 33–44.

[5] Benson, D. J., 1992. "*Computational Methods in Lagrangian and Eulerian Hydrocodes*," Computer Methods in Applied Mechanics and Engineering, vol. 99, no. 2–3, pp. 235–394.

[6] Aubram, D., F. Rackwitz, and S. A. Savidis, 2017. "*Contribution to the Non-Lagrangian Formulation of Geotechnical and Geomechanical Processes*," in *Lecture Notes in Applied and Computational Mechanics*, vol. 82, Springer International Publishing, pp. 53–100.

[7] Bakroon, M., R. Daryaei, D. Aubram, and F. Rackwitz, 2018. "*Multi-Material Arbitrary Lagrangian-Eulerian and Coupled Eulerian-Lagrangian Methods for Large Deformation Geotechnical Problems*," in Numerical Methods in Geotechnical Engineering IX: Proceedings of the 9th European Conference on Numerical Methods in Geotechnical Engineering (NUMGE 2018), pp. 673–681.

[8] Bakroon, M., R. Daryaei, D. Aubram, and F. Rackwitz, 2018. "*Implementation and Validation of an Advanced Hypoplastic Model for Granular Material Behavior*," in 15th International LS-DYNA® Users Conference, p. 12.

[9] Hallquist, J., *LS-DYNA® theory manual*, no. March. California: Livermore Software Technology Corporation, 2006.

[10] Wriggers, P., 2006. "*Computational Contact Mechanics", Second Ed., Springer*.

[11] Schweiger, H. F., 2002. "*Results From Numerical Benchmark Exercises in Geotechnics*," in *5th European Conference on Numerical Methods in Geotechnical Engineering (NUMGE 2002)*, P. Mestat, Ed. Paris, pp. 305–314.

MEMBRANE BEHAVIOUR OF CLAY SOILS PERMEATED WITH MULTI-ELECTROLYTE AQUEOUS SOLUTIONS

Nicolò Guarena*, *Department of Structural, Geotechnical and Building Engineering, Politecnico di Torino, corso Duca degli Abruzzi 24, 10129 Torino, Italy, nicolo.guarena@polito.it*

Andrea Dominijanni, *Department of Structural, Geotechnical and Building Engineering, Politecnico di Torino, corso Duca degli Abruzzi 24, 10129 Torino, Italy, andrea.dominijanni@polito.it*

Mario Manassero, *Department of Structural, Geotechnical and Building Engineering, Politecnico di Torino, corso Duca degli Abruzzi 24, 10129 Torino, Italy, mario.manassero@polito.it*

ABSTRACT

Osmosis is known to play a key role in reducing the transport rate of contaminants through the natural and engineered clay barriers that are used for a number of geoenvironmental applications, such as the lining of waste disposal facilities. Although a significant body of experimental research has focused on the quantification of osmotic phenomena in smectite clays permeated with single-electrolyte solutions, no evidence has been provided about the membrane behaviour of clays in solute mixtures and, specifically, about the so-called osmotic anomalies that have been documented in the biological and chemical literature for fine-porous charged diaphragms in the presence of two or more electrolytes. In view of the similarities between such fine-porous media and smectite clays, the aim of the paper is to illustrate the physico-chemical mechanisms that govern semipermeable membrane behaviour in multi-electrolyte systems, and to identify suitable test conditions for the experimental assessment of the aforementioned phenomena in clay soils.

Keywords: Anomalous Osmosis, Bentonite-Based Barrier, Landfill Liner, Reflection Coefficient.

1. INTRODUCTION

Smectite clays (e.g. bentonites), in addition to extremely low hydraulic conductivity values ($< 10^{-10}$ m/s) when permeated with diluted solutions and self-healing properties due to the high swelling potential, are also able to exhibit semipermeable membrane behaviour, as the transport of solvent is permitted while the migration of ion species is partially restricted. Clay membranes have large enough pore sizes to accommodate hydrated ions and, therefore, the selective restriction of charged solutes cannot be attributed to the steric hindrance, which arises when the molecules have a larger size than the membrane pores, but should instead be attributed to the electrical interactions that occur between the ions in solution and the clay particles [1], which carry a net negative charge as a consequence of the isomorphic substitution of lower-valence cations for higher-valence cations within the crystal lattice.

Although a conservative assessment of the performance of geoenvironmental containment barriers that wholly or partly consist of smectite clays can be obtained by modelling pollutant migration according to the classical advective-diffusive transport theory, natural and engineered clay barriers are generally able to restrict contaminant migration more effectively as a result of their semipermeable properties, which lead to the chemico-osmotic counter-advection and a decrease in the pore volume that is accessible to solute transport [2]. Thus, in view of the

advantages that arise from the ability to model coupled flow phenomena in clay soils, extensive research has been conducted over the past few decades in order to gain a better understanding of the fundamental mechanisms that govern membrane behaviour, which is usually quantified through the laboratory measurement of the reflection coefficient, ω, also known as the chemico-osmotic or membrane efficiency coefficient [3]. The reflection coefficient of natural clays is generally considered to vary from zero ($\omega = 0$), in the case of the absence of membrane behaviour, to unity ($\omega = 1$), in the case of ideal or perfect clay membranes that are able to completely prevent anions from entering the pores, even though the range of variation of such a phenomenological parameter is not restricted to 0 and 1 on a thermodynamic ground [4]. Accordingly, lower values of ω than zero ($\omega < 0$) are classified as manifestations of "negative anomalous osmosis", whereby the volumetric flux of water is directed against the osmotic pressure gradient under isobaric conditions [5], and larger values of ω than unity ($\omega > 1$) are regarded as manifestations of "positive anomalous osmosis", which results in the transport of solutes against their concentration gradients [6].

Most experimental studies concerning the assessment of the reflection coefficient of clays have been devoted to analysing the extent to which membrane behaviour is affected by the soil porosity and the salt concentration of the permeating solution [7, 8, 9], the valence of the ion species and the clay mineralogical composition [10, 11], the effective confining stress [12] and the degree of water saturation [13]. However, all the aforementioned studies dealt with aqueous solutions of a single electrolyte, and thus did not account for the influence of the simultaneous presence of two or more different electrolytes in the pore solution. In this regard, the biological and chemical literature provides evidence of both negative [14] and positive [14, 15] large osmotic volume flows under isobaric conditions in electrically charged fine-porous membranes, which separate aqueous solutions of two electrolytes with different counter-ions (i.e. charge polarity opposite to that of the membrane) and the same co-ion (i.e. charge polarity equal to that of the membrane). Yaroshchuk et al. [6] were the first to measure larger values of the reflection coefficient than unity for a cation exchange membrane, namely a phenolsulfonic acid-formaldehyde condensation product, which separated two aqueous solutions containing sodium chloride and hydrochloric acid.

As smectite clays are characterised by the same osmotic properties as the typical ones of cation exchange membranes, this study has been aimed at discussing the conditions under which clay soils are expected to exhibit anomalous membrane behaviour, when the permeating solution consists of a mixture of different electrolytes. The scope of the discussion is therefore to stimulate further experimental research in order to verify the existence and magnitude of such anomalous osmotic phenomena, which can be of relevance for many geotechnical and geoenvironmental applications that deal with pollutant control in the subsoil.

2. TRANSPORT EQUATIONS FOR A SEMIPERMEABLE MEMBRANE

On the basis of pioneering models that were developed to simulate the movement of solvent and solutes through fine-porous charged diaphragms, such as biological tissues, reverse-osmosis membranes and polyelectrolyte gels, Dominijanni and Manassero [16] derived the macroscopic transport equations of a porous medium that behaves as a selectively permeable membrane by upscaling (i.e. volume-averaging over the capillary cross-section) the Navier-Stokes equation for the volumetric flux of the solution and the Nernst-Planck equations for the mass fluxes of the ion species at the microscopic scale. Such an upscaling procedure, which is equivalent to neglecting the dispersive effect that is caused by the pore-scale fluctuation of the state variables, yields the following equations:

$$q = -\frac{k_\varphi}{\gamma_w}\left(\frac{\partial \bar{u}}{\partial x} + F\frac{\partial \bar{\varphi}}{\partial x}\sum_{i=1}^{n} z_i \bar{c}_i\right) \tag{1}$$

$$J_i = q\bar{c}_i - n_m D_i^* \frac{\partial \bar{c}_i}{\partial x} - n_m z_i \frac{F}{RT} D_i^* \bar{c}_i \frac{\partial \bar{\varphi}}{\partial x} \qquad \text{for } i = 1,...,n \tag{2}$$

where q is the macroscopic volumetric flux of the solution, k_φ is the hydraulic conductivity at zero electric potential gradient, γ_w is the water weight per unit volume (9.81 kN·m^{-3}), $\bar{u}$ is the hydraulic pressure within the pore solution, x is the position along the macroscopic transport direction, F is Faraday's constant (9.6485 C·mol^{-1}), $\bar{\varphi}$ is the electric potential within the pore solution, z_i is the electrochemical valence of the i-th ion species, $\bar{c}_i$ is the concentration of the i-th ion species within the pore solution, J_i is the macroscopic mass flux of the i-th ion species, n_m is the soil porosity associated with the conductive pores, D_i^* is the effective diffusion coefficient of the i-th ion species ($D_i^* = \tau_m \cdot D_{0,i}$), τ_m is the matrix tortuosity factor, $D_{0,i}$ is the free-solution or aqueous-phase diffusion coefficient of the i-th ion species, R is the universal gas constant (8.314 J·mol^{-1}·K^{-1}) and T is the absolute temperature.

As a consequence of the negative electric charge of the solid skeleton, the hydraulic pressure and the concentration of the ion species within the pore solution are discontinuous with respect to the corresponding state variables of the external bulk solutions, which are hypothesised to be in equilibrium with the porous medium at its boundaries. In particular, by combining the definitions of the electrochemical potentials of the components of both the pore and bulk solutions with the Donnan equations [16], the pore solution state variables can be expressed in the following form:

$$\bar{c}_i = c_i \Gamma_i = c_i \exp\left[-z_i \frac{F}{RT}\left(\bar{\varphi} - \varphi\right)\right] \qquad \text{for } i = 1,...,n \tag{3}$$

$$\bar{u} = u - \Pi + \bar{\Pi} \tag{4}$$

where Γ_i is the partition coefficient of the i-th ion species, φ is the electric potential within the external bulk solution, c_i is the concentration of the i-th ion species within the external bulk solution, u is the hydraulic pressure within the external bulk solution, Π is the osmotic pressure within the external bulk solution ($\Pi = RT\sum_{i=1}^{n} c_i$) and $\bar{\Pi}$ is the osmotic pressure within the pore solution ($\bar{\Pi} = RT\sum_{i=1}^{n} \bar{c}_i$). Smectite clays behave like negatively charged semipermeable membranes, thus the partition coefficient results to be larger than one for cations (positive adsorption), while it is expected to range between zero and one for anions (negative adsorption). The introduced ion partition coefficients can be determined by coupling Equation 3 with the statement of macroscopic electroneutrality in the pore ($\bar{c}_{sk} = \sum_{i=1}^{n} z_i \bar{c}_i$), where $\bar{c}_{sk}$ are the moles of the solid skeleton electric charge per unit volume of the conductive pores.

3. REFLECTION COEFFICIENT UNDER CLOSED-SYSTEM BOUNDARY CONDITIONS

Dominijanni et al. [17] have shown that the test configuration which is commonly referred to as "closed hydraulic control system" allows a direct measurement of the global value of the reflection coefficient, ω_m, to be obtained. Briefly, the clay specimen is interposed between two compartments through which electrolyte solutions with different chemical composition are circulated, while the volumetric flux of water is hindered across the soil. When these conditions are maintained over time, a difference in hydraulic pressure arises between the specimen boundaries under steady-state conditions, and the measured global value of the reflection coefficient is therefore given by:

$$\omega_m = \left(\frac{\Delta u}{\Delta \Pi} \right)_{q=0;I=0} \tag{5}$$

where I is the electric current density ($I = F \sum_{i=1}^{n} z_i J_i$), and the finite differences are defined as the values in the first compartment solution, which are denoted by a prime, minus those in the second compartment solution, which are denoted by a double prime (i.e. $\Delta u = u' - u''$ and $\Delta \Pi = \Pi' - \Pi''$).

By imposing the condition of a null volumetric flux of solution (q = 0), Equation 1 yields the following relationship:

$$\frac{\partial u}{\partial x} = \frac{\partial \Pi}{\partial x} - \frac{\partial \overline{\Pi}}{\partial x} - F \, \overline{c}_{sk} \, \frac{\partial \overline{\varphi}}{\partial x} \tag{6}$$

where the gradient in the electric potential of the pore solution is obtained by substitution of Equation 2 in the condition of null electric current density (I = 0):

$$\frac{\partial \overline{\varphi}}{\partial x} = -\frac{RT}{F} \frac{\sum_{i=1}^{n} z_i D_i^* \frac{\partial \overline{c}_i}{\partial x}}{\sum_{i=1}^{n} z_i^2 \overline{c}_i D_i^*} . \tag{7}$$

For the case in which the clay specimen is in equilibrium with solutions consisting of electrolyte mixtures, some qualitative conclusions about the conditions whereby anomalous osmotic phenomena may occur can be drawn directly from Equation 6, by assuming that the partition coefficients of anions are close to zero (decreased concentrations within the pore solution), whereas the partition coefficients of cations are much larger than one (increased concentrations within the pore solution). In fact, if μ_i^c represents the chemical potential of the i-th ion species within the bulk solution, Equation 6 can be rewritten in the following way [18]:

$$\frac{\partial u}{\partial x}-\frac{\partial \Pi}{\partial x}=\frac{1}{\sum_{i=1}^{n} z_i^2 c_i \Gamma_i D_i^*}\sum_{i=1}^{n}\sum_{j=1}^{i-1} c_i \Gamma_i c_j \Gamma_j \left(z_j D_j^* - z_i D_i^*\right)\left(z_i \frac{\partial \mu_j^c}{\partial x} - z_j \frac{\partial \mu_i^c}{\partial x}\right). \quad (8)$$

As we are here interested in large positive $\left(\frac{\partial u}{\partial x}-\frac{\partial \Pi}{\partial x} > 0\right)$ and negative $\left(\frac{\partial u}{\partial x}-\frac{\partial \Pi}{\partial x} < 0\right)$ osmotic anomalies, it should be pointed out that such phenomena are not likely to be observed if only one cation is present in the solution, regardless of the number of anions that are produced by the electrolyte dissociation, given that the product $\Gamma_i \Gamma_j$ is small. However, the presence of at least two cations with the same electrochemical valence ($z_i = z_j$) is not sufficient to give rise to anomalous membrane behaviour, as differences in both the cation mobilities ($D_i^* \neq D_j^*$) and the chemical potential gradients $\left(\frac{\partial \mu_i^c}{\partial x} \neq \frac{\partial \mu_j^c}{\partial x}\right)$ are necessary in the latter case.

Finally, the integration of Equation 6 over the length of the clay specimen, *L*, allows a physical identification of the global reflection coefficient to be obtained:

$$\omega_m = \left(\frac{\Delta u}{\Delta \Pi}\right)_{q=0;I=0} = \left(1-\frac{\Delta \overline{\Pi}}{\Delta \Pi}\right) - F\,\overline{c}_{sk}\,\frac{\Delta \overline{\varphi}}{\Delta \Pi} \quad (9)$$

where the finite difference in the electric potential of the pore solution results to be given by:

$$\Delta \overline{\varphi} = -\frac{RT}{F}\int_0^L \sum_{i=1}^{n} \frac{z_i D_i^*}{\sum_{j=1}^{n} z_j^2 \overline{c}_j D_j^*}\frac{\partial \overline{c}_i}{\partial x}\,dx\,. \quad (10)$$

Equation 9 allows the different physical mechanisms that contribute to determining the measured reflection coefficient to be appreciated. In particular, osmosis in clay soils can be interpreted as the superposition of a true chemico-osmotic component $\left(\Omega_c = 1-\frac{\Delta \overline{\Pi}}{\Delta \Pi}\right)$, which originates from the electrostatic repulsion of the anions by the negatively charged clay particles, and an electro-osmotic component $\left(\Omega_e = -F\,\overline{c}_{sk}\,\frac{\Delta \overline{\varphi}}{\Delta \Pi}\right)$, whereby the gradient in the electric potential of the pore solution, under null electric current density conditions, builds up in response to the different diffusivities and electrochemical valences of the migrating cations.

A particularly interesting case is represented by the experimental conditions that were analysed by Yaroshchuk et al. [6], namely when there are two electrolytes with the same anion and a difference in concentration of only one electrolyte is established across the porous medium. The concentration of the second electrolyte, which is referred to as the background electrolyte, is the same in both of the compartments that are separated by the porous medium. If the absolute

values of the electrochemical valences of all the ion species are unitary, Equation 3 shows that the partition coefficients of the two cations assume the same value and are equal to the reciprocal of the partition coefficient of the common anion. Under the aforementioned conditions, Equation 10 can be rewritten as follows:

$$\Delta\bar{\varphi} = -\frac{RT}{F}\int_{\bar{c}_3'}^{\bar{c}_3''} \frac{\left[\left(D_1^* - D_3^*\right) + \frac{\bar{c}_{sk}}{2\bar{c}_3}\frac{c_B}{\sqrt{\bar{c}_3\left(\bar{c}_3 + \bar{c}_{sk}\right)}}\left(D_1^* - D_2^*\right)\right]}{\left[\bar{c}_{sk}D_1^* + \bar{c}_3\left(D_1^* + D_3^*\right) + c_B\sqrt{1 + \frac{\bar{c}_{sk}}{\bar{c}_3}}\left(D_2^* - D_1^*\right)\right]} d\bar{c}_3 \tag{11}$$

where c_B is the concentration of the background electrolyte within the bulk solution, and the subscripts 1, 2 and 3 stand for the cation associated with the electrolyte whose concentration is varied across the porous medium, the cation associated with the background electrolyte and the common anion, respectively.

The electric potential difference, $\Delta\bar{\varphi}$, can be calculated both numerically and analytically, as the integrand that appears in Equation 11 can be reduced to a rational function for which, by definition, an antiderivative always exists. Such a calculation has been performed for the case of the Wyoming Bentonite tested by Kemper and Rollins [10] at a total porosity n = 0.8 (i.e. $\bar{c}_{sk}$ = 56.25 mM), by assuming that the clay specimen is placed between two aqueous solutions, which consist of sodium chloride (NaCl) and hydrochloric acid (HCl) mixtures, and that, alternately, sodium chloride (Figure 1) or hydrochloric acid (Figure 2) represents the background electrolyte ($D_{0,\mathrm{Na}}$ = 1.33·10^{-9} m^2/s; $D_{0,\mathrm{H}}$ = 9.31·10^{-9} m^2/s; $D_{0,\mathrm{Cl}}$ = 2.03·10^{-9} m^2/s).

The predicted positive (ω_m up to 1.5) and negative (ω_m down to -0.5) anomalous values of the reflection coefficient are due to the difference in diffusivity between the Na^+ and H^+ ions.

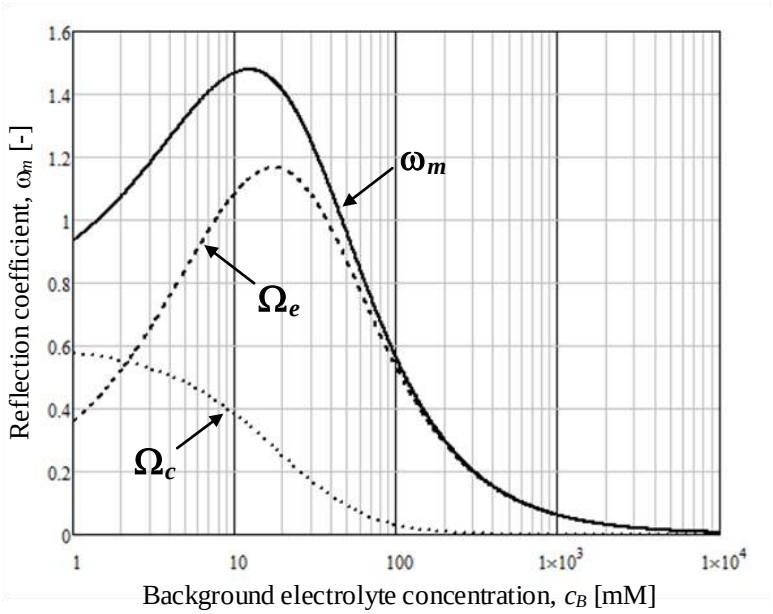

***Figure 1**. Chemico-osmotic (Ω_c) and electro-osmotic (Ω_e) components of the measured reflection coefficient (ω_m). c'_{HCl} = 5 mM ; c''_{HCl} = 20 mM ; $c'_{NaCl} = c''_{NaCl} = c_B$.*

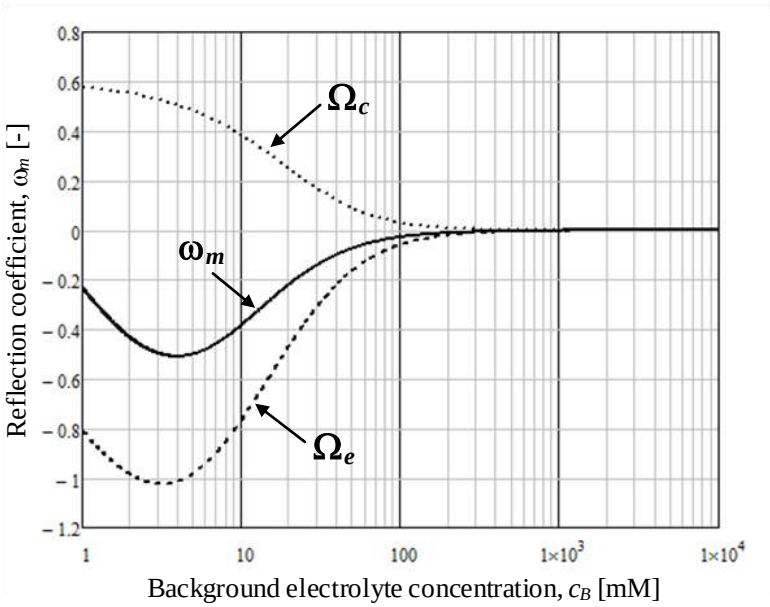

***Figure 2**. Chemico-osmotic (Ω_c) and electro-osmotic (Ω_e) components of the measured reflection coefficient (ω_m). $c'_{NaCl} = 5$ mM ; $c''_{NaCl} = 20$ mM ; $c'_{HCl} = c''_{HCl} = c_B$.*

4. CONCLUSIONS

The mechanistic model developed by Dominijanni and Manassero [16] has here been adopted to provide insight into the physico-chemical mechanisms which, at the pore-scale, govern semipermeable membrane behaviour of smectite clays. In particular, when the clay specimen is tested under closed-system boundary conditions, the contribution of electro-osmosis to the measured membrane efficiency coefficient plays a major role for the case of electrolyte solutions containing two or more cations with different mobilities, whereas the aforementioned contribution is found to be negligible for single-electrolyte systems. On the basis of the theoretical predictions worked out in this paper, membrane behaviour in multi-electrolyte systems can cause both positive anomalous osmosis, which results in a better containment performance than expected for ideal semipermeable membranes, and negative anomalous osmosis which, on the contrary, results in a worse containment performance than expected for non-semipermeable porous media. As far as positive anomalous osmosis is concerned, in addition to the increased membrane efficiency, the persistency of membrane behaviour also seems to be enhanced in comparison to single-electrolyte systems, for which the threshold concentration (i.e. the average concentration across the specimen at which $\omega \sim 0$) was experimentally observed to be about 200 mM [19].

REFERENCES

[1] Shackelford, C.D., Lu, N., Malusis, M.A., 2019. "*Research challenges involving coupled flows in geotechnical engineering*", In: Geotechnical Fundamentals for Addressing New World Challenges, Eds.: N. Lu and J.K. Mitchell, Springer International Publishing AG, Cham, Switzerland, 357 pages.

[2] Dominijanni, A., Manassero, M., 2008. "*Influence of membrane behavior on contaminant transport through Geosynthetic Clay Liners*", GeoCongress 2008: Characterization, Monitoring, and Modeling of GeoSystems, pp. 814-821, 9-12 March 2008, New Orleans, Louisiana.

[3] Malusis, M.A., Shackelford, C.D., Maneval, J.E., 2012. "*Critical review of coupled flux formulations for clay membranes based on nonequilibrium thermodynamics*", Journal of Contaminant Hydrology, 138-139: 40-59.

[4] Dominijanni, A., Manassero, M., 2012a. "*Modelling the swelling and osmotic properties of clay soils. Part I: The phenomenological approach*", International Journal of Engineering Science, 51: 32-50.

[5] Röttger, H., Woermann, D., 1993. "*Osmotic properties of polyelectrolyte membranes: Positive and negative osmosis*", Langmuir, 9(5): 1370-1377.

[6] Yaroshchuk, A.E., Röttger, H., Woermann, D., 1993. "*Osmotic properties of a cation exchange membrane: Reflection coefficients of a solute larger than 1 in a system with aqueous mixed electrolyte solutions*", Berichte der Bunsengesellschaft für Physikalische Chemie, 97(5): 676-680.

[7] Malusis, M.A., Shackelford, C.D., 2002. "*Chemico-osmotic efficiency of a geosynthetic clay liner*", Journal of Geotechnical and Geoenvironmental Engineering, 128(2): 97-106.

[8] Musso, G., Cosentini, R.M., Dominijanni, A., Guarena, N., Manassero, M., 2017. "*Laboratory characterization of the chemo-hydro-mechanical behaviour of chemically sensitive clays*", Rivista Italiana di Geotecnica, 51(3): 22-47.

[9] Dominijanni, A., Guarena, N., Manassero, M., 2018. "*Laboratory assessment of semipermeable properties of a natural sodium bentonite*", Canadian Geotechnical Journal, 55(11): 1611-1631.

[10] Kemper, W.D., Rollins, J.B., 1966. "*Osmotic efficiency coefficients across compacted clays*", Soil Science Society of America Journal, 30(5): 529-534.

[11] Kemper, W.D., Quirk, J.P., 1972. "*Ion mobilities and electric charge of external clay surfaces inferred from potential differences and osmotic flow*", Soil Science Society of America Journal, 36(3): 426-433.

[12] Malusis, M.A., Kang, J.B., Shackelford, C.D., 2013. "*Influence of membrane behavior on solute diffusion through GCLs*", International Symposium on Coupled Phenomena in Environmental Geotechnics, pp. 267-274, 1-3 July 2013, Torino, Italy.

[13] Sample-Lord, K.M., Shackelford, C.D., 2018. "*Membrane behavior of unsaturated sodium bentonite*", Journal of Geotechnical and Geoenvironmental Engineering, 144(1): 04017102.

[14] Grim, E., Sollner, K., 1960. "*True anomalous osmosis in multi-solute model membrane systems*", Journal of General Physiology, 44(2): 381-392.

[15] Woermann, D., 1972. "*Transport von Ionen entgegen ihrem Konzentrationsgefälle durch Kationenaustauscher-Membranen mit endlicher mechanischer Permeabilität*", Chemie Ingenieur Technik, 44(4): 158-163.

[16] Dominijanni, A., Manassero, M., 2012b. "*Modelling the swelling and osmotic properties of clay soils. Part II: The physical approach*", International Journal of Engineering Science, 51: 51-73.

[17] Dominijanni, A., Guarena, N., Manassero, M., 2019. "*Phenomenological analysis and physical interpretation of the reflection coefficient of clays*", 8th International Congress on Environmental Geotechnics, Volume 3, pp. 156-163, 28 October - 1 November 2018, Hangzhou, China.

[18] Yaroshchuk, A.E., 1995. "*Osmosis and reverse osmosis in fine-charged diaphragms and membranes*", Advances in Colloid and Interface Science, 60(1-2): 1-93.

[19] Shackelford, C.D., Meier, A., Sample-Lord, K.M., 2016. "*Limiting membrane and diffusion behavior of a geosynthetic clay liner*", Geotextiles and Geomembranes, 44(5): 707-718.

CRITICAL SLIP SURFACE DETERMINATION IN SLOPE STABILITY ANALYSIS USING OPTIMIZATION ALGORITHMS

Panagiotis Aivaliotis Apostolopoulos*, *Research Assistant, University of Cyprus, Nicosia, Cyprus, paival01@ucy.ac.cy*

Dimitrios Loukidis, *Assistant Professor, University of Cyprus, Nicosia, Cyprus, loukidis@ucy.ac.cy*

ABSTRACT

Slope stability analysis consists of determining the potential slip surface with the minimum Factor of Safety (FS). Most slope stability software rely on grid or random searches for identifying the critical slip surface, making thus difficult to pinpoint the exact surface with the lowest FS. Moreover, such searches have an unnecessarily high computational cost. Heuristic optimization schemes can be employed to achieve faster and accurate calculation of the critical FS. This paper presents an application to the slope stability problem of two widely used optimization algorithms, namely the Particle Swarm Optimization (PSO) and the Genetic Algorithm (GA). It is shown that PSO is able to achieve an acceptable result in a very short amount of time for simple slope stability problems. GA is slower, but it has the capability of avoiding erroneous convergence to local minima in the case of reinforced slopes. Finally, a hybrid algorithm combining the GA and PSO schemes is considered in order to achieve an improved computational performance.

Keywords: Slope Stability, Genetic Algorithm, Particle Swarm Optimization

1. INTRODUCTION

The main objective of slope stability analysis is the determination of the Factor of Safety (FS) characterizing the slope. Current state of practice still relies heavily on the use of limit equilibrium methods, in which calculations are performed for a number of trial slip surfaces aiming at determining the slip surface with the minimum (critical) FS. Most slope stability software perform searches for identifying the critical slip surface that are either completely random ("brute force" approach) or based on a user-specified "grid" of trial slip surface geometries. The former spends an unnecessarily high computational effort, as it does not contain a search strategy and a very large number of random trial slip surfaces needs to be analyzed to accurately solve the problem, while the latter does not guaranty identification of the true critical slip surface. Use of modern heuristic optimization methods in slope stability analysis, such as the particle swarm [1], ant colony [2], genetic algorithm [3,4] or other evolutionary algorithms, are very promising in both increasing the reliability of critical factor of safety calculations and reducing the computation cost. Such schemes, unlike gradient methods, are highly promising as they are known to overcome difficulties stemming from the presence of local minima. Slope stability problems usually exhibit multiple local minima, especially in the case of reinforced slopes. This paper compares the performance of the Particle Swarm Optimization (PSO) algorithm and the Genetic Algorithm (GA), as well as of a hybrid scheme combining PSO and GA, in the analysis of a set of four typical stability problems involving unreinforced and reinforced slopes. Limit equilibrium computations are performed using the method of slices and assuming circular slip surfaces.

2. KNOWLEDGE BACKGROUND

2.1. Genetic Algorithm

The Genetic Algorithm (GA) is a heuristic evolutionary algorithm introduced by Holland [5] as a search algorithm for the solution of difficult optimization problems. It is based on the Darwin's evolutionary principle of survival of the fittest, with a sophisticated yet randomized routine. The algorithm starts by randomly creating sets ("individuals") of values for the problem variables and breeding those individuals to give each time a next generation. Each individual of the population is tested to find its fitness level in terms of the validity of the solution and the magnitude of the resulting objective function value. In the slope stability problem, the individuals are the trial slip surfaces with their geometrical characteristics being the optimization variables. In the case of circular slip surfaces, these can be either the center coordinates (x_O, y_O) and radius R or alternatively the x-coordinates of the end-points (x_1 and x_2) and the inclination of the tangent at the entry point with respect to the horizontal (θ). The objective function is the FS sought to be minimized.

Subsequently, the individuals are stochastically mutated, i.e. random changes in the elements of the variable's vector $\{x_1,x_2,\theta\}$, or cross-bred, i.e. random exchange of values of variables between two individuals to create offsprings that hold similarities to both of their predecessors. The mutation of the population helps avoiding convergence to a sub-optimal solution by keeping the individuals non-homogenous. After each population mutation and cross-breeding round, the individuals are re-evaluated in terms of problem constraints and objective function. This procedure is repeated iteratively until a set of specified stopping criteria are met (e.g. exceedance of a maximum number iteration loops) . An application of the sequence of these steps in the slope stability problem is shown schematically in Figure 1.

In a variation of the above algorithm, called elitist genetic algorithm, a group of best performing individuals (elite group) is separated and stochastic breeding is focused in this group in order to approach faster the global optimum. The process of random mutations is nevertheless retained, so that the algorithm does not lose the ability to overcome local extrema.

GA is a reliable and easy to implement algorithm. However, its evolutionary features are purely stochastic and, as a consequence, it exhibits slower convergence to the optimal solution than other evolutionary-social algorithms. In other words, GA will always provide an accurate estimation of the global best but at the cost of relatively large computational time.

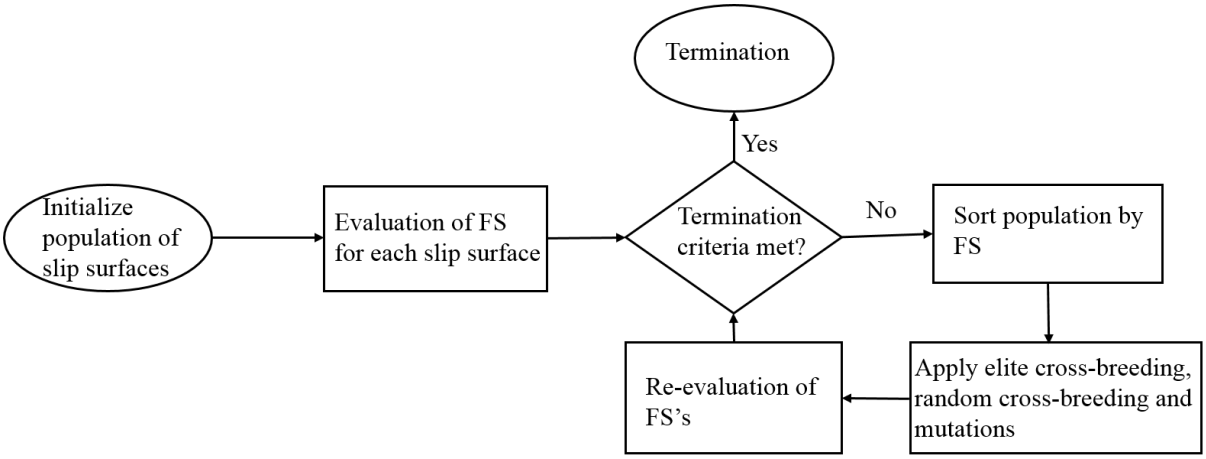

Figure 1. *Flow chart of Genetic Algorithm*

2.2. Particle Swarm Optimization

Particle Swarm Optimization (PSO) is a heuristic global optimization algorithm developed by Kennedy and Eberhart [6]. As in GA, the method starts by generating random sets of problem variables ("particles") and proceeds with optimization by moving these particles in the search space based on simplified social models, such as bird flocking, fish schooling and the swarming theory. Each particle has a vector indicating its position P in space and a vector symbolizing its spatial velocity V (the change of particle position between computation steps). In the case of slope stability analysis with circular slip surfaces, P={x_1,x_2,θ} and V={Δx_1,Δx_2,$\Delta\theta$}. Every particle has also a "memory" of its best position (BP) along with the global best position (GBP) of the entire population, which both are considered to act as attractors. At the start of the computations the particle initial velocities are set equal to zero. Each particle velocity at subsequent steps is set to be directly proportional to the distance of the current particle position from the global best and the distance from its personal best according to the following equation:

$$V_i^{(\text{new})} = wV_i^{(\text{previous})} + c_1 \cdot rand_1 \cdot (P_i - GBP) + c_2 \cdot rand_2 \cdot (P_i - BP_i) \quad (1)$$

where $rand_1$ and $rand_2$ are random numbers in the 0 to 1 range, and c_1 and c_2 are constants scaling the "social" and "personal" speed components, respectively, and w is an "inertia" factor controlling the influence of the current velocity value to that of the next step. The w may be set to decrease as the number of completed steps increases (a technique often termed "damping"). Based on the calculated velocity, the new particle position is updated and re-evaluated with respect to constraints and objective function. This procedure is repeated iteratively until a set of specified convergence and stopping criteria are met (Figure 2).

PSO is generally capable of finding the global optimum with comparatively less computational cost than GA because it relies less on chance in solving the problem thanks to the current global best position acting as an attractor for the other particles. However, the algorithm may occasionally converge to a sub-optimal solution.

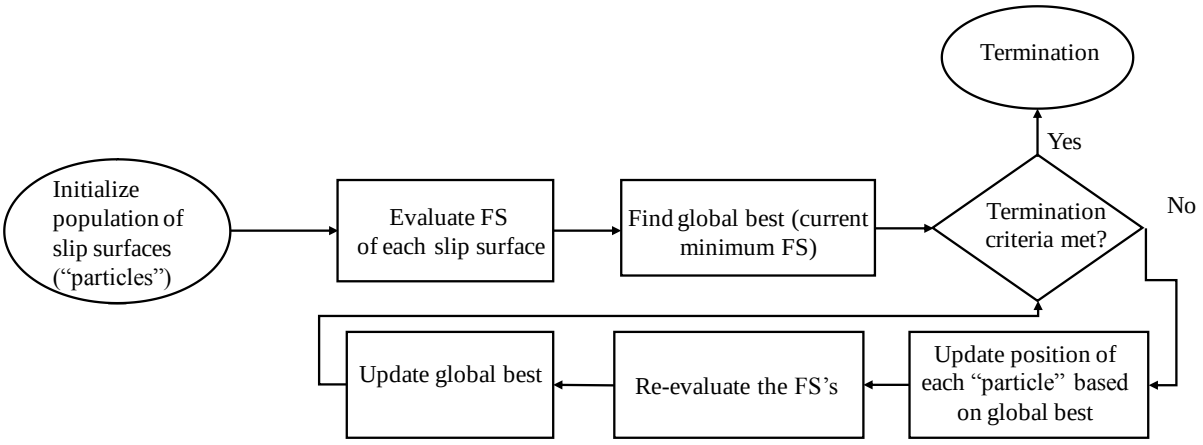

Figure 2. *Flow chart of Particle Swarm Optimization*

3. HYBRID ALGORITHM

The algorithms described in the previous sections have their advantages and disadvantages. The main advantage of the GA is the mutation feature thus has the ability to overcome all local minima, provided that sufficiently large number of steps and corresponding computation time are allowed. PSO usually achieves convergence with less steps but it has no guarantee that it will pinpoint the global and not a local extremum. Researchers have formulated hybrid

algorithms in the past by combining GA and PSO in order to alleviate the inherent shortcomings of each of the individual methods [8,9], with the idea of introducing to PSO an escape possibility from local extrema through random mutations and cross-breeding being quite appealing.

The hybrid algorithm formulated herein, called Swarming Genetic Algorithm (SGA) in the reminder, nests PSO loops inside external loops of GA, as shown in Figure 3. The initialization of the GA population is random. Then a sub-group of specified size of this population is randomly selected to undergo PSO calculations. The sub-group is subsequently re-introduced to the overall population, which then undergoes random mutations and cross-breeding, but also elite cross-breeding. The latter consists of shorting the population according to the calculated FS values and applying cross-breeding among a number of slip surfaces with the lowest values of FS. The rest of the population undergoes random cross-breeding and mutation as in the classical GA.

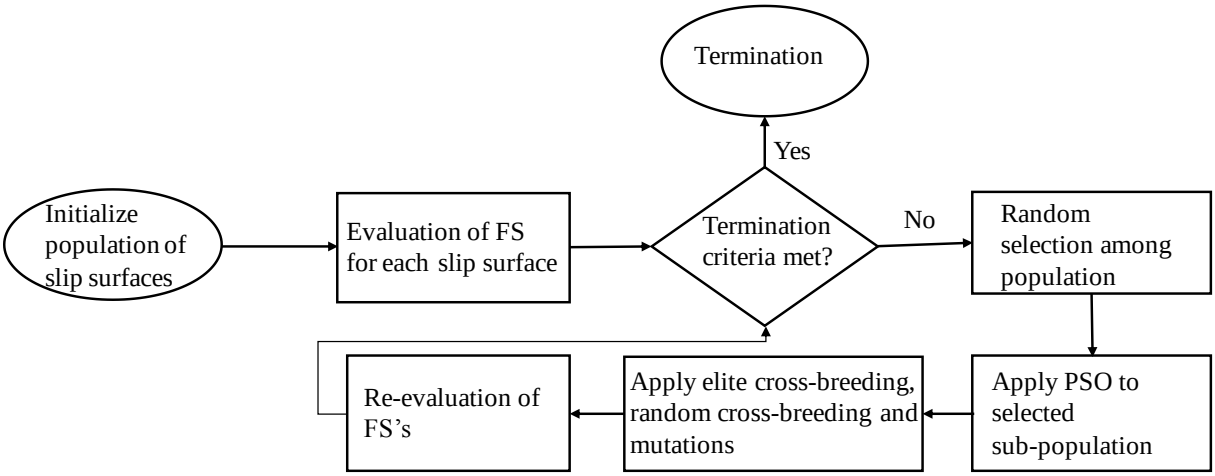

Figure 3. *Flow chart of Swarming Genetic Algorithm*

4. FORMULATION OF THE SLOPE STABILITY PROBLEM

The optimization algorithms are applied herein to slope stability problems solved using the Bishop simplified method of slices [7], which assumes that the slip surfaces have the shape of circular arcs. The slopes are assumed to be uniform and of constant inclination β (Figure 4). According to the Bishop simplified method, in the absence of pore pressures, surcharges and inertial forces other than gravity, the safety factor is given by:

$$FS = \frac{\sum_{i=1}^{N} \frac{c_i L_i \cos a_i + (W_i + F_{i,\text{anchor,y}}) \tan \phi_i}{\cos a_i + \frac{\tan \phi_i \sin a_i}{FS}}}{\sum_{i=1}^{N} (W_i + F_{i,\text{anchor,y}}) \sin a_i - F_{i,\text{anchor,x}} \frac{y_O - y_{anchor,i}}{R}} \tag{2}$$

where c_i and ϕ_i are the soil cohesion and friction angle, respectively, at the base of slice i. The L_i, a_i and W_i are the base length, the base inclination angle and the self weight with respect to the horizontal, respectively. $F_{\text{anchor,i}}$ is the anchor force applied at the top of slice i. For simplicity, the anchor heads are assumed to be placed at the central axis of a given slice.

The origin of the system of coordinates is placed at the toe of the slope. The search ranges for the free variables defining the geometry of each circular slip surface, namely the x-

coordinates of the entry point (x_1) and exit point (x_2), and the entry angle (θ), were specified such that the produced trial surfaces are realistic, thus avoiding waste of computation effort. The search ranges are [-10H , $0.8x_H$] for x_1 and [x_H , max(H/2,$3x_H$)] for x_2. For the entry angle θ, the search range is [-45º , *ground inclination angle*-1º], except for the special case of entry point on horizontal ground, in which case the range was set to [-45º,-0.1º].

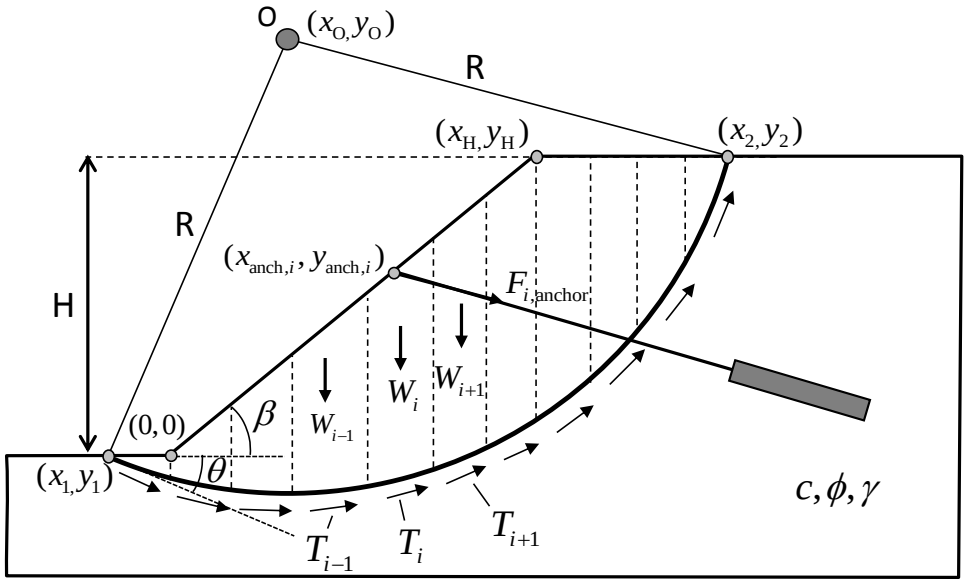

Figure 4. *Schematic of slope stability problem assuming circular slip surface.*

The sliding mass is divided into slices of thickness equal to 5% of the slope height *H*, but with an upper limit of 1m. If a point of change of inclination of the upper (ground surface) or inner (interface between natural ground and fill) boundaries lies inside the width of a slice, then this slice is split in two. The same is true if the slice base intersects interface between two materials.

5. NUMERICAL RESULTS

Four example problems (two unreinforced and two reinforced slopes) are treated with the three algorithms (GA, PSO, SGA) The problem parameters and geometries are presented in Table 1 and Figure 5.

Table 1. *Parameters of example problems*

Problem	**Height *H* (m)**	**Slope angle β (º)**	**Unit weight γ (kN/m^3)**	**Cohesion *c* (kPa)**	**Friction angle ϕ (º)**
A	20	20	20	30	10
B,C,D	10	45	20	30	20

Problem C is produced by introducing to the unreinforced slope of Problem B three anchors placed at 2m, 5m and 8m horizontal distance from the toe of the slope. The total anchor length is 6m, with 1m being the fixed length (grout bulb) (Figure 5c). Each anchor provides a resistance force of 20kN/m, decreased proportionally if part of the fixed length lies inside the failing soil mass. In Problem D, a stabilizing berm is added to the slope of Problem B (Figure 5d). The properties of the berm material (granular fill) are c_{berm}=5kPa, ϕ_{berm}=40º and γ_{berm}=20kN/m^3. Figure 5 also shows the precise FS_{min} and corresponding critical slip circle for

each problem, which were established by exhaustive random searches over the course of a few days.

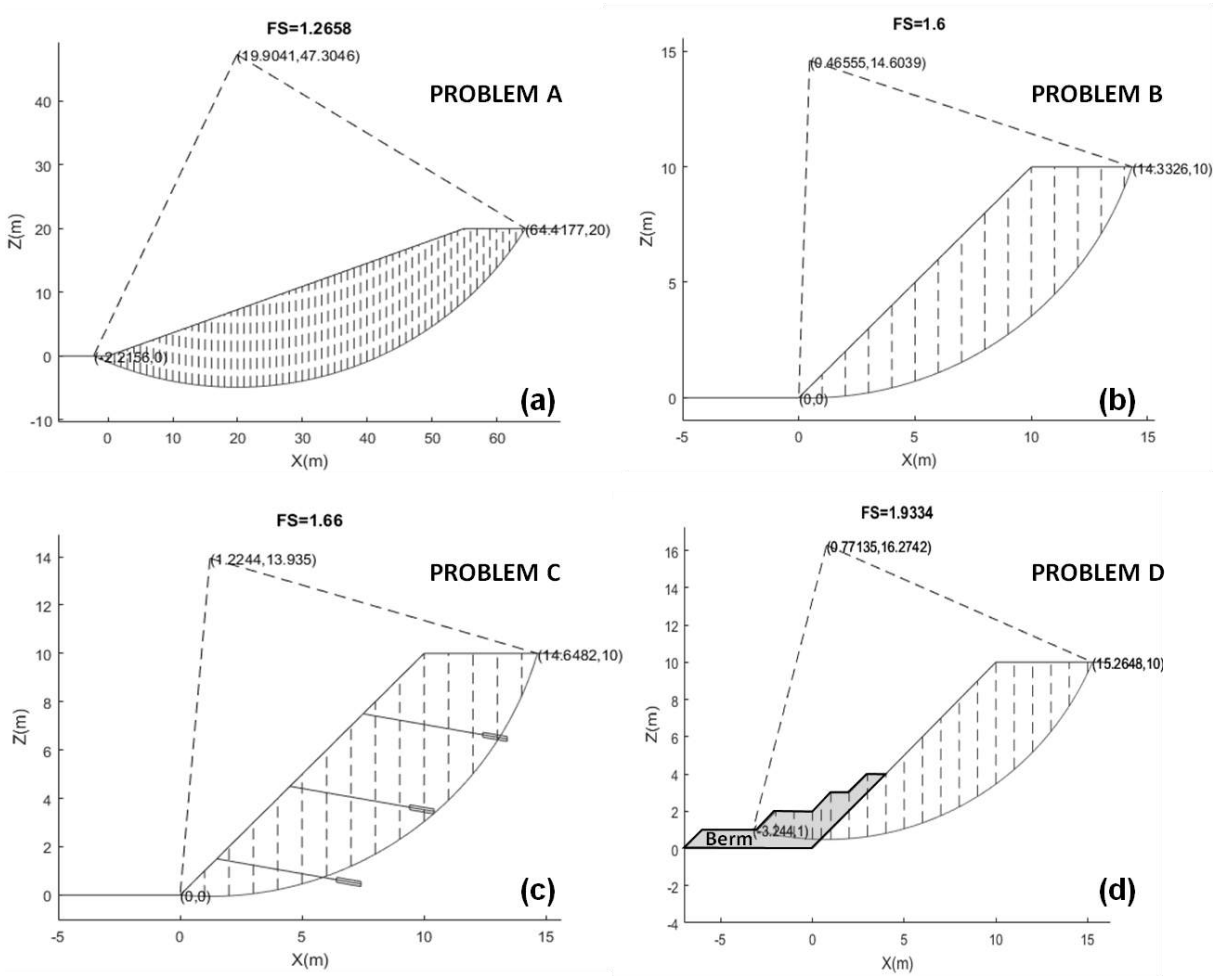

***Figure 5**. Critical slip surface and FS_{min} for the examined problems.*

The computations of the optimization algorithms proceed until a maximum number of interactions (computational loops) equal to 100 is exceeded or until the algorithm finds a solution with relative error less than 0.01% with respect to the exact $FS_{\min}$. For PSO and SGA, c_1=1, c_2=1 and w=0.9^{k-1} in Eq. (2), where k is the current step (interaction) number. For GA and SGA, the percentages of the population that undergo mutation, cross-breeding and elite cross-breeding are 20%, 60% and 20%. In cross-breeding, offsprings are produced by random linear combinations of the parents (e.g. $x_1^{(\text{offspring})} = rand \cdot x_1^{(\text{parent1})} + (1-rand) \cdot x_1^{(\text{parent2})}$). Finally, SGA is executing 10 PSO steps inside each GA step.

The performance of the algorithms was assessed for three population sizes (Table 2). In the case of SGA, the number in parentheses indicates the sub-population that takes part in the PSO computations.

***Table 2.** Algorithm populations*

Algorithm	**Pop1**	**Pop2**	**Pop3**
GA	10	50	100
PSO	10	50	100
SGA	10(10)	50(20)	100(20)

Due to the random nature of the optimization algorithms, each time they are applied to a given problem they exhibit a different success rate and, as a consequence, the assessment of their performance cannot rely on just one application to each problem. Hence, the problems of Figure 5 were solved using the same algorithm 100 times.

Tables 3 and 4 show the maximum error (difference between calculated FS_{min} and exact FS_{min}) from all 100 runs. It can be seen that for simple problems, such as A and B, all algorithms perform very well, with the maximum error rarely affecting the 3rd decimal of FS (Table 3). However, in the case of reinforced slopes, problems C and especially D, the methods GA and PSO exhibit significant errors in the calculated FS_{min} (Table 4). Moreover, PSO in the case of Problem D converges to local minima substantially far from the exact FS_{min} value, even when increased population sizes are considered. On the contrary, the hybrid approach (SGA), performs equally well even in the case of reinforced slopes.

Figure 6 presents the average computational time among the batch of 100 runs performed for each algorithm. It can be seen that GA is the most computationally expensive when large population sizes are employed, while PSO is the fasted. The average computational cost of SGA falls generally between that of PSO and GA despite involving two nested computational loops.

Table 3. *Maximum error in calculated FS_{min} in unreinforced slopes*

Algorithm	**Problem A**			**Problem B**		
	Pop1	***Pop2***	***Pop3***	***Pop1***	***Pop2***	***Pop3***
GA	0.0049	0.0045	0	0.0003	0.0005	0.0125
PSO	0	0	0	0.0007	0	0
SGA	0	0	0	0	0	0

Table 4. *Maximum error in calculated FS_{min} in reinforced slopes*

Algorithm	**Problem C**			**Problem D**		
	Pop1	***Pop2***	***Pop3***	***Pop1***	***Pop2***	***Pop3***
GA	0.0110	0.110	0.0029	0.0347	0.0098	0.0091
PSO	0.0110	0.0010	0.0009	0.1262	0.1256	0.1255
SGA	0.0011	0.0009	0	0	0	0

5. CONCLUSIONS

Three heuristic optimization algorithms, namely Particle Swarm Optimization (PSO), Genetic Algorithm (GA) and Swarming Genetic Algorithm (SGA), were used for the determination of the critical slip surface of uniform slopes with or without stabilization measures. It was found that the hybrid approach (SGA), by combining the computational speed of PSO and the heuristic flexibility of GA, turns to be the best performing. Although more computationally expansive than PSO, it always manages to overcome local minima and converge with good accuracy to the true minimum factor of safety.

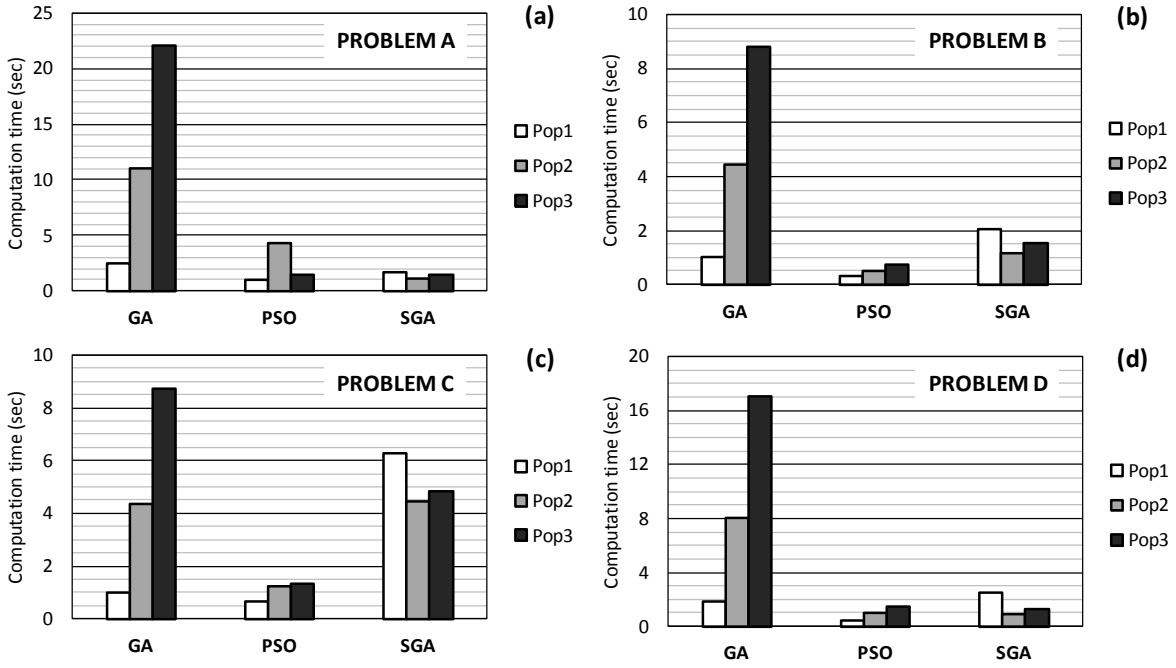

Figure 6. *Average computational times spend by the optimization algorithms.*

REFERENCES

[1] Cheng, Y.M., Li, L., Chi, S., Wei, W.B., 2007. "*Particle swarm optimization algorithm for the location of the critical non-circular failure surface in two-dimensional slope stability analysis*", Computers and Geotechnics, 34(2): 92–103.

[2] Kahatadeniya K.S., Nanakorn P., Neaupane, K.M., 2009. "*Determination of the critical failure surface for slope stability analysis using ant colony optimization*", Engineering Geology, 108(1–2), 133–141.

[3] McCombie, P., Wilkinson, P., 2002. "*The use of the simple genetic algorithm in finding the critical factor of safety in slope stability analysis*", Computers and Geotechnics, 29(8): 699–714.

[4] Zolfaghari, A.R., Heath, A.C., McCombie, P.F., 2005. "*Simple genetic algorithm search for critical non-circular failure surface in slope stability analysis*", Computers and Geotechnics, 32(3): 139–152.

[5] Holland, J.H., 1975. "*Adaptation in natural and artificial systems Ann Arbor*", University of Michigan Press, 975 pages.

[6] Kennedy, J., Eberhart, R., 1995. "Particle swarm optimization", Proc. IEEE International Conference on Neural Networks, pp. 1942-1948. Perth, Australia

[7] Bishop, A.W, 1955. "*The use of the slip circle in the stability analysis of slopes*", Géotechnique, 5(1): 7–17.

[8] Shi, X.H.,. Liang, Y.C., Lee, H.P., Lu C., Wang L.M., 2005, "*An improved GA and a novel PSO-GA-based hybrid algorithm*", Information Processing Letters, 93(5): 255–261.

[9] Dong, N., Wu, C.-H., Ip, W.-H., Chen, Z.-Q., Chan, C.-Y., Yung, K.-L., 2012. "*An opposition-based chaotic GA/PSO hybrid algorithm and its application in circle detection*", Computers and Mathematics with Applications, 64(6): 1886–1902.

NUMERICAL EVALUATION OF THE SOIL BEHAVIOR DURING IMPACT DRIVING OF PIPE-PILES

Reza Daryaei*, *Chair of Soil Mechanics and Geotechnical Engineering, Technische Universität Berlin, r.daryaei@campus.tu-berlin.de*

Montaser Bakroon, *Chair of Soil Mechanics and Geotechnical Engineering, Technische Universität Berlin, m.bakroon@campus.tu-berlin.de*

Daniel Aubram, *Chair of Soil Mechanics and Geotechnical Engineering, Technische Universität Berlin, daniel.aubram@tu-berlin.de*

Frank Rackwitz, *Chair of Soil Mechanics and Geotechnical Engineering, Technische Universität Berlin, frank.rackwitz@tu-berlin.de*

ABSTRACT

During the impact driving of pipe-piles, the soil is influenced in different ways including the void ratio, stress distribution, and plugging formation. Such effects may play an important role in structural design criteria such as the pile's lateral support provided by the soil. Hence, this work is focused on investigating the change in the mechanical characteristics of the soil during impact driving using an advanced numerical analysis tool which is validated against an experimental test. The investigation includes the pile penetration behavior, soil plugging inside the pile, and the change of the lateral stress in the soil during the pile installation. The proposed numerical model is shown to provide similar results compared to experimental measurements. In the simulated test with the current numerical model configuration, the void ratio distribution of the soil is influenced due to pile driving up to a lateral and vertical distance of 2D and 1D, respectively, where D is the pile diameter. Compared to the initial void ratio, the soil inside the pile experienced loosening about 20% while the soil outside is densified about 30% during driving. Moreover, the induced lateral stress inside is more than the one outside the pile, indicating the formation of plugging. Compared to the initial lateral stress state, the pile installation increased the lateral stress up to four times inside and two times outside the pile. Based on the findings of this work, the effects of driving on soil mechanical properties are not minimal and may affect the pile performance including the lateral resistance of the pile. The applied numerical tool, enables the evaluation of the various effects on the soil due to pile driving, leading to a better understanding of the such complex problems.

Keywords: Pipe-Piles, Impact Driving, Soil-Structure Interaction, Multi-Material Arbitrary Lagrangian-Eulerian, Hypoplasticity for Granular Soil

1. INTRODUCTION

Pipe-piles are conventionally used as deep foundation systems, particularly for offshore applications. The choice of the pile installation method depends on various parameters, such as pile dimensions, soil strength, and their interaction. One of the conventional driving methods is the impact installation where the pile is pushed into the soil using a falling mass. Numerical methods have shown great potential as an evaluation tool for geotechnical problems in recent decades. Yet, the installation processes are difficult to simulate using common numerical formulations due to significant and complex soil deformation [1], [9].

In addition, granular soils exhibit a non-linear behavior even during the initial loading which cannot be captured using simple elastoplastic-based constitutive models [2].

The objective of this study is to investigate the impact driving technique by using an advanced numerical model in terms of the required force of the pile installation, pile penetration behavior, plugging formulation inside the pile, and the change of the soil state outside the pile during the installation. Despite showing the potential of the numerical approach in reproducing real geotechnical problems with reasonable accuracy, the outcome of this study shall be considered among the first steps toward a better understanding of the effect of the installation method on the soil stress and void ratio distributions as well as on pile-soil-interaction.

The effect of the installation method on the soil and the neighboring structures have been studied in several works. In a work done by Hartung [3], the effect of the installation method on the bearing capacity for open-ended piles was investigated. It was concluded that in case of impact driving, the soil exhibits different behavior based on its initial density. Depending on its initial density state, the soil around the pile shaft contracts or dilates. Nevertheless, an increase in lateral stress is always observed in areas near the pile tip [3].

Concerning the numerical simulation of pile driving, special care should be given because of the significant local soil deformations and complex material flow usually encountered. These may cause several issues when classical numerical methods based on the Lagrangian formulation are used, including solution divergence, inadequate soil-structure interaction, and accuracy loss. Therefore, a robust alternative numerical technique should be devised.

Recently, a robust numerical alternative called MMALE (Multi-Material Eulerian Arbitrary Lagrangian Eulerian), originally developed for fluid dynamical problems, has been adapted to capture large soil deformation during pile installation [4]. This method has been verified and validated based on various geotechnical problems involving large deformation [4], [5] and, therefore, constitutes a cost-effective evaluation tool for such problems. A recent work done by Daryaei et al. [6], investigated the effect of frequency in achieved penetration depth in the vibratory installation of pipe piles.

The structure of this paper is as follows. In section 2, the state of the art in the numerical modeling of pile installation and complex soil behavior is presented. The numerical model development including the validation is also discussed in section 2. Afterward, the simulation results are presented and discussed in section 3. Finally, the conclusion of this study and outlook on future works are presented.

2. METHODOLOGY

2.1. The MMALE Numerical Approach

The MMALE method can be considered as an advanced mesh-based numerical formulation which benefits from the advantages of both classical Lagrangian and Eulerian formulations of the Finite Element Method (FEM) [1]. In the Lagrangian formulation, the computational mesh moves and deforms in accordance with the material particles, as if mesh points are fixed to the particles. This constraint causes considerable shortcomings when the soil significantly deforms, including large element distortion, solution divergence, or unreliable results. On the contrary, the mesh is fixed in the Eulerian formulation allowing the material to move independently through the mesh. In other word, the solution variables are transported relative to the fixed (original) mesh. Despite solving the large deformations and vorticity issues, additional techniques for treating path-dependent material behavior and tracking material interfaces become necessary in the Eulerian formulation [1].

The MMALE method generally applies a three-step scheme to advance the solution in time. In the first step, the mesh deforms as in the classical Lagrangian formulation. Then, a new less distorted grid is generated. Subsequently, the solution variables are transported to the new mesh as in the Eulerian formulation [7]. In MMALE, multiple materials inside one element can be considered which significantly improves the formulation in case of extremely large deformations. Usually, a material-free or void zone is defined within the grid without mass nor strength, so that other materials can flow into these regions of the physical space. For a more detailed theoretical background of the method, the reader is referred to [7], [8].

2.2. The Hypoplastic Constitutive Equation

The mechanical behavior of soils, especially granular soils, is very complex and requires special treatments. One of the features of granular materials such as sand is its non-linear behavior where the simultaneous elastic and plastic deformation occurs during the loading. [2].

Hence, an alternative concept called the hypoplasticity is introduced which captures the inelastic deformation from the beginning of the loading and does not distinguish between elastic and plastic deformation. The hypoplastic constitutive model is popular for its simplicity where loading and unloading steps are considered in a single incrementally nonlinear equation. The stress rate of the granular material, $\dot{\mathrm{T}}$, is determined by the effective stress, T, intergranular strain, δ, and the void ratio, e [9]:

$$\dot{\mathbf{T}} = \mathcal{M}(\mathbf{T}, \mathrm{e}, \delta) : \mathbf{D} \qquad (1)$$

Besides the stress rate, the void ratio in the Eq. (1) is governed by the minimum and maximum void ratio, e_i and e_d, respectively as well as the critical void ratio, e_c.

Since the introduction of hypoplasticity, numerous material models were developed to adapt the model to various loading conditions. In this study, the hypoplastic equation presented by Niemunis and Herle [9] is used which is the improved version of the hypoplastic equation developed by von Wolffersdorff [10]. The improvement addresses the previous issues of the model in reflecting the accurate strain accumulation during the cyclic loading [9]. Previous application of this version of the hypoplastic material model in large deformation geotechnical problems showed good agreement with experimental results [11].

2.3. Soil-Structure Interaction

The MMALE model developed in this study employs the penalty contact scheme for soil-pile interaction. The contact force is measured based on the arbitrary penetration of the parts. This is considered by adding an additional term (also called a penalty term) to the energy equation as follows [12]:

$$\Pi = \mathrm{E_p} + E_k + \frac{1}{2} k \Delta u^2 \qquad \mathbf{(2)}$$

Where E_p and E_k are potential and kinetic energy, respectively, k is the spring stiffness resembling the contact interface, and u is the arbitrary penetration of two contact parts.

2.4. General Remarks About the Numerical Model

An axisymmetric MMALE model is developed to reduce the computational costs associated with a fully three-dimensional model. The model is developed to back-calculate a small-scale experimental test done at TU Berlin whose configuration is shown in Figure 1.

The rigid pile has 1.5 m height, 0.2 m diameter, and 0.004 m thickness which is modeled using the conventional 2D Lagrangian shell element formulation with reduced integration point and a uniform element size of 0.004 m.

For the soil and void, a mesh with 1.6 m height and 0.85 m radius with the one-point integration MMALE shell element formulation is generated [13]. A structured mesh, ranging from 0.004 – 0.04 m element width is used. The mesh contains the soil up to a height of 1.4 m. A void domain with 0.2 m height, which has neither mass nor strength, is defined above the soil material to enable the soil to move to this domain after penetration starts [13]. The hypoplastic material model is adopted, whose corresponding material constants for Berlin sand are listed in Table 1. The relative density of the soil is Dr=75% ($e_{initial}$=0.465). The initial stress in the soil is defined with assigning the gravity acceleration as 10 m/s2 and using the lateral earth pressure, K_0=0.5.

Table 1. *Hypoplastic material constants for Berlin sand*

φ_c (°)	h_s (Mpa)	n	e_{d0}	e_{c0}	e_{i0}	α	β	m_R	m_T	R	χ	β_r
31.5	230*	0.3	0.391	0.688	0.791	0.13	1	4.4	2.2	1×10^{-4}	6.0	0.2

*The actual value of granular hardness, h_s, is 2300 MPa. This value is reduced by 10% due to low-stress soil state

To define the coupling between pile and soil, penalty contact is defined. A tangential friction coefficient of 0.38 is assigned ($2/3 \tan\phi$). The pile is fixed against horizontal displacements while the lateral sides of the soil are constrained against motion in directions normal to their faces, with fixity applied in all directions at the bottom of the soil.

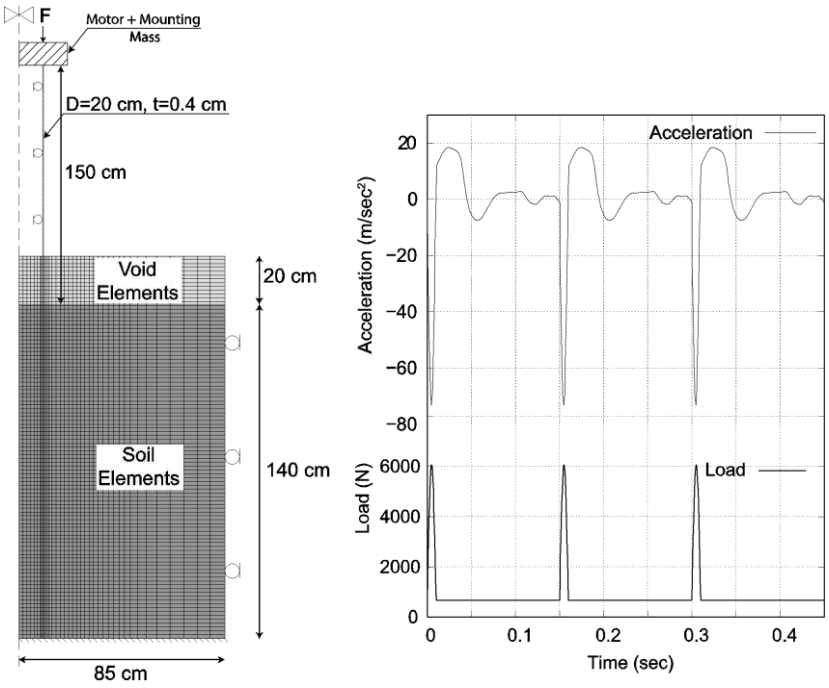

Figure 1. *Numerical model configuration of the pile driving experiment (left) Load application curve and the induced pile acceleration during the impact driving (right)*

The numerical simulation consists of two phases. The pile is embedded at the depth of 0.1 m due to numerical stability considerations. Initially, the pile is let to penetrate by its own weight as was done in the experimental test. Subsequently, the driving force is applied. In the case of the impact driving, the weight and the height of the falling mass is often available, which should be converted to the applied load on the pile head. According to Al-Kafaji [14], one can alternatively use the following equation:

$$f_{max} = \frac{\pi\eta m\sqrt{2gh}}{2t} = \frac{\pi \times 0.765 \times 22.1 \times \sqrt{2 \times 9.81 \times 0.28}}{2 \times 0.01} = 6.224\ kN \quad (3)$$

Where η is the reduction factor due to energy dissipation during impact, m and h are the mass and falling height of the drop weight, t is the impact duration which represents the duration in which the falling mass and the pile are in contact, and g is the gravity acceleration.

The imposed dead load on the pile due to self-weight, motor and mounting is about $F_s = 0.674$ kN. The total duration of the experiment was 354 seconds which corresponds to an impact rate of 0.5 Hz (177 blows). The underlying reason for the long duration was the long intervals between each blow because the mass had to be lifted up and prepared for the next blow. In the numerical model, however, this duration is computationally expensive. The intervals between each blow should be decreased to reach a suitable computation cost. However, the blow intervals should not be placed too close either. In principle, the optimum interval should be determined by evaluating the duration, in which the pile acceleration varies significantly. In other words, the next blow should be applied at the time, at which the pile is at a steady state. Figure 1 shows the acceleration history of the pile due to one impact. In this case, the interval of 0.15 is adequately large enough to avoid overlapping in the acceleration of the pile. The loading history curves of both pile driving methods are shown in Figure 1.

3. RESULTS AND DISCUSSION

The numerical model is validated against an experiment conducted at the laboratory of the Chair of Soil Mechanics and Geotechnical Engineering at Technische Universität Berlin (TU Berlin). Details regarding the test set-up are available in the work done by Le et al. [15]. The experiment includes a half-cylindrical pile with 1.5 m length, 0.004 m thickness, and 0.2 m outer diameters placed in a container filled with the Berlin sand and consists of three rigid steel walls and a glass panel. The pile movement is constrained in the horizontal direction using pile guides.

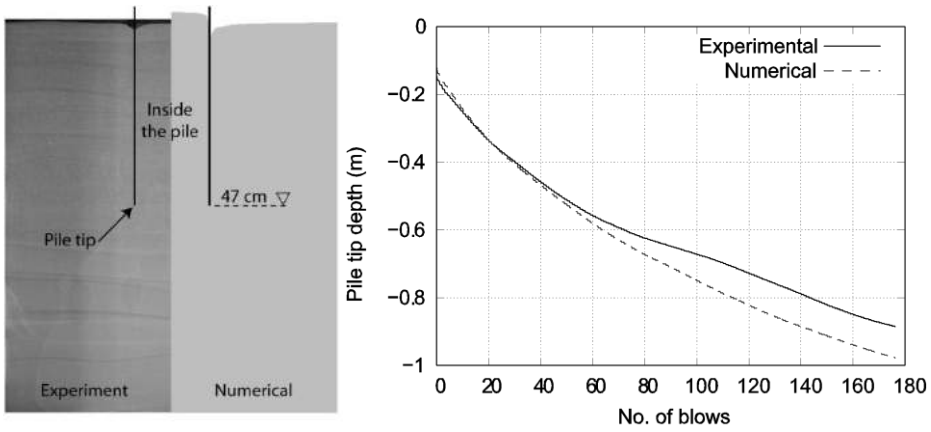

Figure 2. *Comparison of the soil deformation (left), and time-penetration-curve from the numerical models and the experiments (right)*

The deformed shape of the soil inside and outside the pile is compared with the one captured from the experiment in Figure 2. The height of the entrapped soil inside the pile is at this stage overestimated. This can be attributed to the assignment of the reduced granular hardness parameter of the hypoplastic model, h_s, in the constitutive equation due to low confining stress regions [16]. On the other hand, the outer part of the soil surface calculated in the numerical model is in good agreement with what is observed in the experiment. The time-penetration-curves from the model and the experiment is also compared (Figure 2 right). At early stages of driving, the model is close to the experiment. After 60 blows, the numerical model starts to overestimate the penetration. After 120 blows, the penetration rate of both curves become equal.

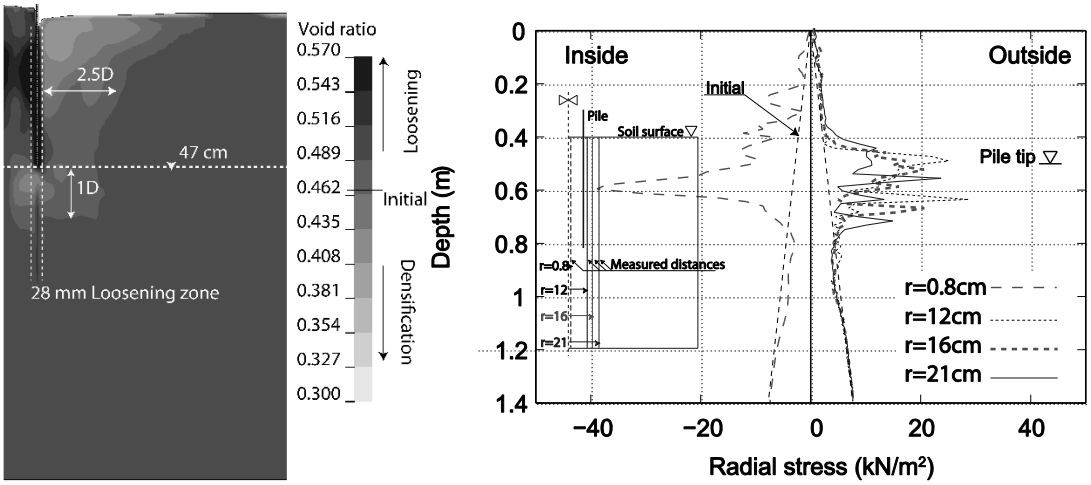

Figure 3*. Void ratio distribution (left) and Horizontal stress distribution over the soil depth inside and outside the pile at the pile tip depth of 0.46 m (right)*

Figure 3 shows the void ratio distribution at the pile tip depth of 0.47 m. The entrapped soil inside the pile exhibits loosening, unlike the outer part. The lateral and vertical influence distance of the soil is 2.5D and 1D, respectively, where D corresponds to pile diameter. Moreover, a thin area around the pile shaft with a width of 0.028 m has also experienced loosening due to the impact force. This loosening may facilitate driving performance by reducing the frictional resistance.

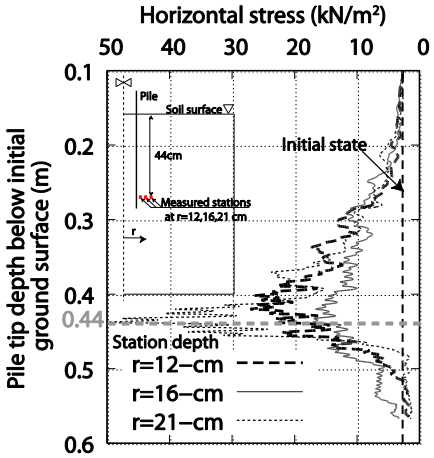

Figure 4. *Horizontal stress history at three stations outside the pile, at the depth of 47 cm during impact (positive value indicates compression).*

The lateral stress distribution over the depth inside and outside the pile at one time stamp is also shown in Figure 3 where the r is the lateral distance of the measuring stations from the axis of symmetry. One station is chosen inside the pile close to the axis of symmetry, r = 0.008 m, and three stations outside the pile at distances of r = 0.12, 0.16, and 0.21 m. The outer wall of the pile is located at a lateral distance of r = 0.1 m. Significant variations are noticed at the depth of 0.4-0.8 m. These variations are along with notable oscillations which can be attributed to the dynamic nature of the impact pile driving. The maximum lateral stress is observed at almost 0.1 m under the pile tip which is two times and four times more than the initial stress outside and inside the pile, respectively. Afterward, the stress decrease until the depth of 0.8 m where the initial stress state of the soil is reached again. In addition, the induced stress due to driving is decreased by 50% from r = 0.12 to 0.21 m.

The induced stress inside the pile is about two times greater than the outside. Therefore, it may be argued that plugging occurs. This cannot be initially concluded from the soil surface in Figure 2 as the surface of the entrapped soil is higher than the surface outside the pile. This can be justified with the fact that at initial stages of the penetration soil heaving was observed. Afterward, this heaving decreases with further driving. In addition, by evaluating Figure 3 it is clearly seen that the plug is formed inside the pile at the final stage of the model.

Figure 4 depicts the change in lateral stress during the driving at three stations located at the depth of 0.44 m and at the same lateral distance of those in Figure 3. Initially, a limited increase in lateral stress is observed up to a depth of 0.25 m. Then, the stress starts to increase rapidly until the pile reaches the depth of the 0.44 m. Afterward, the lateral stress decreases drastically as the pile penetrates further until it reaches the initial stress state at the depth of 0.6 m. The rate of decrease is more than the rate of increase.

4. CONCLUSION

In this study, the effects of impact driving during pipe-pile installation in granular soil is numerically investigated, using the advanced numerical tool MMALE in conjunction with an advanced hypoplastic constitutive equation. The investigation criteria include the induced horizontal stress inside and outside the pile, change in void ratio, and pile penetration.

The penetration curve was initially in good agreement with the experiment. After reaching a time corresponding to one-third of the blows, the numerical model started to overestimate the penetration. After applying two third of the blows, the penetration rate of the numerical model became identical to the one in the experiment and hence the difference was maintained. The final difference in the pile tip depth compared to the experiment was about 10% more.

By evaluating the void ratio, loosening inside the pile and densification outside the pile was observed. The influence area corresponded to 2.5D in lateral and 1D in the vertical direction. Also, a loosening area was formed around the pile shaft due to the disturbance from the driving.

Using the lateral stress, the formation of a soil plug was confirmed. Moreover, a limited depth of the soil was affected during the driving, up to the depth of 2D under the pile tip. At a lateral distance of 2D outside the pile shaft, the values of the induced lateral stress reduced to almost 50% of that in distance of 1D. The maximum lateral stress is two times and four times more than the initial stress outside and inside the pile, respectively. During the penetration, the lateral stress at a stationary point increases as the pile penetrates until it reaches the same depth as the station. Afterward, it starts to decrease at a significantly faster rate than it increased previously.

This study may be considered as a first step toward numerical simulation of impact pile driving. Based on the presented results, the numerical approach is shown to be capable of reproducing complex geomechanical problems relatively close to the experimental test. In addition, it provides a handful of evaluation tools which may be cumbersome or require sophisticated approaches to obtain using other approaches. To this extent, a coupled formulation can be implemented which is expected to simulate the offshore installation problems more accurately.

ACKNOWLEDGMENT

The authors are thankful for the partial financial support obtained from Deutscher Akademischer Austauschdienst (DAAD) with grant number 91561676 and the Elsa-Neumann scholarship of city Berlin (NAFOEG) with grant number T68001.

REFERENCES

[1] Benson, D. J., 1992. "*Computational Methods in Lagrangian and Eulerian Hydrocodes*," Computer Methods in Applied Mechanics and Engineering, vol. 99, no. 2–3, pp. 235–394.

[2] Kolymbas, D., 2012. "*Constitutive Modelling of Granular Materials"*, Berlin, Heidelberg: Springer Berlin Heidelberg.

[3] Hartung, M., 1994. "*Einflüsse der Herstellung auf die Pfahltragfähigkeit in Sand,*" Braunschweig, Techn. Univ.

[4] Bakroon, M., R. Daryaei, D. Aubram, and F. Rackwitz, 2018. "*Multi-Material Arbitrary Lagrangian-Eulerian and Coupled Eulerian-Lagrangian Methods for Large Deformation Geotechnical Problems*," in Numerical Methods in Geotechnical Engineering (NUMGE 2018), p. 8.

[5] Bakroon, M., R. Daryaei, D. Aubram, and F. Rackwitz, 2019. "*Numerical Evaluation of Buckling in Steel Pipe Piles During Vibratory Installation*," Soil Dynamics and Earthquake Engineering, vol. 122, pp. 327–336.

[6] Daryaei, R., M. Bakroon, D. Aubram, and F. Rackwitz, 2019. "*Numerical Investigation of the Frequency Influence on Soil Characteristics During Vibratory Driving of Tubular Piles*," in *International Congress and Exhibition "Sustainable Civil Infrastructures: Innovative Infrastructure Geotechnology*, H. Shehata and C. S. Desai, Eds. Cham: Springer International Publishing, pp. 48–61.

[7] Bakroon, M., R. Daryaei, D. Aubram, and F. Rackwitz, 2017. "*Arbitrary Lagrangian-Eulerian Finite Element Formulations Applied to Geotechnical Problems*," in *Numerical Methods in Geotechnics*, vol. 41, J. Grabe, Ed. Hamburg, Germany: BuK! Breitschuh & Kock GmbH, pp. 33–44.

[8] Aubram, D., F. Rackwitz, and S. A. Savidis, 2017. "*Contribution to the Non-Lagrangian Formulation of Geotechnical and Geomechanical Processes*," in *Holistic Simulation of Geotechnical Installation Processes - Theoretical Results and Applications, ch. 3. Lecture Notes in Applied and Computational Mechanics*, vol. 82, T. Triantafyllidis, Ed. Springer International Publishing, pp. 53–100.

[9] Niemunis, A. and I. Herle, 1997. "*Cohesionless Soils with Elastic Strain Range*," Mechanics of Cohesive-frictional Materials, vol. 2, no. 4, pp. 279–299.

[10] von Wolffersdorff, P. ., 1996. "*A Hypoplastic Relation for Granular Materials with a Predefined Limit State Surface*," Mechanics of Cohesive-frictional Materials, vol. 1, no. 3, pp. 251–271.

[11] Bakroon, M., R. Daryaei, D. Aubram, and F. Rackwitz, 2018. "*Implementation and Validation of an Advanced Hypoplastic Model for Granular Material Behavior*," in 15th International LS-DYNA® Users Conference", p. 12.

[12] Wriggers, P., 2006. "*Computational Contact Mechanics", Second Ed., Springer*.

[13] Hallquist, J. O., 2017. "*LS-DYNA: Theoretical manual*", Livermore Software Technology Corporation, Livermore.

[14] Al-Kafaji, I. K. J., 2013. "*Formulation of a Dynamic Material Point Method (MPM) for Geomechanical Problems"*, Ridderprint BV.

[15] Le, V. H., F. Remspecher, and F. Rackwitz, 2019. "*Numerical Investigation of Installation Effects on the Cyclic Behaviour of Monopile Foundation Under Horizontal Loading*," in *Proceedings of the 1st Vietnam Symposium on Advances in Offshore Engineering*, M. Randolph, D. Doan, A. Tang, M. Bui, and V. Dinh, Eds. Hanoi, Vietnam: Springer, Singapore, pp. 389–394.

[16] Aubram, D., 2013. "*An arbitrary Lagrangian-Eulerian Method for Penetration into Sand at Finite Deformation"*, Aachen: Shaker Verlag GmbH.

A SOPHISTICATED QUALITY CONTROL METHOD IN INFRASTRUCTURE PROJECTS: "CONTINUOUS COMPACTION CONTROL "

Rukiye Korkmaz, *Arcadis, Istanbul, rukiye.korkmaz@arcadis.com*

ABSTRACT

Mega projects require innovative and efficient solutions, especially in quality control. In earthworks, the continuous compaction control has found its way into construction practice as an efficient quality control. Since December 2016, CEN / TS17006 has provided the technical regulations for the use of comprehensive dynamic compaction control as a method of quality control in earthworks by using compaction rollers with integrated measuring and documentation systems. For the practical use at construction sites therewith a gap could be closed**.** At the world's largest infrastructure and earthwork project "Istanbul New Airport", lots of experience and new findings have been gained that have broaden the scope of application of the method. For over 2 years, 40 heavy dynamic compaction rollers (smooth-drum rollers with operating weight of 26t) have been used to monitor the compaction quality of up to 2 million square meters of daily compacted layer surface. The bulk material is mainly middle to high plastic clay**.** Based on the experience gained, it is shown that also the quality of compacted clay soils can be monitored effectively with dynamic compaction control. Statistical evaluations of measured values as well as determined correlations between different parameters explain the practical application possibilities of the method for a modern, comprehensive and effective quality control in earthworks. Therewith the use of conventional test methods can be significantly dispensed. A comprehensive quality control in real time is applied, which is not disturbing the construction process.

Keywords: Infrastructure, Embankment, Quality Control

1. INTRODUCTION

In earthworks constructions quality control/ quality assurance of engineering fill is most essential step. The common QA/QC methods for earthworks compaction verification are in-situ spot tests such as sand cone test and nuclear density gauge test. The test amount of this tests is defined in the specifications as 1 test per a certain square meter. With these spot tests low percentage of material being testing in comparison to the entire compacted area. Advancements in technology have provided a new tool that shows significant promise for improving the efficiency of the compaction and compaction verification processes. Continuous Compaction Control (CCC) technology continuously and instantaneously measures machine parameters, global positioning system (GPS) location, and soil response, while offering nearly 100% coverage of the compaction zone. One of the biggest earths move in the construction history was in Istanbul New Airport Project. To prepare a stable platform for apron, runways and taxiways, 60-meter-high embankments had to be constructed. Because of the tight time limit of the project earthworks quality control was not possible with conventional test methods. So Continuous Compaction Control (CCC) method had been adapted to the project. This paper will present the Continuous Compaction Control (CCC) application in Istanbul New Airport Project earthworks QA/QC.

2. CONTINUOUS COMPACTION CONTROL (CCC)

Continuous compaction control systems are designed to monitor the compaction process just in time while operating the roller. Application of the system improves the ability of the roller operator to track the compaction process directly by observing machine provided values on the screen of the control unit. Well trained and experienced operators might be able to work independently to improve quality of compaction at locations showing insufficient results.

CCC rollers are equipped with acceleration transducers, a data processing and display system and a GPS system (Fig-1). The data processing and display system records, processes and displays the drum - soil interaction. The GPS system records corresponding location (x, y and z coordinates) of the measurements.

Roller integrated continuous compaction control system (CCC) is based on the dynamic interaction between the excited drum of a vibratory roller and the soil that shall be compacted. Vibratory rollers are characterized by a drum that is excited by one or more eccentric masses rotating at a constant speed.

During compaction the roller drum vibrating system is feeding the soil to be compacted continuously with kinetic energy. Both soil density and absorption of kinetic energy is increasing with the level of compaction. By analyzing the vibration behavior, conclusions can be made about the compaction quality. For proper interpretation of CCC measuring values, major influencing parameters as dead weight, amplitude, frequency, operational speed and driving direction of the roller are needed to be considered. Moisture content of soil and evenness of the layer surface are additional parameters which influence the achievable quality of compaction and corresponding CCC measuring results.

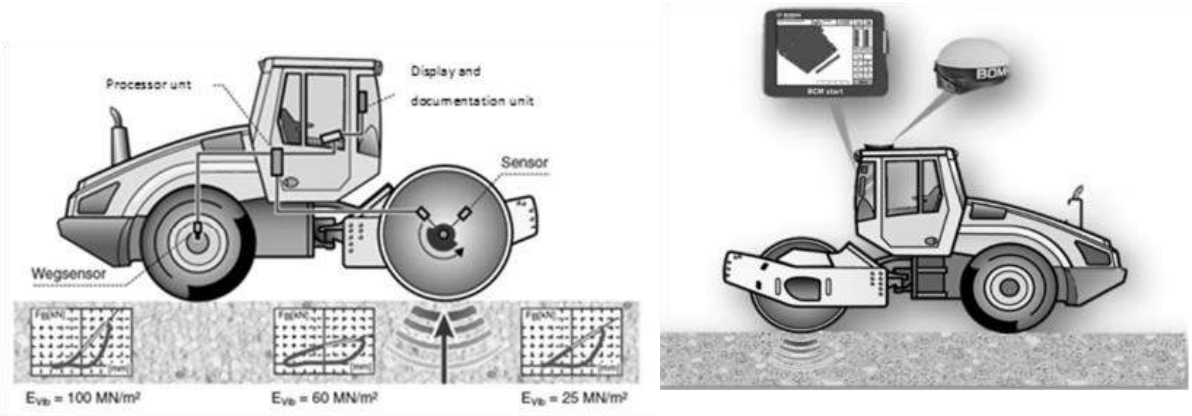

***Figure 1**. Smooth Drum Roller with CCC System*

2.1. Status of Standardization

CCC technology was initiated in Europe in the 1970s and has been used in European practice for nearly 25 years. The first European specifications for roller-integrated CCC methodology was developed in Austria in 1990. Germany was following in 1993 with its own guidelines. These guidelines had been updated in 2014. Today, four European countries have soil compaction QA specifications using roller-integrated CCC (Austria, Germany, Sweden and Switzerland) The U.S. states are beginning to implement pilot specifications (e.g. Minnesota). Principles for application of the CCC testing methodology, evaluation of measuring results and corresponding decision rules are given by the European technical specification CEN/TS 17006 Earthworks – Continuous Compaction Control (CCC), December 2016.

3. ISTANBUL NEW AIRPORT APPLICATION

3.1. Introduction

"Istanbul New Airport", project target for the earthworks construction was up to 1 million cubic meter of fill placement and compaction within a day (24hrs). Considering an average compacted lift thickness of minimum 30 cm, the total lift surface area is estimated to be 3.3 million square meter which had to be managed by the QC program within a 20-hour working period. Based on Turkish and international standards the required scope of QC testing is specified minimum by one in-situ field test per 1,000m² compacted lift surface. Considering above mentioned targeted workload per day, more than 3,300 in-situ spot tests within 20-hrs working period had to be performed and evaluated.

Depending on the type of in-situ testing method and related time amount for execution of each in-situ test, estimated number of staffs had to reach up to more than 200 persons including testing equipment

Therefore, an optimization of testing procedures was essential to increase success and productivity of Quality Control (QC) measures. For this approach roller-integrated continuous-compaction-control (CCC) technology, verified by a certain number of in-situ spot tests, was selected for reaching quality and mass compaction targets and for monitoring compaction success of engineering fill.

Prior to utilization of all CCC systems, provided machine-based values had to be calibrated with the results of in-situ quality control tests to establish correlations between CCC values and engineering parameters of the compacted material as density and / or load bearing capacity.

3.2. Trial Area Construction

In order to receive reliable data from the CCC system it has to be calibrated for each soil type used as engineering fill by large scaled in-situ compaction trials. The layout of the trial field and corresponding laboratory and field-testing programs had been designed by considering the individual fill material properties, available construction equipment and the quality requirements of the project as well. For each type of homogeneous source soil, which shall be used as fill material, individual trials shall be executed for determination of the required parameters and procedures for compaction and quality control measurements.

3.3. Calibration Principles

In earthwork construction requirements on quality of compacted soil layers are normally specified by the relative compaction ratio RC as a function of the soil density. Depending on the applied CCC system interpreted values of the soil stiffness, expressed by the values ks, CMV, CCV or the dynamic load bearing capacity, expressed by the dynamic E-modulus Evib, are being received.

Prior to utilization of the CCC system as quality control testing method the measured values shall be calibrated with the results of conventional quality control test methods to establish the required correlation between CCC and conventional test values. According to the European technical specification CEN/TS 17006 Earthworks – Continuous Compaction Control (CCC), December 2016, a good correlation can be assumed when the coefficient of determination exceeds $R^2 \geq 0.7$. The calibration principle is shown in Figure 2.

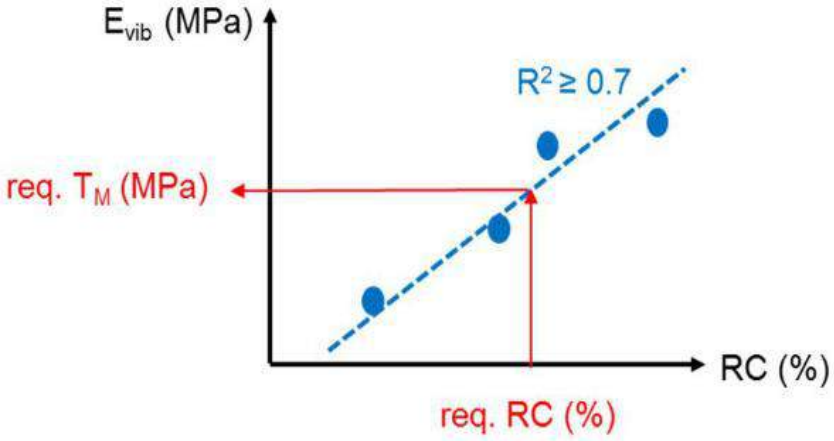

***Figure 2**. Calibration principle for determination of the correlation between CCC values (here: Evib) and conventional parameters (here: RC) and specification of the CCC acceptance value T_M*

The regression analysis should result in a coefficient of determination $r \geq 0{,}70$. If $r \geq 0{,}7$ cannot be achieved, additional tests should be carried out.

If $r \geq 0{,}7$ is still not achieved even after additional tests, then CCC is not permitted for that material

3.4. QA/QC and Approval Procedure of Tested Area

During execution of the CCC measuring process all measured values are recorded and displayed in time on the screen of the documentation unit.

After completion of the testing process on the processed surface of the control area the results will be summarized in a documentation report.

Based on the selected measuring system and roller manufacturer the design of the report and visualization of the data is different but comparable.

It is recommended to configurate the settings of the documentation system accordingly, so that it can be clearly distinguished between CCC values which are below, equal or above the specified CCC acceptance value T_M.

An example for a plan view, displaying recorded measuring results of the control area and the corresponding summary table of the CCC is given in Figure 3 and Figure 4.

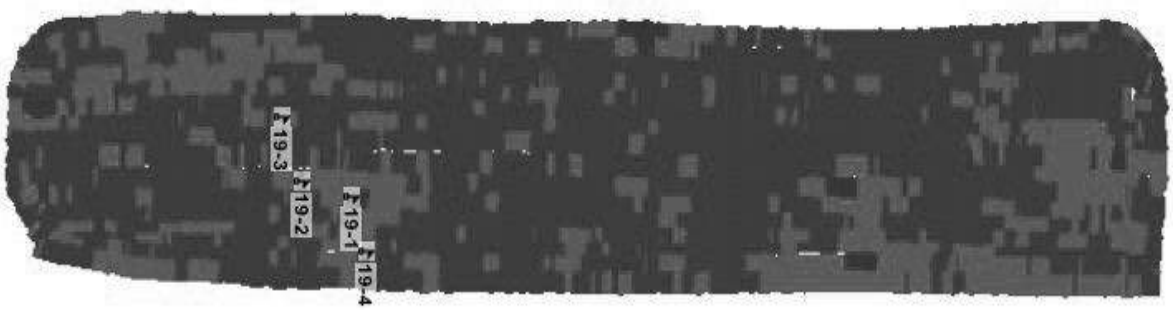

***Figure 3**. Plan View (Example) summarizing CCC measuring Results of a Control Area*

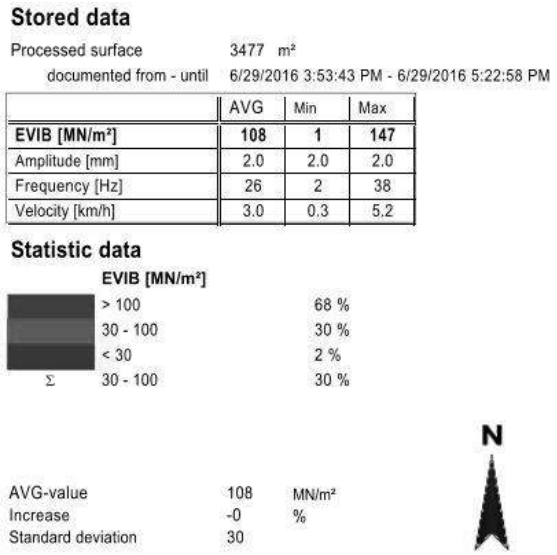

***Figure 4**. Corresponding CCC Summary and statistic Data Table (Example)*

Based on the correlation, the CCC acceptance value T_M shall be specified by considering the 10% minimum quantile. Considering the 10% minimum quantile T_M defines the minimum CCC value which shall be exceeded by ≥ 90% of total recorded values within the control area.

The controlled area shall be checked again by application of additional conventional spot check tests within identified "red" subareas when quantity of CCC values T_M exceeds more than 10%.

Based on the results of the conventional tests within the subarea total area can be accepted in case of values equal or above required values of RC. In case of values lower required RC additional reworking measures as soil replacement or application of additional compaction passes shall be assigned.

4. CONCLUSION

In combination with a good developed method of fill compaction and a corresponding quality control system, application of the CCC system as core instrument for monitoring of the compacted layer quality a high level of testing and quality performance in earthwork construction can be reached.

The actual report intents to create an easy reference for all phases of the CCC implementation and operation. Also, it is important to register that during operational periods results can be quickly evaluated. Areas of insufficient quality can be easily detected, and corresponding corrective measures can be directly initiated when needed.

Finally, is important to emphasize that during the implementation and operation of the CCC system important advantages were observed:

- Reduction quantity of conventional QC testing (80%);
- Applicable for all type of soils;
- Effective construction accompanying QC testing system;
- Delivery of reliable results for assessment of layer compaction quality without options for manipulations as possible by application of conventional test methods;
- Direct and clear identification of areas of insufficient compaction quality;
- Increasing of quality during the evolution of the implementation and training process.

REFERENCES

[1] *Earthworks Continuous Compaction Control (CCC) CEN/TS 17006/2016*.

[2] Hotz, C., "*Continuous Compaction Control (CCC) Hand Book*", Arcadis Report REP-QA00-6 rev00, 31.01.18.

[3] Samaras, A.A., Lamm, R., Treiterer, J., "*Application of Continuous Dynamic Compaction Control for Earthworks in Railroad Construction",* Transportation Research Record, pp 42-46.

[4] Petersen, L., "*Continuous Compaction Control MnRoad Demonstration*", CNA Consulting Engineers, Final Report 2004.

[5] Imran, S.A., Barman, M., Nazari, M., Commuri, S., Zaman, M., Singh, D., 2016. "*Continuous Monitoring of Subgrade Stiffness during Compaction*", School of Electrical and Computer Engineering, The University of Oklahoma, USA, School of Civil Engineering and Environmental Science, The University of Oklahoma, USA, Department of Civil Engineering, Indian Institute of Technology Bombay, Mumbai, India.

[6] Cacciola, D.V., "*Using Continuous Compaction Control Systems Within an Earthwork Compaction Specification Framework"*, M.Sc Thesis, University of Delaware.

[7] White, D.J., Vennapusa, P.K.R.,*"A Review of Roller-Integrated Compaction Monitoring Technologies for Earthworks",* Earthworks Engineering Research Center, Department of Civil Construction and Environmental Engineering Iowa State University.

SEISMIC COEFFICIENT ASSESSMENT OF CONCRETE FACED ROCKFILL DAMS

Selda Durmaz*, *Research Assistant, Muğla Sıtkı Koçman University, seldadurmaz@mu.edu.tr*

Deniz Ülgen, *Assoc. Prof. Dr, Muğla Sıtkı Koçman University, denizulgen@gmail.com*

ABSTRACT

In this study, effects of different parameters on earthquake-induced permanent displacement are scrutinized. A series of pseudo-static and dynamic analyses are performed to investigate the dynamic response of CFRDs with varying slopes and heights. Within the scope of the study, 50m and 200m high dams are subjected to 6 real earthquake records and peak ground accelerations (PGA) of each record are scaled to 0.2g, 0.4g and 0.6g. Downstream and upstream slopes of dams are equal to each other and vary as 1:1.2, 1:1.4, 1:1.6 and 1:1.8. Prior to dynamic analyses pseudo-static analyses are performed using the limit equilibrium approach. Critical slip surfaces are selected at three different heights (0.25h, 0.50h, 0.75h) and seismic coefficients are specified as the 1/2 and 1/3 of the PGA. To find the average acceleration responses of critical slip surfaces two dimensional equivalent linear analyses are carried out using QUAKE/W. Acceleration histories are used to estimate the permanent displacement of CFRDs by utilizing Newmark method. Variation of permanent displacements with respect to FS obtained from pseudo-static analyses. The results are assessed in terms of FS and permanent displacement, to construct a guide to use at the stage of preliminary design of CFRDs..

Keywords: Seismic Coefficient, Concrete Faced Rockfill Dam, Permanent Displacement.

1. INTRODUCTION

Theoretical researches and evaluation of case studies proved the seismic safety of concrete face rockfill dams (CFRD) against the strong earthquake shakings. In terms of engineering perspective, convenience of taller and economical construction and high seismic energy absorption of rockfill material, stimulate the demand. In spite of these advantages, under-designed CFRDs can cause man-made disasters. Therefore, understanding the dynamic response of CFRDs has vital importance. Early studies widely based on factor of safety (FS) calculations of potential sliding block and this parameter alone was insufficient for seismic risk assessment. In time, earthquake induced permanent displacement became mostly used parameter for the seismic performance estimation. Although present deterministic and probabilistic studies cannot cover the well-defined upper boundary needs for permanent displacement, Hyness-Griffin and Franklin [1] suggested a maximum 100 cm deformation to label the dam as safe. Okamoto [2] observed a higher response at crest compared to the other parts of embankment dams, and suggested to be careful to this behavior of crest at design stage. In terms of earthquake induced slope displacements, Bray [3], Bray and Travasarou [4] worked on probabilistic approaches. Their works provided predictive equations for potential seismic displacements. Zhou et al. [5] conducted 1200 analyses to search the effects of slope, dam height, response spectrum of earthquake, width of valley on seismic response of dams. Analyses show that maximum crest accelerations are decreasing with increase in slope (increasing of valley width). Yu et al. [6] worked on earth and rock fill dams. Their results are in direction of decreasing maximum crest accelerations with increasing peak ground accelerations. Seismic

response of these dams are less affected by slope and crests of dams give higher response to earthquake load. Engineers are still looking for a simple and realistic approach to dynamic response evaluation of CFRDs.

Pseudo-static analysis is one of the useful method for the seismic slope stability assessment. The most difficult stage in this method is the selection of pseudo-static coefficient (k_s). There are some suggested values for this coefficient including exact values as 0.05 - 0.15 in the United States, 0.12 - 0.25 in Japan and functional values as 1/2 to 1/3 of peak horizontal acceleration (PHA) recommended by Marcuson [7] and 1/2 of PHA recommended by Hyness-Griffin and Franklin [1]. In this study k_s values are chosen as 1/2 and 1/3 of peak ground acceleration and the analyses results are presented in comparison with permanent displacements.

2. METHODOLOGY AND KEY RESULTS

In this study, effects of different parameters on earthquake-induced permanent displacement are investigated. The results are assessed in terms of FS and permanent displacement, to construct a guide to use at the stage of preliminary design of CFRDs. 50m and 200m high dams are subjected to 6 real earthquake records and peak ground accelerations (PGA) of each record are scaled to 0.2g, 0.4g and 0.6g. Downstream and upstream slopes of dams are equal to each other and vary as 1:1.2, 1:1.4, 1:1.6 and 1:1.8. Input parameters and earthquake motions are given in Table 1 and Table 2, respectively.

Table 1. *Inputs of Dynamic Analyses*

Dam Height (m)	PGA (g)	Internal Friction Angle (ϕ) (°)	Upstream and Downstream Slope
50-200	0.2-0.4-0.6	35-40-45-50	1:1.2-1:1.4-1:1.6-1:1.8

Table 2. *Earthquakes Used in Analyses*

Earthquakes	Date	Fault Mechanism	Predominant Period(s)	Moment Magnitude (M_w)
Cape Mendocino	1992	Thrust	0.12	7.2
Northridge	1994	Thrust	0.22	6.7
Kobe	1995	Strike Slip	0.44	6.9
Düzce	1999	Strike Slip	0.82	7.2
Landers	1992	Strike Slip	0.02	7.3
Tabas	1978	Thrust	0.54	7.4

Prior to dynamic analyses pseudo-static analyses are performed using the limit equilibrium approach. Critical slip surfaces are selected at three different heights (0.25h, 0.50h, 0.75h) as illustrated in Figure 1 and seismic coefficients are specified as the 1/2 and 1/3 of the PGA. Two dimensional equivalent linear analyses are carried out using QUAKE/W to find the average acceleration responses of critical slip surfaces. These histories are used to estimate the permanent displacement of CFRDs by utilizing Newmark [8] method.

Variation of permanent displacements with respect to FS obtained from pseudo-static analyses are shown in Figure 2. As seen in Figure 2a and 2c, permanent displacements are under the

limit value of 100 cm proposed by Hyness-Griffin and Franklin [1] when ks is 1/2 of PGA and FS is larger than 1. When ks is selected as 1/3 of PGA, only a few cases exceed the limit value of 100 cm (Figure 2b and 2d). These results are in agreement with the recommendations of Marcuson [7]. Moreover the findings show that permanent displacements of 50 m CFRD are slightly higher than those of 200 m CFRD. This difference can be attributed to the natural period and damping characteristics of dams.

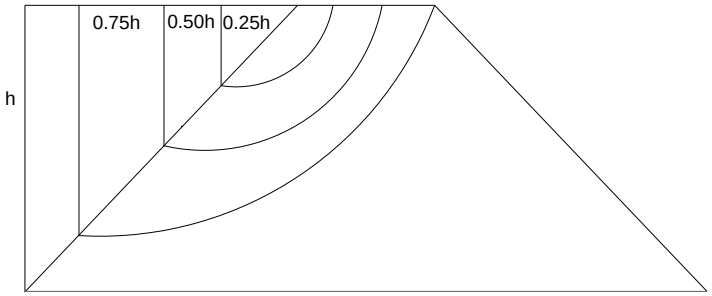

***Figure 1**. Critical slip surfaces*

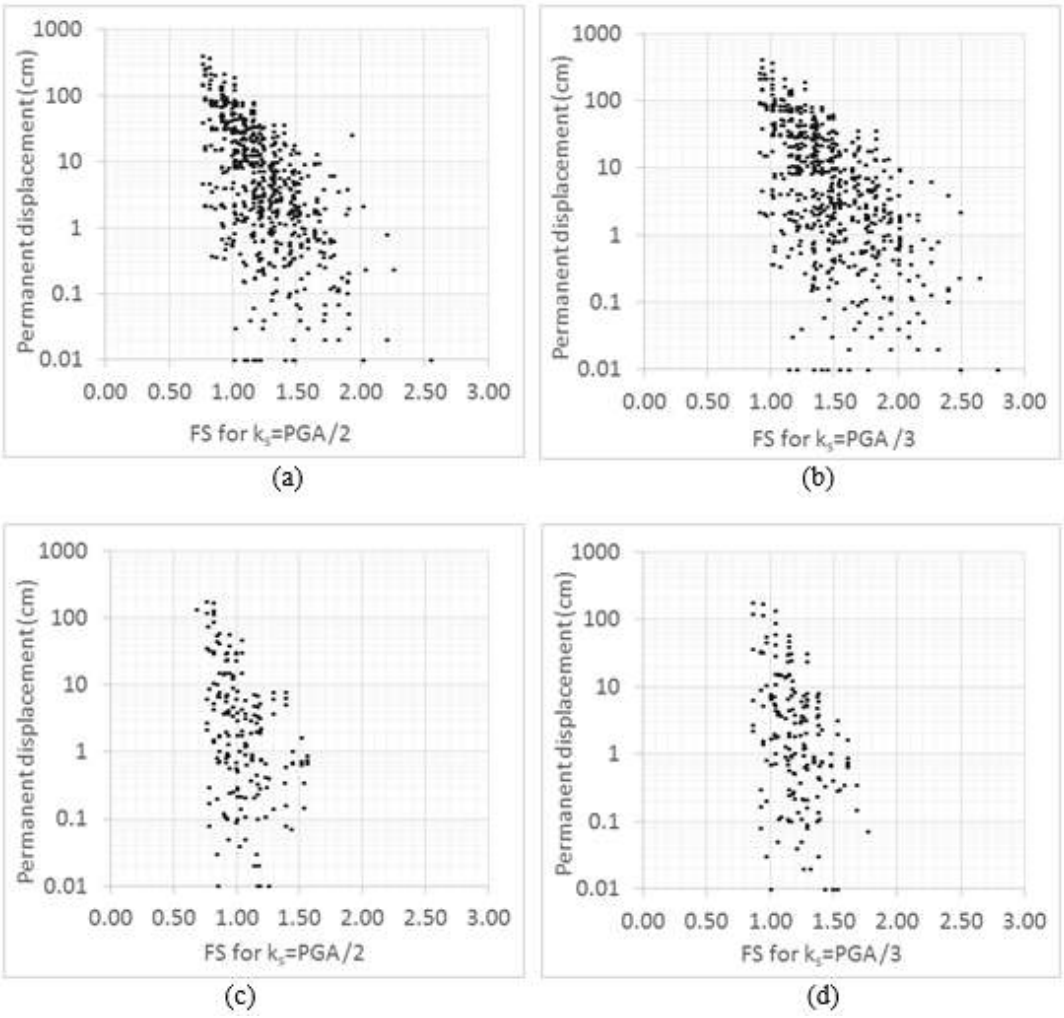

***Figure 2**. Relation between FS and permanent displacement*
(a) 50 m dam with k_s= PGA/2 (b) 50 m dam with k_s= PGA/3
(c) 200 m dam with k_s= PGA/2 (d) 200 m dam with k_s= PGA/3

3. CONCLUSIONS

In the present study, a series of pseudo-static and dynamic analyses are performed to investigate the dynamic response of CFRDs with varying slopes and heights. 6 different real earthquake records with 0.2g, 0.4g and 0.6 g peak ground accelerations are used. In consequence of analyses, seismic coefficients and permanent displacements of CFRDs are scrutinized.

i. Results indicate that acceleration response of dam is less affected by the slope of dam. It is seen that most significant parameters acting on response of CFRDs are earthquake parameters (duration, frequency, PGA).
ii. When the seismic coefficient is used as 1/3 of PGA, exceedance of 100 cm limit value is calculated at a few number of analyses. (Figure 2b and 2d). This results correspond to recommendations of Marcuson [7].

Estimated permanent displacements of 200 m CFRD are slightly lower than those of 50 m CFRD. The most likely reasons for that difference are the natural periods and the damping characteristics of dam.

REFERENCES

[1] Hyness-Griffin, M.E., Franklin, A.G., 1984. "*Rationalizing the seismic coefficient method*", Miscellaneous Paper GL-84-13, US Army Corps of Engineers Washington, DC 20314.

[2] Okamoto, S. 1984. "*Introduction to Earthquake Engineering 2nd Edition*", University of Tokyo Press, pp.466-477.

[3] Bray, J. D., 2007. "*Chapter 14: Simplified seismic slope displacement procedures*." 4th International Conference on Earthquake Geotechnical Engineering-Invited Lectures,

[4] Bray, J. D., and Travasarou, T., 2007. "*Simplified procedure for estimating earthquake-induced deviatoric slope displacements."* J. Geotech. Geoenviron. Eng., 133_4_, 381–392.

[5] Zhou, H., Li, J., Kang, F., 2010. "*Distribution of acceleration and empirical formula for calculating maximum acceleration of rockfill dams*" J. Cent. South Univ. Technol.17: 642−647

[6] Yu, L., Kong, X., Xu, B. "*Seismic response characteristics of earthfill and rockfill dams."* 15th world Conference on Earthquake Engineering, 24-28 September 2012, Lisbon

[7] Marcuson WF, Franklin AG., 1983 "*Seismic Design, Analysis, and Remedial Measures to Improve the Stability of Existing Earth Dams - Corps of Engineers Approach*", in Seismic Design of Embankments and Caverns, T.R. Howard, Ed., New York, ASCE.

[8] Newmark, N.M., 1965."*Effects of earthquakes on dams and embankments*". Geotechnique 15 (2), 139–160.

THE IMPORTANCE OF THE HORIZONTAL STRESSES ON THE BEARING CAPACITY OF A FOUNDATION PILE

Shilton Rica*, *PhD-Student, University of Luxembourg; shilton.rica@uni.lu*

Stefan Van Baars, *Honorary Professor, University of Luxembourg; Stefan.VanBaars@ext.uni.lu*

Borana Kullolli, *PhD-Student, Federal Institute for Material Testing and Research (BAM); borana.kullolli@bam.de*

ABSTRACT

In case one wants to predict or design the bearing capacity of a foundation pile and there are no possibilities to perform an in-situ test, such as a Cone Penetration Test, the pile bearing capacity is in most cases estimated with analytical formulas. The most known and used method is the Meyerhof method published some decades ago. There are also other design methods such as the Janbu method or the Vesić method. These analytical methods are all derived from a certain failure mechanism around the pile tip, which is, in most cases, an extrapolation of the Prandtl's wedge failure mechanism. This failure mechanism was originally developed for a shallow (infinite) strip foundation, though. Therefore, it represents a plane failure mechanism. Numerical simulations on loaded foundation piles performed with the Plaxis software show however, that the failure mechanism of a foundation pile represents a far more complex three-dimensional failure mechanism around the pile tip.

In addition, the existing analytical methods for foundation piles are based on the vertical stresses in the soil, as if the failure mechanism is the same as of a shallow foundation. Numerical simulations, performed in Plaxis show that, not the vertical, but the horizontal stresses, play an important role on the pile bearing capacity. Plaxis represents the stresses in the soil by using the K_0 procedure. So, different horizontal soil stresses are obtained for different values of the lateral earth pressure coefficient K_0. The results show that the pile tip bearing capacity depends strongly on the horizontal stresses in the soil, but only for $K_0 \leq 1$. The same results were observed by using a Material Point Method (MPM). Consequently, the analytical methods should estimate the pile bearing capacity based on the horizontal stresses, in case these are lower than the vertical stresses.

Keywords: Foundation Pile, Horizontal stress, Analytical Design Methods.

1. INTRODUCTION

The bearing capacity of foundation piles is very often estimated by using the Meyerhof formula [1] (based also on [2]). The pile bearing capacity is considered to be a sum of the pile shaft friction and the pile tip bearing capacity. The shaft friction is based on the horizontal stresses in the soil along the pile shaft (the horizontal stresses are calculated with K_0 procedure; $\sigma_h = K_0 \times \sigma_v$). The tip bearing capacity is based on the bearing capacity factors which are the surcharge, the cohesion and the self-weight bearing capacity factor, see equation (1). The last two terms can be neglected for piles installed in sandy soils. In most cases, the pile tip is based on sandy soil, which means that the cohesion in the soil is zero or a small value that can be neglected. In addition, the pile diameter is very small in comparison with the pile length. So

only, the first term of equation (1) is required for piles installed in sand. Therefore, regarding the surcharge bearing capacity, only two basic parameters have to be known. First, the shear strength of the soil which is characterised by its cohesion c and its friction angle ϕ (for sandy soils c = 0 kPa). Second, the weight of the soil layers from ground level to the pile tip level, which are only taken into account as a surcharge effect, q.

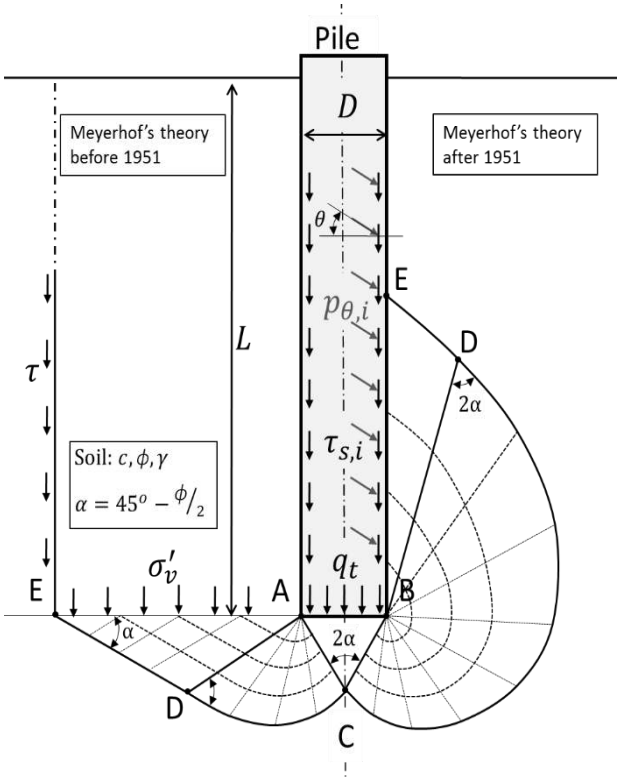

$$q_t = s_q\, q\, N_q + s_c\, c\, N_c + s_\gamma \frac{1}{2} \gamma'\, D\, N_\gamma \quad (1)$$

$$q_t = s_q\, q\, N_q \implies F_{t,c} = q_t\, A_t = s_q\, q\, N_q\, A_t$$

$$\begin{cases} s_q = 1 & \text{for } \phi = 0 \\ s_q = 1 + 0.1 * K_p\, D/L & \text{for } \phi \geq 10^o \end{cases}$$

$$q = \sigma'_v = \gamma'\, L = (\gamma_{soil} - \gamma_{water})\, L$$

$$N_q = e^{\pi \tan \phi}\, K_p$$

$$A_t = \pi\, D^2/4$$

***Figure 1**. Failure mechanism for the pile foundation (based on from [1])*

Where:

q_t	the unit pile tip bearing capacity
s_q	the surcharge shape factor of the pile tip
N_q	the surcharge bearing capacity factor
γ'	the effective self-weight of the soil
σ'_v	the effective vertical stresses at the pile tip
A_t	the surface of the pile tip
K_p	the passive soil pressure coefficient
γ_{soil} , γ_{water}	the unit self-weight of the soil (in natural condition) and the unit self-weight of the water

The maximum pile tip bearing capacity, according to the existing analytical methods, is calculated similarly as the bearing capacity of a shallow strip foundation, which means it is also based on the Prandtl-wedge failure mechanism [3] including the extension made by [4] which takes into account the surcharge effect. This entails simply using the 2-dimensional solution of a shallow strip foundation, multiplied with shape factors to obtain a 3-dimensional failure mechanism, disregarding the shear strength (but not the weight) of the soil above the foundation plane, see Figure 1 (left).

Figure 2 shows a figure published by [5], which was republished by [6 and 7], which shows the bearing capacity factor for shallow round footings N_q (which is in fact $s_q N_q$). [8] and [5] proposed N_q values, which solutions are based on the failure mechanisms given respectively in Figure 3 and Figure 4. The failure mechanism of [6] is shown in Figure 2.

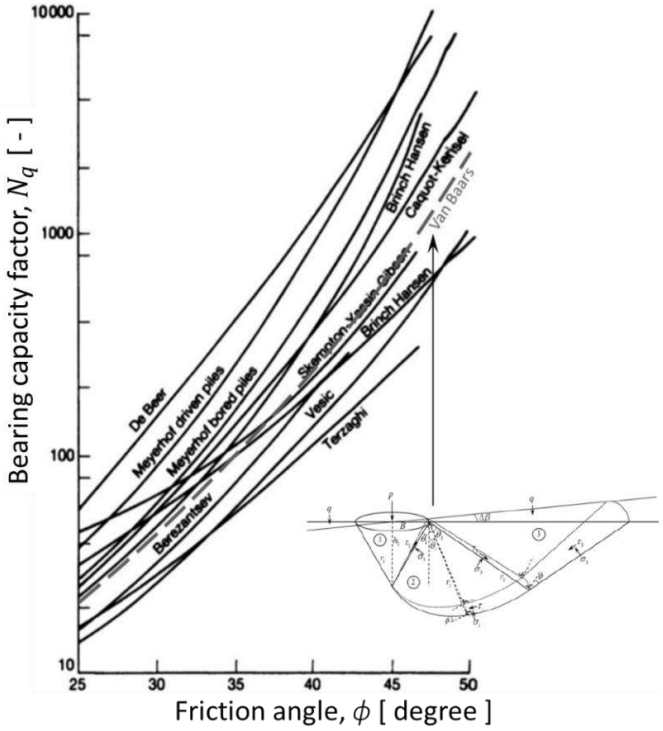

Figure 2. *Surcharge bearing capacity factor [6]*

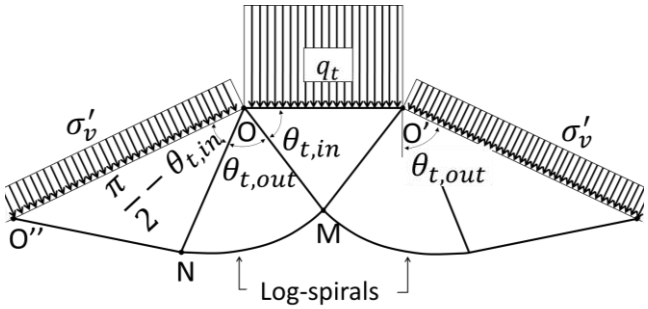

Figure 3. *Janbu model [7]*

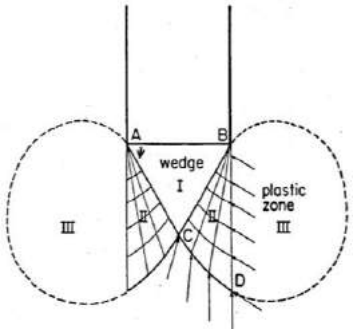

Figure 4. *Vesić model [5]*

2. PLAXIS SIMULATIONS FOR SMALL PILE HEAD DISPLACEMENT

2.1. Plaxis Numerical Simulation

The loading of a pile can be modelled with Finite Element (FE) models, such as Plaxis. The installation of a pile deals with large deformations of the soil, which cannot be handle with FE models. The pile installation effects can only be taken into account if a Material Point Method (MPM) is used because this method is able to handle large deformations. However, [9] showed that Plaxis could be used to represent large deformation simulations with the help of the Press Replace Method (PRM), but no good results can be obtained with this unfortunately.

Nevertheless, the FEM can be used to represent a simplified pile load test, where small deformations occur. The software used in this research is Plaxis, which is a FEM software developed in the Netherlands. The results of [10] and [11], are based on the same numerical model. Simplified pile tests are performed for four different values of the lateral earth pressure coefficient (K_0 = 0.3, 0.5, 0.8, 1.0). By doing so, different horizontal stresses in the soil are tested, while keeping the vertical stresses the same.

Generally, to obtain the pile bearing capacity, the pile head displacement is required to be 10 % of the pile diameter, D, at which a full tip resistance is mobilised [3]. In order to obtain a better insight in the pile bearing behaviour the pile head displacement will even reach 25 % D in the simulations of this article.

These simulations are made for a flat tip reinforced concrete pile, with a diameter of D = 0.4 m and a length of L = 10 m, see Figure 5. The pile is assumed to be already installed in the soil prior to the pile load test. In this case, only small deformations will occur in the soil. Due to this assumption, the pile installation effects are not taken into account. Thus, the simulation represent a simplified pile test simulation. These simplified simulations give the bearing capacity of a foundation pile disregarding the installation effects. The obtained bearing capacities are compared for the different K_0 values.

The foundation pile is installed in a homogeneous sandy soil of which the parameters are given in Figure 5. The selected constitutive material model, which represents the soil, is the Mohr-Coulomb model, and the groundwater level is at ground level. The soil is considered as a drained material, which means that the stiffness and the strength are defined in terms of the effective stresses.

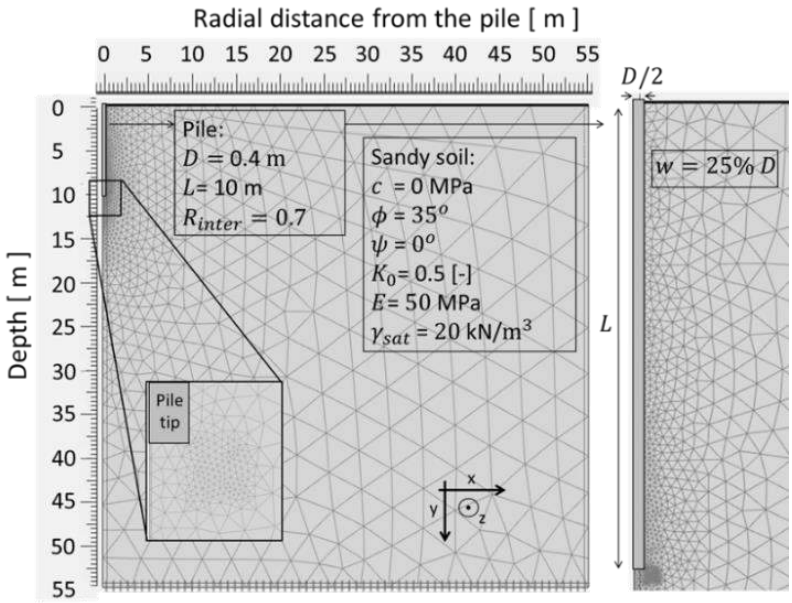

***Figure 5**. Pile model in PLAXIS [9]*

Figure 6 shows clearly the strong influence of the lateral earth pressure coefficient on the pile tip bearing capacity. This is in fact the influence of the horizontal stresses on the pile tip bearing capacity.

The pile tip bearing capacity has an almost linear dependency with the horizontal stress in the soil. This linear dependency is even more obvious for the pile shaft bearing of which it is evident to have a linear relationship with the horizontal stress. For a given soil type, i, at a given depth,

h_i, and considering δ_i as the soil-pile pile interface, the pile shaft friction can be calculated by equation (2).

$$F_{s,i} = \sigma'_{h,i} \tan(\delta_i) = K_{0,i}\, \sigma'_{v,i} \tan(\delta_i) = K_0 \left[\left(\gamma_{soil,i} - \gamma_{water}\right) h_i \tan(\delta_i) \right. \quad (2)$$

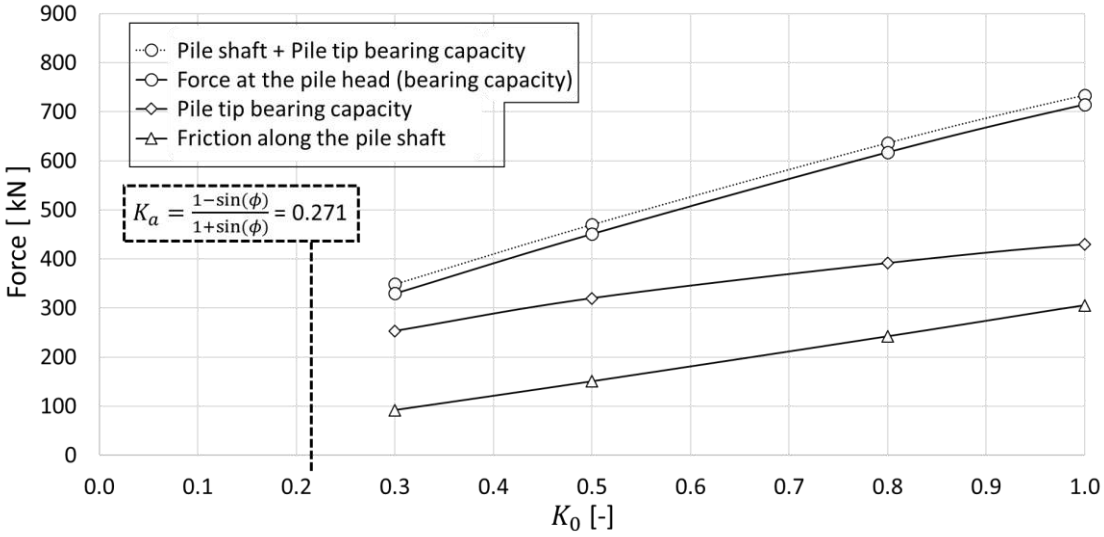

***Figure 6**. Total pile bearing capacity*

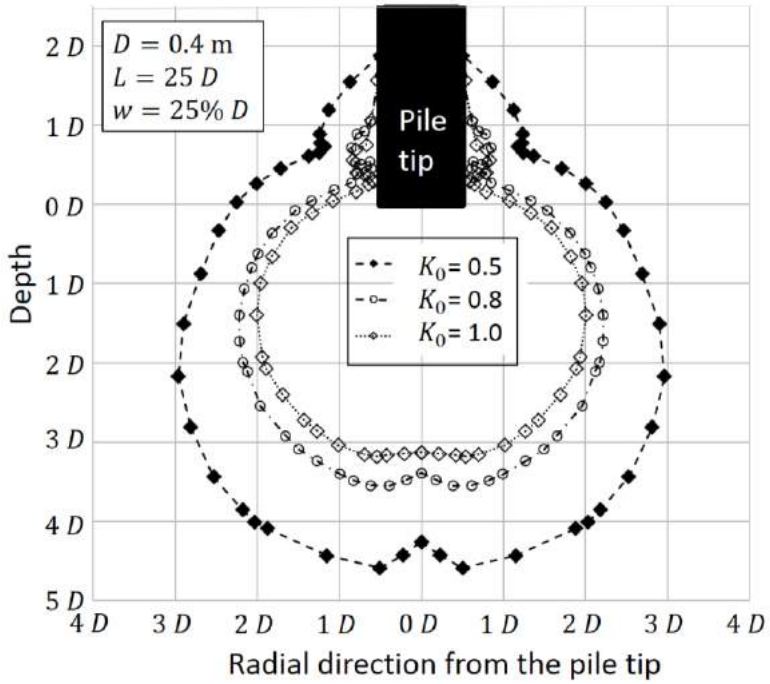

***Figure 7**. The plastic zone around the pile tip versus K_0*

According to [11] showed that a plastic zone of 2 *D* above and 5 *D* below the pile tip is occurring during the pile loading process. This size of the plastic zone is found for a wished in place foundation pile, for installed piles in a MPM simulations, a slightly larger zone is found. Figure 7 shows the plastic zone around the pile tip for different values of the lateral earth pressure coefficient, K_0, for the same pile head displacement. By increasing the value of this parameter, the plastic zone gets smaller. This might be due to the hoop/horizontal stresses in the soil around the pile tip, which have higher values for a higher value of the K_0 parameter. Due to this, the pile tip bearing capacity and the pile shaft friction increase. Consequently, the total pile bearing

capacity increases as well. The influence of the K_0 values or, in other words, the influence of the horizontal stresses, on the size of the plastic zone, is shown in Figure 7.

3. MPM SIMULATIONS FOR LARGE PILE HEAD DISPLACEMENT

3.1. MPM Numerical Simulation

The same geometry and parameters, as for the Plaxis simulations, have been used for the simulations with the Material Point Method (MPM), see Figure 8. In the Plaxis simulations the pile was a wished in place pile, while in the MPM simulations the pile is pressed in (jacked), in a similar way as the done by [12] who showed a cone penetration testing (CPT) installation process. The functioning of this MPM is described by [13].

The pile is a flat tip jacked pile with a length L = 10 m and a diameter D = 0.4 m (L/D = 25). The MPM simulations are able to handle large deformations/displacements, so the pile installation effects are taken into account. The foundation pile is jacked at a rate of 0.02 m/s, equal to the rate of a CPT. The soil-pile friction angle is considered to be 2/3 of the internal frictional angle of the soil. A very rough surface is considered for the pile tip, so it enables the creation of a bulb of soil that remains below the pile tip moving almost at the same rate as the pile installation. The mesh of the numerical model is shown in Figure 9. Based on [13] the numerical model must be divided in 2 big areas; the moving mesh area and the storage area (for more details see [12] and [13]). The initial vertical stresses in the soil are based on the unit weight of the soil. The K_0 procedure is used to reproduce the horizontal stresses. So, if the K_0 value is changed, the values of the horizontal stresses in the soil change as well. Three different values of K_0 are considered: 0.3, 0.5 and 0.8.

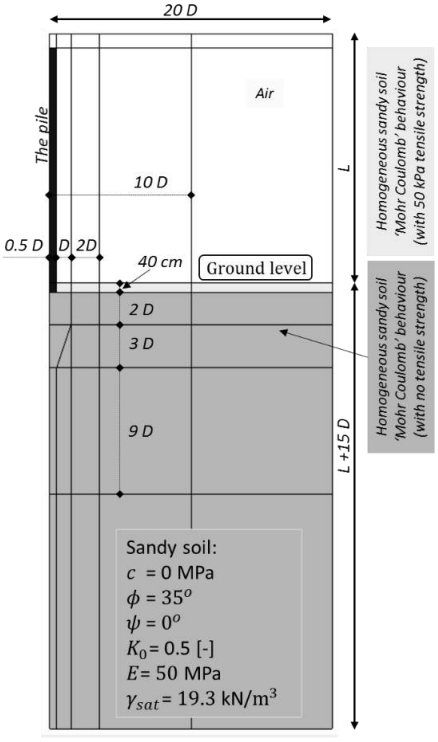

Figure 8*. The numerical foundation pile model in MPM, geometry and material.*

At the very start of the pile installation, a very large displacement was observed for the soil at the edge of the tip. For this reason, a layer of 40 cm having a tensile strength of 50 kPa had to be places as a surcharge. This soil layer has the same parameters as the sand except the fact of having a tensile strength other than zero, see Figure 8. While the pile is considered as a simple

weightless linear elastic object, which is penetrating the soil, no information can be obtained from the volume of the pile, except from its surfaces.

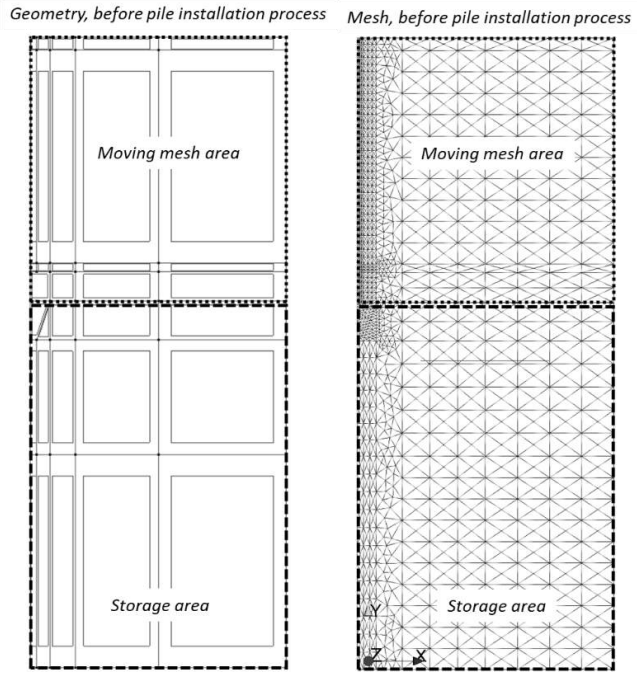

***Figure 9**. The moving mesh area and storage area before the pile installation process.*

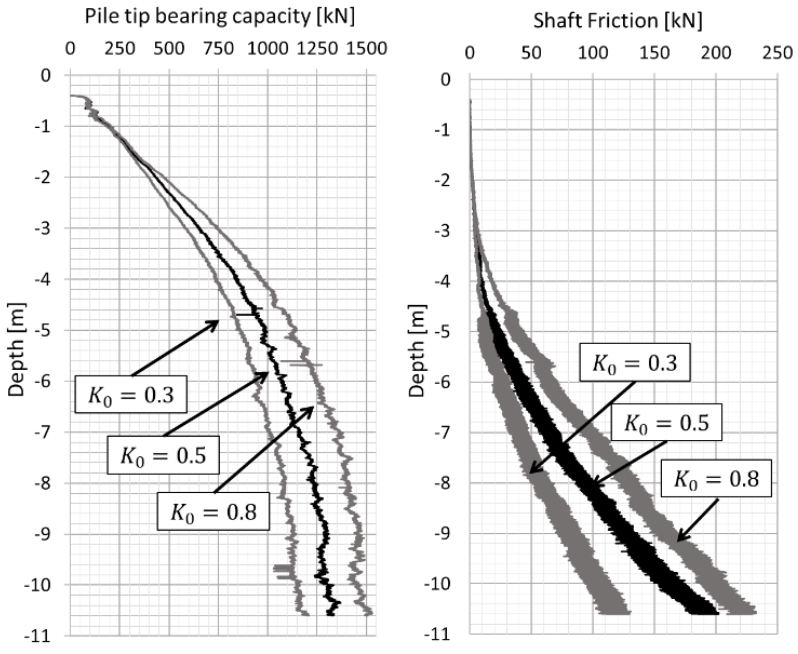

***Figure 10**. MPM pile bearing capacity regarding the K_0 values.*

The results of these MPM simulation are shown on Figure 10. The figure shows the pile tip bearing capacity (left) and the pile shaft friction (right). The results show clearly e influence of the K_0 value on both the shaft and the pile bearing capacity during the pile installation process. Therefore, the horizontal stresses have a strong influence on the total pile bearing capacity. The pile bearing capacity has an almost linear dependency with the horizontal stress in the soil, as for the case of the Plaxis simulations.

4. CONCLUSION

The article shows Plaxis and Material Point Method (MPM) simulations of a pile foundation. The Plaxis simulations represent very well a pile loading test for a wished in place pile, while MPM simulations represent very well a pile installation process as well as the pile loading test.

The size of the plastic zone, observed by Plaxis simulations, depends strongly on the hoop/horizontal stresses in the soil. A smaller plastic zone was found when the hoop/horizontal stresses in the soil are increased.

The Plaxis simulations (small deformations) and the MPM simulations (large deformations) show that the hoop/horizontal stresses play a very important role on the pile bearing capacity. Therefore, the existing analytical methods, used for the design of the pile bearing capacity, should be based on these hoop/horizontal stresses.

REFERENCES

[1]Meyerhof, G. G., 1951. "*The ultimate bearing capacity of foundations*", Géotechnique, 2(4):301-332

[2] Terzaghi, K., 1943. "*Theoretical soil mechanics"*, J. Wiley, New York.

[3] Prandtl, L., 1920. *"Über die härte plastischer körpe".* Nachrichten von der Gesellschaft der Wissenschaften zu Göttingen, Mathematisch-Physikalische Klass*e*, Feb. 1920, pp. 74-85.

[4] Reissner, H. ,1924. "*Zum Erddruckproblem*", Proc., 1st Int. Congress for Applied Mechanics, C. B. Biezeno and J. M. Burgers, eds., Delft, the Netherlands, pp. 295–311.

[5]Vesić, A.S., 1977. "*Design of pile foundations*", National Cooperative Highway Research Program, Synthesis of Highway Practice, No. 42, Monograph, Mar. 1977.

[6]Van Baars, S., 2014. "*The inclination and shape factors for the bearing capacity of footings*", *Soils and Foundations*, 54(5).

[7]Van Baars, S., 2018. "*100 Year Prandtl's Wedge"*, Monograph, IOS Press BV (The Netherlands). University of Luxembourg, April 2018.

[8]Janbu, N., 1976. "*Static bearing capacity of friction piles*", Proc. of the 6th European Conference on Soil Mechanics and Foundation Engineering, Vol. 1, , pp. 479–488, Vienna, Austria, March. 1976

[9]Engin, H. K., R. B. J. Brinkgreve, and A. F. Tol, 2015. "*Simplified numerical modelling of pile penetration–the press‐replace technique"*, International Journal for Numerical and Analytical Methods in Geomechanics, 39(15):1713-1734.

[10]Rica, S. and Van Baars, S. 2018a. "*De gevolgen van de restkracht bij een paalfundering*", Geotechnie*k*, Maart 2015, pp. 20-26.

[11]Rica, S., and Van Baars, S., 2018. "*The influence of a thin weak soil layer on the pile bearing capacity*", In International Conference on Deep Foundations and Ground Improvement, Urbanization and Infrastructure Development, Rome, June 2018, pp. 308-317

[12]Galavi, V., Tehrani, F. S., Martinelli, M., Elkadi, A. S., & Luger, D., 2018. "*Axisymmetric formulation of the material point method for geotechnical engineering applications*". In NUMGE 2018: Proc. of the 9th, European Conference on Numerical Methods in Geotechnical Engineering, Vol. 1, pp. 427-434, June 25-27 2018 , Porto, Portugal.

[13]Kafaji, I. K. A., 2013. "*Formulation of a dynamic material point method (MPM) for geomechanical problems"*. PhD dissertation, University of Stuttgart, March 2013.

FINITE ELEMENT-BASED GEOTECHNICAL RISK ANALYSIS FOR ANCHOR-SUPPORTED DEEP EXCAVATIONS

Sinem Bozkurt*, *Akademi Project Eng. Consulting Ltd. Co., Turkey, sinem-boz@hotmail.com*

Sami Oguzhan Akbas, *Department of Civil Engineering, Gazi University, Turkey, soakbas@gmail.com*

ABSTRACT

Evaluation of the reliability of deep excavation support systems designed by deterministic finite element method requires the inclusion of the effect of soil variability in conjunction with probabilistic analysis. In this context, a 20 m-deep excavation case history with anchored drilled shaft support in the Sogutozu district of Ankara designed with conventional deterministic methods was investigated. The mean soil strength parameters were determined by back analysis via inclinometer readings. Experimental results indicate that sand-gravel bands, which are common in Ankara Clay have the potential to cause a significant decrease in the anchorage capacity. Thus, considering this effect, variability of soil parameters on wall structural capacity and wall lateral displacement is evaluated in detail. For this purpose, the finite element analyses were performed in conjunction with a Python scripting software and the reliability of the anchored deep excavation designed with the conventional methods is examined probabilistically. Geotechnical parameters of the over-consolidated Ankara Clay produced by Monte Carlo simulation method were used in the finite element analyses. The results were evaluated within the context of acceptable reliability levels recommended by several geotechnical and structural codes.

Keywords: Deep Excavations, Risk Analysis, Monte Carlo Simulation, PLAXIS, Python

1. INTRODUCTION

Probabilistic analysis of geotechnical structures with conventional deterministic methods generally do not have the ability to explicitly consider the effect of soil variability in excavation-induced deformations. Incorporating probabilistic concepts into numerical analyses of complex geotechnical structures generally leads to a computational effort often not feasible from a practical point of view [1]. However, recent technological developments in numerical engineering have made reliability-based design easier to be incorporated, and have allowed the addition of soil variability during the calculation phase.

Numerous methods have been used to determine the reliability of geotechnical designs based on probability theory. The most commonly used methods in reliability-based design include the first-order reliability method (FORM), point estimation method (PEM) and Monte Carlo simulation (MCS). Today, Monte Carlo simulation is the most prominent method among these three methods used in the design phase (Fig. 1).

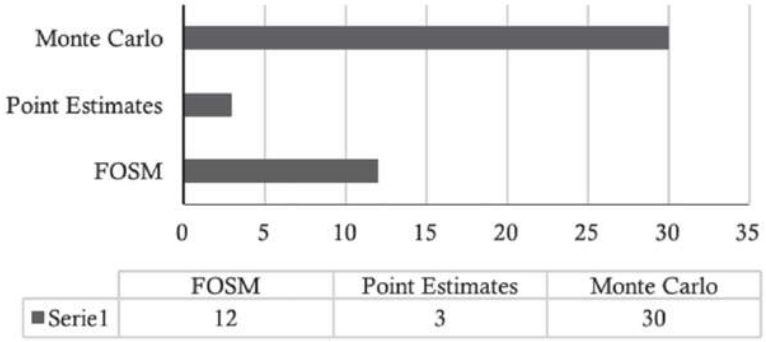

Figure 1. *Simulation methods used on different papers in reliability-based designs in Geotechnics ([2])*

Recently in the literature, studies on the reliability-based design of deep excavations and slopes using PEM, FORM and MSC have shown an increase (e.g., [3, 4, 5 and 6]). Monte Carlo simulation method is a numerical method in which a mathematical or an empirical parameter is randomly calculated in a given distribution [7]. Simultaneous calculation of multiple input data of random variables without physical testing and computer simulations can be performed relatively easily. A typical MCS flow chart is presented in Fig. 2.

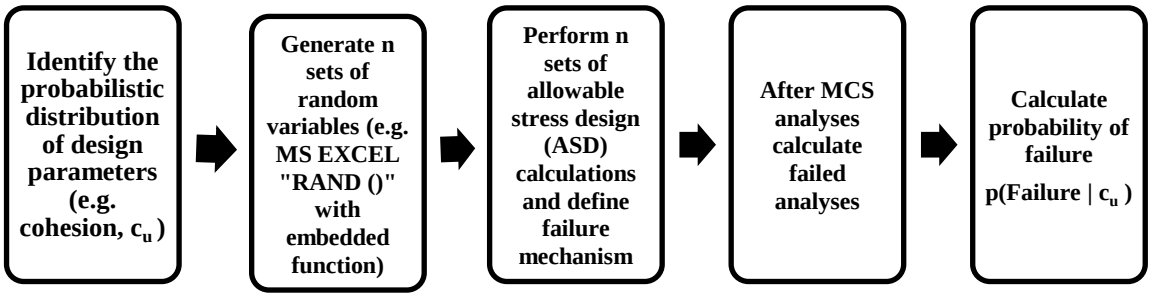

Figure 2. *MCS flow chart (Modified from [8])*

Computer-aided statistical analyses and calculations are needed to understand the failure mechanism and determine conditions beyond the strength and serviceability limits and to finalize geotechnical designs in accordance with engineering decisions. In this context, firstly, the statistical distribution of the variables constituting the problem should be decided. Then, for reliability problems, a limit equilibrium function (P=R-L) should be checked. The system failure mechanism can be defined by the load (L) and resistance (R) operators. Failure can be described as not only the fail of the all the basic elements in geotechnical design, but also the exceedance of the resistance forces (L>R) or the limit conditions. If the limit equilibrium function (P) is smaller than zero, the system will fail. According to n sets of simulations performed, probability of failure (p_f) can then be determined simply by calculating the number of failed analyses (n_f) with Eq.(1).

$$p_f = \frac{n_f(P=R-L\leq 0)}{n} \tag{1}$$

After calculation of p_f, system reliability index (β) can be evaluated by Eq. (2). Φ operator is the standard normal probability distribution function.

$$\beta = -\Phi^{-1}(p_f) \tag{2}$$

It was observed that the number of analyses was selected as 1000 in many geotechnical studies that employed MCS (e.g., [9, 6]). [10] states that the number of simulations required for 95% confidence interval will be 1000 iterations with 0.03 error margin.

According to [11], it was suggested that the number of analyses to be carried out could be determined by considering the situation in which the change in the probability of failure is approaches a fixed value. The required number of analyses can be controlled according to [11] through convergence of β and p_f. The ability to reflect the desired distribution of the probability density function (PDF) of the system variables can only be achieved by performing a sufficient number of random analyses. This can be seen as the main disadvantage of the MCS, as this can be a time-consuming process.

2. CASE STUDY

In this study, MCS-FEM analyses of a 20 m-deep excavation case history [12] of an anchored drilled shaft support system designed for the temporary excavation of Movenpick Hotel in Ankara was conducted. 6 rows of pre-stressed ground anchors and 65 cm diameter piles are used in the support system. Contribution of the traffic surcharge load is taken as 10 kPa. During construction period, ten inclinometers were placed in specific coordinates. [12] conducted a comprehensive study in order to compare finite element results to those determined by inclinometer readings. Soil parameters are estimated by SPT-N and PI relation using [13] method in order to simulate field inclinometer readings in [12]. According to the data obtained from the inclinometers, the maximum lateral displacement (δ_h) on the anchored drilled shaft support recorded as 26 mm was obtained via finite element back analysis.

In the current study, the effect of soil variability on the anchored drilled shaft support's lateral displacement was evaluated. Firstly, anchored drilled shaft support was resubjected to back analysis to model inclinometer readings. Then, after determining the mean values of the geotechnical parameters through back analysis, statistical parameters were defined in accordance with the case study [12]. For this purpose, finite element analyses with PLAXIS 2D were performed with Python scripting software and the reliability of the deep excavation designed with the conventional method is examined by the MC simulation method.

Anchored drilled shaft support was subjected to back analysis with finite element method (PLAXIS) in order to model approximately 26 mm lateral displacement that was measured in the field. Clay layers were modelled using Hardening Soil (HS) material model as used in [12]. The geometry used in the analyses is presented in Fig. 3.

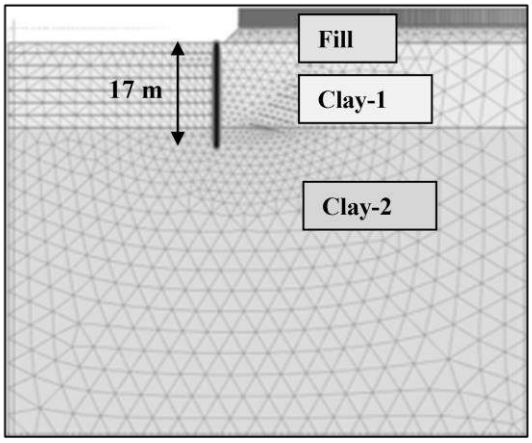

Figure 3. *PLAXIS 2D Deep excavation geometry*

The same parameters described in [12] for fill and clay layers were used in the back analysis. The target displacement value of 26 mm according to inclinometer data was reached in order to model the wall behavior realistically. Soil parameters that are the basis for risk analyses are presented in Table 1.

Table 1. *Soil parameters used in back analysis*

Parameter	Fill	Clay-1	Clay-2	Unit
Material Model	HS	HS	HS	-
Type	Drained	Drained	Drained	-
E_{50}^{ref}	12000	55000	110000	kN/m^2
E_{oed}^{ref}	12000	55000	110000	kN/m^2
E_{ur}^{ref}	36000	165000	330000	kN/m^2
c′	3	20	25	kN/m^2
ϕ′	25	25	25	°

According to deterministic analysis performed with PLAXIS finite element software, maximum lateral displacement and moment values were calculated as 26 mm and 236.7 kNm/m respectively (Fig. 4-5).

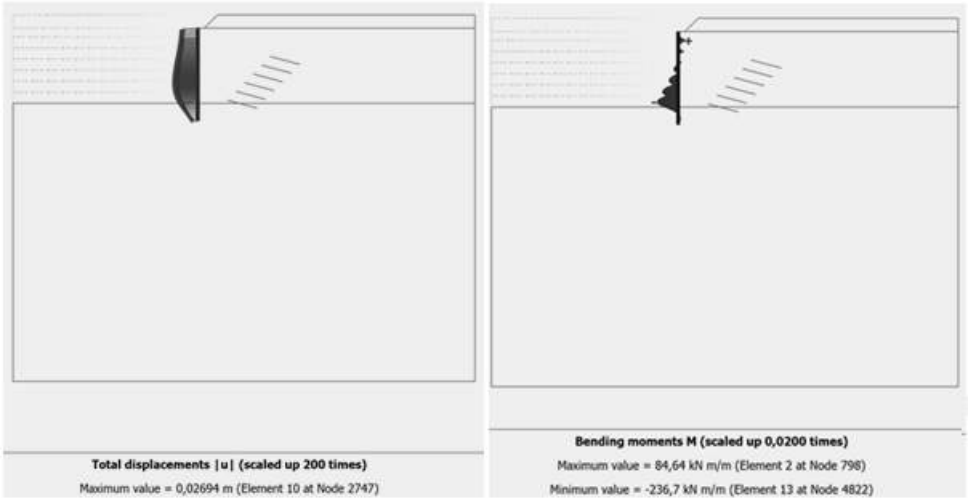

Figure 4. *Maximum lateral displacement and moment value obtained from PLAXIS 2D*

3. FAILURE MECHANISMS AND LIMIT STATE FUNCTIONS

In the context of anchored deep excavation's risk assessments, three main mechanisms should be examined:

- Support failure (pile etc.)
- Exceedance anchor capacity
- Soil failure

The system failure is considered to be exceedance of the wall lateral displacement and pile structural limit. As a result of the PLAXIS 2D analyses, if the 3 m-deep fill layer do not collapse or the plastic limits are not exceeded, the analyses are considered to be successful, and a message written by user is displayed via Python virtual environment. This success statement is not associated with the reliability. It just means that the results of the analyses can be obtained for risk assessment whether the failure mechanism is within the limits or not. However, during analyses if the plastic limits are exceeded or soil is failed during the analyses, the result screen displays "soil collapse" or "load advancement" warnings as error codes indicating that the system has failed.

Failures caused by soil failure and exceedance of plastic limits need to be stored separately during the iterative analyses. To determine limit structural capacity of pile, the load resistance factor was taken as 1.5 according to [14]. In PLAXIS analyses, 0.3% of the excavation depth proposed in [15] and [16] was accepted as the limit failure value.

4. SOIL VARIABILITY IN ANKARA CLAY

Anchored drilled shaft support construction was conducted in Ankara Clay. According to [12] soil profile was idealized in 3 layers: Fill, Clay-1 and Clay-2. Soil variability of Ankara Clay was defined for only Clay-1. For finite element analyses, it was assumed that only Clay-1 layer which contains all of the anchors and effects lateral movement directly had variable geotechnical parameters. The characteristics of the Clay-2 and Fill layers were considered to be deterministic. The assumed probability distribution for Clay-1 layer's strength parameters is log-normal, and mean statistical parameters of this layer were assigned by back analysis. Coefficient of variation (COV) values for Clay-1 parameters were estimated using [17]. The estimated statistical parameters for Ankara Clay are presented in Table 2.

***Table 2**. Statistical parameters used in risk analyses*

Soil variability of Clay-1 layer			
Parameter	c_u (kPa)	c' (kPa)	ϕ' (°)
Mean, μ	200	20	25
Coefficient of variation, COV	23		13

In the analyses, the sand-gravel bands which are common in Ankara Clay were taken into consideration in order to investigate the effect on support system behavior. The effect of sand-gravel bands in Ankara Clay was included by applying variable anchor loads. Therefore, no separate sand-gravel layer had to be defined. [18] states that these bands cause a rapid decrease in anchor capacity, with anchor test failure loads that range between 70-200 kN. Ankara Clay's sand-gravel band content was investigated using 37 borehole logs presented by Akademi Project in Ankara. According to this data, with the probability of 15% an anchor will be within the sand-gravel band, otherwise construction will be in clay layer with the 400 kN pre-stress capacity, as stated in [12]. By means of the probability of existence of sand-gravel content, pre-stress load range was assigned to anchors iteratively in a random way under uniform distribution assumption. In case an anchor fixed length is located within the sand-gravel band, which has a probability of 15%; a pre-stress value between 70-200 kN was applied to the anchors, instead of the 400 kN given in the case history ([12]). For this purpose, a uniform probability distribution function from Python software was used in finite element analyses.

5. RELIABILITY ANALYSES

100, 300, 500 and 1000 simulations were conducted to estimate the required number of iterations for reaching a constant reliability index value in the analyses. According to results obtained from 1000 simulations, maximum lateral displacement and moment values of drilled shaft wall, reflect the assumed log-normal distribution. Fig. 5 shows the distribution of the histograms for 1000 simulations.

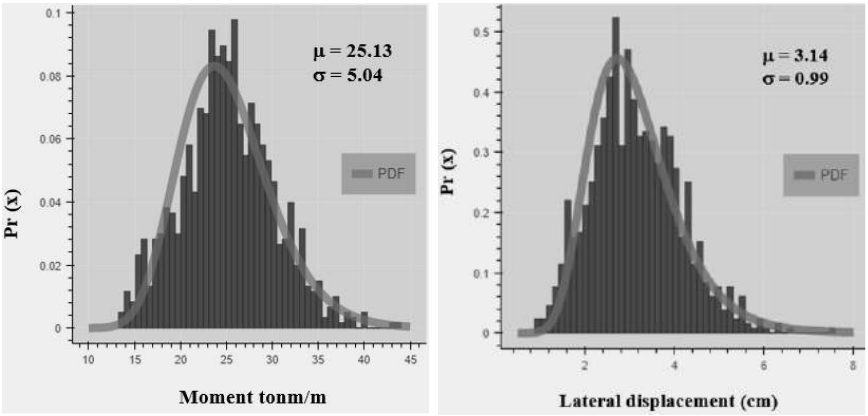

Figure 5. *M-C FEM lateral displacement and pile moment histogram (1000 simulations)*

Within the scope of risk assessments, it can be argued that errors of the soil collapse in 3 m-depth fill layer and load advancement failures can be neglected considering that the construction of the structure has been completed without failure by a large scale of displacement in the short term (without drainage) condition.

MCS analyses were conducted in order to examine two issues affecting the system reliability: the exceedance of the wall lateral displacement (Fig. 6a) and the pile structural capacity limits (Fig. 6b).

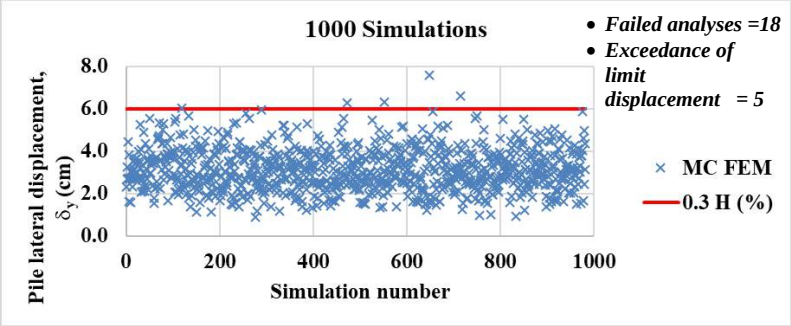

(a)

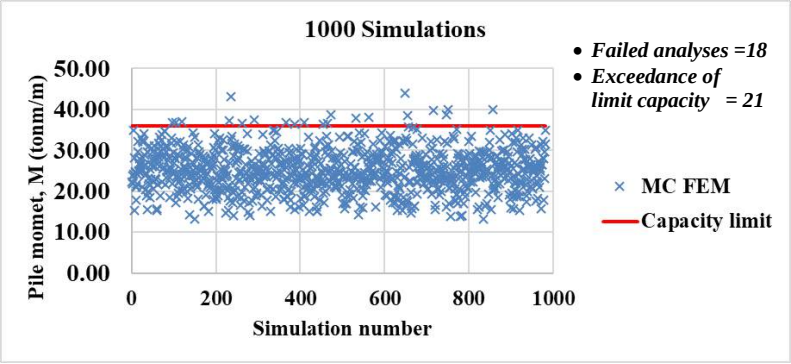

(b)

Figure 6. *M-C FEM failed analyses (a)lateral displacement and (b)pile moment histogram*

Within the scope of the anchored drilled shaft support's reliability assessment, the results of the analyses are presented in Table 3.

***Table 3**. Risk analyses' results*

Max. number of iterations, (n)	Limit lateral displacement and moment exceedance	p_f (%)	β
100	2	2.0	2.05
300	8	2.7	1.93
500	15	3.0	1.88
1000	26	2.6	1.94

Taking into consideration of the afore-mentioned points, sufficient simulation number for this case history can be chosen as 500. After 500 simulations probability of failure and reliability index approaches a nearly constant value.

Risk analyses have shown that in Ankara Clay, considering sand-gravel band's adverse impact on anchor capacity results in a remarkable drop in the reliability. β value was measured as approximately 1.9, and this value is below the acceptable limit defined as 2.3 according to [19].

6. CONCLUSIONS

The reliability of an anchored deep excavation support system has been investigated considering the soil variability within Ankara Clay in conjunction with the sand-gravel content based on the previous studies. With back analyses, lateral wall displacements measured as 26 mm in the field were recalculated and a large number of iterative analyses were performed to assess the probability of failure.

During the construction process of anchored deep excavations performed in sand-gravel bands in Ankara Clay, the impact of the loss of anchor capacity should not be underestimated during the design phase. A comprehensive field and laboratory study and anchorage tests in the field should be carried out, sand-gravel band presence should be determined, and the design should be confirmed. The effect of sand-gravel band existence in Ankara Clay on wall system behavior was examined and the reliability of the system was determined to be below the limits. This assessment is based on the assumption that Anchorage capacities are not field-tested.

The fact that deep excavations designed by traditional methods provide traditional safety coefficients does not mean that the design is safe. Because, traditional methods include uncertainties that cannot be taken explicitly into account and this should encourage the designer to perform probabilistic analyses to determine the system failure level.

Even if the number of the analyses in MCS create a disadvantage in the elapsed time, it is important to conduct adequate number of analyses to correctly interpret the results of the reliability analyses. To specify the number of analyses, reliability index values should converge for the specified failure mechanism.

REFERENCES

[1] Schweiger, H. F., Peschl, G. M., 2005. *"Reliability Analysis in Geotechnics with the Random Set finite Element Method"*, Computers and Geotechnics, 32, 422-435.

[2] Viviescas, J., Osorio, J., Cañón, J., 2017. *"Reliability-Based Designs Procedure of Earth Retaining Walls in Geotechnical Engineering"*, Obras y Proyectos, 22, 50-60.

[3] Goh, A. T., Kulhawy, F. H., 2005. *"Reliability Assessment of Serviceability Performance of Braced Retaining Walls Using a Neural Network Approach"*, International Journal for Numerical and Analytical Methods in Geomechanics, 29(6), 627-642.

[4] Rippi, A., 2015. *"Structural Reliability Analysis of a Dike with a Sheet Pile Wall-Coupling Reliability Methods with Finite Elements"*, MSc. Thesis, Delft University of Technology.

[5] Janssen, J. J., 2016. *"Research on the Safety Level of a Diaphragm Wall in River Dikes, Using a Monte Carlo Analysis"*, MSc. Thesis, Delft University of Technology.

[6] Akbas, B., 2015. *"Probabilistic Slope Stability Analysis Using Limit Equilibrium, Finite Element and Random Finite Element Methods"*, MSc. Thesis, Middle East Technical University, Ankara.

[7] Wang, Y., Schweckendiek, T., Gong, W., Zhao, T., Phoon, K. K., 2016. *"Direct Probability-Based Design Methods"*, Reliability of Geotechnical Structures in ISO2394, London: CRC Press, 193-223.

[8] Wang, Y., Au, S.K., Kulhawy, F.H., 2011. *"Expanded Reliability-Based Design Approach for Drilled Shafts"*, ASCE Journal of Geotechnical and Geoenvironmental Engineering, 137 (2), 140–149.

[9] Tang, Y. G., 2011. *"Probabilistic Analysis of the Deflection of Retaining Wall in Deep Excavation"*, GeoRisk 2011: Geotechnical Risk Assessment and Management, American Society of Civil Engineers, 963, Atlanta, ABD.

[10] Baecher, G. B., Christian, J. T., 2003. *"Reliability and Statistics in Geotechnical Engineering"*, Cornwall: John Wiley and Sons Inc.

[11] Ahmed, A., Soubra, A., 2011. *"Subset Simulation and Its Application to a Spatially Random Soil"*, GeoRisk 2011: Geotechnical Risk Assessment and Management, American Society of Civil Engineers, pp. 209, Atlanta, ABD.

[12] Calısan, O., 2009. "Ankara Kilinde Yapılan 20 m Derinliğinde Bir Kazının Geri Analizi", *Prof. İsmet Ordemir'i Anma Toplantısı ve 5. Odtü Geoteknik Mühendisliği Sempozyumu*, pp. 1-12, Middle East Technical University, Ankara.

[13] Duncan, J. M., Buchignani, A. L., 1976. *"An Engineering Manual for Settlement Studies"*, Berkeley: Dept. of Civil Eng. Univ. of California.

[14] AASHTO, 2012. "*LRFD Bridge Design Specifications",* American Association of State Highway and Transportation Officials, Washington, DC.

[15] Long, M. (2001, March). *"Database for Retaining Wall and Ground Movements due to Deep Excavations"*, J Geotech Geoenviron Eng, 127(3), 203-224.

[16] Wang, R., Liu, G. B., Liu, D. P., Ma, Z. Z., 2008. *"Discussion on Design Method for Retaining Structures of Metro Station Deep Excavations in Shanghai"*, Proceedings of the 6th International Symposium (IS-SHANGHAI 2008), Shanghai, China.

[17] Akbas, S. O., Kulhawy, F. H., 2010. *"Characterization and Estimation of Geotechnical Variability in Ankara Clay: A case history"*, Geotechnical and Geological Engineering, 28(5), pp. 619-631.

[18] Ergun, U., 1987. *"Ankara Zeminlerinde Yapılan Bazı Ankraj Deneyleri"*, Zemin Mekaniği ve Temel Mühendisliği İkinci Ulusal Kongresi, pp. 489-495, İstanbul, Turkey.

[19] CSA (2014). *"Canadian Highway Bridge Design Code"*, Canadian Standards Association, Mississauga.

THE EFFECT OF ULEXITE ADDITIVE ON THE ENGINEERING PROPERTIES OF SAND-BENTONITE MIXTURES FOR LINERS

Ş.Gizem Alpaydın*, *Dokuz Eylul University, The Graduate School of Natural and Applied Sciences, gizem.alpaydin@gmail.com*

Yeliz Yükselen-Aksoy, *Dokuz Eylul University, Department of Civil Engineering, yeliz.yukselen@deu.edu.tr*

ABSTRACT

Sand-bentonite mixtures are usually used for impervious barriers at nuclear waste repositories, municipal solid waste landfill liners, etc. These mixtures must keep their strength and hydraulic conductivity properties without any changes for a very long time. The literature studies have shown that high temperature and thermal cycles have negative effects on the hydraulic conductivity and strength of soils. For example, hydraulic conductivity increases in the presence of high temperature. For that reason, the resistivity of sand-bentonite mixtures should be increased against high temperatures when they are used in liners. Boron minerals are used in order to increase the thermal resisitivity of materials in industry. Hence the boron mineral namely; ulexite can be added to the sand-bentonite mixtures in order to improve strength and hydraulic conductivity properties of these mixtures against high temperature or thermal cycles. In this study, the compaction, consolidation and shear strength properties of ulexite added sand-bentonite mixtures were investigated at room temperature. Additionally, the shear strength behavior of ulexite added sand-bentonite mixtures were investigated at high temperature (80°C).

The sand-bentonite mixtures were prepared which contains 10% bentonite. The 10% and 20% ulexite were added to these mixtures. The mixtures were prepared according to the compaction test results (dry unit weight and optimum water content+2%). According to the test results, as the ulexite additive reduced the optimum water content value, increased the maximum dry unit weight. For consolidation tests, when the ulexite was added to the sand-bentonite mixtures, amount of the total vertical strain (compressibility) increased as the ulexite percentage increased. The maximum shear stress value of sand-bentonite mixtures in the presence of ulexite at 80°C was generally higher than those of at room temperature.

Keywords: Boron, Ulexite, Shear Strength, Consolidation, Compaction, Temperature.

1. INTRODUCTION

Energy structures such as nuclear waste repositories, energy piles, geothermal energy structures, heat storage systems, buried high voltage cables, CO_2 sequestration plants, etc. directly connect to the soil and cause thermal heat changes on the underlying soils. For example, it is necessary to understand the behavior of soil at temperatures up to 100°C due to the necessity of radioactive disposal [1]. Heat is generated as a result of decomposition of organic compounds and biochemical processes of wastes in landfills. Such heat may adversely affect the soil in a hydraulic and mechanical way in terms of long-term behavior in landfills. Previous studies have shown that high temperatures affect hydraulic conductivity, volume change (compressibility-swelling) and shear strength parameters of soils [1, 2, 3]. When bentonite was heated to 100°C, a decrease in cohesion and an increase in the internal friction angle were observed [4]. The

shear strength of the normally consolidated clay increases when the soil temperature increases or subjecting to a temperature history [1]. Hydraulic conductivity increases with increasing temperature because of the change in fluid viscosity depending on temperature. The hydraulic conductivity of compacted bentonite at 80°C was investigated to be 3-4 times higher than that measured at 20°C [3]. Change in soil behavior depending on temperature is explained with clay interparticle forces and viscous shear resistance of adsorbed water [5].

Sand-bentonite mixtures are commonly used in landfill liners and nuclear waste repositories. Because bentonite is a material with low hydraulic conductivity and high water retention capacity. Bentonite is a highly swelling clay and shrinks when becomes dry. Therefore, it is used by mixing with sand in landfills. There is a need for thermally resistive and durable soil layers at the nuclear waste landfills and around the energy structures. For that reason, boron mineral addition to the sand-bentonite mixtures may increase the durability of these soil mixtures against to high temperature.

Natural borates are used to define concentrated boron ores such as; tincal, colemanite, and ulexite. Ulexite is a boron mineral which is quite rich in terms of sodium and calcium minerals ($NaCaB_5O_9.8H_2O$). Boron is used in many application areas like energy, metallurgy, cement, glass and ceramic. For example, in the production of heat-resistant glassware and high-quality glass for use in electronics and space research boron minerals are used. Boron mineral significantly reduces heat expansion of the glasses, protects the glass against acid and scratches. Boron is known with its resistance against high temperature. For that reason, the ulexite added sand-bentonite mixtures may show high resistance against high temperatures and thermal cycles.

The objective of this study is to investigate the compaction, consolidation, shear strength behavior of sand-bentonite mixtures with boron mineral namely; ulexite. The effect of ulexite on the consolidation (at room temperature) and shear strength behavior (at room temperature and 80°C) were investigated.

2. MATERIALS AND METHODOLOGY

2.1. Materials

In this study, sand, Na-bentonite and boron mineral, namely; ulexite were used. The Na-bentonite was supplied from Eczacıbaşı Esan Mining Company. Ulexite were gathered from Eti Mining Operations General Directorate of Turkey. The physico-chemical properties of these materials are summarized in Table 1.

***Table 1**. The physico-chemical properties of bentonite, sand and ulexite samples*

	Bentonite	Sand	Ulexite
Specific gravity	2.70	2.63	1.98
Liquid limit (%)	476.0	-	33.4
Plastic limit (%)	70.1	-	25.1
Plasticity index (%)	405.9	-	8.2
pH	9.5	-	-

For all experiments, Na-bentonite and sand were used after drying for 24 hours in the oven (105°C). The sand and bentonite were sieved through No.6 (3.35mm) and No.200 (0.075mm) sieves after drying, respectively. The initial water content values of the ulexite were determined for each test and considered at the sample preparation.

The percentages of the bentonite, sand, ulexite in the mixtures and the test set-up are shown in Table 2. The samples were named as abbreviation of bentonite as "B", sand as "S" and ulexite as "U". For example, 9B-81S-10U sample contains 9% bentonite, 81% sand and 10% ulexite. While preparing the mixture, 10% or 20% of the total dry mixture was ulexite, then 10% of the remaining part was bentonite and 90% sand.

Table 2. *Test set-up*

Test Sample	Compaction tests	Consolidation tests	Direct shear tests	
			Room temperature	80°C
100U	✔	✔	✔	✔
10B-90S	✔	✔	✔	✔
9B-81S-10U	✔	✔	✔	✔
8B-72S-20U	✔	✔	✔	✔

2.2. Methodology

2.2.1. Compaction tests

The compaction tests were carried out in accordance with ASTM D698 (2012e2) [6]. Firstly, dry materials were prepared at the specified percentages and mixed in a basin. Then the water was added by spraying and the mixture was blended homogeneously. The sample was prepared in four different water contents for each experiment. Subsequently, the samples were placed in plastic bag and kept for 24 hours.

The experiments were carried out by applying Standard Proctor energy in the automatic compactor. In this test, the mixtures were compacted into 2 layers by falling the 2.5 kg hammer from 305 mm. In addition, 43 drops were applied to each layer to obtain the Standard Proctor energy. After completion of the experiment, the soil was removed from the mold by hydraulic jack. At the end of the test, the representative sample was taken from the compacted soil and dried in the oven (105°C) for water content determination.

2.2.2 Consolidation tests

Consolidation tests were performed according to ASTM D2435 (2011) [7]. For consolidation tests, the samples were prepared as at the 2% wet side of the optimum water content and the dry unit weight value corresponding to this water content. The prepared sample was placed into the ring by compaction with a wooden tamper. The ring was placed in a cell filled with water and seating pressure (6.86 kPa) was applied for 24 hours. Then loading was started. When the deformations reached to negligible level the next loading was started. Load increment ratio (LIR) was applied as 1.0. After the consolidation completed the sample was unloaded to 196 kPa then to 49 kPa. It was waited until swelling completion at each unloading step.

2.2.3. Direct shear tests

In this study, direct shear tests were performed under consolidated-drained (CD) conditions [8]. Firstly, dry materials were mixed according to the predetermined percentages, then water was added and mixture mixed homogenously. The prepared sample was placed in the square mold in three layers by compaction with wooden tamper according to the parameters obtained from the Standard Proctor test. The mold was waited for 24 hours in a tray filled with water to allow the sample to be saturated, and weight was placed on the sample to prevent swelling. Then the sample was carefully placed to the shear box and after being consolidated the shear part was

started. The water and soil were heated during the consolidation and shear parts. The specially designed heat rod was used to elevate the temperature to 80°C and thermostat was used to keep the temperature constant. The temperatures of the soil and water were measured by two different K-type thermocouples. The thermocouples were connected to the digital thermometer which recorded and stored the temperature data.

3. RESULTS AND DISCUSSIONS

3.1. Compaction Tests Results

The compaction parameters of 10B-90S mixtures were determined in the presence of 10% and 20% ulexite. The Figure 1 shows the compaction characteristics of the 10B-90S mixtures in the presence of ulexite.

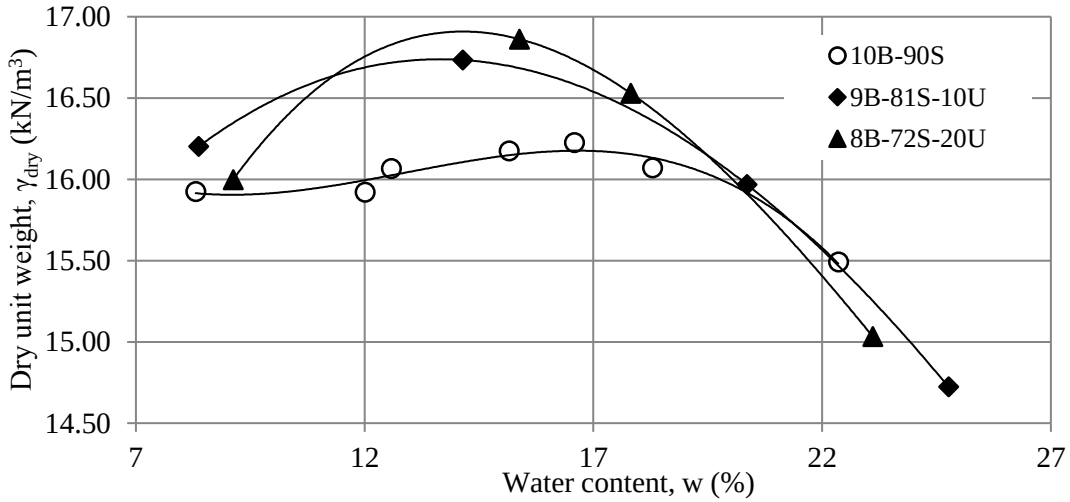

Figure 1. *Compaction curves of 10% sand-bentonite mixtures in the presence of ulexite*

As shown in Figure 1 ulexite addition to 10B-90S mixtures reduced the optimum water content while increased the maximum dry unit weight. As ulexite additive percentage increases in the mixture the $\gamma_{d,max}$ value increases. As it is seen, it is clear that the all percentages of ulexite decreased the w_{opt} value. However, the highest decrement in w_{opt} value is seen in the presence of 10% ulexite. The compaction parameters of only ulexite were also obtained. As a result of this test γ_{dmax} value of ulexite is 13.83 kN/m^3, the w_{opt} value is 21.5%. The w_{opt} value of ulexite increased compared to the 10B-90S mixture, while the γ_{dmax} value decreased. The compaction parameters obtained from compaction tests are given in Table 3.

Table 3*. Compaction parameters of all mixtures and ulexite*

Sample	w_{opt} (%)	γ_{dmax} (kN/m^3)
100 U	21.5	13.83
10B-90S	16.5	16.19
9B-81S-10U	13.5	16.78
8B-72S-20U	14.2	16.87

3.2. Consolidation Tests Results

The compression curves of 10B-90S mixtures are given in the presence of ulexite in Figure 2. When the ulexite admixture was added to the 10B-90S mixture, it is clear that it increases the amount of vertical strain (compressibility). The vertical strain amount of 10B-90S mixture increased from 6.6% to 8.1% in the presence of 10% ulexite additive and to 12.44% with 20% ulexite.

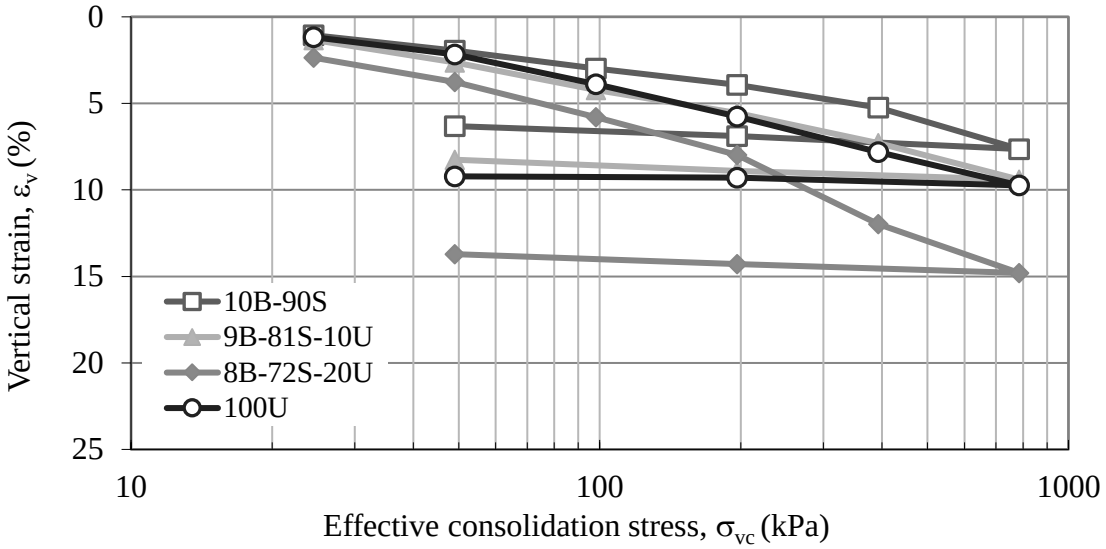

Figure 2. *Vertical strain-effective stress relationships for 10% sand-bentonite mixtures in the presence of ulexite*

When ulexite is added to 10B-90S mixtures, it is seen that the amount of swelling decreases. The amount of swelling decreased to 1.14% in the presence of 10% ulexite and 1.09% in the presence of 20% ulexite. Increasing the amount of ulexite from 10% to 20% did not significantly change the amount of swelling.

The total vertical strain values at the compressibility and swelling tests are given in Table 4.

Table 4*. Total vertical strain of test specimens*

Sample	Total vertical strain (compressibility) (%)	Total vertical strain (swelling) (%)
10B-90S	6.58	1.34
9B-81S-10U	8.07	1.14
8B-72S-20U	12.44	1.09
100U	8.57	0.53

3.3. Direct Shear Tests Results

The shear strength parameters of 10B-90S mixtures were determined in the presence of ulexite under room temperature and 80°C. Table 5 shows the shear strength parameters obtained from the direct shear tests at room temperature and 80°C.

The internal friction angle value of ulexite, which was 21.2° at room temperature, increased to 35.4° under 80°C, indicating a marked increase in the internal friction angle value with increasing heat. The cohesion value of ulexite, which was 26.8 kPa, decreased to 12.1 kPa under 80°C. In the direct shear tests, when the ulexite additive was added to the 10B-90S mixtures, the internal friction angle values decreased while the cohesion values increased at room temperature. The internal friction angle value of the 10B-90S mixture, which is 33.6°, decreased to 31.3° with 10% ulexite and to 22.1° with 20% ulexite. The internal friction angle and cohesion values of sand-bentonite mixtures increased with ulexite addition under high temperature (80°C). The internal friction angle value of the 10B-90S mixture at room temperature increased under elevated temperature (80°C).

Table 5*. The shear strength parameters of the sand-bentonite mixtures in the presence of ulexite at room temperature and 80°C*

Sample	Room Temperature		80℃	
	Ø′(°)	c′ (kPa)	Ø′ (°)	c′ (kPa)
10B-90S	33.6	51.7	32	47.3
9B-81S-10U	31.3	57.8	34.7	49.8
8B-72S-20U	22.1	54.8	32.8	50
100U	21.2	26.8	35.1	12.1

Figure 3 shows shear stress-normal stress graph of 10B-90S mixtures in the presence of ulexite at room temperature and 80°C temperature.

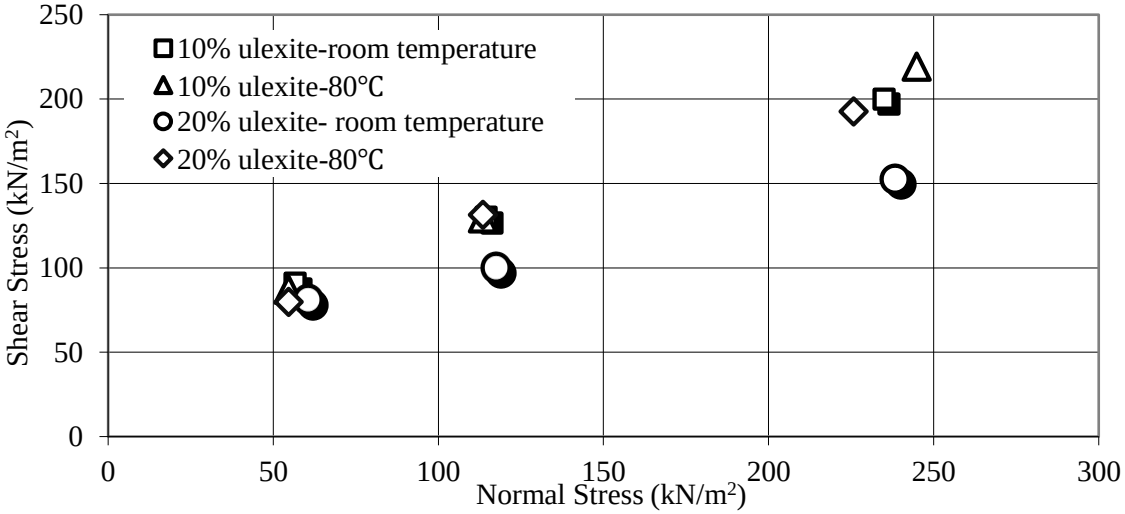

Figure 3. *Shear stress-normal stress graph of 10% sand-bentonite mixtures in the presence of ulexite*

The maximum shear stress values of the 10B-90S mixtures decreased as the ulexite additive ratio increased at room temperature. It is seen that the maximum shear stress values increase at 80°C. However, in general, the maximum shear stress values of 10% ulexite additive mixtures are higher than those of 20% ulexite mixtures. The maximum shear stress behavior of the 20B-80S mixtures at room temperature was similar to that of the 10B-90S mixtures. The shear stress value decreased as the ulexite content increased. According to the results of the tests performed at 80°C, the maximum shear stress was generally increased as the percentage of ulexite

increases. Figure 4 shows the relationship between the maximum shear stress and ulexite content of the mixtures at room temperature and 80°C.

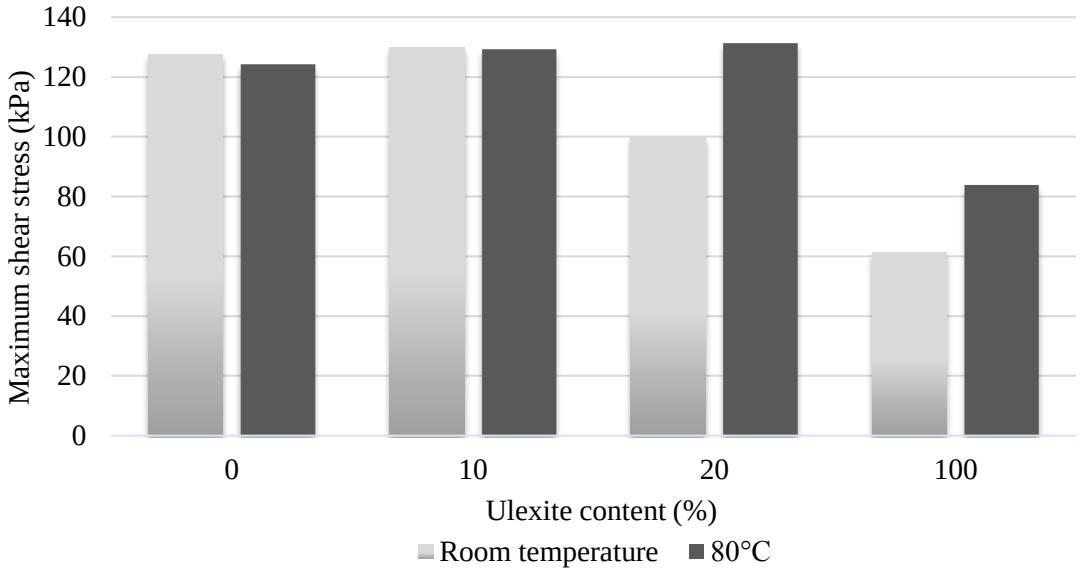

Figure 4. *Maximum shear stress-ulexite content of mixtures at room temperature and at 80°C*

As shown in Figure 4, a significant increase in maximum shear stress was observed with increasing temperature, especially for 8B-72S-20U mixture.

4. CONCLUSIONS

In this study, engineering properties of sand-bentonite mixtures in the presence of ulexite were studied, shear strength behavior was examined at room temperature and at 80°C. According to the tests results, the ulexite additive resulted an increase in the $\gamma_{d,max}$ of the sand-bentonite mixtures and decrease in the w_{opt} value. In addition, when the ulexite was added to the sand-bentonite mixtures, amount of the total vertical strain (compressibility) increased as the ulexite percentage increased. However, the amount of swelling decreased in the presence of ulexite. However, the increase in ulexite from 10% to 20% did not cause a significant change in swelling value. According to the direct shear test results, when the sand-bentonite mixtures were heated to 80°C, the Ø′ value and c′ value decreased. Although the Ø′ value with the ulexite additive decreased at room temperature, it increased at 80°C. Furthermore, the Ø′ value of sand-bentonite mixtures in the presence of ulexite at 80°C was higher than the sand-bentonite-ulexite mixtures at room temperature as well as the non-additive sand-bentonite mixture at 80°C. In addition, the maximum shear stress value of sand-bentonite mixtures in the presence of ulexite at 80°C was generally higher at room temperature. The results of this study have shown that ulexite additive has a promising effect on the shear strength behavior of sand-bentonite mixtures. The further studies are needed on the long term behavior of ulexite added sand-bentonite mixtures under high temperatures.

ACKNOWLEDGEMENT

This study is supported by The Scientific and Technological Research Council of Turkey (TÜBİTAK) (Grant no. 217M553). The authors are grateful for this support.

REFERENCES

[1] Abuel-Naga, H.M., 2006. "*Experimental Evaluation of Engineering Behavior of Soft Bangkok Clay Under Elevated Temperature*", Journal of Geotechnical and Geoenvironmental Engineering, 132(7):902- 910.

[2] Pusch, R., 1990. "*General Microstructural Model for Qualitative and Quantitative Studies of Smectite Clays*", SKB Technical Report, 90-43, Stockholm, Sweden.

[3] Cho, W.J., Lee, J.O. and Chun, K.S., 1999. "*The Temperature Effects on Hydraulic Conductivity on Compacted Bentonite*", Applied Clay Science, 14:47-58.

[4] Wang, M.C., 1990. "*The Effect of Heating on Engineering Properties of Clays*", Physico-Chemical Aspects of Soil and Related Materials, ASTM STP 1095, Philadelphia, 139-158.

[5] Abuel-Naga, H.M., 2007. "*Effect of Temperature on Shear Strength and Yielding Behavior of Soft Bangkok Clay*", Soils and Foundations, 47(3):423–436.

[6] ASTM D4318-98, 1999. "*Standard Test Methods for Laboratory Compaction Characteristics of Soil Using Standard Effort*", ASTM International, USA.

[7] ASTM D2435/D2435M–11, 2011. "*Standard Test Methods for One-Dimensional Consolidation Properties of Soils Using Incremental Loading*", ASTM International, USA.

[8] ASTM D3080/D3080M–11, 2012. "*Standard Test Method for Direct Shear Test of Soils Under Consolidated Drained Conditions*", ASTM International, USA.

A RHEOLOGICAL MODEL TO DESCRIBE THE MECHANICAL RESPONSE OF EARTH EMBANKMENTS ON PILED FOUNDATIONS

Viviana Mangraviti*, *Politecnico di Milano, viviana.mangraviti@polimi.it*

Luca Flessati, *Politecnico di Milano, luca.flessati@polimi.it*

Claudio di Prisco, *Politecnico di Milano, claudio.diprisco@polimi.it*

ABSTRACT

Piled foundations are largely employed as settlements reducers in artificial embankments based on soft soil strata. Despite of their well-documented effectiveness, the complex interaction processes taking place within both the embankment and the soft foundation soil to transfer loads to piles, are not yet fully understood. Engineering design methods are generally based on simplified approaches not allowing to quantitatively evaluate total and differential settlements at the top of the embankment during and after the construction. Depending on the construction time, hydro-mechanical coupled phenomena may affect or not the accumulation of delayed settlements at the top of the embankment.

In this paper, a rheological model capable of describing the consolidation process taking place in embankments of fixed geometry is presented. The model, derived from the results of an extensive of non-linear 3D finite difference numerical campaign, allows to quantitatively estimate the evolution of settlements at both the top and the base of the embankment with time.

Keywords: Embankments, Constitutive Modelling, Ground Improvement.

1. INTRODUCTION

With the aim of reducing settlements at the top of earth embankments on soft soil strata, piled foundations have been widely used in the past. Despite the well-documented effectiveness of this technique, the complex interaction mechanisms, transferring vertical loads toward the piles, are not fully understood. The approaches suggested in the most used design standards ([1] and [2]) to analyze the response of this type of "geo-structures", based on the concept of "arching effect" ([3] and [4]), allow to estimate the stresses applied to the pile neglecting the embankment settlements.

In di Prisco et al. [5] a rheological model to interpret the mechanical response of a piled embankment based on dry soft soil was proposed. This rheological model relates the increment in the embankment height to the increment in both average and differential settlements. In this paper, the authors intend to extend the model to the case of embankments based on saturated soils. The construction process is here disregarded and considered as instantaneous.

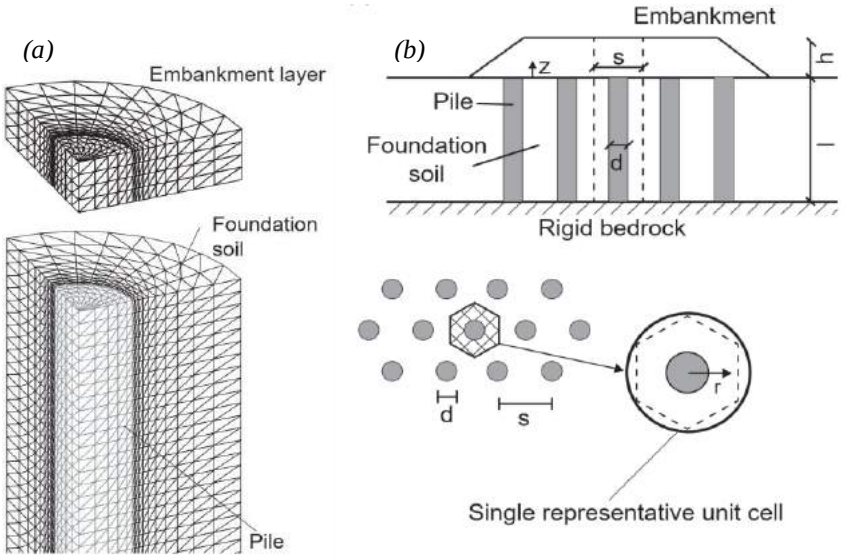

Figure 1. *(a) numerical discreization of the problem; (b) geometry of the problem.*

2. METHODOLOGY

The numerical model (Figure 1.a) has been realized by means of FLAC3D code (Itasca Consulting Group).

Only one axisymmetric cylindrical cell has been considered by disregarding flank effects (Figure 1.b). The cell is composed of: (i) one pile of diameter *d* and length *l*, (ii) surrounding soil and (iii) embankment stratum of thickness *h*. The diameter of the whole cell *s* is assumed to be coincident with the pile spacing. On the lateral boundaries and at the base of the domain normal displacements are not allowed. The concrete pile is modelled as a linear elastic cylindrical inclusion. The mechanical behaviour of both the foundation and the embankment soil is assumed to be elastic-perfectly plastic. The failure condition is given by the Mohr-Coulomb criterion and the flow rule is assumed to be non-associated. Smooth interface elements are introduced between pile and foundation soil.

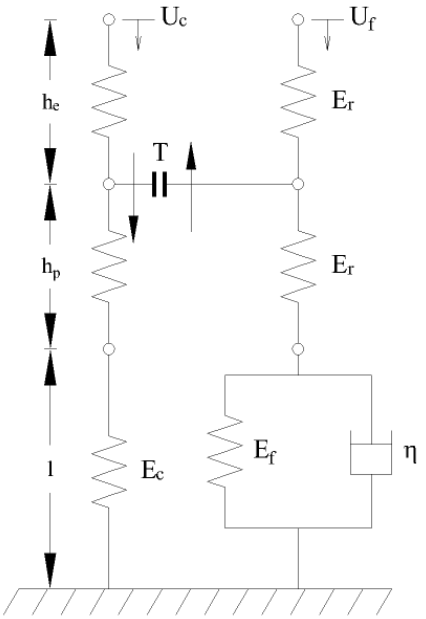

Figure 2*. Rheological model*

The modified rheological model (Figure 2) seems to be capable of simulating the evolution of the displacements at the top of the embankment above the column (U_c) and the foundation soil (U_f) with time. The model depends on: (i) the geometry of the unit cell, (ii) the soil unit weight, (iii) the stiffness moduli (for the column E_c, the foundation soil E_f and the embankment E_e). In Figure 2 h_p represents the height of the yielded portion of the embankment ("process" height); whereas the height corresponding to the plane of equal settlements is defined as h_e. *T* in Figure 2 represent the load transferred toward the pile during the consolidation process.

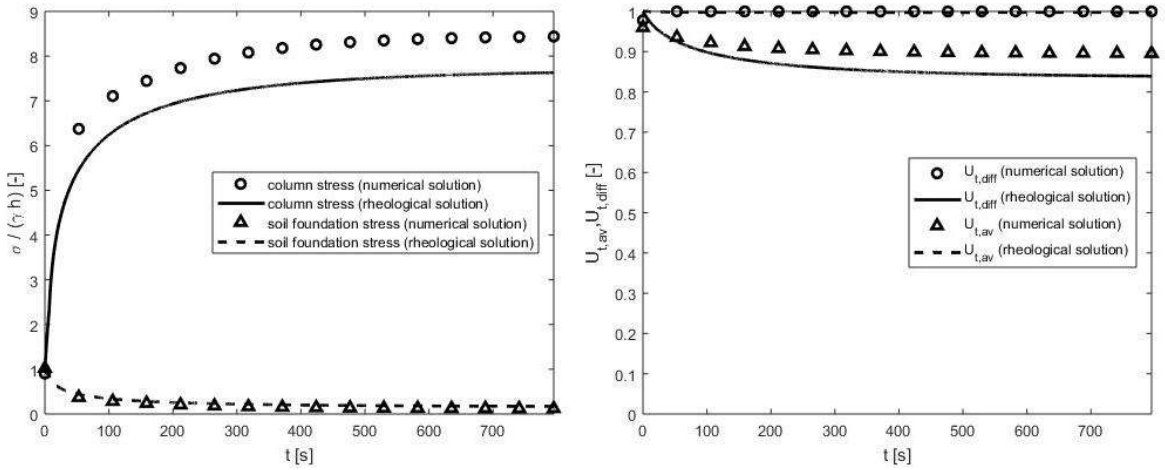

Figure 3. *Comparison between rheological model and numerical model. (a) normalized stress acting on the column and on the foundation soil; (b) normalized differential and average displacements.*

3. RESULTS

For the sake of brevity, the results relative to one reference geometry (d = 0.5 m, s = 1.5 m and l = h = 4 m) are discussed. The constitutive parameters employed are enlisted in Table 1.

Table 1. *Mechanical parameters*

	Unit weight (kN/m3)	**Young modulus (MPa)**	**Poisson's ratio (-)**	**Friction angle (°)**	**Dilatancy angle (°)**
Column	25	30000	0.3	-	
Embankment	18	10	0.3	30	0
Foundation soil	18	1	0.3	40	0

With the aim of validating the model, the obtained results have been compared with the numerical results. A satisfactory agreement in the development of the stress acting on both the column and the foundation is obtained (Figure 3.a).

In Figure 3.b both the average and differential displacements at the top of the embankment (ut,av and ut,diff, respectively) have been normalized with respect to the displacement that would be obtained for the corresponding system without piles (u_0) as it follows:

$$U_{t,av} = 1 - \frac{u_{t,av}}{u_0}$$

$$U_{t,diff} = 1 - \frac{u_{t,diff}}{u_0}$$

The non-dimensional differential displacement at the top of the embankment ($U_{t,diff}$) is 1 for both the models (Figure 3.b), meaning that the dimensional differential settlement in nil. The agreement in the average displacements ($U_{t,av}$) of the rheological model is also satisfactory.

4. CONCLUSION

In this paper, a rheological model capable of reproducing the mechanical response of embankments positioned on a piled foundation is presented. The model considers the evolution with time of stress and settlements. The model results have been validated against 3D numerical analyses data. Due to the satisfactory agreement, according to Authors the model can be employed as a preliminary design tool of pile supported embankments.

REFERENCES

[1] EBGEO, 2010. "*Empfehlungen für den Entwurf und die Berechnung von Erdkörpern mit Bewehrungen aus Geokunststoffen*" vol. 2. German Geotechnical Society, Auflage (in German).

[2] BS8006-1, 2010. "*Code of Practice for Strengthened/reinforced Soils and Other Fills"*, British Standards Institution.

[3] Marston, A. & Anderson, A. O., 1913. "*The theory of loads on pipes in ditches and tests on ce-ment and clay drain tile and sewer pipe"*, Bullettin No. 31 Engineering experiment station.

[4] Terzaghi, K., 1943. "*Theoretical soil mechanics"*. Chapman And Hali, Limited John Wiler And Sons, Inc; New York.

[5] di Prisco, C., Flessati, L., Frigerio, G. and Galli, A., 2019. "*Mathematical modelling of the mechanical response of earth embankments on piled foundations"*, Géotechnique, Accepted for pubblication.

MAIN CAUSES OF INJECTION BORE ANCHORS FAILURES WITHIN CIS COUNTRIES

Vladimir Matsiy*, *LLC SLC GeoProekt, Kuban State Agrarian University, vmatsiys@gmail.com*

ABSTRACT

This paper involves discovering how specific steel characteristics and technological processes influence the slope stability and safety of automobile roads in sites where there is a danger of landslides. Ground anchors became quite common landslide protection engineering measure in the last decade within CIS countries. Struggle between various ground anchor manufacturers causes variety of bore-injected ground anchors in their construction and their technical details. Furthermore, increasing some of steel characteristics can cause decrease of other important steel properties. On this point we can observe cases, when ground anchor walls break down, and other cases, when due to the problems with construction corrosion appears on the geotechnical structures. The aim of this research was to compare "good" and "bad" cases of ground anchor implementation and determine optimal properties (hardness, rigidity, etc.) of anchor components.

Keywords: Geotechnical Engineering, Ground anchors, Landslide protection, Landslide Risk, Russia.

1. INTRODUCTION

Last decades due to the development of transportation infrastructure there are loads of works within hazardous areas. In many cases development of automobile roads and railways imply excavations and affection on the integrity of soil missives. Moreover, different actions on the construction site of the road in landslide zones, especially within mountainous areas, can cause slope instability. So there was a need in not only technical and financial efficient engineering protection complex of measures, but also "easy to" deliver and install system. In that injection bore ground anchors became a salvation. After Ischebeck Titan breakthrough product has shown its advantages a number of bore-injected ground anchor enterprises have appeared. The compete for the pocketbooks of customers between them all brought various cases of ground anchor implementation. Even more, according to the results of some works we can see the extent of several factors (materials, cement and sand grout slurry, transportation, etc.).

2. INJECTION BORE ANCHORS

2.1. Injection Bore Anchor Components

Injection bore anchors consist of threaded hollow steel bar, nut, plate, couplers (sleeves) and spacers [1]. Every component has its purposes. Otherwise every component of each injection bore anchor should be made by one manufacturer. Composing ground anchor from components made by different enterprises could lead to the various failures of this construction due to the difference between threads, sizes, etc.

Also there is another significant component of this construction – grout. Grout is a protection layer of ground anchor. It provides not only shearing stress protection, but also anticorrosive protection. Secondary, delivery of cement allows to get rid of drill cuttings from the borehole and increase bearing capacity of injection bore anchors. The list of requirements for grout are prescribed within number of CIS standards. Brief requirements are given in table 1.

Table 1. *Prescribed grout properties*

Property	Unit of measurement	Prescribed values
Density	g/cm^3	> 1.8
Cement setting time	Hour	> 1
Hardening temperature	°C	8-10
Compressive strength in 7 days	MPa	> 21
Compressive strength in 28 days	MPa	> 30
Relative viscosity	Second	< 30

In case of building in areas with low temperatures additives should be used. Also, to stabilize temperature conditions from low to normal (above 8-10°C) ash is most financial and technological efficient measure.

2.2. Stress-Strain Curves

In debates, which ground anchors are better there is a quite common argument – sustainability for stresses of a steel bars. But in many cases the more loads could steel bars bear, than harder it is. According to the resistance of the materials studies [2] we now the stress-strain curves (figure 1). Low-carbon steels are ductile. When stresses become intolerable, this steel starts to deform on the point "Y". Their yield stress capacity is long enough, before failure appears on the point "F".

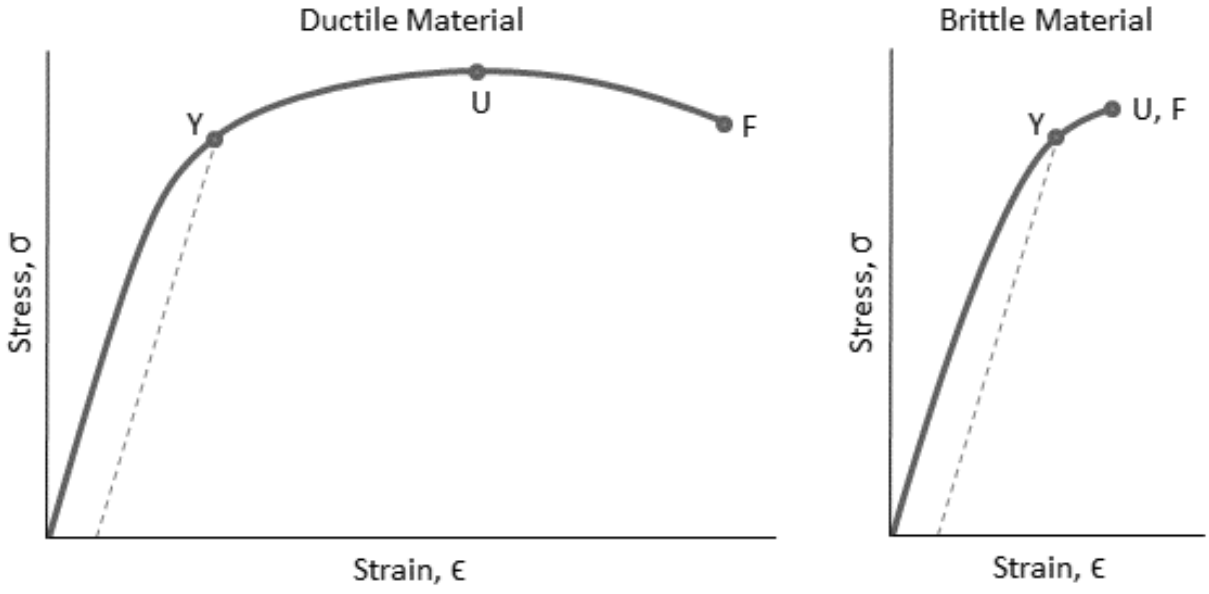

Figure 1*. Stress-strain curves*

High-carbon steels are not applicable in bore-injected ground anchor systems for a several reasons. According to the figure 1, the steel should be ductile. It is very important in case of ground anchor can lose its bearing ability, so in the moment, when stresses are not tolerable, considerable strain could be visualized and measures could be taken on time. Otherwise, financial and social losses could be much more horrifying. In some cases, it is pretty useful to install sensing systems [3] to control the deformations and take urgent measures and maintenance, if stress is more than enough.

3. INJECTION BORE ANCHORS IMPLEMENTATION CASES

3.1. Bad Cases of Bore-Injected Ground Anchors Implementation

Due to the significant implementation increase of the ground anchors many failures appear. There are number of reasons for it. First of all is about steel bars mechanical properties. The difference between national standards and distinctions between steel grades cause a number of failures, that we can classify in two types: high-carbon steel bar deformations during the drilling process and failures during the exploitation. Broken anchor is shown on figure 2. There were two main causes of its failure. The first cause was the brittle steel that threaded steel bar had been made from. Another reason of this kind of failure was the drill bit. As it is shown on the figure 3 drill bit was misshapen badly, while the drilling process. Moreover, there is only one opening in the drill bit and it is straight to the drilling destination. It means, that grout cannot go up within the borehole and cover the steel bar. Consequently, injection bore anchor loses its bearing capacity and brakes down. The fundamental problem – is quite meagre regulatory framework.

Figure 2*. Shear of the anchor steel bar*

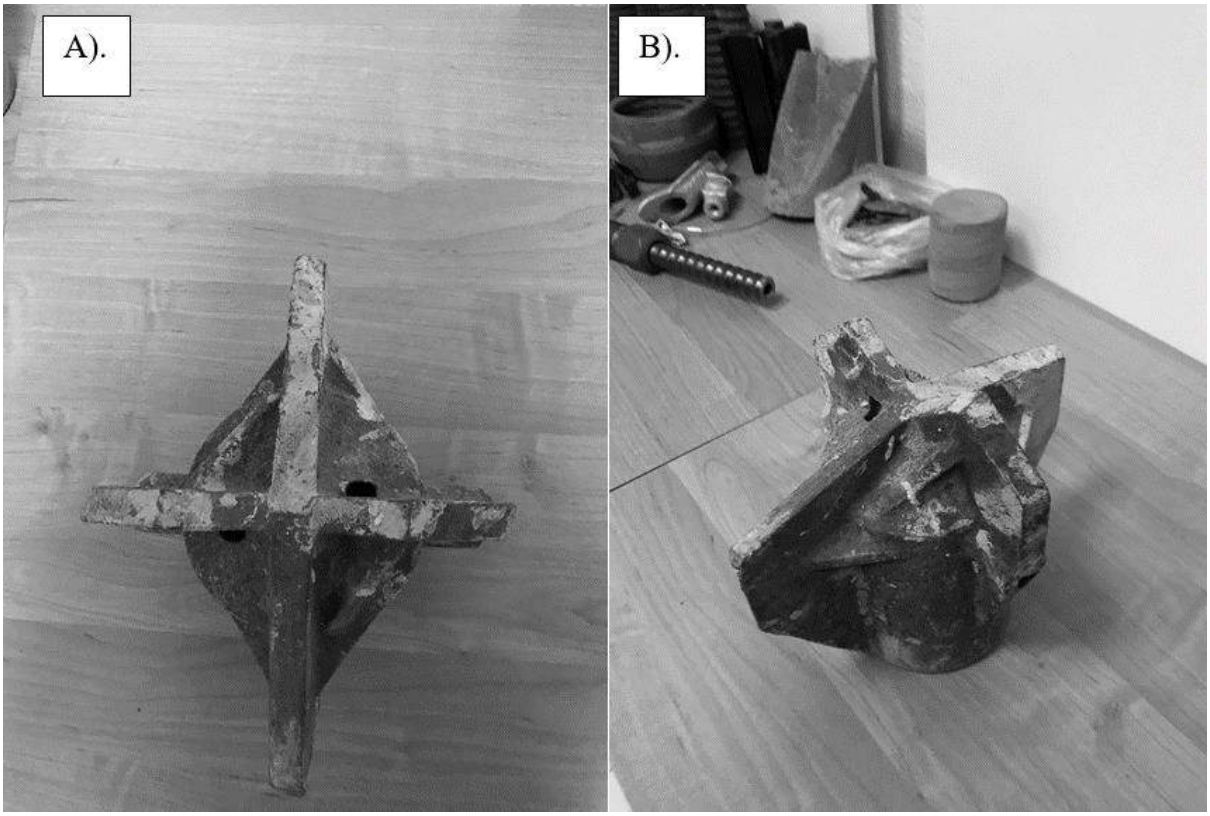

***Figure 3**. Misshapen ground anchor drill bit*

Protection from corrosion is another important factor to retain bearing capacity. Another point of anti-corrosion protection is various chemical covers. Failure (figure 4) appeared due to the poor anti-corrosion covers. Information about corrosion protection presented in EN 1537:2014 [4], but CIS countries do not work with EN standards. Again, regulatory framework should be reworked to solve this kind of problems.

***Figure 4**. Corrosion of the construction*

Figure 5*. Poor grout of the injection bore anchor*

The grout coating of the steel bars is one from many anti-corrosion measure. Cement envelops the steel bar, so if there are some micro deformations in steel surface, integrity of the engineering structure will be retained. Poor grout, caused by number of reasons (bad drill bit construction, low pressure while grouting) otherwise can cause serious damage to the construction (figure 5). Observing a number of experimental injection bore anchors it was found that the modulus of elasticity (E) of the steel bar, used for that type of construction should be equal to 210 N/mm^2. This Young's modulus value provides enough strain resistance of steel bar-grout system.

3.2. Ways the Failures Could Be Prevented

On behalf of the program of harmonization of the European and Russian standards a several upheavals appeared. One of many is that translated EN's has a lot of references to another European documents, that still not imported into the national standard program. Analyzing national standards, the main cause of unfavorable condition was found. Alongside of the ground anchor popularization there is a need for number of national standards within CIS countries. Each standard should regulate each branch of its implementation (design, production, installation, anticorrosive measures, etc.). So, the most efficient way to solve that problem would be to rework the building rules and governmental requirements for the ground anchors, dividing some building rules into particular documents that should encompass various fields, where this type of construction is used (soil-nails, micropiles, ground anchors).

4. FURTHER DISCUSSION

As some recommendations there are several things, that should be followed, when ground anchors are chosen as an engineering protection measure of the slope. Steel bars should be made of ductile material. High-carbon steels are quite an unfavorable option, due to their properties. Recommended mechanical properties for steel bars are shown in table 2. Values in table 2 are provided by long-term experiments that were held on a construction sites.

Table 2. *Recommended mechanical properties for the steel bars*

Property	Unit of measurement	Recommended values
Yield stress	N/mm^2	430-600
Tensile strength	N/mm^2	550-730
Elongation	%	17
Impact toughness (-20°C)	J/cm^2	40
Impact toughness (-50°C)	J/cm^2	27

5. CONCLUSION

The problem of the injection bore ground anchors failure can be eliminated. It will, however, take time, money, and a combined effort on the part of many specialists. Restriction for using ground anchor components from various manufacturers is one of the most rapid and effective measures. The bore-injected system should be produced by one manufacture and makers should be responsible for their production, especially for defects and aberrations. Moreover, there is a need for complex design approach within CIS standards.

ACKNOWLEDGEMENT

I want to bring my acknowledgments to my father, professor Sergey Matsiy for his patience and for being an example to follow. Also I express my sincere thanks to the collective of the LLC SLC GeoProekt for knowledge they gave me.

REFERENCES

[1] Santhosh H.P., Chethan Gowda, R.K., Rajashekhara Swamy, H.M., 2016. "*Analysis, design and construction of tie-back anchor for coffer dam*", International Journal of Civil Engineering and Technology (IJCIET), Volume 7, Issue 6, November-December 2016:371-377.

[2] Anonymous, 2014. "*Mechanical Properties of Materials*", Retrieved 15 March, 2019 from https://mechanicalc.com/reference/mechanical-properties-of-materials.

[3] Choi S.W., Lee J., Kim, J.M., Park, H.S., 2013. "*Design and Application of a Field Sensing System for Ground Anchors in Slopes",* Sensors, https://doi.org/10.3390/s130303739.

[4] DIN EN 1537-2014, 2014. "*Execution of special geotechnical works – Ground anchors*", DIN, EU.

SIMSG ISSMGE

MUĞLA SITKI KOÇMAN ÜNİVERSİTESİ

ZMGM
ZEMİN MEKANİĞİ VE GEOTEKNİK MÜHENDİSLİĞİ DERNEĞİ

WORKSHOP ON

CHALLENGES OF OFFSHORE GEOTECHNICAL ENGINEERING

25th September, 2019

Bodrum, Muğla-Turkey

Phillip WATSON
UWA-TC209 Chair

Harun Kürşat ENGİN
NGI

Gülin Tjelta YETGİNER
EQUINOR

Bas van DIJK
ARCADIS

Mehmet Barış Can ÜLKER
ITU

Antonia MAKRA
FUGRO

Joint Event of

1st MYGEC
1st Mediterranean Young Geotechnical Engineers Conference

&

27th EYGEC
27th European Young Geotechnical Engineers Conference

FUGRO

SIMSG ISSMGE

MUĞLA SITKI KOÇMAN ÜNİVERSİTESİ

ZMGM
ZEMİN MEKANİĞİ VE GEOTEKNİK MÜHENDİSLİĞİ DERNEĞİ

A SERIES OF INTERNATIONAL EVENTS FOR GEOTECHNICAL ENGINEERS

23-27 September, 2019

Kefaluka Resort Hotel Bodrum, Muğla-Turkey

1st MYGEC

1st Mediterranean Young Geotechnical Engineers Conference

23-24th September, 2019

27th EYGEC

27th European Young Geotechnical Engineers Conference

26-27th September, 2019

WORKSHOP

Challenges of Offshore Geotechnical Engineering

25th September, 2019

FUGRO

ZEMİN ETÜD ve TASARIM A.Ş.

TREVI

BODTO T.C. BODRUM TİCARET ODASI BODRUM CHAMBER OF COMMERCE